# A Portable EIT System for Emergency Medical Care


By:

Seyedeh Bentolhoda Ayati

Supervisors:

Dr Kaddour Bouazza-Marouf

Dr David Kerr


A thesis presented to


Wolfson School of Mechanical and Manufacturing Engineering

Loughborough University


March 2016

To my husband and my parents in Iran

**Acknowledgments**

First and foremost, Dr Kaddour Bouazza-Marouf and Dr David Kerr deserve all my gratitude in the past four years. I appreciate that they offered me this opportunity to research in the field of Electrical Impedance Tomography and their continuous support for my whole 4-year PhD study. I could have achieved nothing without their guidance, patience and instruction in the ways of the research world along the journey. I will never forget this pleasant and valuable experience in my entire life. I would like to thank Mr Pete Bracey, the electronic technician in Loughborough University who was a really great help in construction of the EIT system.

I owe what I am to my family in Tehran, Iran. Life alone and away from home made me realize how much I love my family. My deepest gratitude goes to my beloved family for their moral and financial support, without their support my study in the UK would not have been possible. My heartfelt gratitude goes to my beloved husband for his enormous support, encouragement through the most difficult times, without whom indeed I would not have been able to finish this thesis. Special thank goes to my friends, Parisa, Sina, Hossein, Goli, Abolfazl and Somayeh for their support, without them, living in the UK would not have been possible.

# Table of Contents

## Chapter 4. Construction and Evaluation of an EIT System



## Chapter 5. Electrode Layout Optimization



## Chapter 6. Studies Using Ovine Model

## List of Figures

## List of Tables

**Claims of Originality**

The original works are listed as follows:

- Construction of an EIT system with capability of the diagnosis of haematomas pre-hospitalisation or by first-responders when a CT scanner is not available,
- Construction of an EIT system with capability of showing electrode connection failure to the user.
- Detection of epidural and subdural haematomas using EIT.
- Investigation on an optimised electrode layout to prevent unnecessary movements of patient‘s head and the electrode connections to the head would be very quick to configure in emergency care situations.
- Application of hemi-array electrode layout on head.
- Introduction of a novel electrode layout with minimal number of electrodes in an optimised layout, semi-array.
- Implementation of phantom experiments using semi-array and generation of images using weighted pseudo inversion method.
- Application of optimised electrode layouts, hemi-array and semi-array, on head *in vitro* experiments.
- Conduction of *in vitro* experiments using ovine models.
- Introduction of a new experimental method in which the position of the simulated haematoma is known *a priori*.
- Investigation into localization of the simulated haematomas *in vitro* with the accuracy of centesimal.

## Glossary

| | |
|---|---|
| Δ | Accuracy |
| ACT | Adaptive Current Tomography |
| APT | Applied Potential Tomography |
| CCS | Constant Current Source |
| CDP | Conductivity Difference Profile |
| CT | Computer Tomography |
| DDS | Direct Digital Synthesizer |
| EIT | Electrical Impedance Tomography |
| FA | Full Array |
| FEM | Finite Element Method |
| HA | Hemi Array |
| IA | Instrumentation Amplifier |
| ICH | Intracerebral Haemorrhage |
| IVH | Intraventricular Haemorrhage |
| MCU | Microcontroller Unit |
| MRI | Magnetic Resonance Imaging |
| MUX/DEMUX | Multiplexer and De-multiplexer |
| PCB | Printed Circuit Board |
| ROI | Region of Interest |
| PS | Power Supply |
| PSF | Point Spread Function |
| QI | Quantity Index |
| SA | Semi Array |
| SNR | Signal to Noise Ratio |
| TSVD | Truncated Singular Value Decomposition |
| WMNM | Weighted Minimum Norm Method |
| WPI | Weighted Pseudo Inversion |

**Abstract**

Electrical Impedance Tomography (EIT) is a medical imaging technique in which images of tissue conductivity within a body can be inferred from surface electrode measurements. The main goal of this study is to develop a portable EIT system incorporating an optimized electrode layout to detect intracranial haematomas for use in emergency care. A growing haematoma can cause severe and even permanent damage to the delicate tissue of the brain, morbidity, and eventual death of the patient. No capability is at present available for the diagnosis of haematomas pre-hospitalisation or by first-responders. The lack of this crucial information can lead to bad decisions on patient management, and in particular, where to send the patient. Blood has a high electrical conductivity contrast relative to other cranial tissue and can be detected and monitored using electrical impedance methods. EIT is a non-invasive, low-cost monitoring alternative to other imaging modalities, and has the potential to detect bleeding and to localize the approximate bleeding site. A device of this nature would reduce treatment delays, save on costs and waste, and most significantly, positively impact patient outcomes.

The first step was a numerical simulation study on FE models. The full array and the hemi-array electrode layouts were modelled and the anomalies were simulated in different positions with different sizes. The results were obtained using TSVD and WMNM reconstruction methods by COMSOL linked with MATLAB. The simulated anomalies were detected for all the positions using both layouts; however those from the full array were in general superior to the hemi-array.

In order to perform realistic experiments, a prototype EIT system was constructed in the laboratory. The constructed EIT has 16 channels and operates in the frequency range of 10 kHz to 100 kHz with a temporal resolution of 100 frames per second and high level of accuracy of 93.5 %. The minimum number of 8 electrodes was chosen in this study for emergency care. Minimizing the number of electrodes speeds up the electrode setup process and avoids the need to move the patient's head in emergency care.

In the second part of this study, phantom experiments were performed to find an optimised electrode layout for emergency care. The full array and the hemi-array were investigated using phantom experiments. As expected, the full array layout had the best performance in

general; however, the performance of the hemi-array layout was very poor. Thus a novel optimised electrode layout (semi-array) for emergency care was proposed and evaluated in phantom experiments. For the hemi-array and the semi-array layouts, measurement sensitivity depends strongly on the anomaly location since the electrodes are not placed all over the head. The HA layout performed very badly, with the best radial localization error of 0.8100 mm, compared to the SA layout with the worst error of 0.2486 mm. Some reconstructed anomalies located far from the electrodes in the posterior region were almost invisible or erroneous for the hemi-array layout; however, it is enhanced by using the semi-array layout.

Finally, *in vitro* experiments were conducted on ovine models. In most of the experiments carried out by other researchers, since the location of the simulated anomalies was not known and the simulated blood was normally injected into the body or the head, localization of the anomalies was not considered and the quantity of the injected blood was investigated solely. In our new method of experiment, the position of the anomalies was known *a priori* and thus could be compared accurately to the EIT results. The full array and the semi-array layouts were compared in terms of detection, localisation and size estimation of haematomas. As expected, the full array layout was found to be more robust than the semi-array layout with the best mean value of the localization error of 0.0564 mm and the worst QI error of around 30%.

Using a minimum number of electrodes in an optimised layout is always desirable in clinical applications. The semi-array 8-electrode layout prevents unnecessary movements and the electrode connections to the head would be very quick in emergency care. Although the semi-array 8-electrode layout reduced the sensitivity of the measurements, the findings from the experiments indicated its potential to detect and monitor haematomas and probably extend its application for emergency applications where the required accuracy is not critical.

CHAPTER

1

# Introduction

## 1. Clinical Need

Brain injuries occur more frequently than breast cancer or AIDS. In England alone, the National Institute of Health and Clinical Excellence (NHS) recently estimated that around 700,000 people are treated in the emergency departments for head injuries every year. Amongst these emergency department attendances, 30% are children (age<16) and the highest rate belongs to the age range between 15 and 24 years old (Dinsmore 2013, Treasure 2007, Patel *et al.* 2005). Due to the substantial number (around 8 people per 100,000) of related deaths, head injury is the main cause of fatality among young adults and children in the UK and may become the most common global cause by 2020 (Dinsmore 2013). The most common causes of head injury in the UK are falls, motor vehicle collisions, sporting injuries and assaults (Yates 2007). Intracranial haematomas are pockets of blood that build-up within the cranial vault as a result of haemorrhage from a head injury.

### 1.1.Haematoma

A haematoma is a localised swelling that is filled with blood as a result of a haemorrhage, which is an active bleed that can be spontaneous or caused by trauma. The blood is usually

clotted or partially clotted, and the haematoma may grow in size depending on the rate of the absorption of the blood clot by the body. An increase in size of the haematoma is a serious condition. Such pockets of blood increase the intracranial pressure on the brain, impairing the ability of the brain to function and worsening the neurological condition of the patient. If left unchecked, the growing haematoma will cause severe and even permanent damage to the delicate tissue of the brain, and even the eventual death of the patient. The development of the haematoma from benign to symptomatic can be sudden and a patient can change from lucid to a state of rapid neurological deterioration over a very short period of time. Haematomas are typically diagnosed by neurological assessment in the emergency room followed by a Computer Tomography (CT) scan. CT scanners are not portable and thus a diagnosis cannot be made until the patient is delivered to the hospital. There are effective and well established neurosurgical treatments for haematomas with good rates of survival, provided that neurosurgical provision is available, and neurosurgical treatment can be administered with expedience. The time taken for injury-to-diagnosis-to-treatment is a key factor in patient outcome, and must be minimised for a patient to make a full recovery. Current clinical guidelines dictate that patients requiring neurosurgical assistance should be treated within four hours (Wysoki et al. 1998, Hadded et al. 2000).

Hematomas based on the area of occurrence and their location, are usually classified as follows (Figure 1-1):

- *Epidural* Haematomas, occur because of trauma and a tear in an artery, often to the temple, where the middle meningeal artery is located. They form between the skull and the dura-mater. Because of the way the dura-mater is attached to the skull, small haematomas can apply significant extra pressure on the brain (OhioHealth 2005).
- *Subdural* Haematomas, occur because of trauma and a tear in veins beneath the dura-mater in the brain. A subdural haematoma is very close to the brain and may cause a serious problem. Based on how quickly the subdural haematoma occurs from the time of injury, it can be classified into *chronic*, *sub-acute*, and *acute*. A chronic haematoma is developed from a very slow bleed which takes days or even weeks to appear. This type of subdural haematoma is not very dangerous. The second type is more serious and occurs between 2 to 10 days from the day of injury. An acute haematoma, which

occurs within the first 24 hours of the injury, is the most dangerous but a less common type, (OhioHealth 2005).

- *Intracerebral* Haematomas, occur within the brain parenchyma itself due to bleeding caused by a trauma or uncontrolled high blood pressure (OhioHealth 2005).

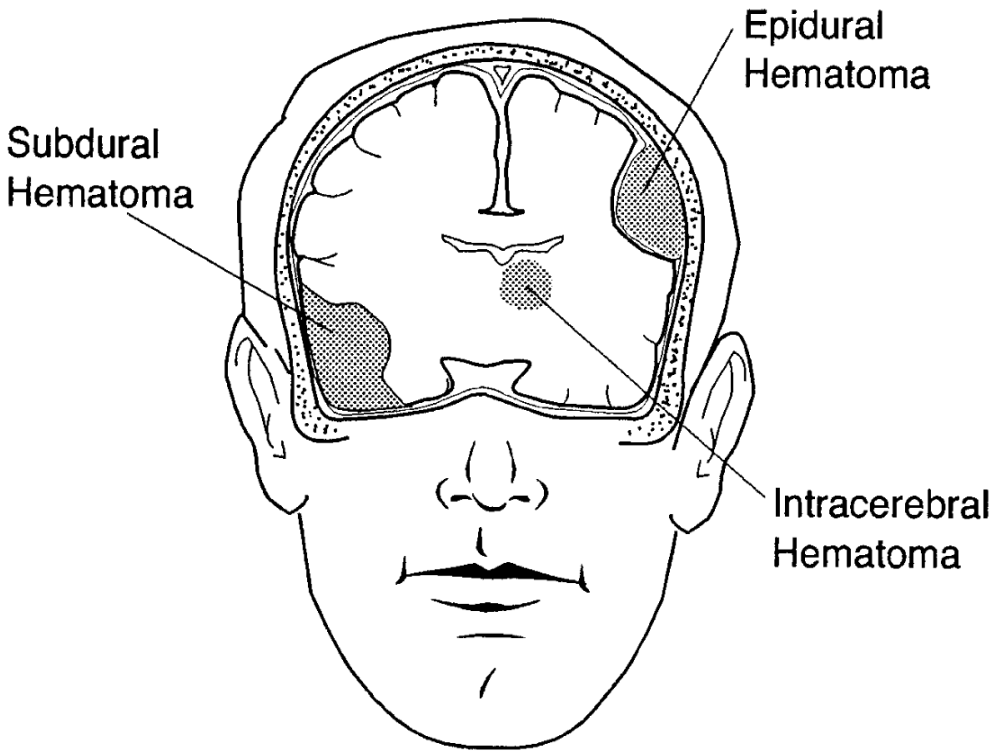


Figure 1-1 Types of Haematomas (OhioHealth 2005).

### 1.2.Current Modalities for the Monitoring of Haematoma

Imaging of the head is the first action taken when a patient arrives in the emergency department on suspicion of head injury, to identify the necessity of urgent surgical intervention or stabilization to prevent further injury. The current appropriate imaging technique used in the *acute* phase is CT scanning which is able to detect space-occupying haematomas within 30 seconds. However, CT scanning in the UK is not always available for 24 hours a day, and in cases of multiple traumas, it may not be possible to scan the patient until they have been adequately stabilised. Although the sensitivity and resolution of Magnetic Resonance Imaging (MRI) is higher than that of CT, the transporting requirement of ill patients and equipment compatibility restrict using this method in *acute* cases. MRI is normally used for *subacute* imaging in order to improve information about prognosis while

recent studies have illustrated the poor capability of CT in prognosis. The availability of MRI is also restricted in the UK to use for imaging of some head injuries (Yates 2007).

No capability is available for the diagnosis of haematomas pre-hospitalisation or by first-responders. The lack of this crucial information can lead to bad decisions on patient management, and in particular, where to send the patient. For example, should the patient be sent to a nearby local hospital for stabilisation, or to a regional neurosurgical centre, which may be further away, but is equipped for emergency neurosurgery? A recent report by the National Confidential Enquiry into Patient, Outcome and Death (NCEPOD) (Treasure 2007, Patel *et al.* 2005) found that: 1) More than half of patients that required neurosurgical advice were taken to hospitals with no on-site neurosurgical provision, 2) only 14% of patients requiring secondary transfer to a neurosurgical centre had access to neurosurgical treatment within four hours, and 3) patients treated in a non-neurosurgical centre had a 26% increase in mortality and a 2.15 fold increase in risk of death compared to patients treated at a neurosurgical centre. First responders, and those responsible for pre-hospital care, need more information on the neurological condition of their patient. In particular, they require information on potentially evolving haematomas which may need prompt and rapid action. This information is vital for proper triage, and to ensure the best possible decisions are made for the patient's welfare.

There is thus a direct and urgent clinical need for a robust, low-cost, and portable device which can: 1) accurately detect the presence of a haematoma in high risk patients, and which can be used in the earliest phases of triage; 2) continuously track the development of a haematoma in real-time when serial CT scanning is unsuitable or impossible, e.g. intensive care; and 3) provide a primary means of haematoma detection when a CT scanner is not available, e.g. remote communities, offshore environments, developing countries, and battlefields.

A device of this nature would reduce treatment delays, save on costs and waste, and most significantly, positively impact patient outcomes. It would also provide a primary and possibly sole method of haematoma detection when MRI or CT scanning are unavailable or impossible. The time from injury-to-treatment is a key factor in patient recovery, and earlier diagnosis leads to earlier treatment. This ensures the optimum patient route – e.g. local hospital or neurosurgical centre – can be chosen and the best course of clinical care followed

for the patient's particular needs. Costs and waste are reduced by improving patient management, by precluding the need for expensive and perilous secondary transport from local hospital to specialist centre, and by reducing costs associated with prolonged patient morbidity. Patient outcomes benefit from reduced delays in treatment and the ability to continuous track a haematoma.

Haematomas are typically diagnosed using MRI or CT scan in hospitals; however, these imaging techniques are not portable and suitable for continuous monitoring and determining the rate of bleeding and involve large personnel or equipment cost. Because blood has a high electrical conductivity contrast relative to other cranial tissue, its appearance can be detected and monitored using electrical impedance methods. Electrical Impedance Tomography (EIT) is a non-invasive, portable, low-cost monitoring alternative to these imaging systems, and has the potential to measure bleeding rate and approximately localize the bleeding site (Henderson 1978). EIT is a medical imaging technique which reconstructs the images of the internal electrical properties within a body from electrical measurements made at a series of electrodes attached to the surface. EIT has been studied in different clinical areas such as brain imaging, thorax imaging and breast imaging (Holder 2005).

## 2. Medical Imaging

Imaging of the internal organs is one of the most important aspects in modern medicine in the diagnoses of diseases. The history of medical imaging was initiated when Wilhelm Conrad Röntgen in 1895 produced an image of his wife's hand using his newly invented x-ray machine. Then it was improved to the Computerised Tomography technique, CT-scan, in the 70's (Bautz 2005). The next technique, Emission Computed Tomography (ECT), came with the utilisation of radiopharmaceuticals (Cassen *et al.* 1949). The CT-scan and ECT rely on ionizing radiation; therefore their finite potential detriment limits their usage especially for pregnant women and children (Elliott 2005). MRI, pioneered in the 1970s, (Kandel *et al.* 1991) produces images by displacing the equilibrium magnetisation vector with a radio frequency (RF) pulse then observing the signal as the magnetisation vector returns to equilibrium (Lauterbur 1973). Although the above mentioned techniques carry some superiority in terms of spatial resolutions, they also pose some disadvantages: high cost, invasive, and non-portable. It is also difficult to use these techniques continuously as a long-term monitoring tool for patients due to radiation damage and non-portability. Their detection

efficiency depends much on the expertise of the operators. Some clinical symptoms may be apparent after some hours and even days of losing critical amounts of blood, which is dangerous for patients and might lead to complications and sometimes coma, disability and eventually death. Therefore an imaging technique that offers low cost, non-invasive, compact, portable and continuous monitoring for suspected bleeding would be of massive use in urgent care facilities, or in home healthcare settings. Electrical Impedance Tomography (EIT) at the scene of an injury would be an affordable and practical way for early detection by creating initial imaging and permitting rapid treatment.

### 2.1.Electrical Impedance Tomography

Electrical Impedance Tomography is a novel medical imaging method which reconstructs images of the distribution of the internal electrical properties of an object inside a body based on non-invasive voltage measurements on its boundary (Henderson 1978). Data acquisition is performed through an array of electrodes which are attached to the surface of the object under investigation while electrical currents are passed to the electrodes. Sequences of small, harmless alternating currents, typically of frequencies between 1-100 kHz and amplitudes of between 1-10 mA, are injected into the object through one pair of electrodes and the corresponding boundary electric potentials are measured over the same or a predefined set of the remainder of the electrodes. The process is repeated for numerous different current injection configurations and voltage measurement sequences. An estimation of the spatial distribution of the electrical properties inside the object is reconstructed by using the measurement data and the background conductivity distribution within the area of interest. Figure 1-2 illustrates a typical EIT system.

### 2.2.EIT Applications

EIT has numerous applications in many areas, mainly clinical, industrial and geophysical. The first study using EIT was published in 1930 for a geological application (Stefanesco *et al.* 1930). EIT has also been used for industrial purposes such as imaging of fluid flows in pipelines (Dickin 1996), imaging material distribution within process vessels (Heikkinen *et al.* 2006), crack detection (Alessandrini *et al.* 1999), detecting air bubbles in pipelines (Ijaz et al. 2008), detecting the free surface between liquid and air (Tossavainen *et al.* 2004), imaging heterogeneities of sandy samples (Borsic *et al.*2005), groundwater studies (Nobes 1996), detecting corrosion faults in metallic plates (Vilhunen *et al.* 2002), landmine detection by the

military (Wort *et al.* 1999, Wexler *et al.* 1985) and monitoring of tanks for the milk processing industry (Sharifi *et al.*2011). EIT has been used in clinical applications based on the large variation in the electrical property of human tissues of different organs. The main clinical EIT applications are monitoring pulmonary ventilation and perfusion (Campbell et al. 1994, Adler et al. 1997, Frerichs 2000, Newell et al. 1992, Eyuboglu et al. 1989, Brown et al. 1992), monitoring gastric emptying (Dijkstra et al. 1993, Smallwood et al. 1993, Barber 1990), monitoring brain function (Holder 1993), breast cancer detection (Kerner et al. 2002), and haemorrhage detection (Eyuboglu et al. 1989, Smallwood et al. 1993, McArdle et al. 1988, Murphy et al. 1987, Sadleir *et al.* 2009). It is the interest of this study to develop EIT for medical imaging. Ultimately the main focus is detection and characterisation of haematoma inside the skull.

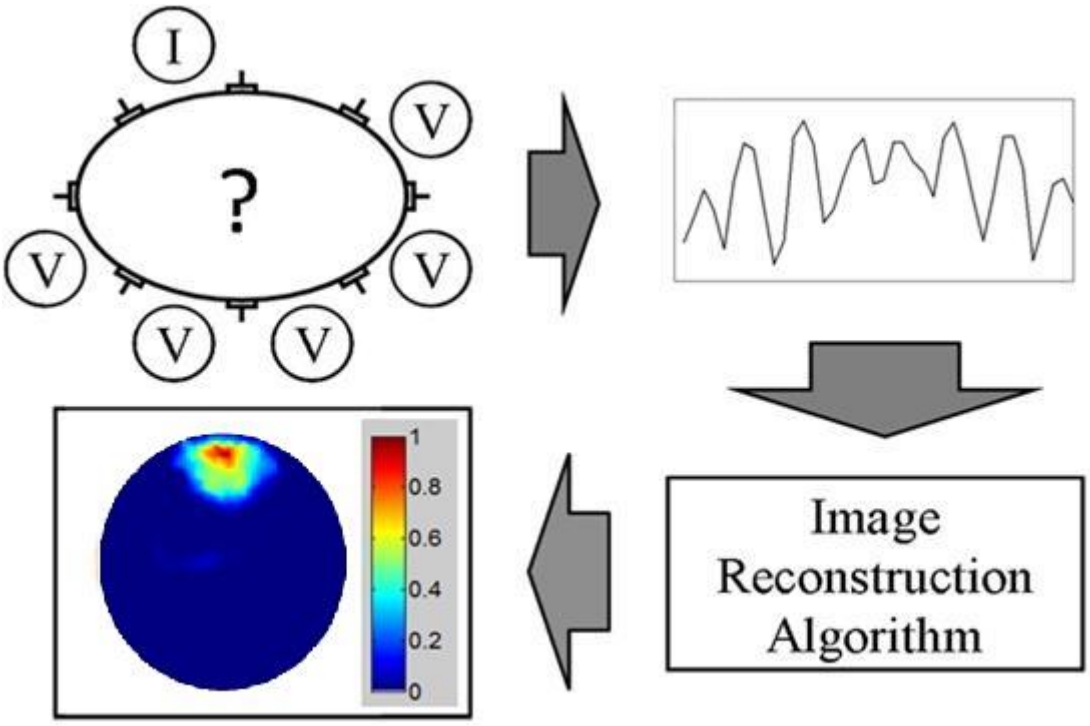


Figure 1-2 Schematic of a typical EIT system. The data is collected using electrodes and processed by an image reconstruction algorithm to produce an image.

### 2.3.EIT Medical Applications

The first use of EIT as a medical imaging technique was proposed by (Henderson *et al.* 1978) and was initially applied to chest imaging (Brown *et al.* 1987, Metherall *et al.* 1996). EIT is used in clinical applications as a diagnostic and monitoring method due to its potential to

distinguish between healthy and abnormal components of an organ based on the electrical property variation of these components according to their state of health (Stoy *et al.* 1982). Changes to the relative volume of these components such as circulating blood or inspired air affect the organ's impedance (Walker et al. 2000, Sha et al. 2002, Keshtkar 2007). Table 1-1 lists the resistivity of different human tissues. Blood is generally easily detectable in the brain since it has a conductivity of one third of that of the cerebrospinal fluid (CSF), which is normally present in the ventricles, and therefore a resistivity increase would be detected in the ventricles during bleeding (Geddes *et al.* 1967, Faes et al. 1999). EIT is a promising tool to detect such impedance changes and has also the potential to quantify the amount of bleeding. Previous use of EIT to estimate the volume of conductive anomalies for some physiological events such as the changes of pulmonary liquid volume (Adler et al. 1997, Adler et al. 1996a), bleeding volume within the pelvic bowl (Thomas et al. 1994), bleeding volume inside the ventricles (Blott et al. 2000), and bleeding rate inside the peritoneum (Sadleir *et al.* 2001) demonstrated its potential for quantitative evaluation. EIT has been successfully employed in several clinical areas such as neuroscience as a new imaging method, for imaging in acute stroke, or for localizing the seizure onset zone in epileptics undergoing pre-operative assessment for neurosurgery (Holder 2005). In terms of internal bleeding EIT provides the potential for long-term continuous bedside detection and monitoring of the occupied space. Using EIT in clinical applications is fast, safe, simple, inexpensive, portable, non-invasive and not operator dependent. The capability of EIT to provide a non-ionizing imaging system is suitable for long term monitoring in surgical planning and diagnosis in comparison to conventional medical imaging techniques.

**Table 1-1:** Resistivity values for tissues (Barber *et al.* 1984).

| **Tissue** | **Resistivity (Ωm)** |
|---|---|
| CSF | 0.65 |
| Blood | 1.54 |
| Liver | 3.5 |
| Cardiac muscle (longitudinal) | 1.6 |
| Cardiac muscle (transverse) | 4.24 |
| Grey matter | 2.84 |
| White matter | 6.82 |
| Lung (out-in) | 7.27-23.63 |
| Bone | 166 |

## 2.4.EIT Systems

EIT was first developed for use in medical applications in 1976 as an impedance camera for producing thoracic images (Henderson et al. 1978). In 1978, EIT was used to study pulmonary oedema by an instrument using a 100 kHz signal to drive 144 electrodes located around the chest. This image was reconstructed assuming that current flowed in straight lines through the body (Henderson et al. 1978). In 1983, Barber and Brown further pioneered impedance tomography and introduced the first system of electrical impedance tomography (Barber et al. 1983). Their 16-electrode APT machine was designed to generate images of the human thorax by employing electrical currents to the body using a pair of opposite electrodes, and measured voltages between adjacent noncurrent-carrying electrodes placed on the periphery of the region to be imaged while current was flowing (Barber et al. 1983).

Since the publication of the first EIT system, many medical EIT systems have been designed and developed for different purposes. The Rensselar's Adaptive Current Tomographs (ACT4) system was designed for use in pulmonary function imaging (Ross 2003). The Dartmouth group designed an EIT system operating between 10 kHz and 10 MHz using 64 electrodes for breast imaging (Halter et al. 2004). The OXBACT system was designed for thoracic imaging by the Oxford Brookes group in intensive care hospital environments et al. 2008). The KHU Mark1 (Oh et al. 2009) and KHU Mark2 (Wi et al. 2009) systems were developed recently for research and commercial purposes in Kyung Hee University, Korea. The Epack1, Epack2 and Epack3 have been designed for the application of intraperitoneal bleeding detection EIT in the University of Florida (Sadleir et al. 2009). The UCLH Mk1b and UCLH Mk2 systems were designed to operate in frequencies between 225Hz and 77 kHz using 16 electrodes for imaging brain function (Yerworth et al. 2003, Yerworth et al. 2002). UCLH Mk 2.5 was recently designed for acute stroke imaging operating between 20Hz-256 kHz (McEwan et al. 2006).

In the neurosciences, non-invasive imaging can be categorised into two broad areas, structural imaging of variations or abnormalities in the brain and functional imaging of normal and abnormal brain activity. The Sheffield Mark 1 EIT system (Brown et al.1987) was the first system used by UCL, for the recording of brain function in animals. This system produced 10 images per second using a ring of 16 electrodes to employ an adjacent current pattern of 5 mA (peak-to-peak) at 5 kHz. Their studies demonstrated the potential of EIT as

an imaging tool in circumstances where blood volume changes occur in the brain. This system was further developed to version Mk2 (Smith et al. 1995) and Mk3.5 (Wilson et al. 2001). The latest system has the capability for 64 electrodes and recording at 30 frequencies simultaneously. This system was validated with tank studies using 30 different frequencies between 2 kHz and 1.6 MHz. It produced acceptable and reproducible images of multi-frequency objects such as a banana in a saline-filled tank (Holder 2005, Yerworth et al. 2003). The University of Manchester group built up a new 32-channel EIT system for brain function imaging with temporal resolution of 100 frames per second and a SNR of 80 dB, operating in the frequency range of 10 kHz to 100 kHz (Rafiei Naeini 2008). A group in the University of Oxford used EIT system to image the whole head for the first time (Murphy et al. 1987). This EIT system based on 16 electrodes was used for imaging neonatal intra-ventricular haemorrhages at 16 frames per second (McArdle et al. 1988). However, no worthwhile data were produced, mainly due to significant artefacts such as breathing movement, variations in cerebral blood flow, heart electrical activity and the infant movement (Murphy et al. 1987, Holder 2005). Nevertheless their early studies have indicated the possibility of using EIT for this application. The next generation of EIT systems will be much smaller in size and use newer technologies. Recently, using EIT for structural imaging of the brain is increasing such as detection of intra-ventricular haemorrhage in a neonatal piglet (Sadleir et al. 2009, Tang et al. 2010), Detection of intracranial haemorrhage in a piglet model (Xu et al. 2010), subarachnoid haemorrhage detection (Dai et al. 2010) and for haemorrhagic stroke determination (Tehrani et al. 2010). Tehrani et al. reported a simulation study on the feasibility of detecting changes in a haemorrhagic lesion located close to the scalp. A realistic FE head model with 31 electrodes was used. To evaluate EIT in detection of changes of ICH (Intracerebral Haemorrhage), a haemorrhagic lesion close to the scalp was created. This could be visually observed in a time difference reconstruction when baseline noise was less than 0.005%.

## 3. Aims and Objectives

The objectives of the work carried out in this study are listed as follows.

1. To develop a portable EIT system incorporating an optimized electrode layout for use in emergency care.

Using an EIT system in clinical applications is safe, low-cost, portable, non-invasive and not operator dependent in comparison to conventional medical imaging techniques. The

implementation of a fast and portable imaging system for continuous monitoring as a routine clinical emergency imaging method will have a significant impact on improving patient outcomes. The proposed EIT system would be used for the early detection and monitoring of haematoma at home, work or in the ambulance during transfer to larger care facilities. This system should be easy and quick to apply. It would also provide a primary and possibly sole method of haematoma detection when MRI or CT scanning is unavailable or impossible.

One future goal is to make this system available as a routine clinical procedure on emergency care. This portable system would have the capability of being carried by the patients after injury or surgery and warn of the existence of any bleeding inside their heads. The proposed system will record the patient details, and store these data to present to a surgeon

2. To reduce and optimize the number of electrodes and their positions to prevent unnecessary movements.

Using a minimum number of electrodes is always desirable in clinical applications since it may speed up the electrode setup process. An optimised electrode layout would also prevent the unnecessary moving or lifting of the patient in emergency applications. The common number of electrodes used in brain imaging applications is 16 or more in a ring or 3D layout. It is intended to reduce the number of electrodes to eight and the position of the electrodes to an optimized layout. The connection of the 8 electrodes to the head in emergency care would be faster and any failed connections would be easier to spot. Using 8 electrodes in a ring layout over the anterior of the head would allow placement mostly on the region of the head which does not have hair; therefore, the connections are more reliable and the possibility of failure is very low.

Using 8 electrodes in the proposed optimised layout may lead to a lower sensitivity in the regions far away from the electrodes. However, more electrodes leads to difficulty of placement and implementation in clinical applications and also some studies have shown that having more measurements may not directly relate to improvements of measurement sensitivity. The EIT image reconstruction is an *ill-posed* problem, meaning that small measurement noise can cause large image artefacts, so another challenging issue in optimised EIT systems is the generation of meaningful images. Therefore, in order to produce meaningful images the problem has to be regularized and some constraints and corrections need to be considered.

One future goal is to mount the 8 electrodes on a belt-like assembly around the head which would make the electrode connection faster and easier. The position of the electrodes and the distance between them would be fixed and not changeable.

3. To detect, localize and quantify intracranial haematomas *in vitro.*

It is essential to evaluate and calibrate the performance of an EIT system that is to be used as an assistive medical system. It is intended to prepare realistic and practical phantom experiments to evaluate the EIT system. Ovine model experiments will be also conducted to investigate the true quality of the proposed optimized layouts to detect, localize and quantify the simulated haematomas. In most of the experiments carried out by other researchers, simulated blood was normally injected into the body or the head and the investigation of the blood location was not considered accurately *in vitro*. Since the actual location of the blood was not known, the quantity of the injected blood was solely considered. Therefore, it is intended to set up an experimental method in which the position of the anomalies are known *a priori* and thus can be compared accurately to the localization results.

One future goal is to detect and quantify any bleeding in a real human head model.

## 4. Outline of the Thesis

This thesis is organized as follows.

In Chapter 1, the clinical need and the significance of existence of an EIT system for emergency care was presented which leads to the ultimate goal of this study. Haematomas and current modalities to monitor haematomas were described. It was pointed out that there is a direct and urgent clinical need for a robust, low-cost, and portable device to detect and monitor haematomas when serial CT scanning is unsuitable or a CT scanner is not available. Then, an introduction about EIT and its applications was given. In Chapter 2, a literature review of EIT methods was given. The forward problem, measurement strategies and electrode layout configurations in EIT were described and the inverse problem, image reconstruction and its regularization in EIT were discussed. In Chapter 3, the first step of this study was demonstrated, which was the numerical simulation study using FE models. The forward and inverse models were generated to obtain images. The full array and the hemi-array layouts were designed to compare their performance to detect and localise the simulated anomalies. In Chapter 4, to perform realistic experiments, the construction and the hardware of the proposed EIT system were described. The performance of this system was evaluated

using primary phantom experiments. More phantom experiments were conducted using the constructed EIT system and the results were presented in Chapter 5. A novel optimised electrode layout (semi-array) was introduced. The advantage of the proposed optimised electrode layout for emergency application was analysed based on the results from phantom experiments. In Chapter 6, the optimised electrode layout was further investigated using ovine models. The details of the *in vitro* experiments were explained. The accuracy of detection, localization and quantification of the simulated intracranial haematomas were demonstrated. In Chapter 7, the results were summarized and discussed. Suggestions for further work were presented in Chapter 8.

CHAPTER 2

# The EIT Methods

## 1. The Forward Problem

The so-called forward problem in EIT is to predict the measured boundary electric potentials from the known applied current density and a combination of the internal conductivity estimation with boundary conditions using a particular model. The concept of the forward problem is illustrated in Figure 2-1. When the model is simple, such as circular geometries in 2D or a spherical shape in 3D, with a homogenous conductivity distribution (Holder 2005, Fuks et al. 1991, Pidcock et al. 1995a, Pidcock et al. 1995b) the forward problem can be solved analytically. However, for the complex geometries and complicated conductivity distributions which are common in medical applications, numerical methods such as the Finite Element Method (FEM) are required to implement the prototype model and predict the output signals (Brenner et al. 1994, Miller et al. 1990).


Figure 2-1 The concept of the EIT forward problem

### 1.1. Formulation of the Forward Problem

In an EIT experiment, a small alternating current is applied to an array of electrodes which are attached around the object, and the resulting voltages are measured on the remaining electrodes. In the following, by assuming that an electromagnetic field is established within a body, Ω, the mathematical model for EIT is derived from Maxwell's equations (Holder 2005, Goharian 2007, Malmivuo et al.1995)

$$\nabla \times \mathrm{E} = -\frac{\partial \mathrm{B}}{\partial \mathrm{t}} \tag{1}$$

$$\nabla \times \mathrm{H} = \mathrm{J} + \frac{\partial \mathrm{D}}{\partial \mathrm{t}} \tag{2}$$

where $\nabla \times$ is the curl operator, E is the electric field, B is the magnetic induction, H is the magnetic field, J electric current density and D the dielectric displacement. Moreover, in a linear isotropic medium the following relations are valid

$$\mathrm{D} = \varepsilon \mathrm{E} \tag{3}$$

$$\mathrm{B} = \mu \mathrm{H} \tag{4}$$

where ε and μ are the electrical permittivity and magnetic permeability respectively. In this study, isotropic properties are assumed. Plane wave definitions for the electrical field and the magnetic field are $\mathrm{E}(\mathrm{x},\mathrm{t}) = \mathrm{Re}(\mathrm{E}(\mathrm{x}).\mathrm{e}^{\mathrm{i}\omega\mathrm{t}})$ and $\mathrm{B}(\mathrm{x},\mathrm{t}) = \mathrm{Re}(\mathrm{B}(\mathrm{x}).\mathrm{e}^{\mathrm{i}\omega\mathrm{t}})$. Using these definitions, equation (1) and (2) are rewritten as the time harmonic Maxwell's equations

$$\nabla \times \mathrm{E} = -\mathrm{i}\omega\mu\mathrm{H} \tag{5}$$

$$\nabla \times \mathrm{H} = \mathrm{J} + \mathrm{i}\omega\varepsilon\mathrm{E} \tag{6}$$

where ω is the angular frequency. The current density J is comprised of $\mathrm{J_c} = \sigma\mathrm{E}$, which is the conduction current density, and $\mathrm{J_s}$ which is the internal current density source such as the brain or heart activity.

$$J = J_c + J_s \tag{7}$$

In EIT $J_s$ is typically zero at frequency ω (Lionheart et al. 2005). Therefore equation (6) can be rewritten as

$$\nabla \times H = (\sigma + i\omega\varepsilon)E \tag{8}$$

The quasi-static approximation (Lionheart et al. 2005) is usually used in order to further simplify Maxwell's equations. The quasi-static approximation is a valid assumption since the frequencies of injected alternating currents are small (Vauhkonen 1997). Using the quasi-static approximation, it can be assumed that ωμH is negligible in equation (5) and the electrical field can be defined as

$$E = -\nabla u \tag{9}$$

where a scalar u is the electrical potential. Substituting Equation (9) into Equation (8) and taking the divergence of both sides, the governing equation for Electrical Impedance Tomography is obtained as follows

$$\nabla.(\sigma + i\omega\varepsilon)\nabla u = 0 \tag{10}$$

If direct or low frequency currents are applied, equation (10) can be rewritten as

$$\nabla.(\sigma\nabla u) = 0 \tag{11}$$

This is the equation that recovers the electric potential u inside the body, Ω. Equation (11) is the governing equation for Electrical Resistance Tomography. But generally EIT researchers used equation (11) as the governing equation since the capacitive term in the biological tissue is negligible at less than 100 kHz frequency (Goharian 2007, Lionheart et al. 2005). In this work, Equation (11) will be used as the governing equation.

### 1.2. Boundary Conditions

The governing equation is a second order elliptic partial differential equation (PDE). Therefore, boundary conditions (BC) need to be specified to solve this equation. In practice, there are two options to define the boundary conditions. One is to inject current as a BC and measure voltages and the other one is to apply voltage as a BC and measure currents. Since it is inaccurate to measure current using a voltage source, thus requiring more complex hardware (Saulnier 2005), in this work injecting current and measuring voltages has been considered. Alternating currents are injected into the electrodes on the surface, $\partial\Omega$, of the body. In order to account for electrode interactions within the object, a reasonable and appropriate model should be developed. In the following section the boundary conditions, i.e., the electrode models are briefly discussed.

#### 1.2.1. Continuum Electrode Model

The Continuum Model is the simplest of the models used in EIT. The model assumes that there are no electrodes facing the boundary of the object, but the model assumes that the current density, J, is a continuous function on the entire boundary of the object. In this case, the relation

$$\mathrm{J}.\mathrm{n}|_{\mathrm{inside}} = -\mathrm{J}.\mathrm{n}|_{\mathrm{outside}} \qquad \text{on } \partial\Omega \tag{12}$$

is valid. Here n is the normal vector to the boundary of the object, $\partial\Omega$. Furthermore, by using equation (9), equation (12) can be recast as a Neumann boundary condition:

$$\sigma\frac{\partial \mathrm{u}}{\partial \mathrm{n}} = -\mathrm{J}.\mathrm{n} \equiv \mathrm{j} \tag{13}$$

where j is the negative normal component of injected current. Equation (13) together with equation (11) is called the Continuum Model. This is a poor model due to the unknown current density, J, for real experiments. In practice, the currents which are injected through the wires and the discrete electrodes are known (Vauhkonen et al. 1997).

#### 1.2.2. Gap Model

The Gap Model assumes discrete electrodes on the surface of an object. The injected current j is represented as

$$j \equiv \sigma \frac{\partial u}{\partial n} = \frac{I_l}{A} \qquad \text{on } \varepsilon_l, l = 1,2, \dots, L \tag{14}$$

$$j \equiv \sigma \frac{\partial u}{\partial n} = 0 \qquad \text{on } \partial\Omega \backslash \{\varepsilon_1 \cup \varepsilon_2 \cup \dots, \varepsilon_L\} \tag{15}$$

where A is the area of the electrode ($\varepsilon$), $I_l$ is injected current into the $I^{th}$ electrode and L is the number of electrodes. The shunting effect of the electrodes and contact impedance are ignored in both the Continuum and the Gap models (Goharian 2007).

### 1.2.3. Shunt Model

The Shunt Electrode Model refines the Gap Model by considering the shunting effect of the electrode (Holder 2005). The conventional way to model the very high conductivity of the electrodes is to impose a constraint by assuming a constant potential, $V_l$, on each electrode. Also the model states that the net current density through the surface of an electrode has to be equal to the total injected current

$$\int_{\varepsilon_l} \sigma \frac{\partial u}{\partial n} ds = I_l \qquad \text{on } \varepsilon_l, l = 1,2, \dots, L \tag{16}$$

$$u = V_l \qquad \text{on } \varepsilon_l, l = 1,2, \dots, L \tag{17}$$

where $V_l$ is the measured voltage on the $I^{th}$ electrode. This model ignores the contact impedances of electrodes (Somersalo et al. 1992). The model is completed by defining an arbitrary choice of ground to ensure existence and uniqueness of the result.

$$\sum_{l=1}^{L} V_l = 0 \tag{18}$$

The results from the Shunt Model unfortunately do not match to experimental data (Goharian 2007, Cheng *et al.* 1989). The Shunt Model does not take into account an electrochemical effect that takes place at the contact between the electrode and the body. This effect is the formation of a thin, highly resistive layer between the electrode and the body.

### 1.2.4. Complete Electrode Model

The Complete Electrode Model is a refinement of the Shunt Electrode Model in which the contact impedance between the electrodes and the object is considered (Somersalo et al. 1992, Paulson et al. 1992). The contact impedance layer exists between the surface of the metal electrode and the object either in medical applications or in phantom studies with ionic solutions. The effect of the contact impedance between the electrode-surface interface is a voltage drop when the voltages are measured on the current carrying electrodes (Hua et al. 1991). This modifies the shunting effect so that the assumption of constant voltage under the electrode is no longer valid. If both the shunting effect of the electrodes and the contact impedance are taken into account the complete electrode model is obtained. This model has improved the accuracy of the simulated voltages to be comparable to the precision of the data acquisition system (Cheng et al. 1989, Goharian 2007). In this model the equation (17) is replaced by following equation

$$u + z_l \sigma \frac{\partial u}{\partial n} = V_l \qquad \text{on } \varepsilon_l, l = 1,2, \dots, L \tag{19}$$

Where $z_l$ is the contact impedance between the $I^{th}$ electrode and the object. The complete electrode model consists of the following equations and the boundary conditions (Polydorides et al. 2002)

$$\nabla.(\sigma \nabla u) = 0 \qquad \text{on } \Omega \tag{20}$$

$$u + z_l \sigma \frac{\partial u}{\partial n} = V_l \qquad \text{on } \varepsilon_l, l = 1,2, \dots, L \tag{21}$$

$$\int_{\varepsilon_l} \sigma \frac{\partial u}{\partial n} ds = I_l \qquad \text{on } \varepsilon_l, l = 1,2, \dots, L \tag{22}$$

$$\sigma \frac{\partial u}{\partial n} = 0 \qquad \text{on } \partial\Omega \backslash \{\varepsilon_1 \cup \varepsilon_2 \cup \dots, \varepsilon_L\} \tag{23}$$

Equation (21) states that the surface measured voltages on each electrode consist of the voltage on the boundary surface underneath that electrode plus the voltage dropped across the

electrode impedance. Equation (22) states that the integral of the current density over the electrode surface is equal to the total injected current to that electrode. Finally, equation (23) means that there is no current entering or leaving the boundary of the object on the inter-electrode gap. In addition, the following two conditions for the conservation of charge and an arbitrary choice of ground are needed to ensure existence and uniqueness of the result (Goharian 2007):

$$\sum_{l=1}^{L} I_l = 0 \qquad \text{(Conservation of Charge)} \tag{24}$$

$$\sum_{l=1}^{L} V_l = 0 \qquad \text{(Choice of a ground)} \tag{25}$$

In order to solve the complete electrode model, which is called the forward problem, commercial finite element software (COMSOL, Burlington MA) was used in this study.

### 1.3. Data Collection

EIT creates a cross-sectional image of the internal conductivity distribution of the brain using the voltage measurements produced by injecting current to the electrodes placed over the surface. The EIT system can be categorized based on the number of electrodes which are used to employ current either as a Pair Drive system or a Multiple Drive system (Holder 2005). In Pair Drive systems, a single current source is used to apply electrical current to a body using a pair of electrodes, and the voltages are measured between another non-driving pair of electrodes. The driving and measuring electrodes are switched to a different pair of electrodes, and so on, in order to collect a complete set of possible measurements between all electrode pairs. This approach is known as Applied Potential Tomography (APT).

The Multiple Drive system, also known as Adaptive Current Tomography (ACT), uses N current sources to drive current simultaneously in more than two or maybe all electrodes while voltages are also measured on multiple electrodes. The latter has greater ability to distinguish subjects (distinguishability) but more hardware complexity (Isaacson 1986). The voltage measurement strategy is mainly divided into two-electrode and four-electrode methods. In the two-electrode method, voltage measurement is done using the same pair of electrodes which are carrying the current. In the four-electrode method, the current-carrying electrodes have not been used to measure voltages. Normally in practice the current-carrying

electrodes are not used for voltage measurements to avoid uncertainties that can arise from the changes of contact impedances in electrodes and the associated increase in measurement error (Borsic 2002). By using a separate pair of electrodes for measuring voltage, the resistance of electrode-skin interface and most of the skin impedance will be excluded in measurements.

### 1.3.1. Electrode Configuration and Connection

In the following section, some of the usual EIT electrode configurations are discussed.

***The Full Array (FA)***

In the Full Array electrode layout, all electrodes are located around a 2D object boundary with equal spaces in between. This method is used to ensure projected current is axially symmetric within the assumed object shape (Barber et al.1987). 16 electrodes are normally used in a 2D array with the same 22.5˚ angle between adjacent electrodes. In order to use 8 electrodes for this model, the angle between two adjacent electrodes is set at 45˚ as shown in Figure 2-2.

***The Hemi-array (HA)***

In the Hemi-array electrode layout, 8 electrodes are positioned on the anterior surface of the body for a patient in emergency cases where the body cannot be moved. This method was used to detect intra-peritoneal haemorrhage (Sadleir et al. 2008). The electrodes are located in 2D with the same angle of 22.5˚ between adjacent electrodes and 225˚ between the bottom pair as illustrated in Figure 2-3. The measurement sensitivity of this method is low in the region which is furthest away from the electrodes.

***Electrode Arrays in 3D***

A 3D expansion of the Full Array, for example using three or four layers of 16-electrode Full Array configurations can be positioned over the volume of interest which is near to cylindrical in shape. These so called Rectangular electrode arrays have also been considered for breast cancer detection (Mueller et al. 1999). In practice for head imaging, a modified 10-20 EEG electrode layout has been normally used (Tidswell et al. 2001). Alternatively, the ‘Cz-RING’ layout uses one electrode located at a position Cz, and the other 15 electrodes are placed equidistantly about the equator of a sphere as indicated in Figure 2-4. This

configuration has been used for head imaging to detect intra-ventricular haemorrhage of neonatal subjects (Sadleir et al. 2009).

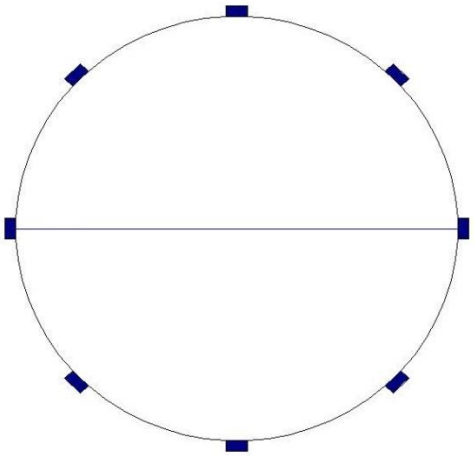

Figure 2-2 Illustration of 8-electrode Full Array applied on the boundary of a disk object.

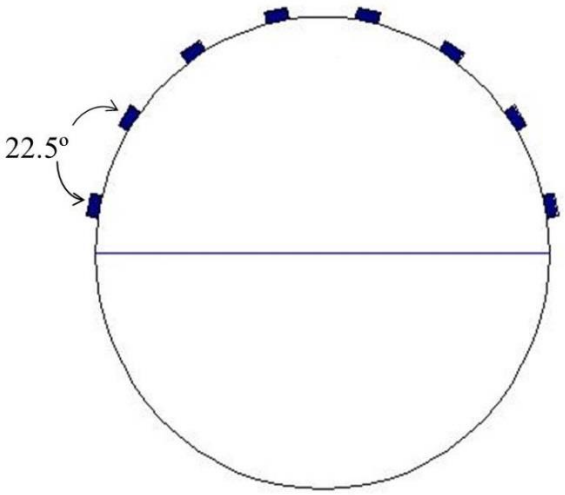


Figure 2-3 Illustration of 8-electrode Hemi-Array applied on the boundary of a disk object.

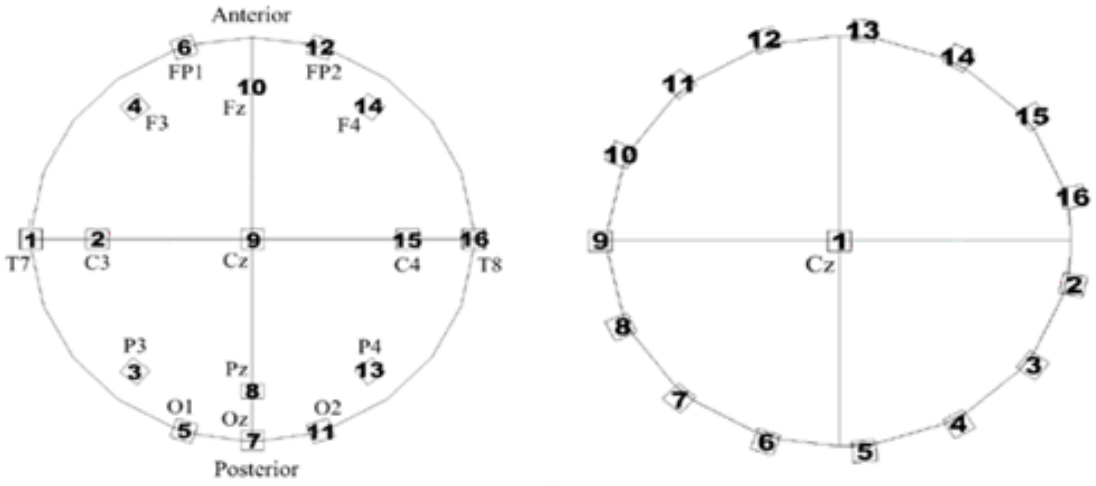


Figure 2-4 EEG layout and Cz-RING layout (Tang 2002).

### 1.3.2. Current Patterns in EIT

Before considering how to reconstruct the impedance images from a set of data measurements, it is worthwhile to plan how and what data needs to be measured. In general measurements of impedance are performed by applying a current to some or all of the electrodes connected to a conductive region and the resulting voltage is measured using a pair of non-driving electrodes. To achieve the maximum amount of information, this is repeated for all the independent measurements by different patterns. There are a number of variations of EIT measuring patterns based on injecting current or applying voltage and measuring outputs by using the same or different electrodes. Some of these measurement patterns are described below.

***Pair Drive Instruments***

Pair drive instruments use a single current source to apply electrical currents to the body. A pair of electrodes is used to apply current and the voltage differences are measured from another non-driving pair of electrodes. The driving and measuring electrodes are switched in order to collect all the possible measurement combinations between the electrodes. This approach is known as Applied Potential Tomography (APT). In the following the most common configurations used in medical applications are presented.

**Adjacent Method (Neighbouring)**

The most commonly used four-electrode injection approach is the Adjacent Drive method also known as the Neighbouring method (Barber et al. 1987, Hua et al. 1988). In this method,

the electrical current is applied to the body through a pair of adjacent electrodes. The voltages differences are collected from another pair of adjacent electrodes which are not carrying current. The voltages are measured while the current is applied to the body. The input pair of electrodes is switched over all adjacent electrode pairs and the measurement procedure is repeated for all possible adjacent pairs to produce a complete voltage data set. Data collection for a 16-electrode system is shown in Figure 2-5. Table 2-1 shows the complete sequence of measurements using the adjacent electrode configuration in the 8-electrode case. This method yields a total of $L(L-3)$ measurements for L electrodes. Due to reciprocity, only half the measurements are independent (Malmivuo et al. 1995). For instance, using 8 electrodes, the total number of independent adjacent measurements is (8×5)/2=20. In this method, the current distribution is very non-uniform as the current is mostly driven in the outer region of the object; therefore, the sensitivity at the periphery is good but poor at the centre. This problem makes the ill-posed nature of the inverse problem even worse (Malmivuo et al. 1995).

**Table 2-1:** Complete sequence measurements using 8-electrode adjacent electrode configuration.

| Input pair | Output pairs |
|---|---|
| (E1, E2) | (E3, E4), (E4, E5), (E5, E6), (E6, E7), (E7, E8) |
| (E2, E3) | (E4, E5), (E5, E6), (E6, E7), (E7, E8), (E8, E1) |
| (E3, E4) | (E1, E2), (E5, E6), (E6, E7), (E7, E8), (E8, E1) |
| (E4, E5) | (E1, E2), (E2, E3), (E6, E7), (E7, E8), (E8, E1) |
| (E5, E6) | (E1, E2), (E2, E3), (E3, E4), (E7, E8), (E8, E1) |
| (E6, E7) | (E1, E2), (E2, E3), (E3, E4), (E4, E5), (E8, E1) |
| (E7, E8) | (E1, E2), (E2, E3), (E3, E4), (E4, E5), (E5, E6) |
| (E8, E1) | (E2, E3), (E3, E4), (E4, E5), (E5, E6), (E6, E7) |

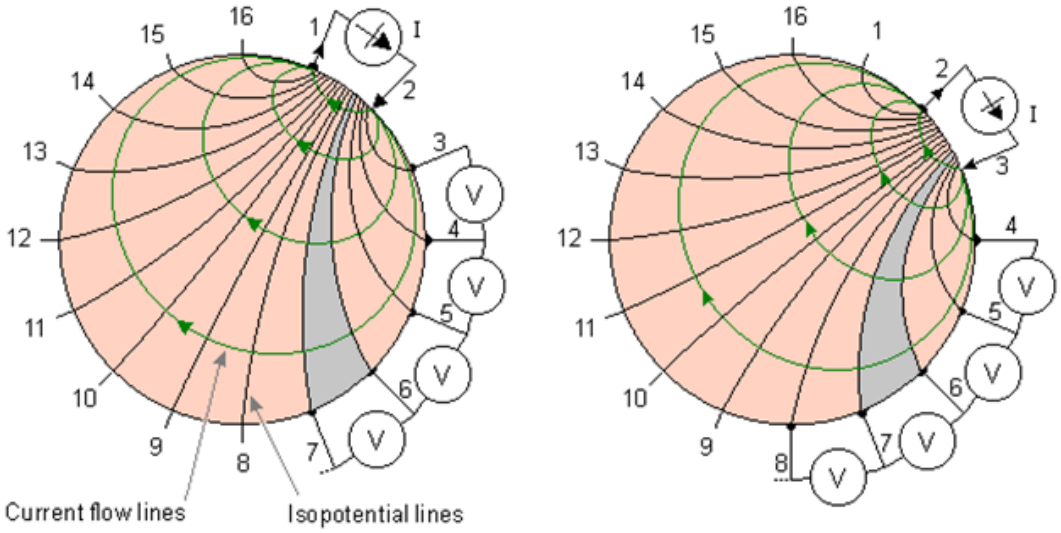


Figure 2-5 Neighbouring method.

**Cross Method**

In the Cross method, to improve the current distribution over the object, current is injected to a pair of electrodes which are more separated from each other (Hua et al. 1988). This method with 16 electrodes is shown in Figure 2-6. At first, one electrode is selected as a current reference (electrode number 16) and one as a voltage reference (electrode number 1) next to the current reference electrode. Then electrical current is applied to a current reference electrode and one of the even numbered electrodes and the voltage is measured on all other electrodes with respect to the voltage reference electrode. The measurement sequence is then repeated to measure a second data set by switching the current and voltage reference electrode. Table 2-2 shows the sequence of measurements using the cross electrode configuration in the 8-electrode case. The Cross method by using 8 electrodes produces 2×3×5=30 measurements of which only 25 are independent. This method has a more uniform current distribution in comparison to the Adjacent method and better sensitivity over the entire region except in the periphery (Malmivuo et al. 1995).

**Table 2-2:** The complete sequence measurements using 8-electrode cross electrode configuration.

| Input pair | Output pairs |
|---|---|
| (E8, E2) | (E1, E3), (E1, E4), (E1, E5), (E1, E6), (E1, E7) |
| (E8, E4) | (E1, E2), (E1, E3), (E1, E5), (E1, E6), (E1, E7) |
| (E8, E6) | (E1, E2), (E1, E3), (E1, E4), (E1, E5), (E1, E7) |
| (E3, E5) | (E2, E4), (E2, E6), (E2, E7), (E2, E8), (E2, E1) |
| (E3, E7) | (E2, E4), (E2, E5), (E2, E6), (E2, E8), (E2, E1) |
| (E3, E1) | (E2, E4), (E2, E5), (E2, E6), (E2, E7), (E2, E8) |

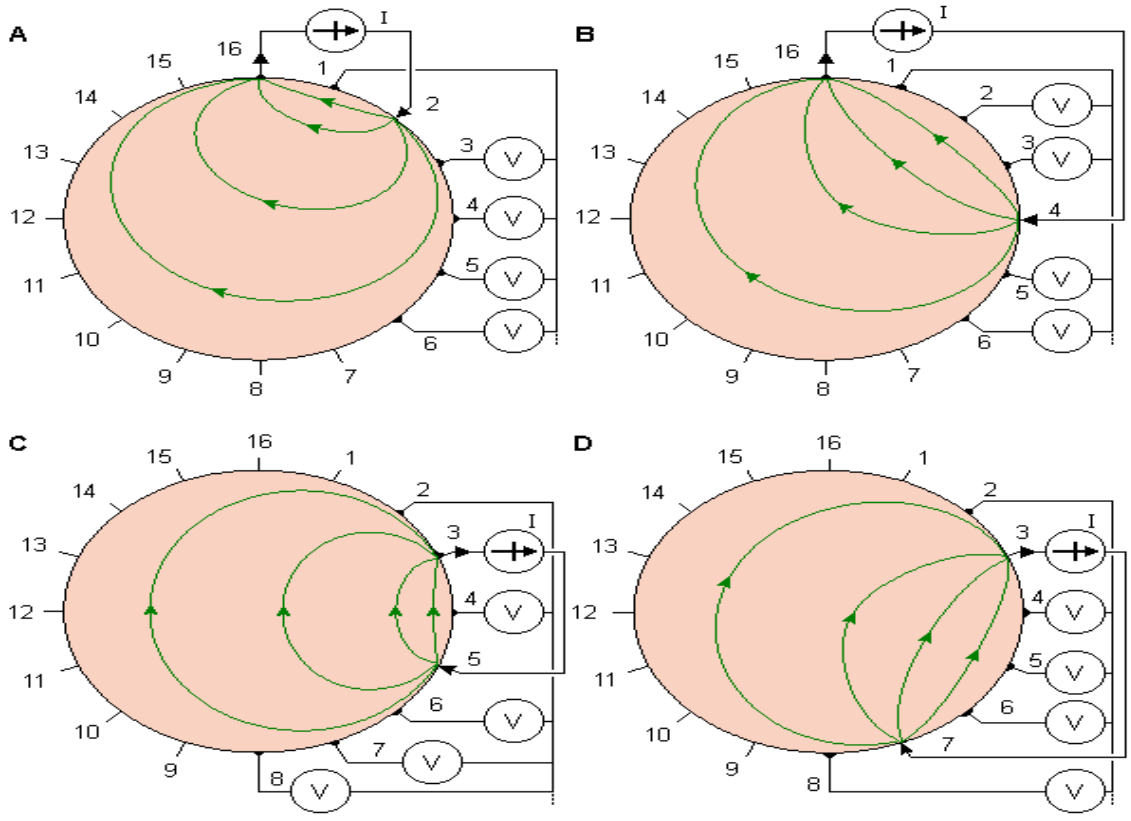


Figure 2-6 Cross method, A) electrode number 16 is selected as a current reference electrode and current is applied to electrodes 16 and 2. Voltage measurement is performed with respect to electrode number 1 which is selected as a voltage reference electrode. B) Current applied to electrodes 16 and 4 and voltages measured with respect to electrode 1. C) Current applied to electrode 3 (reference electrode) and 5 and voltage measurement performed with respect to electrode 2 (reference electrode) D) Current applied to electrodes 3 and 7 and voltages measured with respect to electrode 2.

### Opposite Method

In the Opposite method, the current distribution is more uniform and sensitivity is better than that of the Cross method. Measurement sensitivity and SNR in the domain centre are improved (Avis et al. 1994); however, the number of measurements is less than for the Adjacent method. In this method, current is injected into a pair of diametrically opposed electrodes and the voltage reference electrode is selected from one of the electrodes adjacent to the current injecting electrodes (Hua et al. 1988). Boundary voltage measurements are made using adjacent pairs of all combinations selected from the rest of the electrodes as shown in Figure 2-7. For an L-electrode system, $L(L-4)$ measurements are produced in total but only half of them are independent. Table 2-3 shows the complete sequence of measurements using the Opposite Electrode configuration in the 8-electrode array case. This indicates that localization accuracy may improve, but image resolution may not. In cerebral imaging, the presence of the skull prevents the current from entering the brain, significantly decreasing measurement sensitivity and SNR. The Opposite current injection method has been suggested for cerebral imaging (Bayford et al. 1996). Where opposite or approximately opposite current injection was used for 3D cerebral imaging, more accurate localization was expected (Tidswell et al. 2001, Dong et al. 2005, Romsauerova et al. 2006).

**Table 2-3:** The complete sequence of measurements using 8-electrode opposite electrode configuration.

| Input pair | Output pairs |
|---|---|
| (E1, E5) | (E2, E3), (E3, E4), (E6, E7), (E7, E8) |
| (E2, E6) | (E3, E4), (E4, E5), (E7, E8), (E8, E1) |
| (E3, E7) | (E1, E2), (E4, E5), (E5, E6), (E8, E1) |
| (E4, E8) | (E1, E2), (E2, E3), (E5, E6), (E6, E7) |
| (E5, E1) | (E2, E3), (E3, E4), (E6, E7), (E7, E8) |
| (E6, E2) | (E3, E4), (E4, E5), (E7, E8), (E8, E1) |
| (E7, E3) | (E1, E2), (E4, E5), (E5, E6), (E8, E1) |
| (E8, E4) | (E1, E2), (E2, E3), (E5, E6), (E6, E7) |

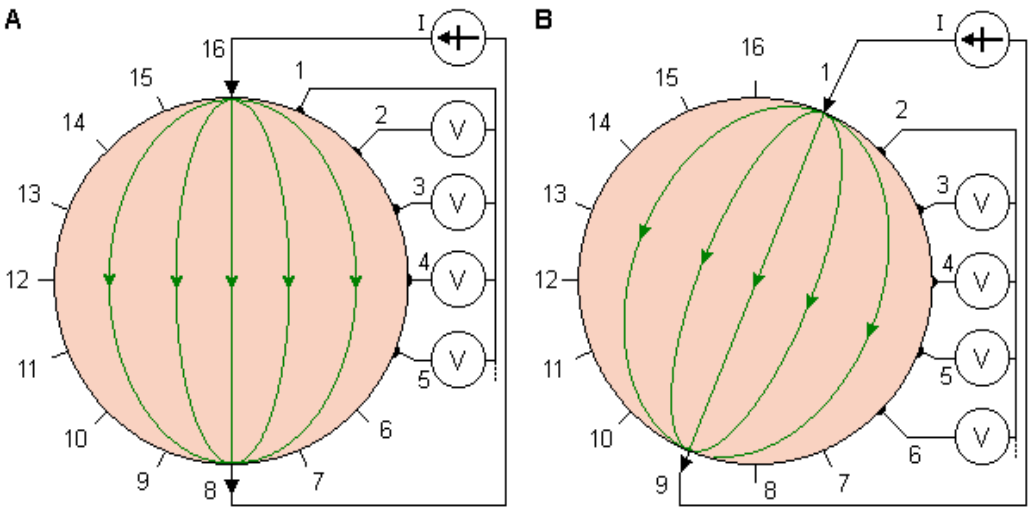


Figure 2-7 Opposite method. A) Current is applied to two opposite electrodes number 16 and 8 and voltage measurement performed with respect to electrode number 1. B) Current applied to electrodes 1 and 9 and voltages measured with respect to electrode 2.

### *Multiple Drive Instruments*

In multiple-drive methods, currents are simultaneously applied to more than two or even to all electrodes and voltages are also measured on multiple electrodes. Compound electrodes should be used for this data collection method. A Compound electrode is composed of two electrodes, a large outer electrode to apply current and a small inner electrode to measure voltage. The current patterns applied to the electrodes can be calculated to be optimal with respect to the measured object in the sense of distinguishability (Gisser et al. 1990). The concept of optimal current in terms of distinguishability in EIT was first considered by calculating the optimal placing of a pair of point drive electrodes on a disk in order to maximize the measured voltage differences between a homogeneous background and an offset circular anomaly (Seagar 1983). The maximum information content of the measurements to improve the distinguishability of two conductivity distributions is the main advantage of the multiple-drive method (Isaacson 1986, Cheney et al. 1992). However, as a current source for each electrode and a perfect calibration technique are required, the hardware complexity is increased (Cook et al. 1994, Zhu et al. 1994).

### *Other Excitation Methods*

There is an excitation method which cannot be classified into any of the above patterns. In this method a single current source instrument is used, but it is connected to several adjacent

electrodes at one time. Voltages are also measured traditionally, as potential differences between single electrodes. The set of current injection electrodes is then "scrolled" around the object by connecting new electrodes at one side and leaving some free at the other. Voltage measurements are repeated for each new configuration. It is shown that in this method the inverse problem is better conditioned than using the traditional pair drive methods (Polydorides et al. 2002).

## 2. The Inverse Problem

The Inverse Problem is to estimate the conductivity distribution from a known set of boundary voltage measurements as shown in Figure 2-8. In the EIT technique, recovering an unknown conductivity from boundary data is an inverse, non-local and ill-posed problem. Some medical imaging methods are termed local, in that the pixels of the images affect only a very small proportion of the measurements. The non-locality issue is one of the difficulties of EIT (Holder 2005). However non-locality is of secondary concern to the ill-posed nature of the problem. The definition of an ill-posed problem was addressed by Hadamard (Lionheart et al. 2005). According to his definition, a mathematical model of a physical problem is well posed if

1) For all admissible data, a solution exists (Existence);
2) For all admissible data, the solution is unique (Uniqueness);
3) The solution depends continuously on the data (Stability).

If these conditions are not met, the problem is considered to be ill-posed. In practice that means small perturbations in the measured boundary voltages can cause arbitrarily large errors in the estimated internal electrical conductivity. To solve this problem, some additional information about the conductivity distribution is needed (Holder 2005).


Figure 2-8 The concept of the Inverse Problem.

## 2.1. Static, Differential and Dynamic Imaging

### Static Imaging

In Static Imaging, sometimes referred to as Absolute Imaging, the absolute value of the conductivity distribution of an object is reconstructed. The properties of the object are not supposed to change during the measurement cycle, hence the term static. The static impedance imaging problem is nonlinear since current flow is a function of an unknown resistivity distribution (Hua et al. 1988, Polydorides et al. 2002, Vauhkonen et al. 1999, Blott et al. 1998, Woo et al. 1993). Due to the inverse and ill-posed nature of the problem, the accuracy of the measured and predicted voltages is crucial in static imaging. The information from the position of electrodes and shape of the object are not perfect; therefore, the forward model will not completely match the experiment with precision. There are also the uncertainties arising from the measurement system, and from solving the forward problem with numerical methods. These errors are particularly common in medical imaging, given the variability of anatomy and the difficulty in placing the electrodes in a repeatable way.

### Differential Imaging

The aim of Differential Imaging is to reconstruct a change in conductivity rather than an absolute value. Such methods reconstruct $\Delta\sigma = \sigma_1 - \sigma_0$ in the hypothesis that $\Delta\sigma$ is small, and the problem linearisable:

$$\Delta u = S\Delta\sigma \tag{26}$$

where S is a constant matrix and $\Delta u = u_1 - u_0$ is the difference between a reference voltage datum $u_0$ acquired for $\sigma_0$ and a second data set $u_1$ acquired for $\sigma_1$. The main medical application of this imaging technique is temporal phenomena imaging, such as impedance changes during respiration (Adler et al. 1996a, Adler et al. 1996b). The data set $u_0$ is acquired at a time $t_1$ for which the conductivity $\sigma_0$ is assumed as reference, the data set $u_1$ is acquired at a later time $t_2$ for which the conductivity change needs to be calculated. By reconstructing the conductivity change $\Delta\sigma$, parameters of medical interest such as pulmonary ventilation can be estimated. The main advantage of using the Differential technique, especially in medical applications, is that the errors arising from the uncertain positioning of the electrodes and uncertain knowledge of the patient's shape are cancelled by taking the difference of two data sets.

**Dynamic Imaging**

In Static Imaging, constant conductivity during the acquisition period is assumed. In the Differential technique, imaging is performed based on the assumption that the conductivity is varying slowly, in such a way that two successive data sets differ, but the conductivity can be approximated as constant during the acquisition period. The aim of Dynamic Imaging is to reconstruct fast conductivity changes. The conductivity is assumed to vary rapidly in comparison with the time period needed by the instrumentation to acquire a single image (Vauhkonen 1997). The changes are however assumed to be slow with respect to the acquisition period of a single pattern. Since this technique reconstructs the change in conductivity that occurs over some time interval, it is commonly used in medical applications such as imaging of fast flowing liquids transporting resistive objects (Seppänen et al. 2001a, Seppänen et al. 2001b) and thoracic imaging (Vauhkonen et al. 1999). Dynamic Imaging is widely used to improve the stability of the reconstructed images in the presence of problems such as unknown contact impedance, inaccurate electrode positions, poorly known boundary shape, non-linearity, and the use of 2D approximations for 3D electrical fields (Lionheart 2004).

## 2.2. Image Reconstruction Algorithms

One of the most difficult and challenging aspects of EIT is solving the Inverse Problem. It is impossible to reconstruct a reasonable image and obtain stable solution without implementing some special modification approaches. There are several ranges of techniques for solving ill-posed problems, of which the majority of them dealing with stability and uniqueness are called Regularization. Regularization is performed to remove the ill-posed nature of the problem by implementing *a priori* information about the solution (Borsic 2002).

In order to solve the Inverse Problem, its non-linearity should be linearized and its ill-posed nature should be regularized. There are various methods to solve the inverse conductivity problems and reconstruct the images from the measurement data set, which can be categorized as follows (Mueller et al. 2002):

1) Non-iterative linearization-based algorithms (Barber 1989)
2) Iterative algorithms solving the full nonlinear problem (Molinari et al. 2001, Borcea 2001)

3) Layer-stripping algorithms (Somersalo et al. 1991)
4) D-bar algorithm (Siltanen et al. 2000)

The linearization-based algorithms are based on the constraint that only small conductivity variation is permitted inside the body, so that the change of the potential on the boundary is linear. The Barber-Brown back-projection method (Barber et al. 1984), one-step Newton methods (Cheney et al. 1990) and sensitivity matrix method (Sadleir et al. 2009) are examples of non-iterative linearization-based algorithms. This algorithm is usually referred to as a dynamic imaging or a difference imaging technique and can be useful to estimate the amount of bleeding rate.

EIT is a non-linear problem in nature; however the clinical application results of EIT are obtained from linear algorithms only (Bayford 2006). The full non-linear problem has been mostly solved by iterative methods based on output least-squares (Kallman et al. 1992), the equation error formulation (Kohn et al. 1990), high contrast asymptotic theory (Borcea 2001), or statistical inversion (Kaipio et al. 2000). These algorithms nearly always tend to solve the static reconstruction problem for more accurate absolute conductivity values. However, they may be too slow to converge, and the reconstructed values will always have large oscillations. Therefore, an appropriate regularization is always necessary; however, this may blur features and boundaries. Numerical simulations and tank experiments have obtained successful results using these algorithms; however, no success has yet been obtained from clinical subjects (Bayford 2006). The main reason is the electrode contact impedance which is hard to accurately characterize, and tends to vary over time when making clinical measurements. The other reason is the object shape deformation during measurement, as this may create artefacts in the reconstructed images.

The layer-stripping algorithm is a promising method because it is fast and addresses the full non-linear problem (Somersalo et al. 1991). The implementation of this algorithm involves first finding the impedance on the boundary by using voltage measurements that corresponds to the highest spatial frequency. The outermost layer is then mathematically stripped away. This process is then repeated, layer by layer, until the full domain is solved. This algorithm works well on a continuum electrode model. However, no available layer-stripping algorithm works well on a complete electrode model (Cheney 1999).

The D-bar method (Siltanen et al. 2000) is a newly developed non-iterative direct reconstruction algorithm. It is based on the 2-D global uniqueness proof of Nachman (Nachman 1996). It solves the full nonlinear problem, so it has the potential of reconstructing conductivity values with high accuracy. However, the D-bar algorithm is a 2D reconstruction algorithm in nature. Developing a D-bar method for 3D still remains a challenge (Cornean et al. 2006).

### 2.3. Formulation of Linearized Algorithm

The one-step linearization based algorithms are standard theory which are time efficient and have proved effective in real-time imaging applications (Cheney et al. 1990). For a fixed input current pattern and an object shape, a boundary voltage measurement V can be written as a function of conductivity distribution σ as in equation (27),

$$V = f(\sigma) \tag{27}$$

when there is a small perturbation $\Delta\sigma$ on the original conductivity distribution $\sigma_0$, the boundary measurement changes from $f(\sigma_0)$ to $f(\sigma_0 + \Delta\sigma)$.

Time difference imaging is used to reconstruct images of small conductivity changes from measurement changes over time. In EIT, a sequence of difference images can be obtained in real-time, which is desirable for continuous monitoring or functional imaging applications. For small conductivity change $\Delta\sigma$ away from the reference conductivity distribution, the measurement $f(\sigma)$ can be expanded as a Taylor series at $\sigma_0$ in equation (28).

$$V = f(\sigma_0) + f'(\sigma_0).\Delta\sigma + \frac{f''(\sigma_0).\Delta\sigma^2}{2!} + \cdots + \frac{f^n(\sigma_0).\Delta\sigma^n}{n!} + \cdots \tag{28}$$

A linear approximation of the problem can be obtained by neglecting the high order terms in equation (28). The linearized form of the problem is expressed by equation (29).

$$V \cong f(\sigma_0) + f'(\sigma_0).\Delta\sigma \tag{29}$$

Equation (30) can then be obtained as $f(\sigma_0)$ is the reference measurement, $V_0$ and $f'(\sigma_0)$ the Jacobian,

$$V - V_0 = \Delta V \cong f'(\sigma_0).\Delta\sigma \tag{30}$$

The inverse problem is usually solved using a numerical approach such as the finite element method. Thus equation (31) provides a discrete format of equation (30), which becomes a set of linear equations.

$$\Delta V = S \times \Delta\sigma \tag{31}$$

where S is the sensitivity matrix. Hence the nonlinear inverse problem in equation (28) has been linearized to equation (31). In equation (32), all the terms of the components in equation (31) are laid out in matrix form,

$$\begin{bmatrix} \Delta V_1 \\ \Delta V_2 \\ \vdots \\ \Delta V_i \\ \vdots \\ \Delta V_M \end{bmatrix} = \begin{bmatrix} S_{1,1} & S_{1,2} & \cdots & S_{1,j} & \cdots & S_{1,N} \\ S_{2,1} & S_{2,2} & & & & \vdots \\ \vdots & & \ddots & & & \vdots \\ S_{i,1} & & & S_{i,j} & & \vdots \\ \vdots & & & & \ddots & \vdots \\ S_{M,1} & & & \cdots & \cdots & S_{M,N} \end{bmatrix} \cdot \begin{bmatrix} \Delta\sigma_1 \\ \Delta\sigma_2 \\ \vdots \\ \Delta\sigma_j \\ \vdots \\ \Delta\sigma_N \end{bmatrix} \tag{32}$$

The size of the sensitivity matrix depends on the length of vector $\Delta V$ which is the number of voltage measurements on the boundary, and the length of vector $\Delta\sigma$ which is the number of elements (pixels) within the inverse model.

The columns of the sensitivity matrix can be built by using the set of measurements produced by solving the Forward Problem. This approach necessitates solving as many Forward Problems as the total number of elements. However the sensitivity matrix can be calculated with much less computational burden by using the Sensitivity Theorem or Lead Field Theorem (Geselowitz 1971, Murai et al. 1985). This method requires only one forward problem to be solved. Each entry $S_{i,j}$ can be calculated using equation (33).

$$S_{i,j} = -\int_j \frac{\nabla\Phi(\sigma_0)}{I_\Phi} . \frac{\nabla\Psi(\sigma_0)}{I_\Psi} dv_j \quad (33)$$

where i and j are measurement and element indexes respectively. The sensitivity $S_{i,j}$ of each element is a negative integral of the inner product of lead fields due to measurement i over a finite volume of element j ($v_j$). $\nabla\Phi(\sigma\_0)/I\_\Phi$ and $\nabla\Psi(\sigma\_0)/I\_\Psi$ are lead fields generated by the current injection and voltage measurement electrode pairs at conductivity distribution $\sigma_0$, which are called input and output lead fields respectively.

### 2.4. Regularization of the Inverse Problem

Regarding the linearized EIT inverse problem (equation 31) as a general linear algebra problem, the conductivity change $\Delta\sigma$ can be solved by inverting the matrix S. However the total number of measurements is limited by the number of applied electrodes and is typically smaller than the total number of elements. Therefore, S is generally not a square matrix and the equation (31) is an underdetermined problem. In general a non-square matrix cannot be directly inverted, in which case the least squares solution can be obtained instead. In the least squares method, the solution is estimated so as to give the best fit that minimizes the sum of the squared errors of equation (31). However, since the EIT inverse problem is severely ill-posed and small amounts of noise on boundary measurements can cause a large oscillation for the solution, simple least squares solutions will fail to produce meaningful images in EIT image reconstruction. Therefore to obtain a reasonable solution the problem needs to be further regularized.

#### 2.4.1. Singular Value Decomposition

In linear algebra, Singular Value Decomposition (SVD) is an important factorization of a rectangular matrix which has many applications to the study of inverse problems (Bertero et al.1998, Golub et al.1970). In this study, SVD is applied to obtain the pseudo-inverse of matrix S. Using SVD any matrix can be represented as a product of a unitary matrix, a diagonal matrix and another unitary matrix as in equation (34).

$$S = UDV^T \quad (34)$$

where D is a diagonal matrix whose entries are termed the singular values. The rank of D is identical to the rank of S. The singular values are non-negative numbers, arranged in a descending order.

Matrices U and V are unitary matrices whose inverses are identical to their transpose. The columns of U and V are termed the left and right singular vectors of S. Matrices U and V can be expressed as in equations (34) and (35).

$$U = [u_1 \quad u_2 \quad \cdots \quad u_M] \tag{34}$$

$$V = [v_1 \quad v_2 \quad \cdots \quad v_N] \tag{35}$$

$u_i(M \times 1)$ and $v_i(N \times 1)$ are i-th column of U and V respectively which gives equation 36 in column form as below

$$S = [u_1 \quad u_2 \quad \cdots \quad u_M] D \begin{bmatrix} v_1^T \\ v_2^T \\ \vdots \\ v_N^T \end{bmatrix} \tag{36}$$

Consequently, S is the sum of the rank one matrices ($u_i v_i^T$) weighted by diagonal entries of D ($d_i$) as in equation (37).

$$S = \sum_{i=1}^{N} d_i u_i v_i^T \tag{37}$$

### 2.4.2. Condition number

The sensitivity matrix in the EIT Inverse Problem is badly conditioned. Therfore a small error in measurment will generate large errors in the reconstructed image. The condition number is a quantity to represent the condition of a matrix and measures how ill-conditioned the matrix is. The condition number is defined to be the ratio between the maximum and minimum singular values as in equation 38:

$$K(S) = \frac{d_{max}}{d_{min}} \tag{38}$$

where $d_{max}$ and $d_{min}$ are the maximum and minimum singular values of S respectively. A high condition number of a matrix shows that the columns are nearly dependent and indicates

a poorly-conditioned matrix. If the condition number is close to 1, the matrix columns are very independent.

### 2.4.3. Singular Images

Columns of the right singular vector **V** are termed the singular images, and they form the basis of the reconstruction images (Zadehkoochak et al. 1991). These singular images can provide useful insights about how regularization determines spatial resolution in the reconstruction images.

### 2.4.4. Truncated Singular Value Decomposition (TSVD)

In the singular image, the higher order singular values correspond to high spatial frequency components. As a result of the inversion of S, the higher order values that are small will be reciprocated and show as artefacts in reconstruction image. By replacing the small values by zero, image artefacts can be successfully suppressed. Truncated SVD (TSVD) is a common procedure used for discrete ill-posed problems to obtain smooth solutions (Hansen 1987). In order to obtain more reasonable images from the inverse problem, TSVD is used to replace S by a well-conditioned matrix derived from S. The pseudo-inverse of S ($S^+$) is calculated in equation (39).

$$S^+ = VD^+U^T \tag{39}$$

where $D^+$ is a truncated inverse of D. Therefore, the pseudo-inverse $S^+$ can be used as the reconstruction matrix to estimate the conductivity solution as in equation (40).

$$\Delta\sigma = S^+\Delta V \tag{40}$$

The estimated solution by TSVD can be expressed as the weighted sum of rank-one matrices as in equation (41).

$$\Delta\sigma = \sum_{i=1}^{k} \frac{u_i^T \Delta V}{d_i} v_i \tag{41}$$

where k is the truncation number. The value of k is related to the amount of noise in the measurement, ΔV, which is generally unknown (Hansen 1987). Therefore the truncation level k can be determined by approaches such as the L-curve criteria (Hansen 1993).

### 2.4.5. L-curve

To select an adequate truncation level for TSVD, an L-curve criterion was suggested by Hansen (1993). In this method, the solution norm is plotted against the residual norm in a log-log scale. The resulting curve appears concave (L-shaped), hence the name L-curve. The maximum curvature point corresponds to the optimal choice of a regularization parameter (Hansen et al. 1993).

### 2.4.6. Weighted Minimum Norm Method

The sensitivity values are typically greater in a domain close to the electrodes and weaker in further from the boundary electrodes (Oh 2009). Therefore, the existence of an anomaly in the central region or in the back region, away from the electrodes may be blurred or not detected in reconstructions. The FOCal Underdetermined System Solver (FOCUSS) algorithm employs a one-step algorithm which produces a least squares solution based on minimization of a re-weighted norm of the solution (Gorodnitsky et al. 1997). This strategy and its modification are successfully adapted to EIT image reconstruction problems (Clay et al. 2002, Dong et al. 2004). This method is termed the Weighted Minimum Norm Method (WMNM) (Sadleir et al. 2008).

In WMNM, columns of S are equalized in terms of its power before pseudo-inversion. The weighting terms ($w_j$) are defined as in equation (42):

$$w_j = \left(\sum_{i=1}^{M} S_{ij}^2\right)^{-1/2} \tag{42}$$

Using a diagonal weighting matrix W comprised of these terms, the final form of the WMNM regularized solution can be obtained as in equation (43).

$$\Delta\sigma = W(SW)^{+}\Delta V \tag{43}$$

### 2.4.7. Quantity Index

Absolute conductivity values has been estimated using parametric forward models, where the absolute conductivity values producing the best fit to conductivity measurements are suggested (Zhang et al. 2005). However, design of a parametric model can be difficult for certain body parts due to large shape variations from patient to patient (Oh 2009). Here, an integral of EIT images is proposed as a useful measure related to anomaly volume. The quantity defined in equation (44) is termed the Quantity Index (QI), which can be thought of as the average of conductivity change multiplied by the number of elements N.

$$\mathrm{QI} = \sum_{j=1}^{N} a_j \, \Delta\sigma_j \tag{44}$$

For an element (or pixel) j, conductivity change and element area are denoted as $\Delta\sigma_j$ and $a_j$ respectively.

### 2.4.8. Point Spread Function and the Blur Matrix

The problem of a spatially variant imaging system is a main challenge in quantitative EIT. In order to improve the accuracy of quantitative EIT reconstruction, the effect of the spatial variability must be reduced. Therefore, reconstruction blur analysis is used to reduce the errors related with the spatial variance. Previous studies demonstrated improved results by normalizing the Point Spread Function (PSF) by its integral. In this study, integrals of PSF functions are used as normalizing terms to investigate blurring in EIT image reconstruction.

A unit conductivity change in an element (pixel) j within the image can be expressed in vector form as an entry of 1 in the j-th position and zeros elsewhere ($[0 \dots 0\ 1\ 0\ \dots\ 0]^T$)$(1 \times N)$, whose weighted sum is a vector form of the ideal image. The corresponding boundary voltage measurement change of this conductivity change is the j-th column of the sensitivity matrix $S(M \times N)$. Ideally any measurement can be represented as a weighted sum of sensitivity matrix columns. Therefore, the column space of S can be termed the ideal measurement space. A blurred version of the ideal element (pixel) image is obtained from the ideal measurement reconstruction, which is termed the PSF in equation (45).

$$\delta_j = B[0 \dots 0\ 1\ 0\ \dots\ 0]^T \tag{45}$$

where $B(N \times N)$ is the blurring matrix, and $\delta_j$ is the PSF vector for an anomaly in the j-th element. The column space of B is a blurred version of the ideal images. The blur matrix B is defined as a product of the sensitivity matrix and the reconstruction matrix. The definitions of the blur matrix in the context of TSVD and WMNM regularisation are described in equations (46) and (47) respectively.

$$B_t = S^{+}S \tag{46}$$

$$B_w = W(SW)^{+}S \tag{47}$$

### 2.4.9. Normalizing Terms

The column sum of B, defined as $q_j$ to normalize QI is considered as in equation (48).

$$q_j = \sum_{i=1}^{N} B_{ij} \tag{48}$$

The normalization matrix which is a diagonal matrix whose entries are $q_j$'s is used in this study as $Q(N \times N)$ in equation (49).

$$Q = \begin{bmatrix} q_1 & 0 & \cdots & 0 \\ 0 & q_2 & 0 & \vdots \\ \vdots & 0 & \ddots & 0 \\ 0 & \cdots & 0 & q_N \end{bmatrix} \tag{49}$$

### 2.4.10. Pixel-wise Scaling

Pixel-wise scaling (PWS) can be applied for conductivity change reconstruction as it was used by Thomas et al. (1994) in order to reduce variation in quantity estimates. PWS is presented in equation (50) in matrix form.

$$\Delta\sigma = Q^{-1}S^{+}\Delta V \tag{50}$$

### 2.4.11. Weighted Pseudo-inverse

Weighted pseudo-inversion (WPI) is used in this study as a normalization obtained by weighting columns of the sensitivity matrix by terms in Q prior to reconstruction as in equation (51).

$$\Delta\sigma = (\mathrm{SQ})^{+}\Delta\mathrm{V} \tag{51}$$

If SQ is a full-rank matrix, equation (51) will become identical to equation (50). Therefore, WPI should normalize the reconstruction in a similar way to PWS, with an additional advantage of using the truncated pseudo-inverse.

### 2.4.12. WMNM Normalization

The WPI method used in (Oh and Sadleir 2007) was shown to decrease spatial variance of the QI. However, to reconstruct images equation (51) did not produce reasonable images. Using the mathematical framework of WMNM with the form of equation (52), which multiplies Q post-reconstructively would help to obtain meaningful images.

$$\Delta\sigma = \mathrm{Q}(\mathrm{SQ})^{+}\Delta\mathrm{V} \tag{52}$$

The combination of WMNM regularization and WMNM normalization can be used as a normalized reconstruction and would produce normalized images as in equation (53) (Sadleir et al. 2008).

$$\Delta\sigma = \mathrm{QW}(\mathrm{SWQ})^{+}\Delta\mathrm{V} \tag{53}$$

### 2.4.13. Localization of EIT Reconstructions

The position of the anomaly can be estimated from reconstructed images by equation (54).

$$x = \frac{\sum_{i=1}^{ne} \Delta\sigma_i a_i x_i}{\sum_{i=1}^{ne} \Delta\sigma_i a_i}, y = \frac{\sum_{i=1}^{ne} \Delta\sigma_i a_i y_i}{\sum_{i=1}^{ne} \Delta\sigma_i a_i} \tag{54}$$

The expression for anomaly location (x, y) is effectively the 'centre of mass' of the difference image. The values $x_i$ and $y_i$ are the coordinates of the centre of each element. $\Delta\sigma_i$ is the conductivity change reconstructed in the i-th element and $a_i$ is the volume of each element.

**Summary**

In this chapter the various EIT methods were explained. The forward and the inverse problems were described in detail including their physics and equations.

The governing equations for the EIT forward problem with the boundary conditions and the electrode models were reported. In this study the "Complete Electrode Model" was chosen to simulate the forward model, which is described in the next chapter. Since the objective is to use the minimum number of electrodes, the existing 8-electrode configurations and the data collection methods were explained. The Hemi-array electrode layout in which the electrodes are positioned on the anterior surface of the head for a patient in emergency cases where the body cannot be moved was chosen and compared with the Full-array using FE models in the next chapter. The common adjacent current pattern was considered. Adjacent current pattern also makes the hardware and the measurement strategy simple and optimized.

Existing imaging techniques for the EIT inverse problem were reported. The Differential Technique was considered in this study, as especially in medical applications, the errors arising from the uncertain positioning of the electrodes and uncertain knowledge of the patient's shape are cancelled by taking the difference of two data sets. The regularization methods of the inverse problem were described in this chapter. The TSVD and WMNM methods are used and compared to reconstruct the EIT images in the next chapter.

CHAPTER

# 3

# Studies Using FE Model

## 1. Image reconstruction

In order to reconstruct the images using an FE model and solve the EIT problems, an algorithm using COMSOL linked with MATLAB was defined and is presented in Figure 3-1. At first, the geometries of the FE forward and inverse models and their conditions were created in COMSOL. Then from the forward model, voltage measurements and the sensitivity matrix were obtained using MATLAB. The conductivities were calculated by giving the data measurement and sensitivity matrix to the MATLAB files which are presented in appendix A in order to reconstruct images. At the end, the conductivity data was presented as an image using the inverse model.

The process of the reconstruction using MATLAB is presented in Figure 3-2. In this chapter, the head and the anomalies were simulated in the forward model and the images were reconstructed and presented using the inverse model. At first the forward model was simulated homogenously (without any anomalies) and the measurement was performed to obtain the voltage boundary (Homo.mat). Then anomalies were introduced to the geometry and the voltage boundary was re-calculated (Dv.mat). The sensitivity matrix (Sfull.mat) was

also calculated and used to reconstruct the conductivity data (x.mat). The inverse model was used to generate the images from the conductivity data. The details of the forward and inverse models and the anomaly positions are presented in the next sections.

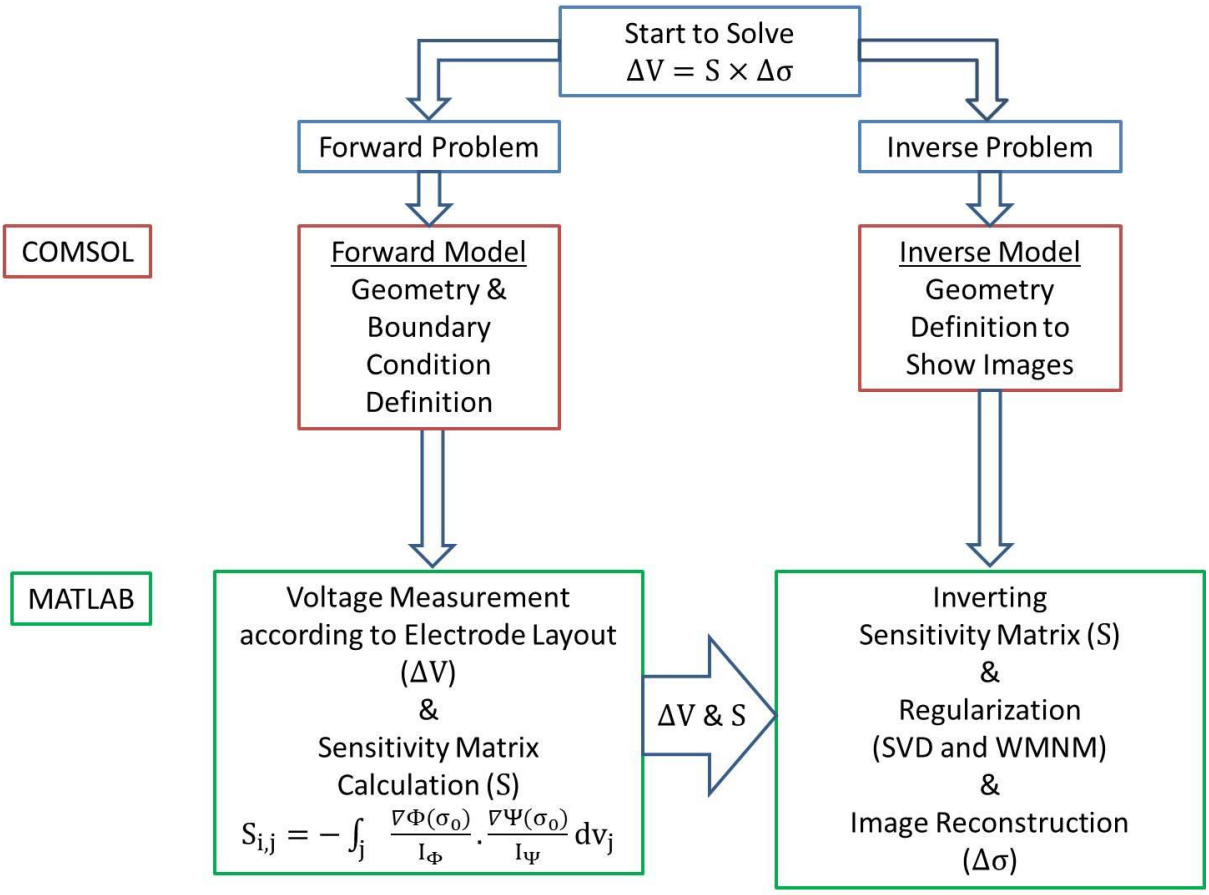


Figure 3-1 Algorithm to solve the EIT problems and reconstruct the images. At first, the geometries of forward and inverse models and their conditions are created in COMSOL. Then from the forward model, voltage measurements and the sensitivity matrix are obtained using MATLAB. By providing the measurement and sensitivity matrix to the reconstruction MATLAB file the conductivities are calculated. At the end, the conductivity data is presented as an image using the inverse model.

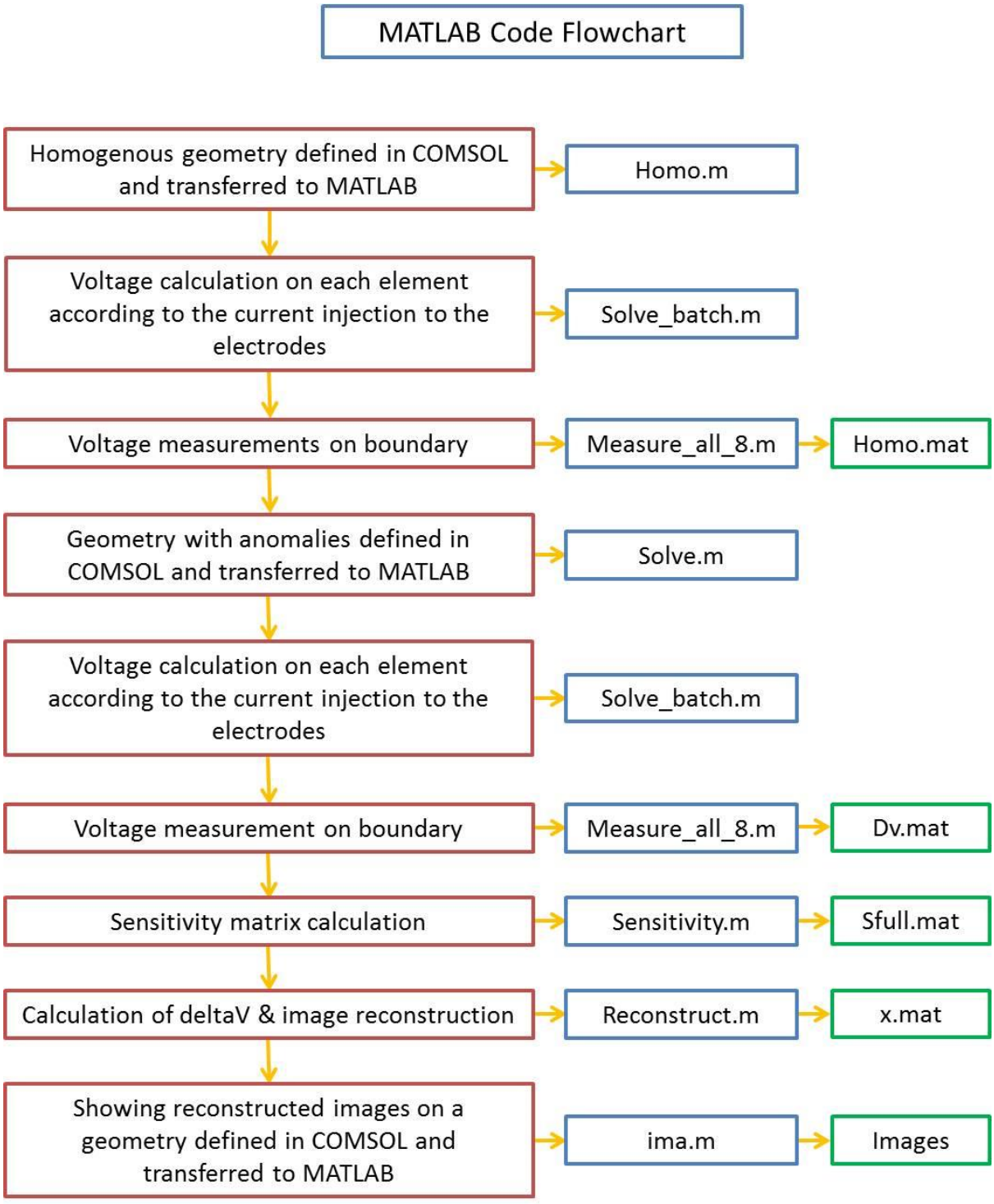


Figure 3-2 MATLAB script flowchart to reconstruct images. At first the forward model are simulated without anomaly and the measurement are performed to obtain the voltage boundary (Homo.mat). Then the anomalies are introduced and the voltage boundaries are calculated (Dv.mat). The sensitivity matrix (Sfull.mat) is also calculated and used to reconstruct the conductivity data (x.mat). The inverse model is used to generate the images from the conductivity data.

## 2. The Forward Model

The forward problem in EIT is to calculate the electric potential **u** inside the brain Ω from the injected current density J for a known conductivity distribution σ. When the defined current J is transmitted through ∂Ω, the corresponding u is generated following equation (20). In order to set up the exact forward model it is necessary to establish the conductivity distribution. In this study, the average brain conductivity value is taken as 1 S/m and is assumed to be isotropic. Point electrodes have been used and the brain is assumed to be a circular shape to further simplify the problem.

The forward problem can be solved analytically when the geometry of the domain is simple and the conductivity distribution is homogenous. However, for more realistic complex shapes with non-uniform conductivity distributions, analytical solutions are generally not available. In EIT, the Finite Element Method (FEM) is normally used to provide numerical approximations of the analytical solution. In FEM, the object domain is subdivided into a finite number of discrete small elements. The elements are triangles in two dimensions (2D) and tetrahedral or hexahedral in three dimensions. Each element consists of nodes and faces (Oh 2009, Goharian 2007).

A 2D disk model with an 8-electrode full array and hemi-array were designed as a forward problem by the Author using COMSOL (COMSOL Multiphysics: Burlington MA). A mesh structure composed of triangular elements is illustrated in Figures 3-3 and 3-4 for the full array and hemi-array respectively. A smaller disk anomaly was designed to fit inside this model. The models were discretized to 1512 and 1506 second order triangular finite elements for the full array and hemi-array respectively. The model parameters are shown in Table 3-1. Figure 3-5 shows the different locations of the anomaly when the anomaly moves from the centre towards the boundary in 4 steps. Anomaly locations with 8-electrode hemi-array (top row) and full array (bottom row). The anomaly is placed at 0, 0.25, 0.5 and 0.75 radius units from the centre with respect to the unit radius.

**Table 3-1:** Forward model parameters

| Parameter | Value |
|---|---|
| Number of electrodes | 8 |
| Electrode array type | Full array or Hemi-array |
| Background conductivity | 1 S/m |
| Anomaly conductivity | 2 S/m |
| Electrode type | Point electrode |

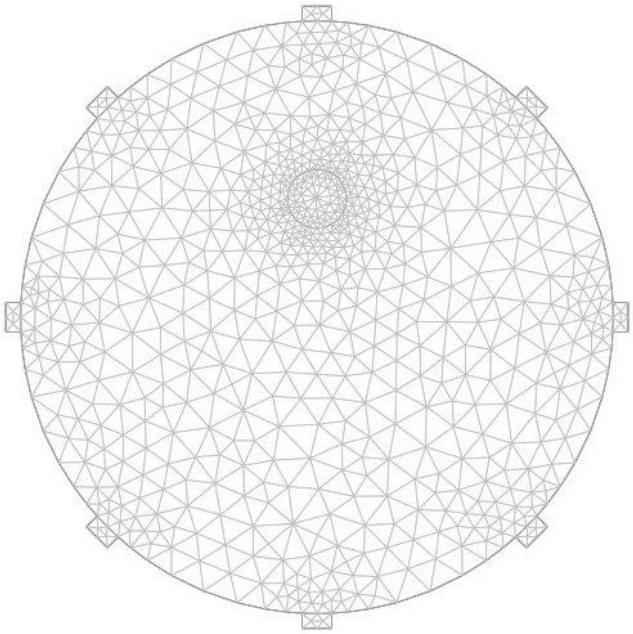

Figure 3-3 Mesh generation for a 2D disk model with an 8-electrode full array.

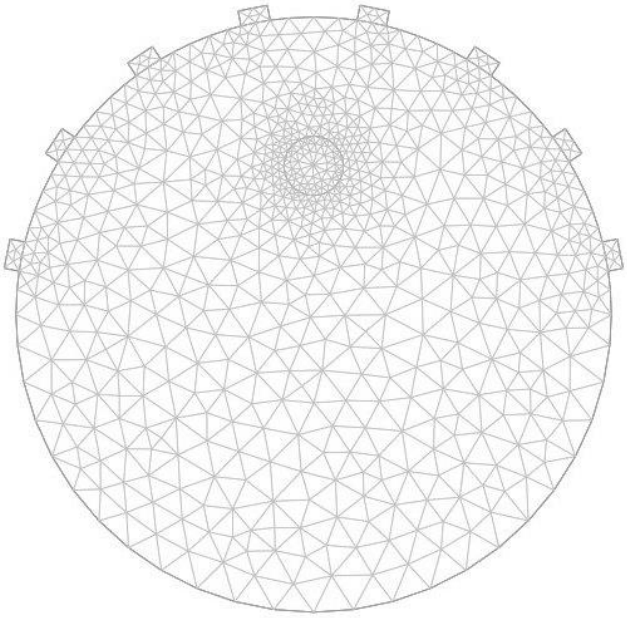

Figure 3-4 Mesh generation for a 2D disk model with an 8-electrode hemi-array.

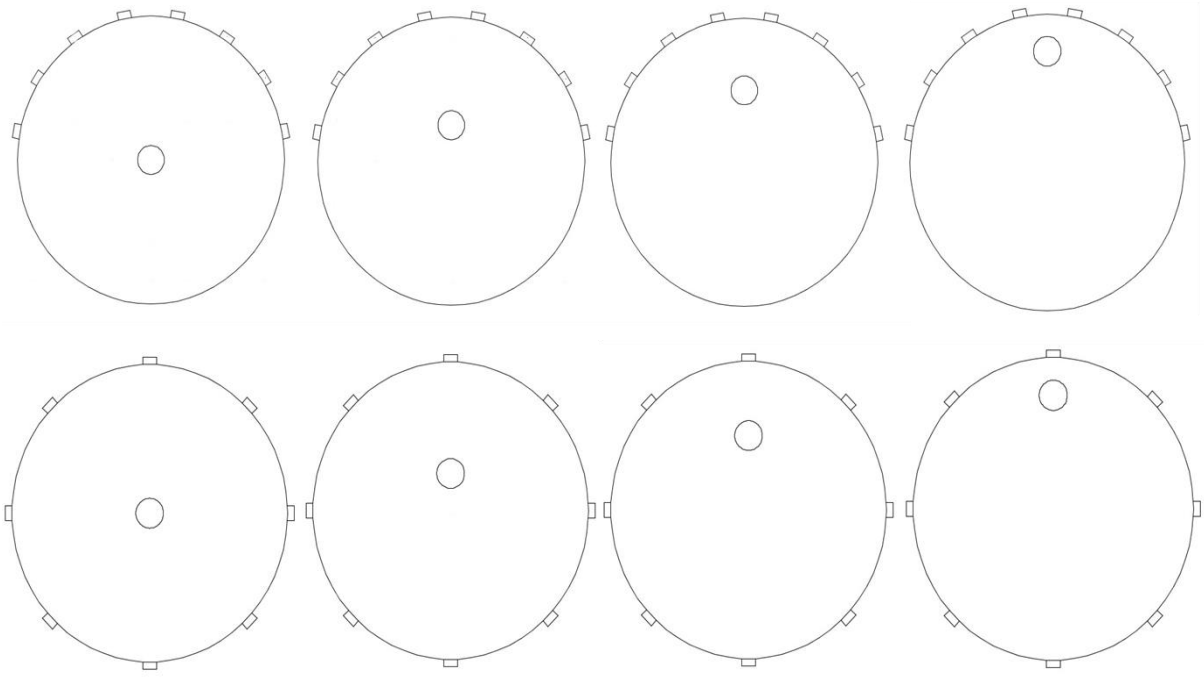

Figure 3-5 Anomaly locations with 8-electrode hemi-array (top row) and full array (bottom row). Anomaly placements are 0, 0.25, 0.5 and 0.75 radius units from the centre.

The solution is approximated as a polynomial function in each element where pixel values are assumed to be constant. If the elements are sufficiently small, the finite element solution is supposed to approach the exact solution closely. The conductivity value for the background is 1 S/m. The inward current density on the boundary of electrode E1 (1 $A/m^2$) and E2 (-1 $A/m^2$) is applied. The rest of the boundary segments were electrically insulated. The plot of the potential of the homogenous disk with current injected between two adjacent electrodes is displayed in Figure 3-6, which shows that the potential is monotonically decreasing from source to sink. The 5 measurements which are all positive quantities and have a 'U' shape for a single drive pair are shown in Figure 3-7. Figures 3-8 and 3-9 show a complete adjacent measurement data set using the Full Array (FA) and Hemi-Array (HA) respectively. The measurements from the electrodes were performed using MATLAB software. The MATLAB script to measure voltages between 8 electrodes in hemi-array layout is presented in appendix A.

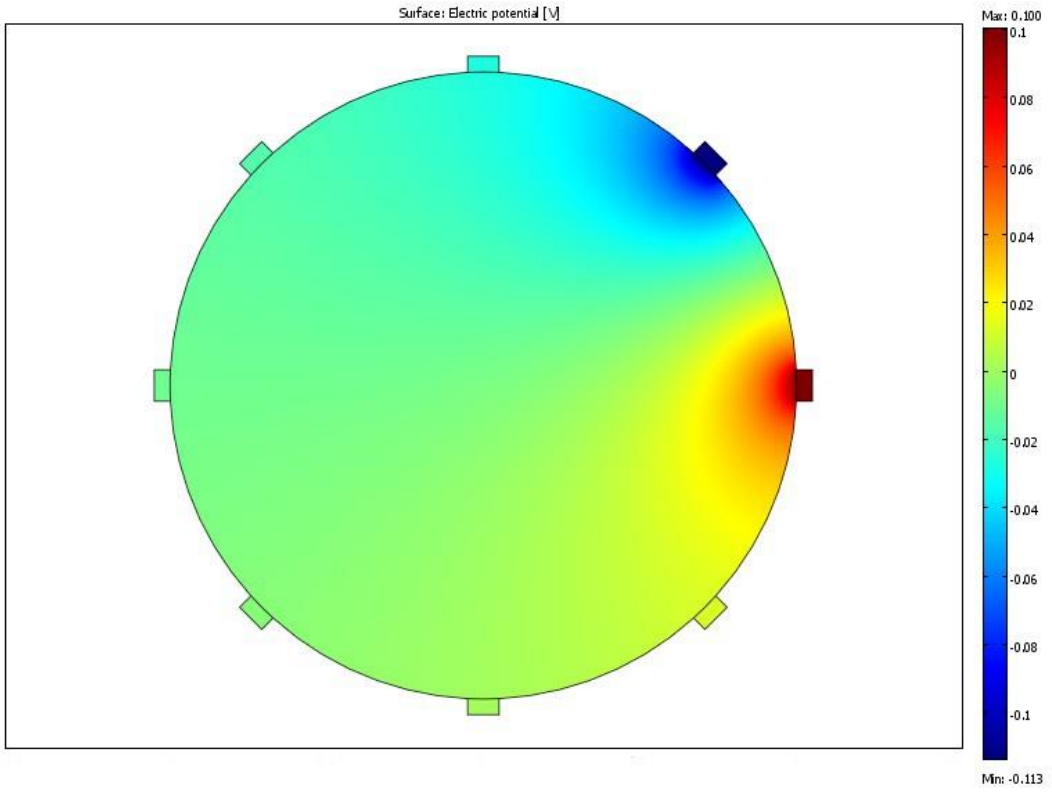


Figure 3-6 A plot of the surface electric potential of a homogenous disk with current injected into a pair of adjacent electrodes.

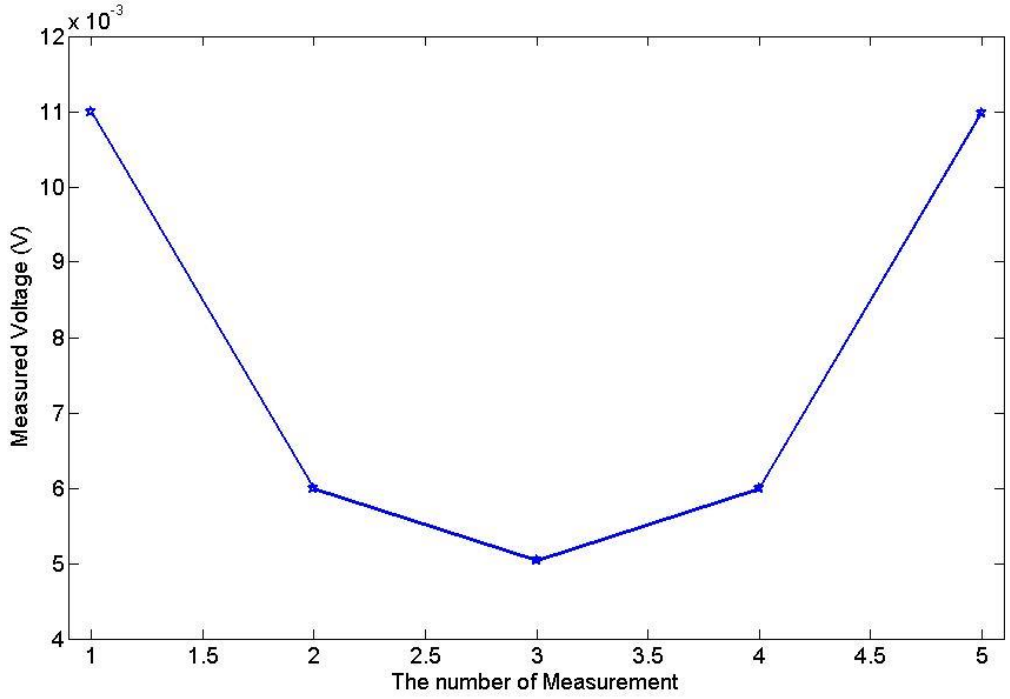


Figure 3-7 The 5 measurements for a single drive pair

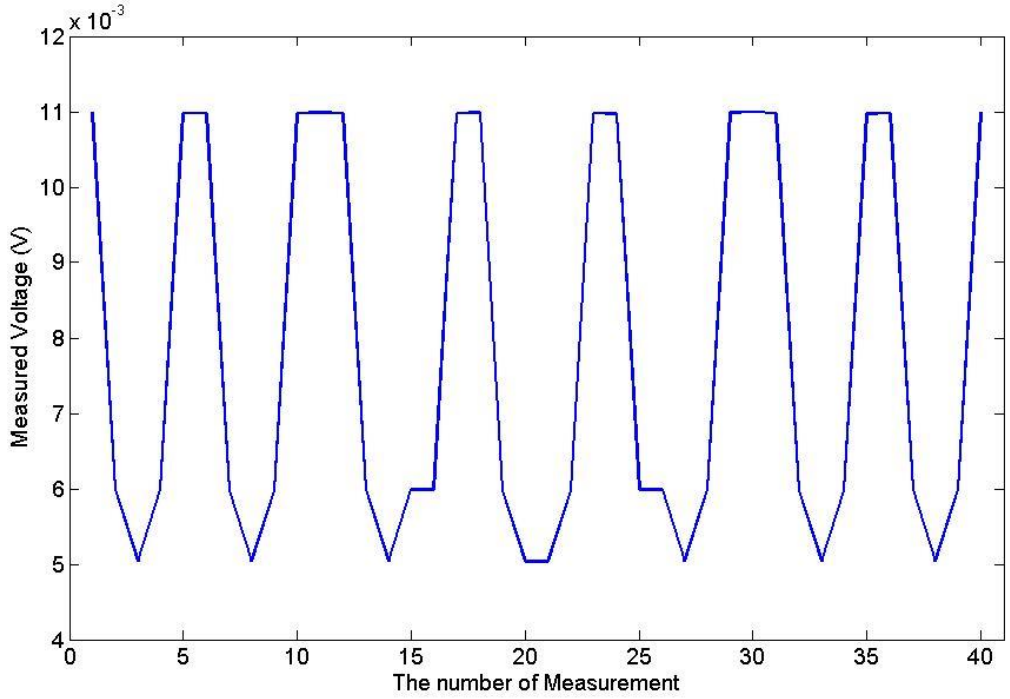


Figure 3-8 A complete homogenous electrode measurement set using a full array

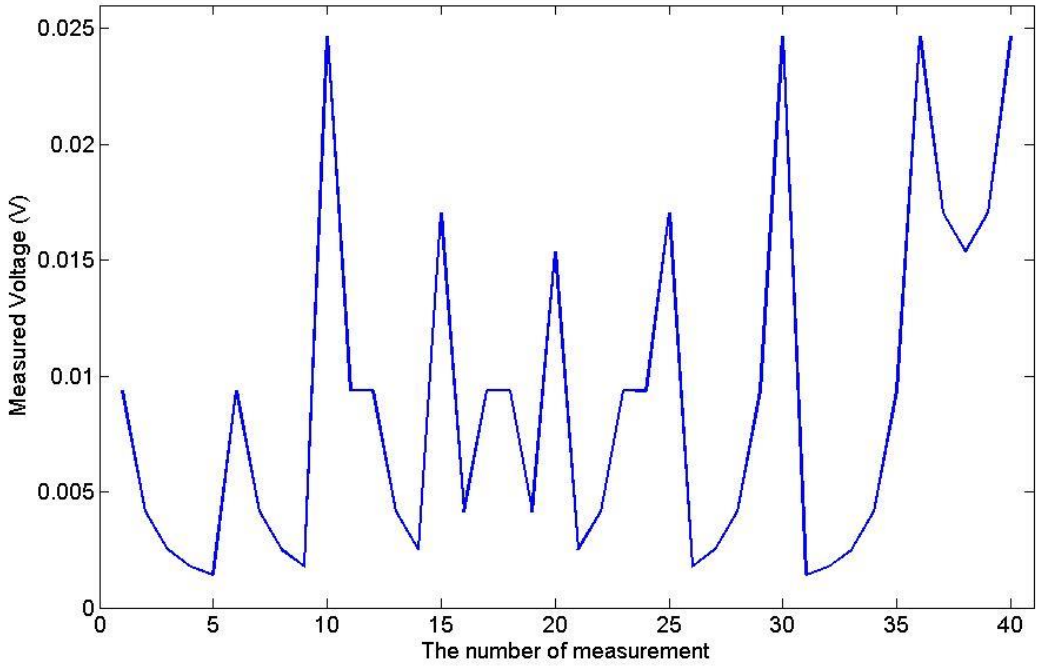


Figure 3-9 A complete homogenous electrode measurement set using a hemi-array

## 3. Inverse Model

A simple structure composed of 1300 elements was designed by the Author as an inverse model. All elements are square, and their areas are the same except the ones lying on the object boundary. Then, the sensitivity matrix was calculated for the inverse model with the uniform conductivity distribution, since accurate knowledge of internal conductivity is not easily available (Meeson et al. 1995).

The sensitivity matrices were calculated for the adjacent electrode configuration in the 8-electrode full array and hemi-array cases according to equation (33). The singular values were obtained from the sensitivity matrices. The first 20 values were found to decrease in a centesimal range, with a sudden discontinuity at the 21$^{st}$ value. From this point, values are very small and close to each other until they decay to zero. To show the singular values for both sensitivity matrices in a wider range, they are plotted in log scale in Figure 3-10. Both curves decay gradually to zero indicating that the inverse problem is ill-posed.

The condition number of the sensitivity matrix for the full array and hemi-array are extremely large as shown in Table 3-2. The high value of the condition numbers indicates that the EIT

inverse problem is severely ill-posed. The hemi-array matrix condition number is larger than that of the full array, indicating that its inverse problem is even more ill-posed. The ranks of both matrices are 20, half the number of total measurements, owing to the reciprocity principle (Malmivuo et al. 1995).

**Table 3-2:** Properties of the sensitivity matrices of 8-electrode full array and hemi-array topologies

| Parameter | Full array | Hemi-array |
|---|---|---|
| Dimensions | 40×1300 | 40×1300 |
| Rank | 20 | 20 |
| Condition Number | $1.4\times10^{17}$ | $3.1\times10^{17}$ |

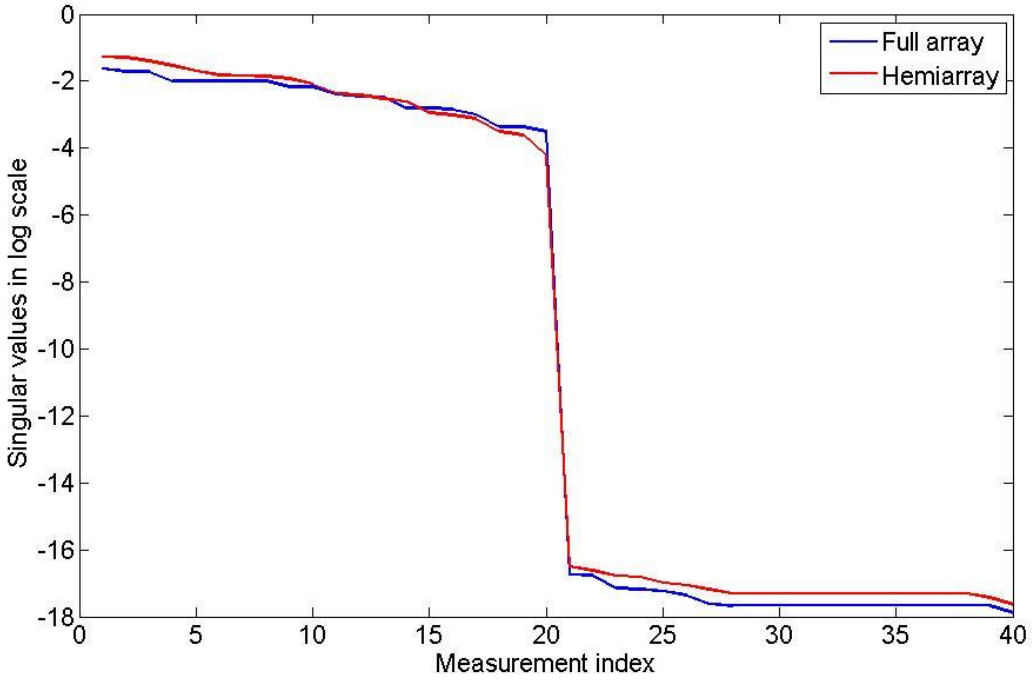


Figure 3-10 Singular value spread of sensitivity matrices for 8-electrode full array and hemi-array.

Reconstruction images are based on the singular images which are the columns of the right singular vector **V** according to equation (35). Singular images illustrate spatial resolution in the reconstructed images. In order to compare the spatial resolution of the FA and HA layouts, the singular images for the FA and HA were obtained and reconstructed. The columns of the right singular vector **V** were obtained and singular images were reconstructed using the inverse model by a MATLAB file which was presented in appendix A.

The singular images for the 8-electrode FA and HA are displayed in Figures 3-11 and 3-12 respectively. The main observation in Figure 3-11 is that the boundary region, which is close to the electrodes, will be described ahead of the central region, which is far away from the electrodes. In Figure 3-12, it is seen that the singular images are unable to describe details of the region which is further away from the electrodes indicating potential difficulties in reconstructing any anomalies.

Figure 3-13 shows the L-curve using the TSVD regularization. The boundary measurement in this work was generated from an anomaly located at the centre of a spherical model equipped with the full array electrode configuration in simulation. It can be seen that the corner of the L-curve is not sharp enough to choose a unique truncation number. However, it is indicated that a truncation number within the range 11-20 will give useful solution. The chosen truncation number in this study is 16.

In order to investigate the effect of the WMNM method, it may be worthwhile to examine the singular value spectra of the sensitivity matrices with and without weighting. In Figure 3-14, the singular value spread of S (TSVD reconstruction), and SW (WMNM reconstruction) are compared. It was found that SW's singular values decrease the most rapidly as the mode number increases to show smooth images.

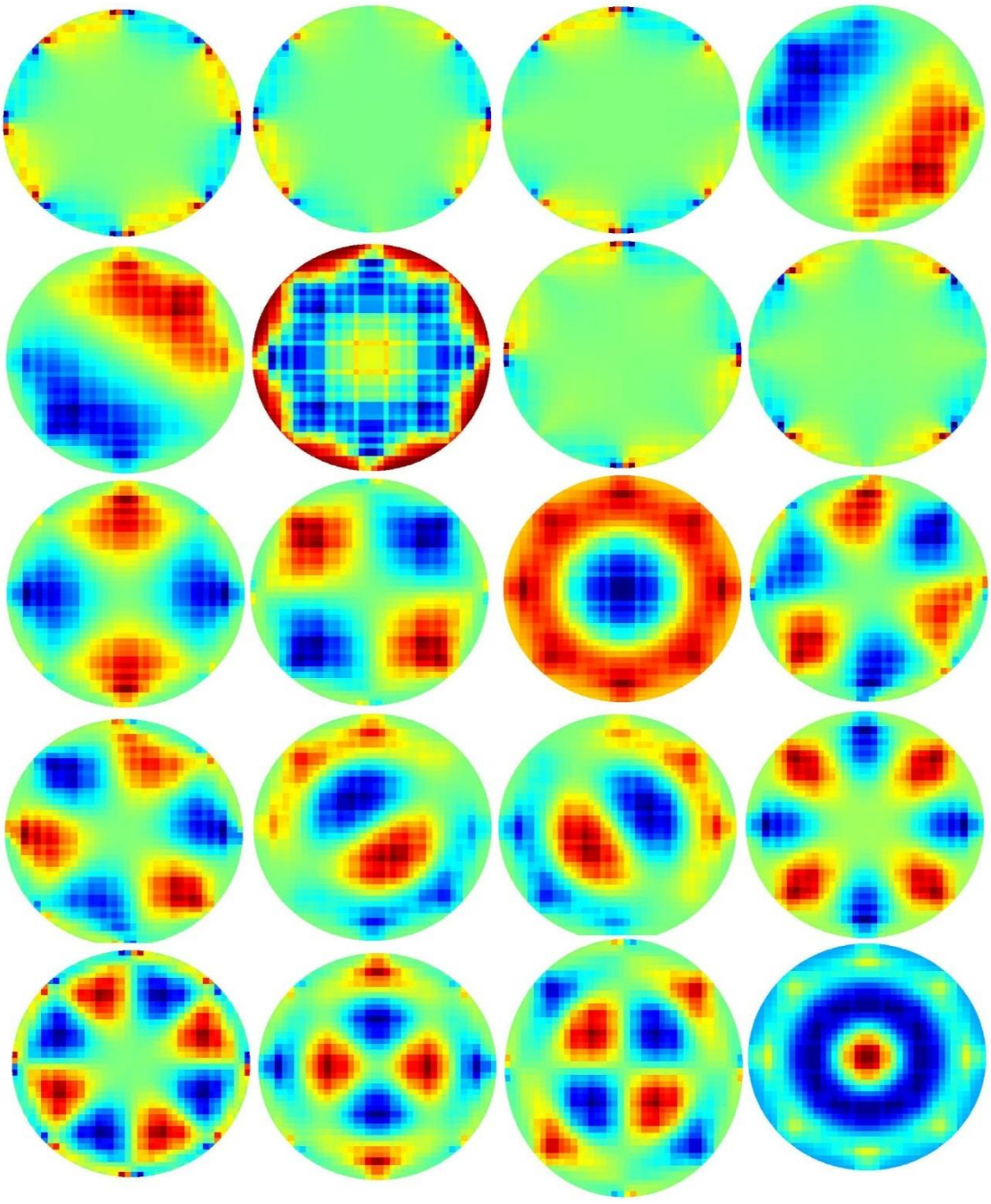

Figure 3-11 Singular images of the full array sensitivity matrix (8-electrodes). The mode number increases from left to right and top to bottom. The colour range is linear from blue to red. Red and blue colours show the highest and lowest values respectively. The main observation is that the boundary region, which is close to the electrodes, will be described ahead of the central region, which is far away from the electrodes.

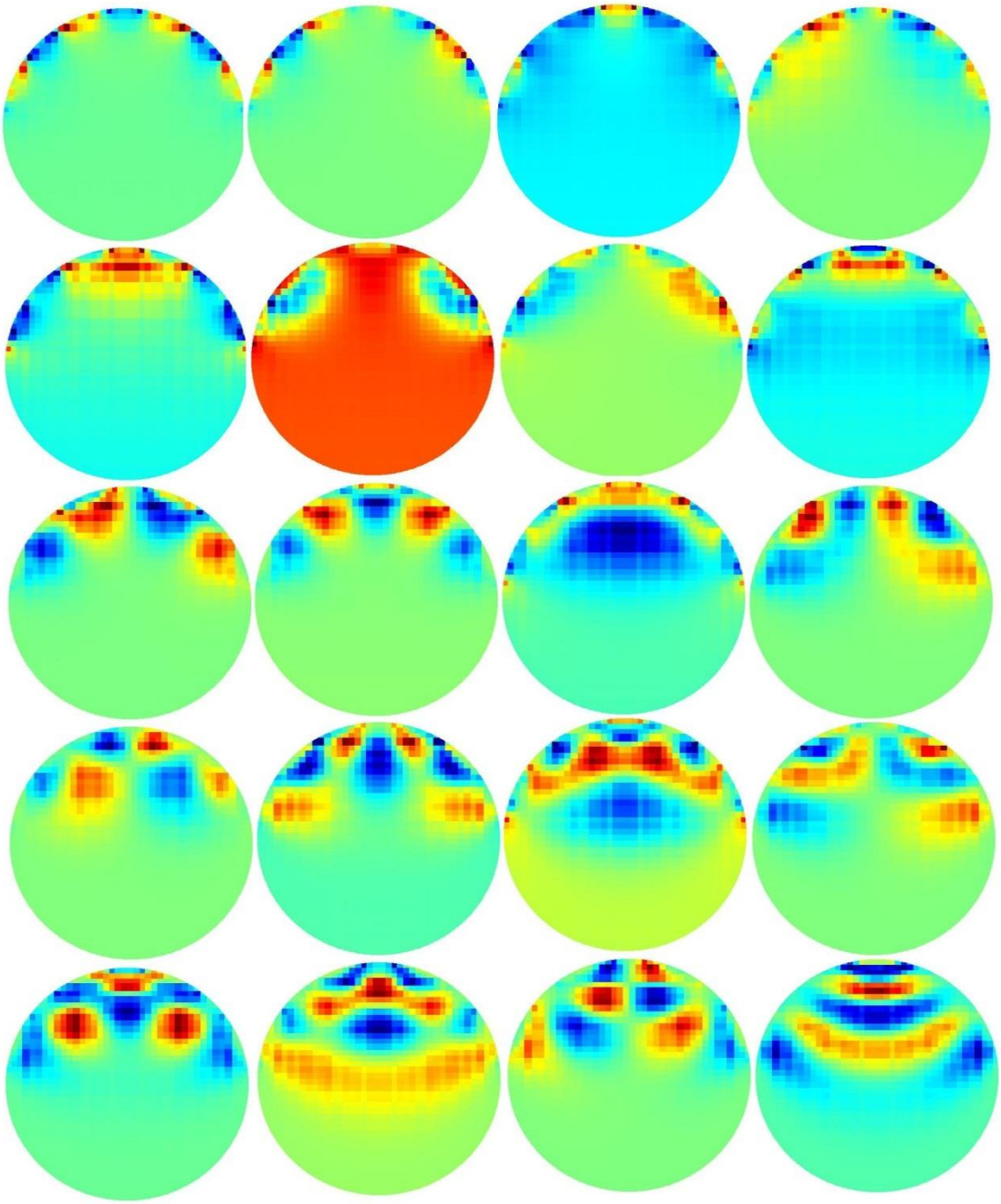

Figure 3-12 Singular images of the hemi-array sensitivity matrix (8-electrodes). The mode number increases from left to right and top to bottom. The colour range is linear from blue to red. Red and blue colours show the highest and lowest values respectively. It is seen that the singular images are unable to describe details of the region which is furthest away from the electrodes indicating potential difficulties in reconstructing any anomalies.

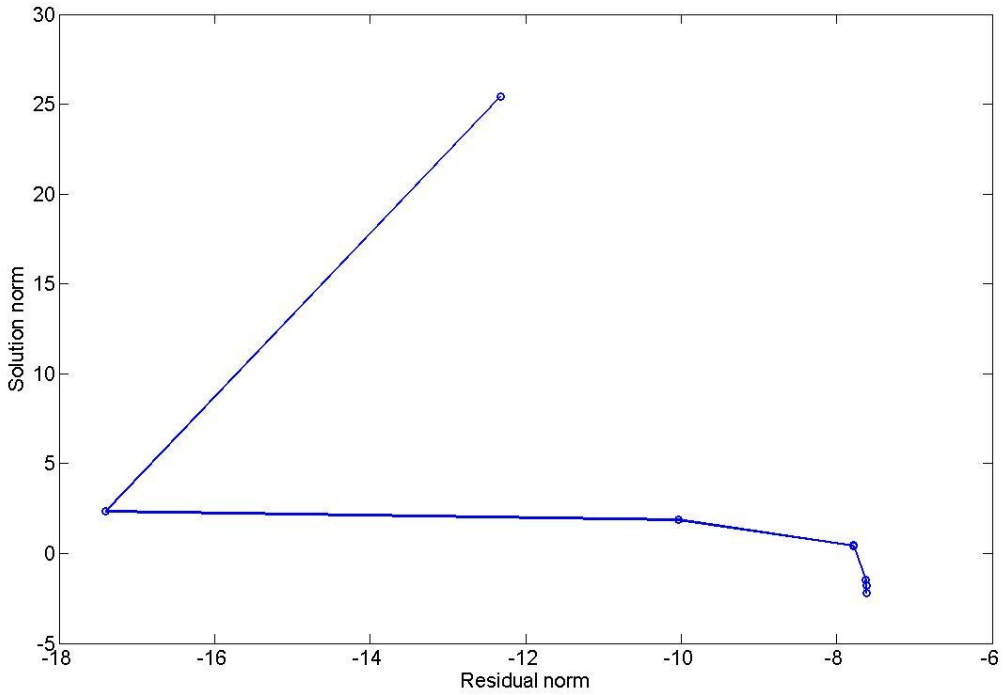


Figure 3-13 The l-curve example in TSVD regularization.

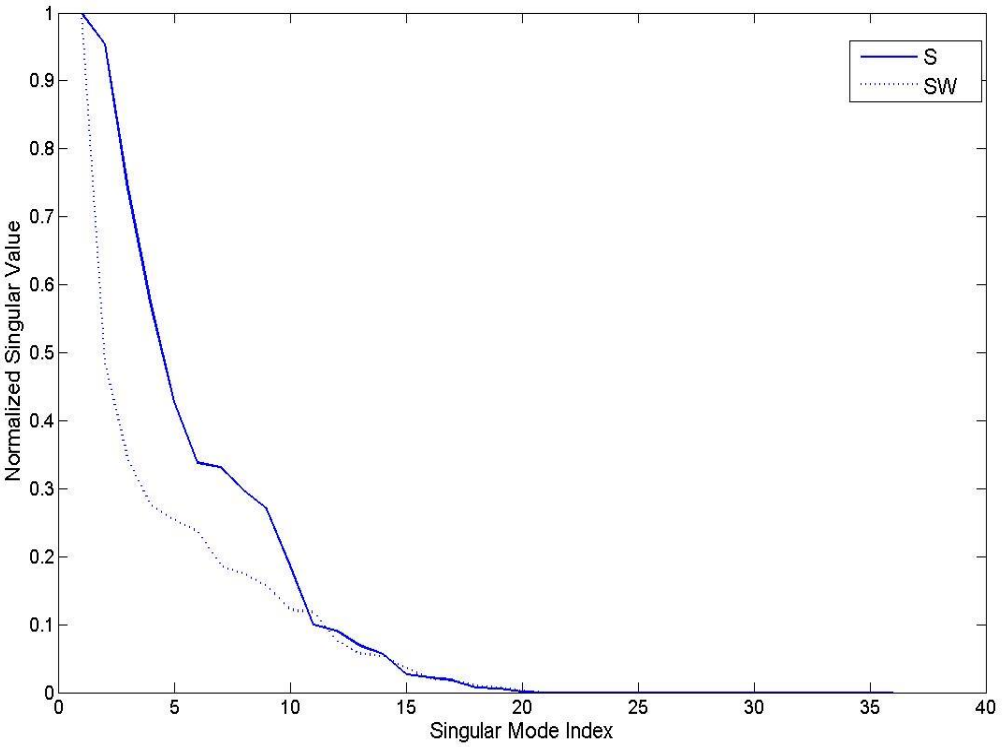


Figure 3-14 Comparison of singular value spectra **S** and **SW** in eight-electrode full array case

## 4. Simulation Results

Numerical simulations were performed to compare the reconstruction algorithm in terms of detection and resolution. The anomaly positions were changed to evaluate the central and edge regions using TSVD and WMNM. The reconstruction algorithm was also evaluated for different sizes of the anomalies.

The pseudo-inverted part of the reconstruction matrix can be understood as pseudo-inversion of a matrix product of the normalization matrix ($Q_t$ or $Q_w$) and the sensitivity matrix ($S$). Matrices $Q_t$ and $Q_w$ were obtained by the author from the equations (46) and (47) respectively with different calculation of the $B$ matrix. Changes of the system matrix condition number owing to this matrix multiplication are presented in Table 3-2.

According to Table 3-3, the choice of the normalization matrix can improve the matrix conditions. In the full array case, $W$ tended to decrease the condition number, while $Q_t$ and $Q_w$ did not. Therefore, decreasing the condition number by choosing a normalization matrix would benefit the reconstruction of the noisy measurements.

**Table 3-3:** Condition number of the normalized system matrices

| System matrix | Condition Number (Full array) | Condition Number (Hemi-array) |
|---|---|---|
| $S$ | $1.4\times10^{17}$ | $3.1\times10^{17}$ |
| $SW$ | $8.98\times10^{16}$ | $5.15\times10^{17}$ |
| $SQ_t$ | $1.36\times10^{17}$ | $9.36\times10^{17}$ |
| $SWQ_w$ | $5.1\times10^{16}$ | $6.2\times10^{18}$ |
| $SWQ_t$ | $5.96\times10^{16}$ | $1.7\times10^{18}$ |

Two-dimensional forward models of a disk containing a single internal anomaly at various locations were designed and solved using COMSOL Multiphysics linked with MATLAB. The FA layout which was shown in Figures 3-3 with anomaly was tested. The FA model has eight boundary electrodes equally spaced in a ring. All the electrodes had the conductivity of

copper ($6\times107$ $Sm^{-1}$). The length of each electrode was 0.1 relative to the disk radius. The models are solved for boundary voltage values subject to adjacent input current patterns using the direct linear system solver UMFPACK. The anomaly was located in four positions as shown in Figure 3-5. The background and anomaly conductivities are set to 1 S/m and 2 S/m respectively representing a unit conductivity change.

Figure 3-15 compares the reconstructed images of the anomaly in different locations for the full array electrode configuration. The images are successfully reconstructed using two different reconstruction matrices. The images of the first column are reconstructed using TSVD and the reconstruction matrix is $\mathbf{S}^{+}$. The MATLAB script to reconstruct the images using TSVD is presented in appendix A. The reconstructed images of the second column are obtained by $W(SW)^{+}$ as a reconstruction matrix using WMNM regularization. The MATLAB script to reconstruct the images using WMNM is presented in appendix A. Using a method based on WMNM regularization produced a more compact central anomaly but more artefacts appeared in the images when the anomaly moved towards to the boundary.

Figure 3-16 compares the TSVD and WMNM methods in terms of resolution which is estimated by the definition of the blur radius (Adler et al. 1996b). Elements that have values greater than half the maximum element value were chosen as the Half Amplitude (HA) set. Then, the resolution was calculated as a square root of the ratio between area of the HA set ($A_{HA}$) and the domain area ($A_0$) as in equation (55).

$$resolution = \sqrt{\frac{A_{HA}}{A_0}} \tag{55}$$

Small and uniform resolution values are regarded to be desirable, indicating less blurring. In Figure 3-16, there is overall enhancement of resolution when using WMNM.

Figure 3-17 presents the reconstructed images of the anomaly with various sizes. The radius of the anomaly was changed to 0.1, 0.05, 0.02, and 0.01 respectively relative to the disk radius. It can be seen that the detectability is decreased with respect to the radius reduction.

The expression for anomaly location (x, y) is effectively the centre of the reconstructed anomaly. The values $x_i$ and $y_i$ are the coordinates of the centre of each element. The

difference between the actual position of the anomaly and its reconstructed location within the xy plane can be calculated as the absolute location errors, $D_{xy}$, quoted as a fraction of the brain radius (Tang *et al.*, 2010) via Eq. (56):

$$D_{xy} = \frac{\sqrt{(\Delta x)^2+(\Delta y)^2}}{R} \tag{56}$$

Performance of the FA and the HA layouts were compared to localise the anomalies in various locations according to the electrode positions. The anomalies were simulated in different positions with the anomaly centre placed successively at a relative radial displacement of 0, 0.2, 0.4, 0.6 and 0.8 from the centre. Anomaly positions varied as a function of angle from 0° to 180° with 5° increments. The results of the localisation study using the FA and the HA layouts are illustrated in Figure 3-18 and Figure 3-19 respectively. The TSVD reconstruction method was used for the FA and the WPI reconstruction method was used for the HA layout. The real and the reconstructed position of the centre of the anomaly are shown using points and star points respectively. The localisation errors are shown by the lines between the points. The simulated anomalies were detected for all the positions using both layouts; however FA results were in general superior to the HA results. Relative radial localisation errors for FE models using the FA and the HA layout are shown in Figures 3-20 and 3-21 respectively. As expected, the HA layout localised simulated anomalies as well as the FA layout, apart from the anomalies placed far away from the electrodes. Localisation errors were larger for reconstructions of the anomalies, with the worst value of $D_{xy}$ being 0.2190 mm using the HA layout, and 0.0803 mm using the FA layout, both values being with respect to unit radius.

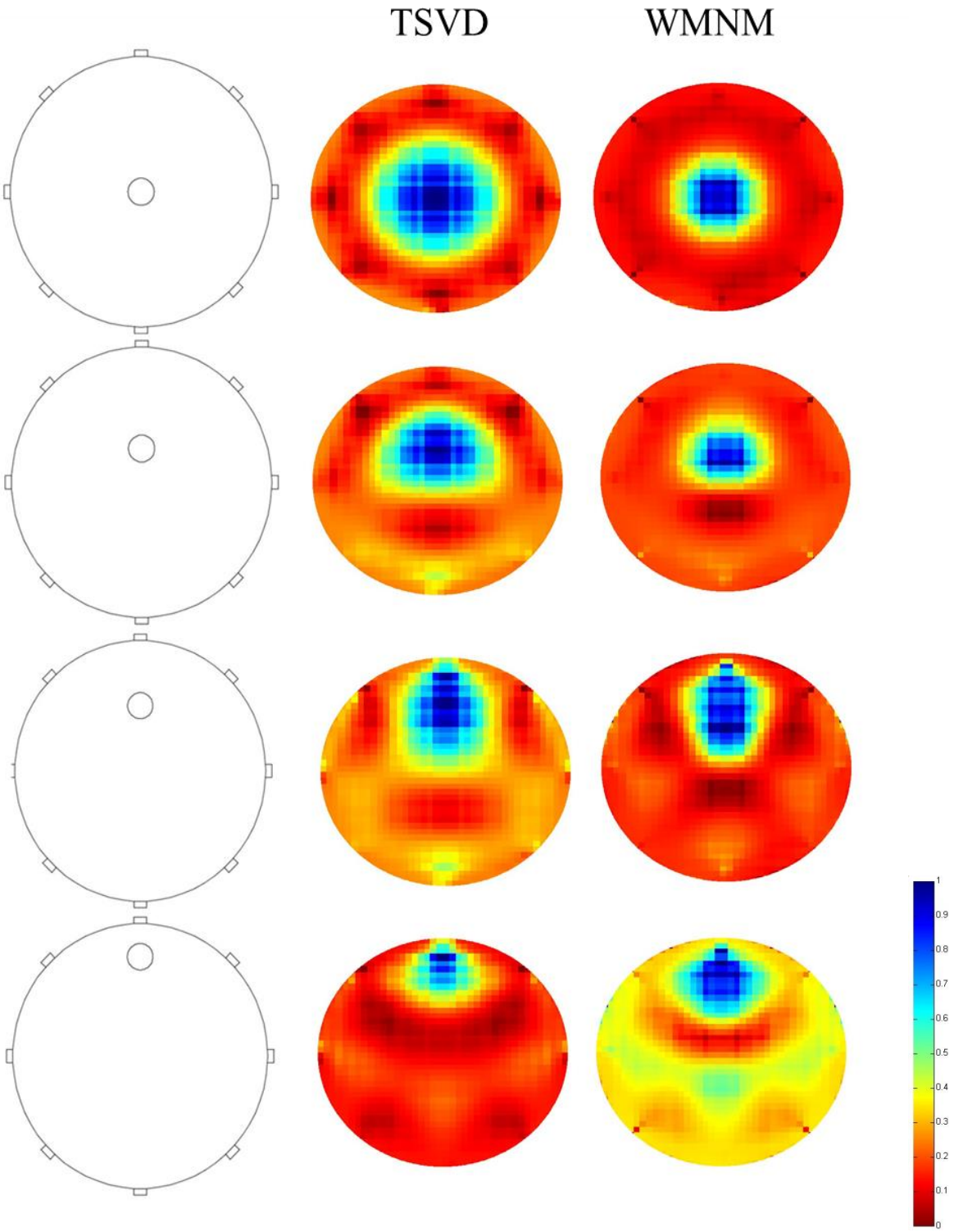


Figure 3-15 A comparison of 8-electrode full array images reconstructed using TSVD and WMNM methods. The images of the first column are reconstructed using TSVD by matrix $\mathbf{S}^{+}$. the images of the second column are obtained using WMNM by matrix $W(SW)^{+}$. Reconstructed images using WMNM produced a more compact central anomaly but more artefacts appeared in the images when the anomaly moved towards the boundary.

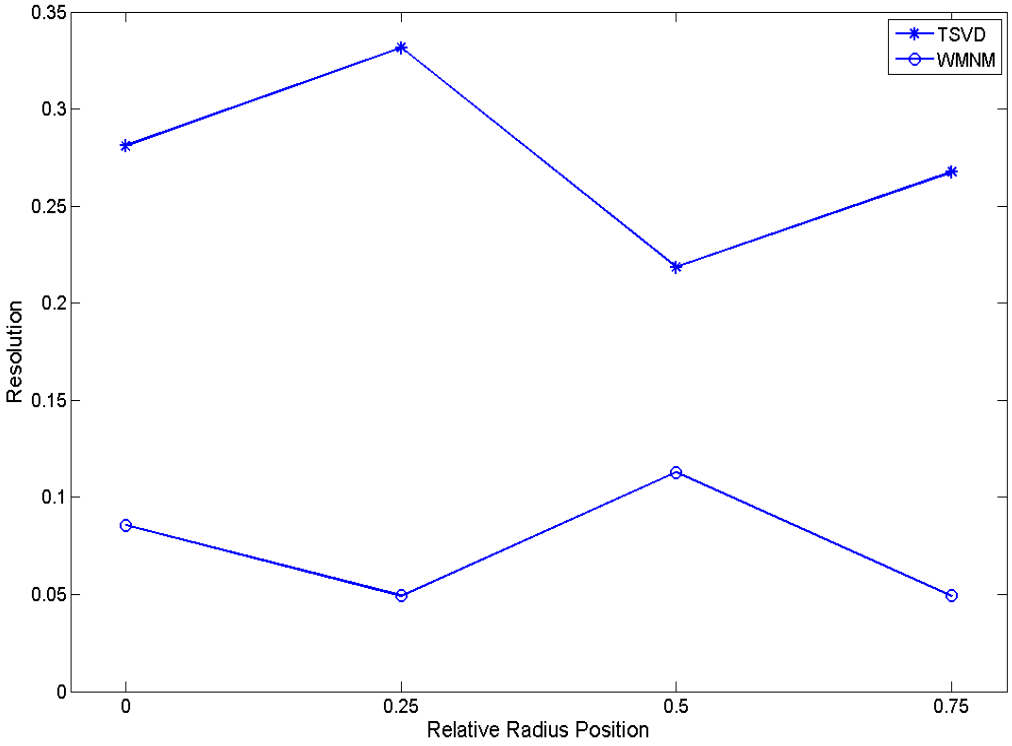


Figure 3-16 A comparison of 8-electrode full array images reconstructed using TSVD and WMNM in terms of resolution

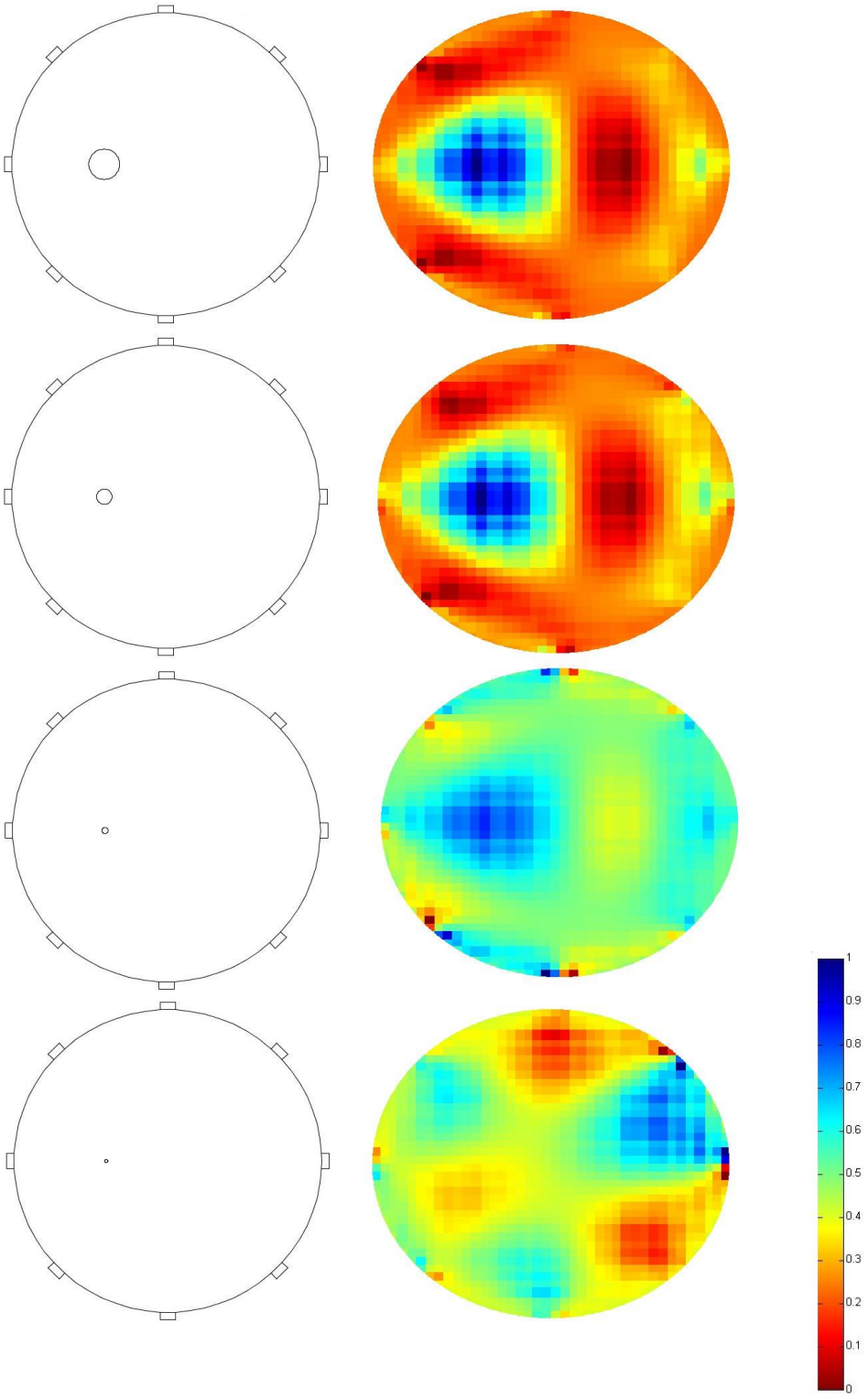


Figure 3-17 The reconstructed images for the anomaly with different sizes. The radius of the anomalies was changed to 0.1, 0.05, 0.02, and 0.01 respectively relative to the disk radius. It can be seen that the detectability is decreased with respect to the radius reduction.

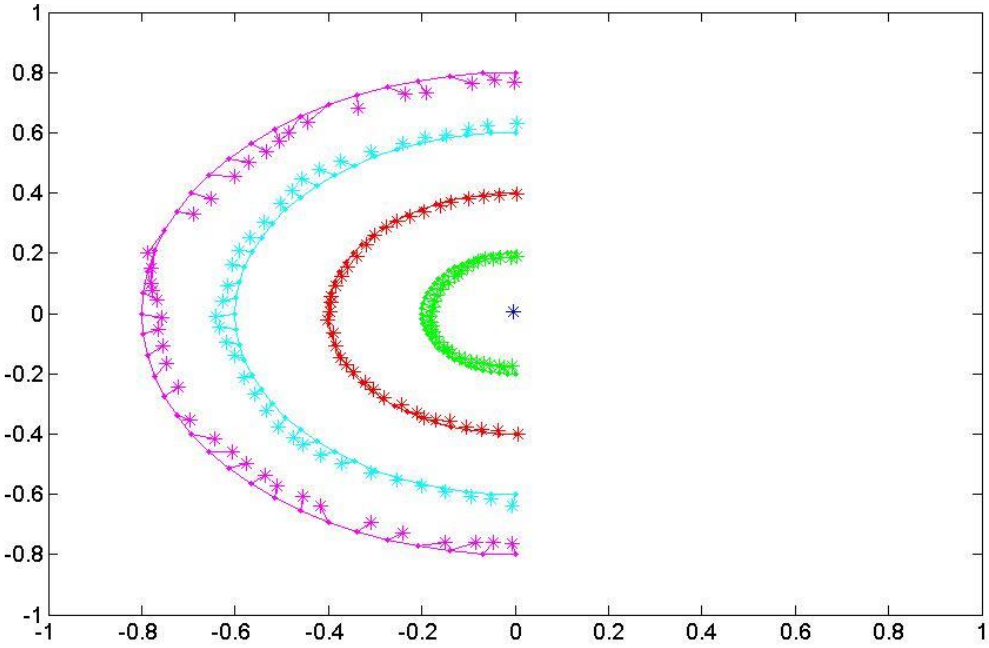


**Figure 3-18:** Localisation of the simulated anomalies on FE model at various positions using the full array (FA) electrode layout. Anomaly positions varied as a function of angle (from 0° to 180° with 5° increments) at relative radius of 0, 0.2, 0.4, 0.6 and 0.8.

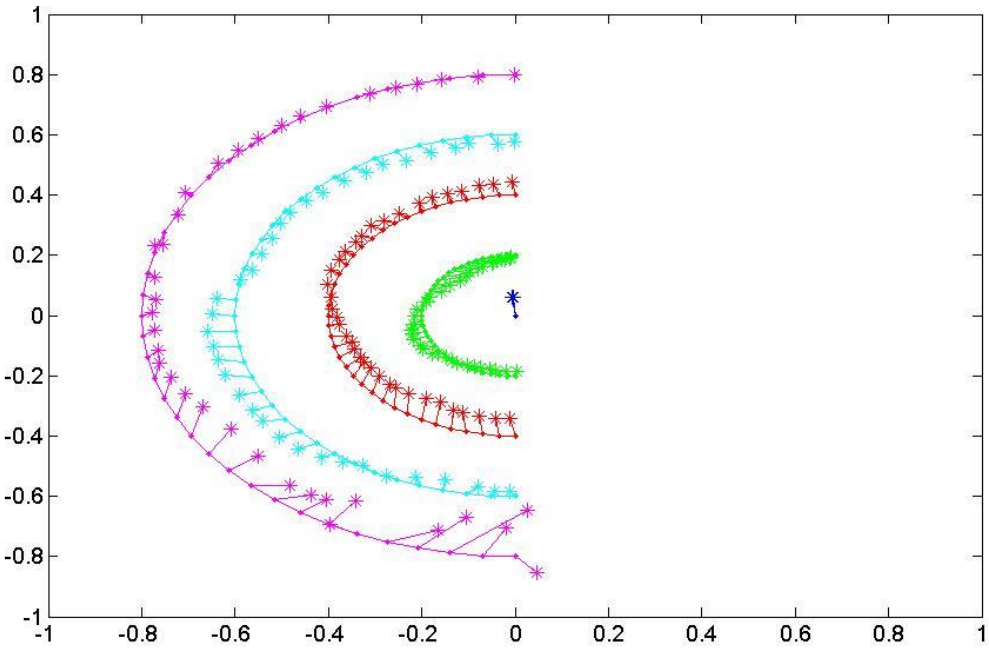


**Figure 3-19:** Localisation of the simulated anomalies on FE model at various positions using the hemi-array (HA) electrode layout. Anomaly positions varied as a function of angle (from 0° to 180° with 5° increments) at relative radius of 0, 0.2, 0.4, 0.6 and 0.8.

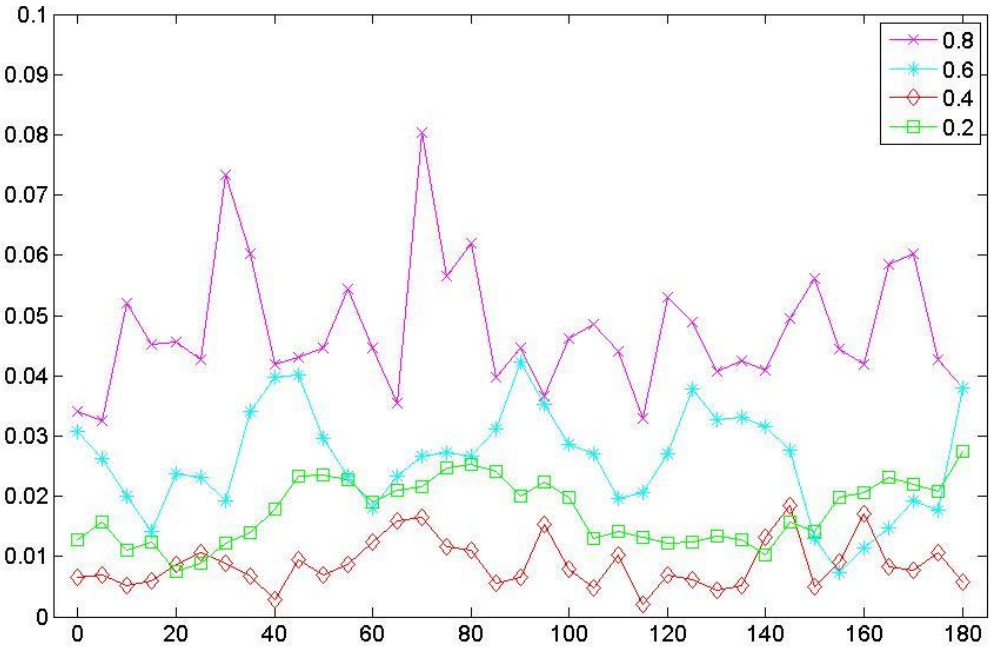


**Figure 3-20:** Relative radius localisation errors, Dxy, of the simulated anomalies on FE models at various positions using the full array (FA) electrode layout. Anomaly positions varied as a function of angle (from 0° to 180° with 5° increments) at relative radius of 0, 0.2, 0.4, 0.6 and 0.8.

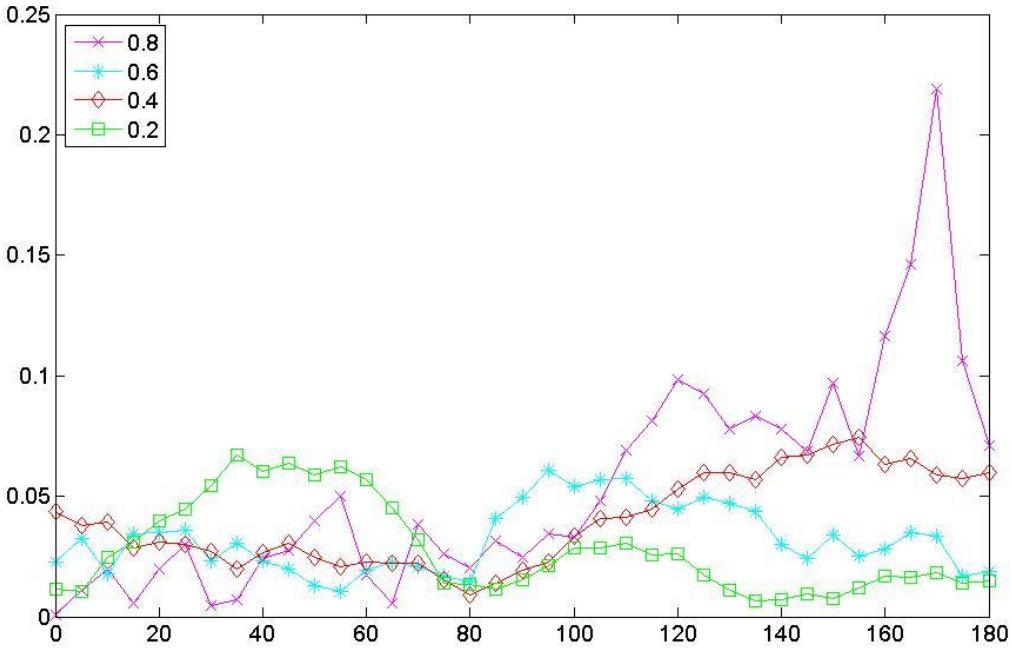


**Figure 3-21:** Relative radius localisation errors, Dxy, of the simulated anomalies on FE models at various positions using the hemi-array (HA) electrode layout. Anomaly positions varied as a function of angle (from 0° to 180° with 5° increments) at relative radius of 0, 0.2, 0.4, 0.6 and 0.8.

## Summary

In this chapter the simulation study using FE models were presented. The forward and inverse models were created to obtain images and detect the simulated anomalies.

The full array and hemi-array layouts were modelled. For the first step, the singular images were reconstructed and compared to study their spatial resolution. The main observation was that the region which is close to the electrodes was described ahead of the region far away from the electrodes. It was clear that the spatial resolution is poor at the back of the head far away from the electrodes in the hemi-array layout in which the electrodes are positioned only on the anterior surface of the head.

A 2D disk model with an 8-electrode full array and hemi-array layouts were designed and compared to detect and localise the simulated anomalies. A smaller disk to simulate the anomaly was designed to fit inside this model. The results were compared when the anomaly moves from the centre towards the boundary with angles from 0° to 180° with 5° increments. Although the full array had a better performance comparing to the hemi-array layout, the hemi-array layout results were acceptable.

The hemi-array layout is desirable due to the position of the electrodes which will be suitable or necessary in emergency care. A minimal number of electrodes would greatly assist electrode attachment, making the task easier and faster in emergency care. Positioning the electrodes only on the anterior of the head would allow immobilisation of the patient especially in cases of multiple trauma. Therefore, the full array and hemi-array layouts were considered for the phantom experiments to study their performance further in the realistic condition. In order to perform phantom experiments, a prototype model of an EIT system was constructed. The details and the hardware structure of the Loughborough EIT system are explained in the next chapter.

CHAPTER

# 4

# Construction & Evaluation of an EIT System

From the simulation study on FE models in the previous chapter, the full array and the hemi-array layouts were considered for use in phantom experiments. In order to perform the experiments, an EIT system was constructed. The structure of a digital, multi-frequency EIT system and its components constructed in the laboratory as a prototype is presented in the next sections. Then the EIT system performance to detect anomalies was evaluated and calibrated based on a systematic methodology using a realistic and practical phantom. The phantom was equipped with 8 stainless steel screws as point electrodes equally spaced around the tank wall in a FA layout. The anomalies were simulated inside the phantom. The instrumentation hardware and image reconstruction were assessed. The assessments were divided into a category of measurements of accuracy and a category of measurements of detectability. The phantom experiments were performed with one and two simulated anomalies, close to each other and far from each other to evaluate the accuracy and detectability of the system.

## 1. Medical EIT systems

Early EIT systems were designed using mainly analogue techniques with many associated problems such as noise, component mismatching, input offset, etc. The speed of previous analogue designs was also limited by factors such as switching transients, multiplexing overhead and conversion delays. Nowadays, EIT systems widely use digital techniques with the advantages of high stability and low noise. The most recent EIT systems are based on advanced technologies which improve their performance, such as high bandwidth and good precision. Moreover, using digital components make upgrading and debugging easier.

### 1.1.Measurement Methods in Medical EIT

In EIT, the imaging of the internal body structure is reconstructed using potential or current measurements made from electrodes on the body surface while a constant current or voltage is applied to two or more electrodes. There are different types of measurement methodologies. A type of measurement in which current is sequentially applied to the body using pairs of electrodes and voltages are measured between adjacent non-current-carrying electrodes called Applied Potential Tomography (APT). This procedure is repeated for current applied between all other pairs of electrodes to obtain a voltage data set (Brown 2003, Saulnier et al. 2001). Adaptive Current Tomography (ACT) is another type of measurement in which an appropriate set of current patterns is specified to apply simultaneously to all electrodes and voltages are measured on each electrode to generate the data required for image reconstruction. This technique can offer greater impedance distinguishability than an APT system, since larger electrode voltages can be produced for a given change in impedance within the body (Saulnier et al. 2001, Liu et al. 2003). This provides the ability to detect smaller impedance variations within the object and consequently allows for greater resolution; however, it requires more complex hardware since a current source for each electrode is used. Moreover, since the sum of all applied current to the body is limited by the current safety regulation, this method cannot be used in vivo (Brown 2003). There is another measurement technique in which a voltage source is used rather than a current source. This technique can simplify the electronics but it is less desirable from the theoretical point of view and tends to increase the sensitivity to electrode placement and size errors (Saulnier 2005, Rafiei Naeini 2008). There are some EIT systems based on applying voltage and measuring the resulting surface currents (Rafiei Naeini 2008, Choi et al. 2003, Hartov et al. 2002, Hartov et al. 2000, Sansen et al. 1992, Zhu et al. 1993).

### 1.2.Current Safety

For the safety of the patient the maximum currents flowing through the leads at different frequencies are defined by the international safety standard for medical equipment, IEC 601-1. IEC is the International Electro-technical Commission (for most countries outside the USA). EN 60601-1 is the European variant and BS EN 60601-1 is the British variant (BSI British Standards, 2006). They give general requirements for the safety of medical electrical equipment (Rafiei Naeini 2008).

For frequencies between 0.1 Hz and 1 kHz, the maximum current is 10 μA (rms) for medical electrical equipment that is directly connected to a patient's heart. In this frequency range, the maximum current for equipment that is not connected directly to the heart is 100 μA (rms). For frequencies greater than 1 kHz, the maximum current is defined as the product of the limits defined for frequencies less than 1 kHz and the frequency, in kilohertz, up to a maximum multiplier of 100. For example, in an item of equipment that is not directly connected to the patient's heart, at 10 kHz, we can pass $100\ \mu A \times 10 = 1\ mA$ (rms) current through the patient. In all medical electrical equipment, to meet the standards set by the IEC, the injected currents should be lower than the limits indicated above (Rafiei Naeini 2008, Ghahary et al.1990).

## 2. EIT Hardware

The structure of the designed EIT system based on a microcontroller is presented in Figure 4-1. The hardware of the EIT system is shown in Figure 4-2. The system can be divided into Microcontroller Unit (MCU), Direct Digital Synthesizer (DDS), Constant Current Source (CCS), Multiplexer and De-multiplexer (MUX/DEMUX) and Instrumentation Amplifier (IA) subsystems. The prototype model has 16 channels and operates in the frequency range of 10 kHz to 100 kHz with a temporal resolution of 100 frames per second. In order to control the data acquisition process, check electrode contact, visualize data and image, the system is connected to a PC through a serial port (RS232). System software, including graphical user interface, was developed using Visual Basic (VB).

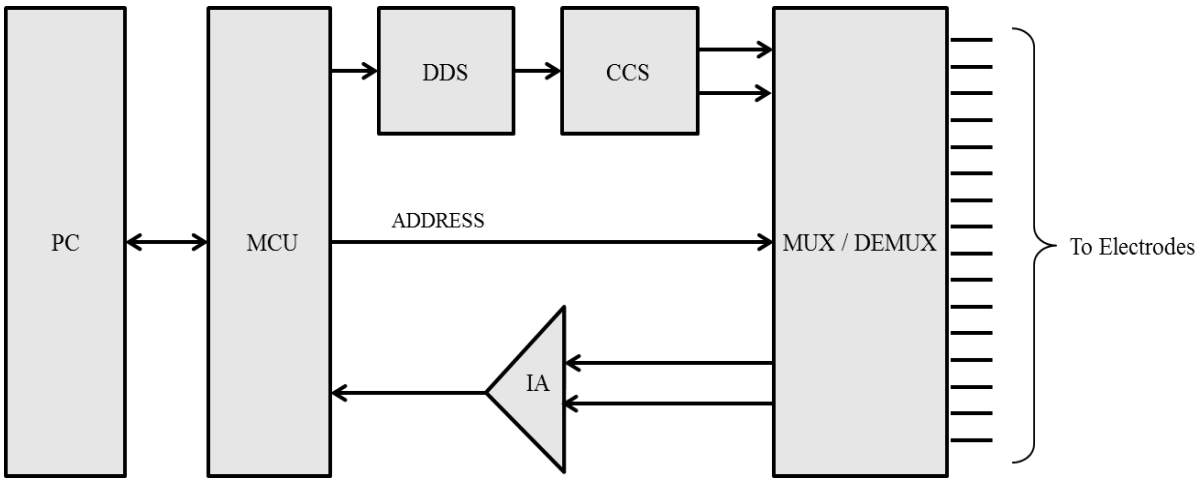


**Figure 4-1:** EIT system architectural overview. This system is based on a microcontroller connected to a PC through a serial port. A graphical user interface was developed using Visual Basic (VB). The Constant Current Source, CCS generates a constant current fed by a signal generated by the Direct Digital Synthesizer, DDS. The measurements were amplified using an Instrumentation Amplifier (IA) to produce a complete voltage data set.

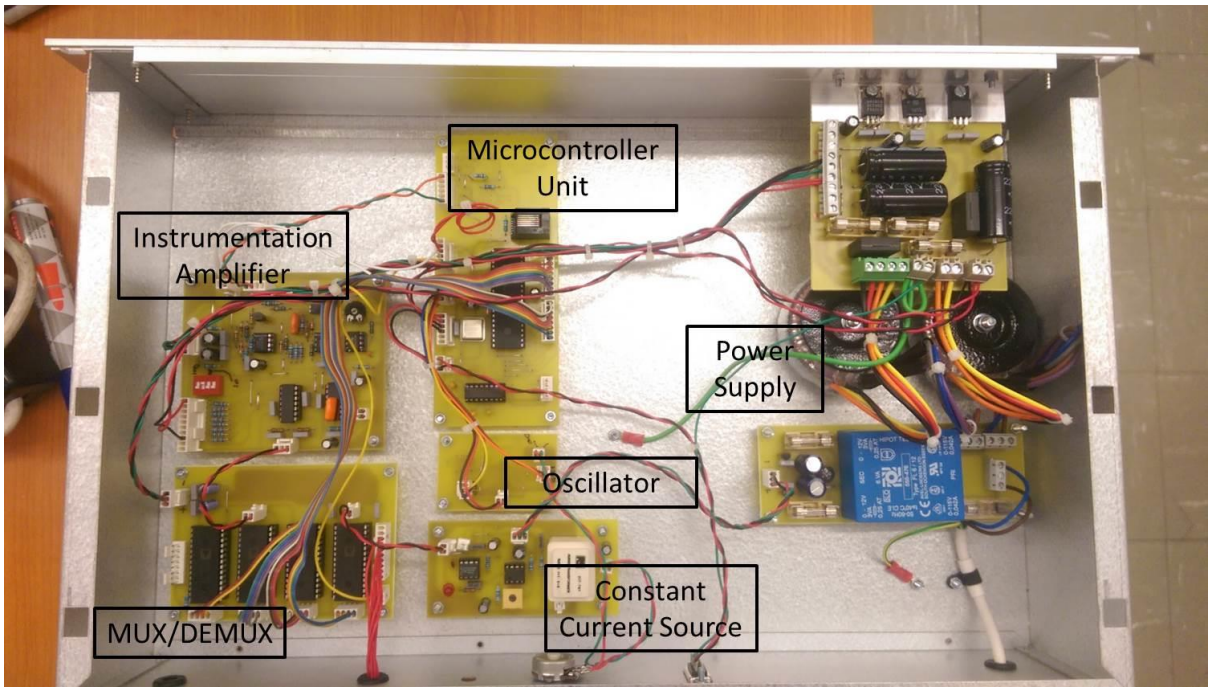


**Figure 4-2** EIT System Hardware

### 2.1.Microcontroller Unit

The MCU has many functions to control the other parts of the system. MCU allows the interface of the hardware to a computer and also controls the MUX/DEMUX. In this system, the Atmega16 is used which is an AVR microcontroller from ATMEL company. It is a high-performance low-power 8-bit microcontroller with 16 Kbytes of In-System Self-programmable Flash program memory and 1 Kbyte Internal SRAM to store data. The electrode addresses are prepared by the MCU in order to send to the MUX/DEMUX. The MCU controls the connection between the electrodes and the system. Applying the excitation current generated by the CCS to the electrodes and measuring voltage by the IA from the remaining electrodes is managed by the MCU. The MCU is connected to a PC via a RS-232 serial communications port. This provides the maximum flexibility without the need to modify the hardware. The Microcontroller allows flexibility in design options such as an arbitrary shape of signal generation and flexibility in the communication between system components and data collection. The MCU also gathers the measured data obtained from the IA through the ADC and transfers them to PC for further processing.

The connection between electrodes and the output of the CCS was controlled by the MCU using outputs A1 and A2. By using outputs A3 and A4, the connection between electrodes and IA to measure the voltages was controlled. Moreover, the MCU can completely disconnect the electrodes from the CCS and IA by enabling MUX/DEMUX using the ENABLE output. The schematic of the MCU and MUX/DEMUX connection is illustrated in Figure 4-3.

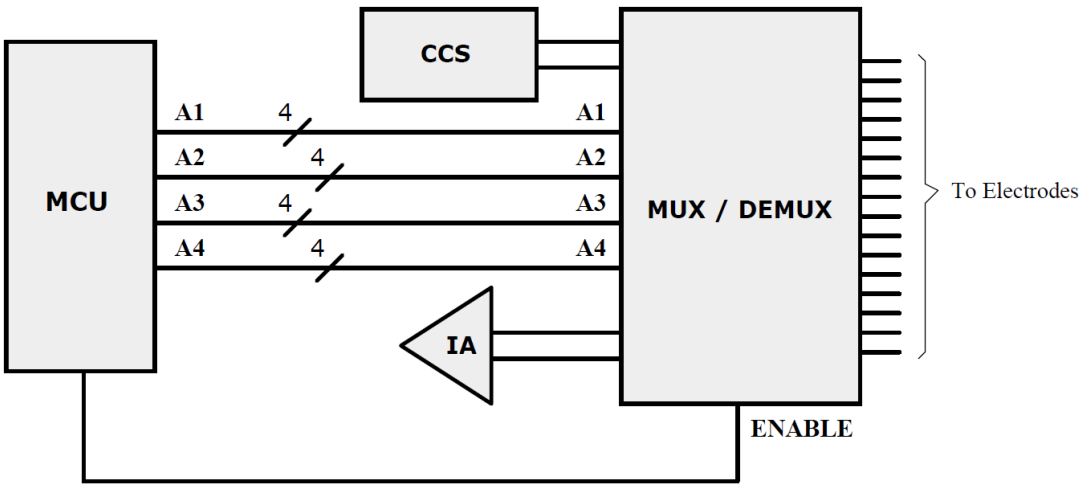

Figure 4-3 MCU and MUX/DEMUX connection.

In this study, the crystal Y1 was used to select the frequency 16 MHz. Pins 14 and 15 (RXD and TXD) were used in order to connect the MCU to the RS232 serial port; however, the voltages in these pins were 0 and 5 V. Therefore, MAX 232 was used to convert the voltages to +12 and -12 and then from J4 was connected to the PC. The circuit of the MCU and MAX232 are shown in Figure 4-4. The MCU and MUX/DEMUX were connected through J5 and J9. J2 was connected to the ADC and the MCU was connected to the programmer by J3 (ISP) in order to do programming. To protect from noise the reset input was connected to Vcc through R1 and a switch, S1, was designed to reset the system manually. The power supply was connected to the MCU by J1 and C1, C2 and C3 were placed to eliminate the power line noise close to the microcontroller as designed in the Printed Circuit Board presented in Appendix B.

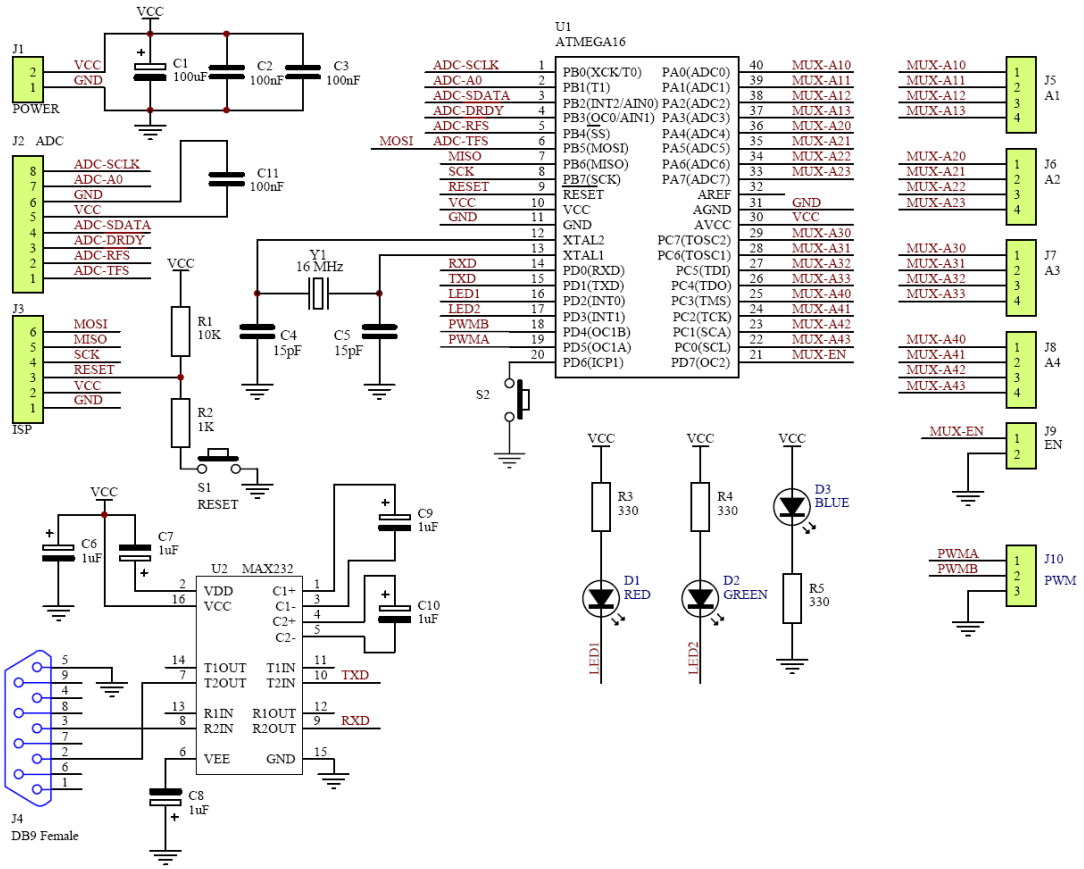


Figure 4-4 The MCU connection circuit.

## 2.2.Waveform Synthesizer

Early EIT systems used analogue oscillators to produce a sinusoidal reference waveform. However, in most recent designs digital waveform synthesis techniques are used. Digital techniques produce sinusoidal waveforms with low harmonic distortion, high stability and better synchronization between the generator and the demodulator is produced (Boone et al. 1997). Furthermore, the digital waveform generators are more effective to use in multi-frequency EIT systems since the operation frequency can be easily changed (Lee et al. 2003). In this study a Direct Digital Synthesizer (DDS), AD9833 produced by Analogue Devices, was used to generate a sinusoidal waveform and its frequency can be selected form 10 kHz to 100 kHz.

## 2.3.Current Source

In EIT systems, a Voltage-Controlled Current Source (VCCS) is used. The current produced by the VCCS is proportional to an input voltage generated by the waveform synthesis block (Boone et al. 1997, Saulnier 2005). An ideal current source should have infinite output impedance over a specific range of frequencies to make the injected current independent of the load properties (Boone et al. 1997, Saulnier 2005). However, in reality the output impedance of current sources is finite, $Z_O$, which provides a path to shunt the output current from the electrode (Cook et al. 1994). The VCCS is designed to convert the sinusoid voltage to a proportional sinusoid current. The current is then used to inject to electrodes on the surface of the body and the corresponding voltage is measured and the images of internal impedance can be reconstructed using complicated algorithms. The Howland current source was chosen as the candidate current source for its simplicity and its high output impedance.
The CCS circuit was shown in Figure 4-5. The PCB design of CCS and its connection to MCU and PS was illustrated in appendix B.

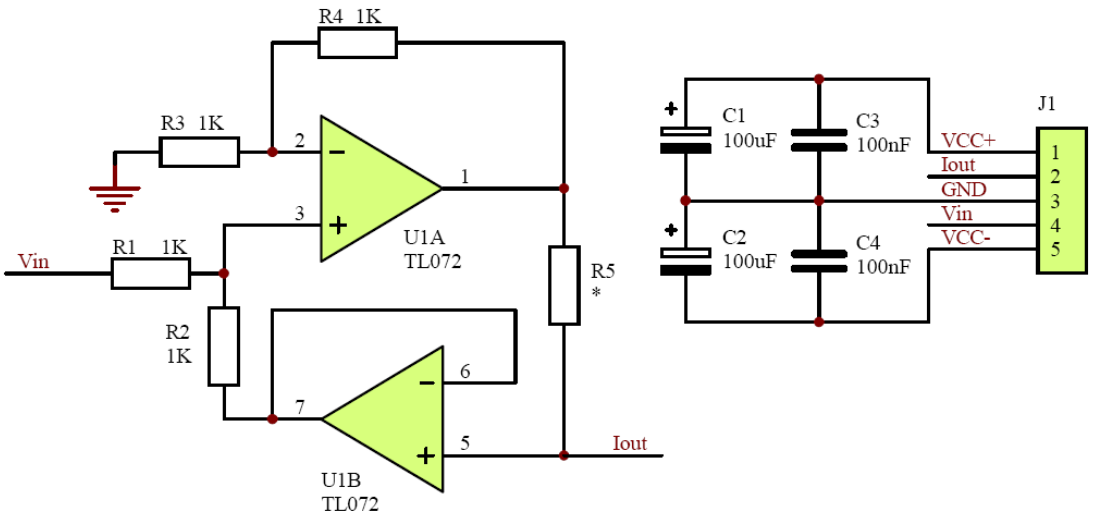


Figure 4-5 The circuit of the CCS.

### 2.4.Voltage Measurement

The effect of contact impedance between electrodes and skin can be neglected due to the high input impedance of the measuring voltage devices. Therefore the voltage measurement technique is recommended and is generally used. There are two methods of measuring the voltages from the electrodes. Some EIT systems measure single-ended voltages where the measurements are made with respect to the ground and some systems measure differential voltages between a pair of electrodes (Saulnier 2005). The main advantage of measuring differential voltages is that the voltage between a pair of electrodes is smaller than the voltage between each individual electrode and the ground potential. This reduces the dynamic range requirements for the measurement part of the instrument (Rafiei Naeini 2008).

In EIT, in order to measure the voltages between electrodes, instrumentation amplifiers (IA) are normally recommended and used. The effect of contact impedance and the common-mode voltage introduced in the EIT systems can be eliminated using an ideal IA due to its infinite input impedance and infinite Common-Mode Rejection Ratio (CMRR). However in reality IAs generally have limited input impedance (but very large) and CMRR, which is large at DC and drops with increasing frequency (Rafiei Naeini 2008, Saulnier 2005). In

order to compensate the limited input impedance of the IAs, buffers between the voltage electrodes and the IAs can be used (Boone et al. 1996).

### 2.5.Multiplexer and De-multiplexer

In this study the MUX/DEMUX is designed for 1 to 16 electrodes using 4 ADG406 from Analog Devices. This is an integrated circuit providing a 16-channel analogue multiplexer which is capable of selecting any one of sixteen channels at switching speeds up to 2MHz. For maximum flexibility, it is desirable to be able to select any pair of electrodes which will be the sources of the injected EIT current or voltages. This selection must be controlled from the host PC. In a typical experiment, the injection electrodes are first selected and voltages are recorded from a set of the remaining electrodes. The injection then proceeds to a different pair of electrodes and the measurements are repeated. The circuit was shown in Figure 4-6. The PCB design of the MUX/DEMUX was presented in appendix B. The block diagram of the connection between MCU, PS, CCS and MUX/DEMUX is illustrated in Figures 4-7.

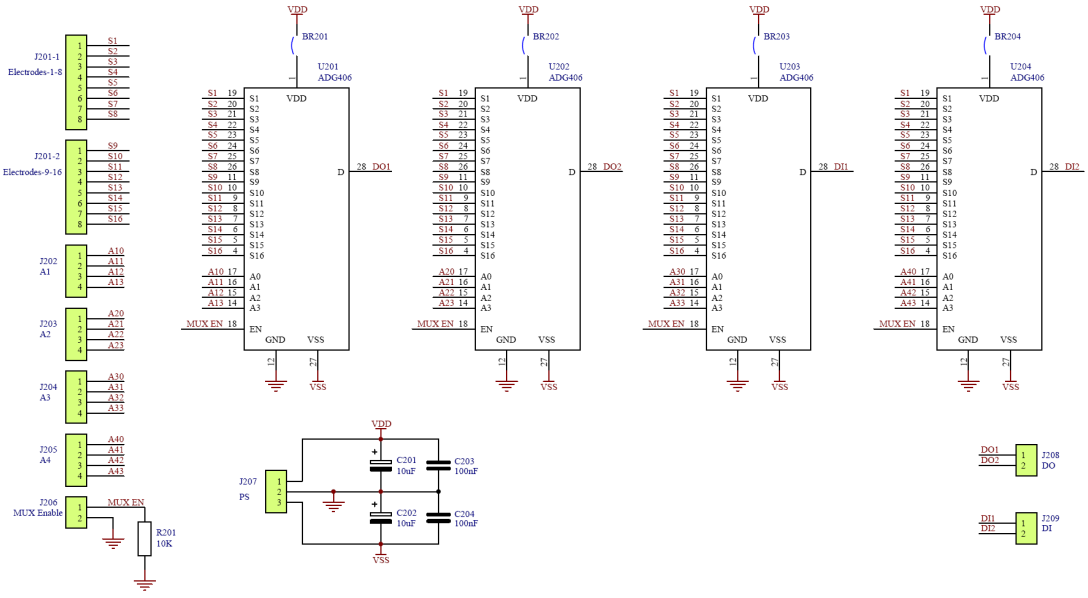


Figure 4-6 The circuit of the MUX/DEMUX.

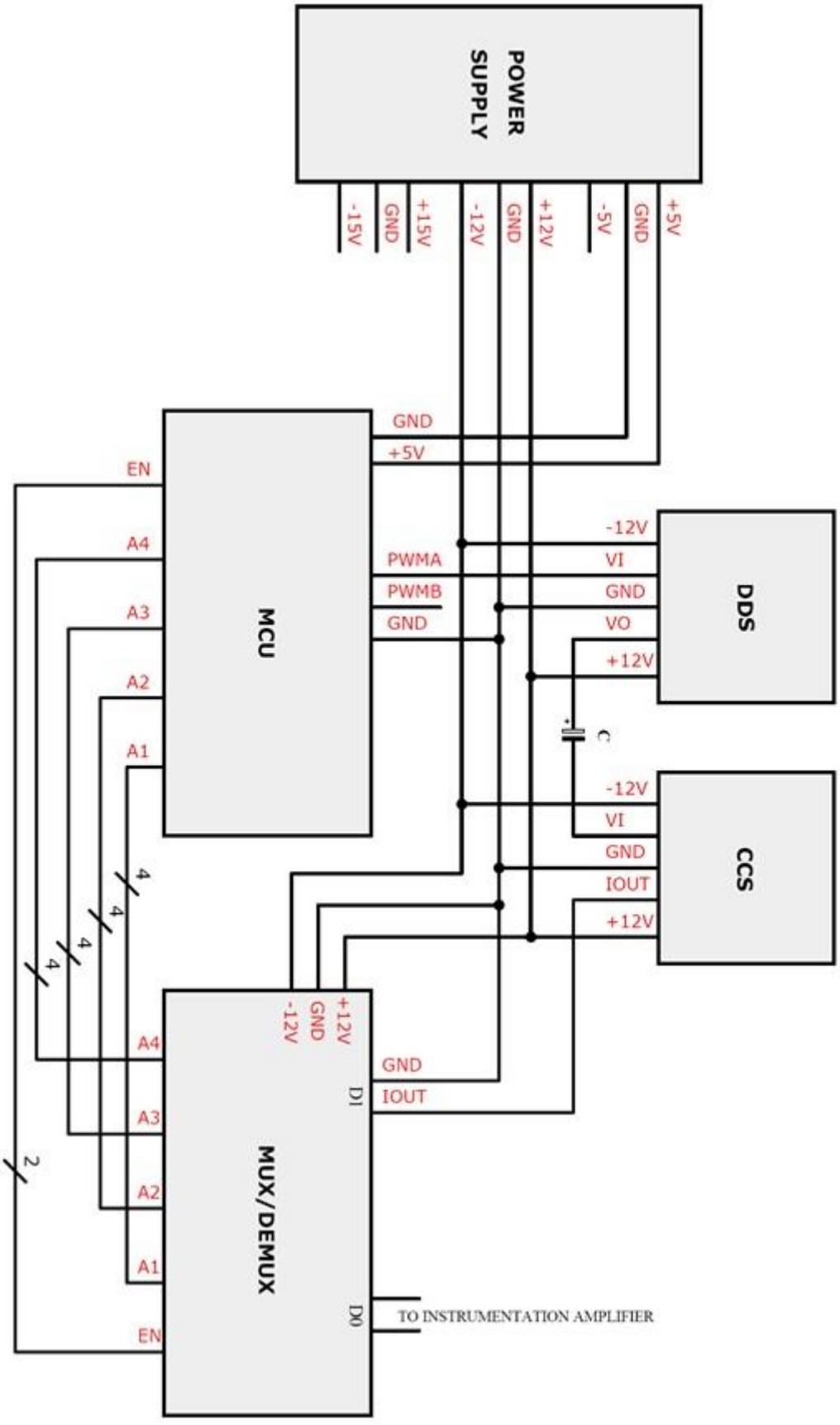


Figure 4-7 MCU, PS, DDS, CCS and MUX/DEMUX connection.

### 3. Phantom Configuration

The EIT system was evaluated using phantom experiments in the presence of realistic noise. The phantom consisted of a shallow polymer tank, eight electrodes, the background solution, and the simulated anomalies (cucumber segments). The tank had a depth of 80 mm and an inner diameter of 144 mm. The phantom was equipped with 8 stainless steel screws as point electrodes (dia. 10 mm) equally spaced in a ring around the tank wall. All the lead wires were of equal lengths to obtain an identical impedance path through all the electrodes in order to reduce the mismatch in electrode impedances. 0.38% saline solution with a conductivity of approximately 1 S/m was used for the background solution. Cylindrical pieces of cucumber with a conductivity of 0.05 S/m were used as anomalies. The anomalies had a diameter of approximately 40 mm and the same height as the tank. The phantom configuration is shown in Figure 4-8 and its parameters are presented in Table 4-1.

**Table 4-1:** Phantom parameters

| Parameter | Value |
|---|---|
| Number of electrodes | 8 |
| Electrode array type | Full array |
| Background conductivity (Saline Solution) | 1 S/m (0.38%) |
| Anomaly conductivity (Cucumber) | 0.05 S/m |
| Electrode type | Point electrode (stainless steel screws) |

Figure 4-8 Phantom Configuration

## 4. Data Collection and Image Reconstruction

The experiment setup is presented in Figure 4-9. The electrodes of the phantom were connected to the EIT system via equal length wires. The EIT system was connected to the PC to control the data acquisition process, check electrode contact, and visualise data and images. Images were reconstructed using the collected data by MATLAB scripts, which are presented in Appendix A.

With reference to Figure 4-1, the CCS (NE5534, Texas Instruments) generated a constant sinusoidal current of 1mA, 10 kHz frequency. It was fed by a sinusoidal signal (1 V (rms)) of the same frequency which was generated by the DDS (AD9850, Analogue Devices). The sinusoidal current was injected into the phantom through one pair of adjacent electrodes and the corresponding boundary potentials were measured over pairs of the remainder of the neighbouring electrodes. The voltages were measured while the current was applied to the phantom. The input pair of electrodes was switched over all adjacent electrode pairs and the measurement procedure was repeated for all possible adjacent pairs to produce a complete

voltage data set according to the adjacent electrode switching protocol. The measured differential potentials were amplified using the IA (PGA202KP, Texas Instruments). The amplified analogue signal was converted to digital and transferred to the PC using the MCU (PIC18F4620).

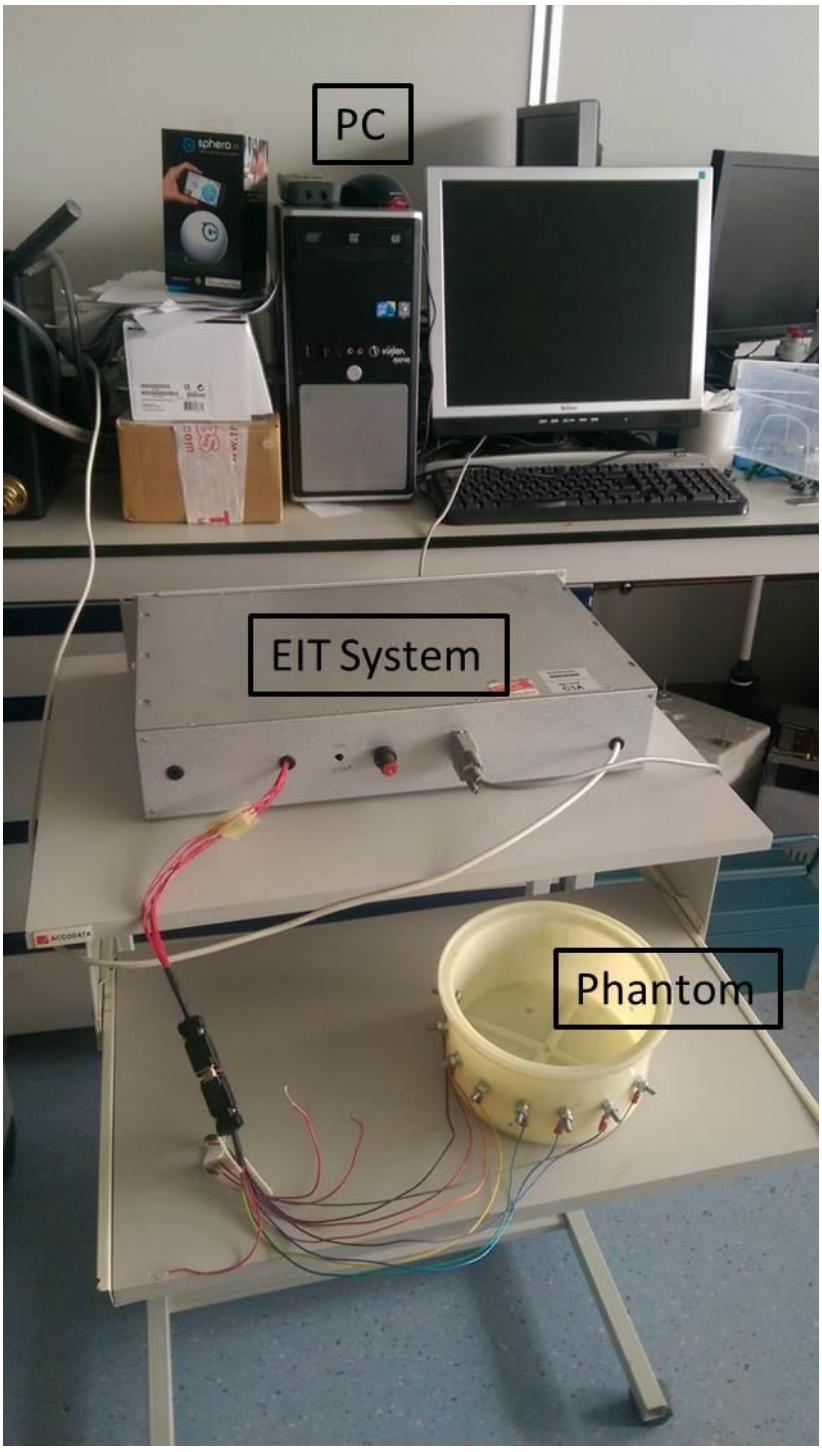


Figure 4-9 Phantom experiment setup

The images were reconstructed using COMSOL Multiphysics and MATLAB. The phantom domain was simulated as a 2D disk model with 8 electrodes. The domain was discretized to 1512 second-order triangular finite elements. Each pixel of the reconstructed images was related to the conductivity changes $\Delta\sigma$, which in turn were related to the differential potential $\Delta V$, measured over the electrodes. This relationship in matrix form was expressed as a system of linear equations as in equation (31). The problem was to find conductivity changes for given measured potentials and calculated sensitivity matrix. The potential data was collected from the phantom experiments and the sensitivity matrix was calculated for a circular model of the phantom with uniform conductivity. The sensitivity matrix is always severely ill-conditioned and has a large condition number. In this study, the sensitivity matrix had a full rank of 20 and the condition number was of the order of $10^{17}$. The Truncated Singular Value Decomposition (TSVD) method was used to regularize the inversion of the sensitivity matrix. The truncation point k, needed to be chosen carefully, less than or equal to the rank of the matrix, as it would otherwise have produced inaccurate images. The truncation point was chosen as 16 in this study.

## 5. Evaluation Methodology

The performance of the EIT system was evaluated according to (Yasin et al 2012) using a systematic approach. In order to assess the noise and accuracy of the system, an acquisition of a sequence of at least 100 frames of data was collected from the homogenous saline-filled tank before anomalies were introduced. A signal to noise ratio (SNR) was calculated to estimate the precision of measurements according to equation (57). The SNR is defined as the ratio of signal amplitude to noise level for each of the measurement channels:

$$\mathrm{SNR_i} = \frac{[\bar{V}]_i}{\mathrm{SD}_{[V]_i}} \tag{57}$$

where $\mathrm{SD}_{[V]_i}$ is the standard deviation of multiple measurements for each channel and $[\bar{V}]_i$ is the mean value of the multiple measurements for each channel.

The closeness of the measured potential data, V to the estimated data set, $V^{(sim)}$ generated by a Finite Element Model of the homogenous tank is described as Accuracy ($\Delta$) of a measurement system (Gagnon et al. 2010). The simulated potentials are normalized to give a

best fit to the real measurement obtained by phantom experiments. The accuracy of the $i^{th}$ channel is described in equation (58).

$$\Delta_i = (1 - \left|[\bar{V}]_i - \left[V^{(sim)}\right]_i\right|) \times 100\% \quad (58)$$

The limits of detectability and distinguishability of contrasts are measured after placing simulated inhomogeneities in the saline solution. The distinguishability is the ability to separate two adjacent targets from one another, while detectability is the ability to distinguish the presence of a target from the null (homogenous tank) (Alder et al, 2010). Potential data are collected for single and multiple inhomogeneities placed at different locations in the phantom domain. Images are reconstructed from these measurements in order to determine the reliability of EIT detection of a single target, and of distinguishing two targets. $z$ , given by equation (59)

$$z = \frac{\hat{X}_q}{s} \quad (59)$$

is a measurement of the EIT system performance, where $\hat{X}_q$ is the mean image in a region of interest (ROI), calculated from multiple reconstructed images and $s$ represents the standard deviation of multiple reconstructed images. The ROI is selected and defined as the image amplitude greater than 1/4 of the maximum value rather than the entire image, in order to avoid contamination of the noise region by image artefacts.

CDP is the conductivity difference profile of the phantom model based on the phantom diameter passing through the reconstructed object centre. It is plotted against the distance of the diameter (Bera et al. 2012).

## 6. Results

Signal to noise ratio and accuracy were obtained from the measured data of the homogenous tank. The average SNR value of the channels was 43.1 dB. The results showed a high level of accuracy with an average accuracy of 93.5 % for the system.

Figures 4-10 and 4-11 show the CDP and the reconstructed images of the phantom with single target from the potential data. The images were successfully reconstructed and the targets at different positions were clearly detected. In the images the blue region which represents conductivity decreasing of 0.95 S/m appeared in the image in accordance with the position of the target. The single target placed at the centre is illustrated in Figure 4-10, and close to the edge of the tank at electrode No. 1 is shown in Figure 4-11. It was observed that the reconstructed CDPs almost follow the CDP of the original object.

The CDP and the images of the phantom with two targets placed in the tank are illustrated in Figure 4-12 and 4-13. In the reconstructed images the main perturbation was produced close to the correct position with localized changes corresponding to the targets. Figure 4-12 shows the reconstruction of the two targets located at the centre of the tank and very close to each other. The targets were detected but not distinguished clearly. In Figure 4-13 the targets were moved away from each other to the edge of the tank at electrodes No. 1 and 5. The targets were clearly detected and distinguished from each other and the reconstructed CDPs almost followed the CDP of the original object.

Detectability and distinguishability were calculated with respect to the position of the targets. The detectability values were found to be high, approximately 50, when a single target was close to the edge of the tank. However, when the target was at the centre of the tank, detectability reduced to around 20. The value of distinguishability increased from 25 to 55 as the targets moved further away from each other.

## 7. Discussions

The latest system used by UCL has the capability for 64 electrodes and recording at 30 frequencies simultaneously. This system was evaluated using phantom experiments and acceptable images were reconstructed from the multi-frequency objects such as a banana in a saline-filled tank (Holder 2005, Yerworth et al. 2003). The EIT system used in the University of Manchester has 32-channels with a temporal resolution of 100 frames per second operating in the frequency range of 10 kHz to 100 kHz (Rafiei Naeini 2008). The latest version of the EIT system used in the University of Florida has 16 electrodes. Its first generation was built in the 1990's. This EIT system was developed with higher data acquisition rate and more advance feature like Bluetooth transmission (Sadleir et al. 2009, Tang et al. 2010). This system has been used for the detection of intra-ventricular haemorrhage (Tang et al. 2010). In

their phantom experimental studies, data were collected with 16 electrodes positioned in FA layout using adjacent current patterns. Each phantom was equipped with 16 electrodes with inner diameter of 19.7 cm. Gel samples were produced to simulate anomalies with diameters of 2cm. Their phantom study presented maximum localization error of 0.1 with respect to unit radius (Sadleir et al. 2008).

The constructed EIT has 16 channels and operates in the frequency range of 10 kHz to 100 kHz with a temporal resolution of 100 frames per second and high level of accuracy of 93.5 %. The quality of the images may be improved by increasing the number of electrodes. However, the objective of this study is to optimize the number and position of the electrodes, in order to speed up the electrode setup process and avoid the need to move the patient's head in emergency care. The constructed EIT system in this study has capability of being much smaller in size and ability to be carried by the patient for its next generation.

One of the issues in practical measurement was the electrode connections. In phantom experiments the electrode connections were easy to check. In real circumstances and *in vitro* experiments when paste was used to connect the electrodes to the head, a system to check the electrode connections may be of great help to the user. The constructed EIT system has a program to monitor the electrode connection and show the user which electrode is not connected.

The other issue in the experiments was position of the electrodes and different shape of the heads which needs to be the same for all the measurements. In the phantom study, the phantoms were the same size and the electrodes (screws) were fastened and fixed to the phantom. However, the differential technique was considered in this study as especially in medical applications, the errors arising from the uncertain positioning of the electrodes and uncertain knowledge of the patient's shape are cancelled by taking the difference of two data sets.

Using 8 electrodes in a ring layout around the phantom restricted the z direction localisation, however the FA and the HA layouts were more preferable than using 16 or 32 electrodes and the overall process is faster. The results are also reliable enough for a useful application to emergency care.

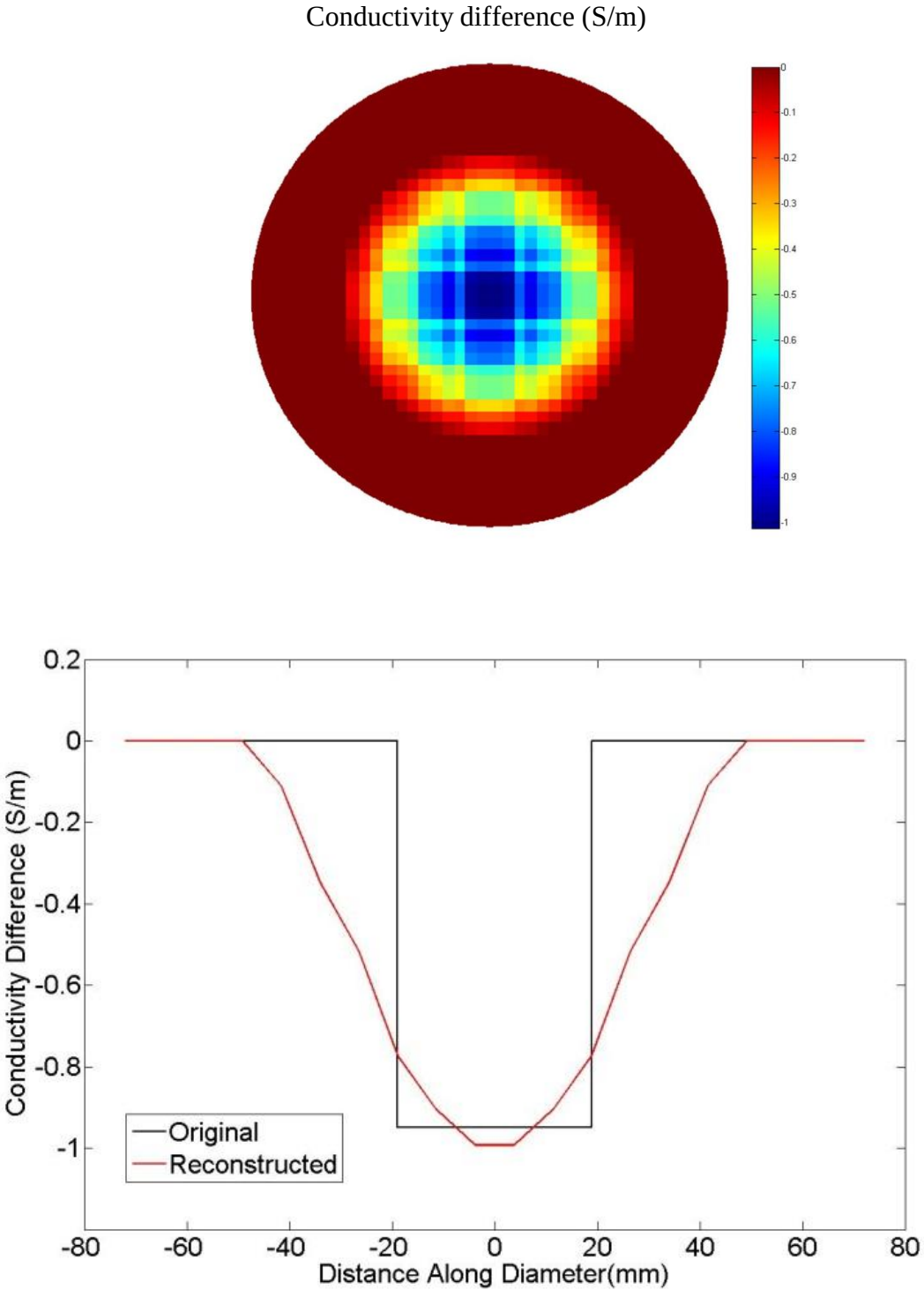


Figure 4-10 CDP and reconstructed image of phantom with one target at centre

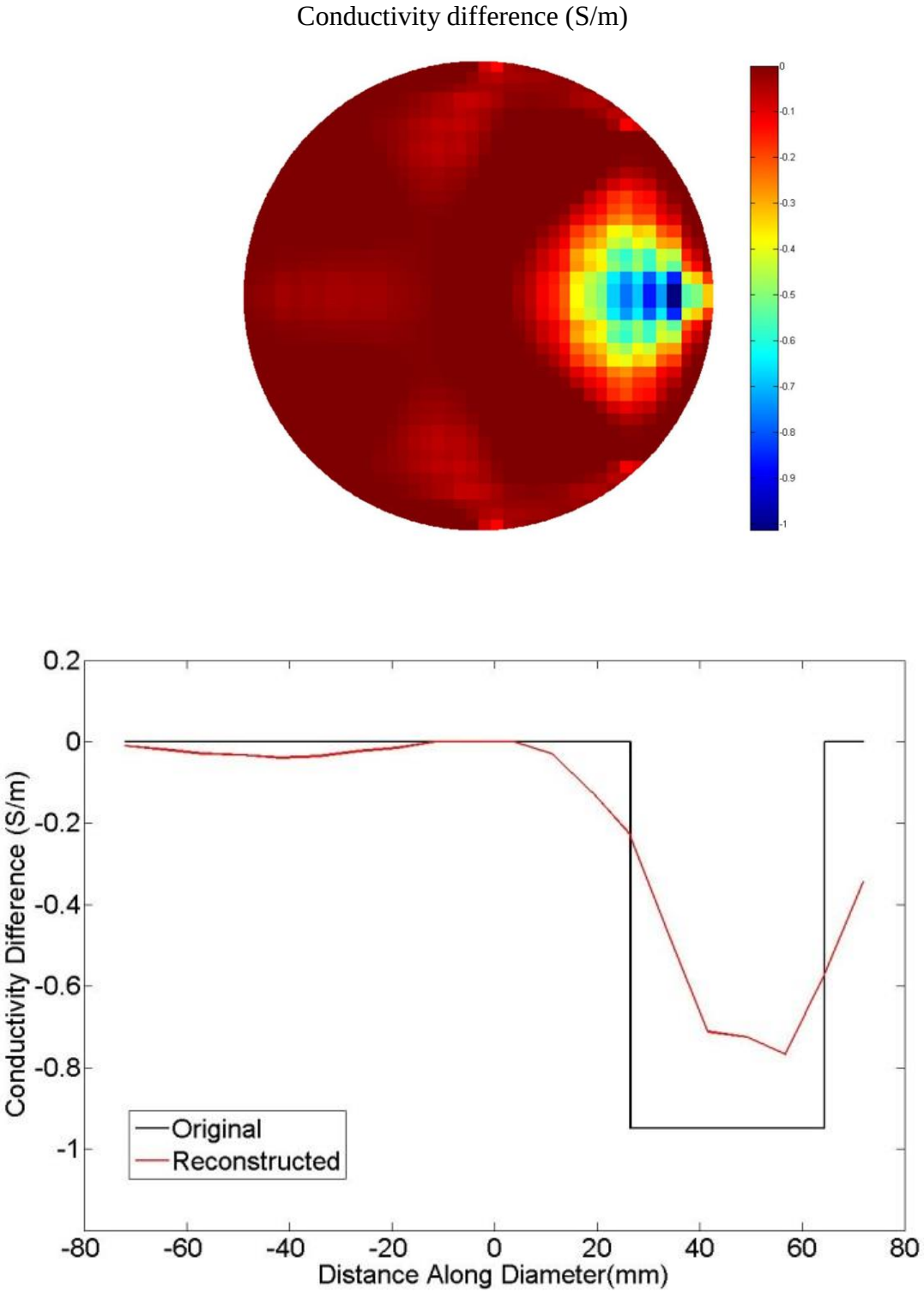


Figure 4-11 CDP and reconstructed image of phantom with one target close to edge of the tank at electrode No. 1

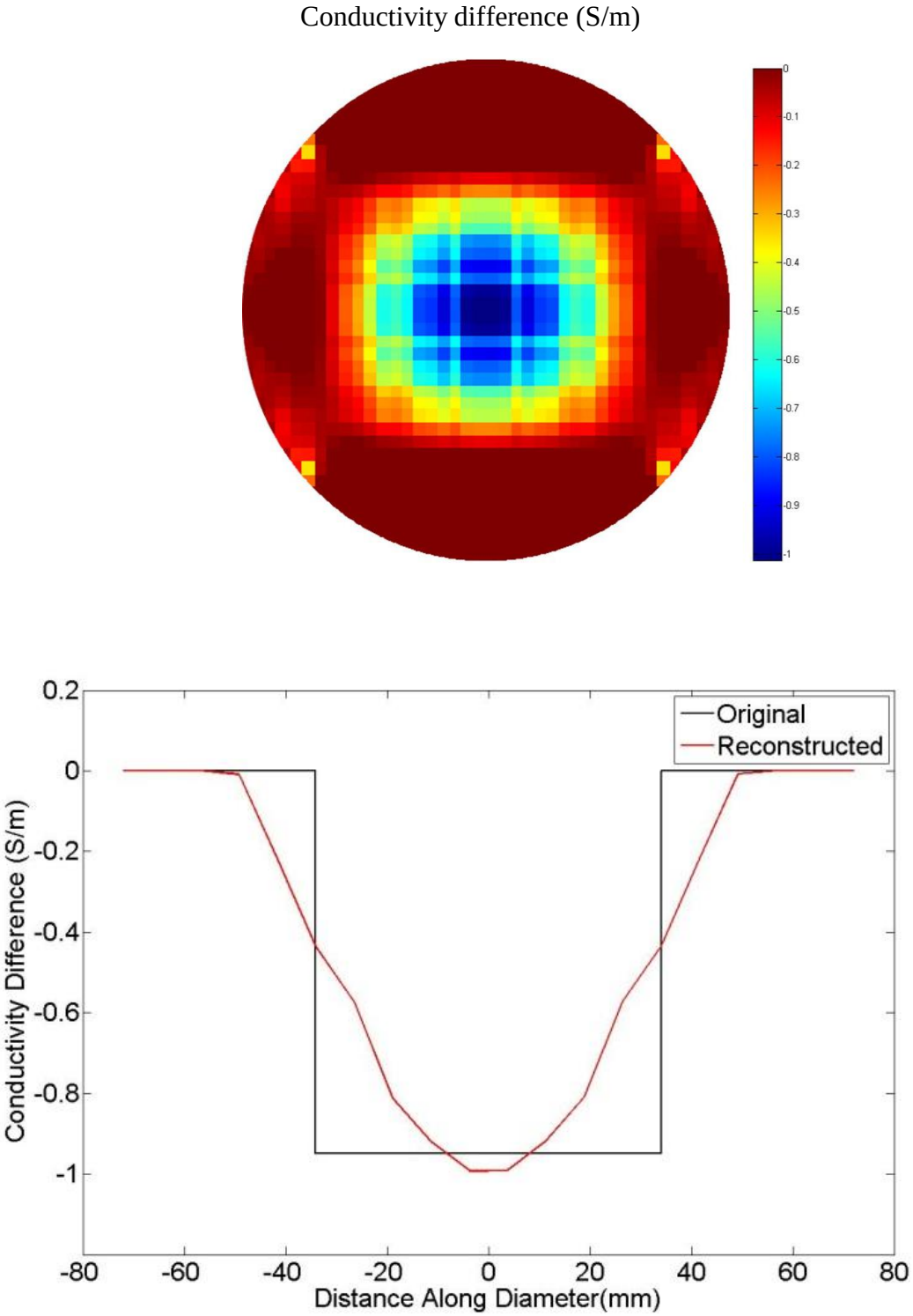


Figure 4-12 CDP and reconstructed image of phantom with two targets at centre

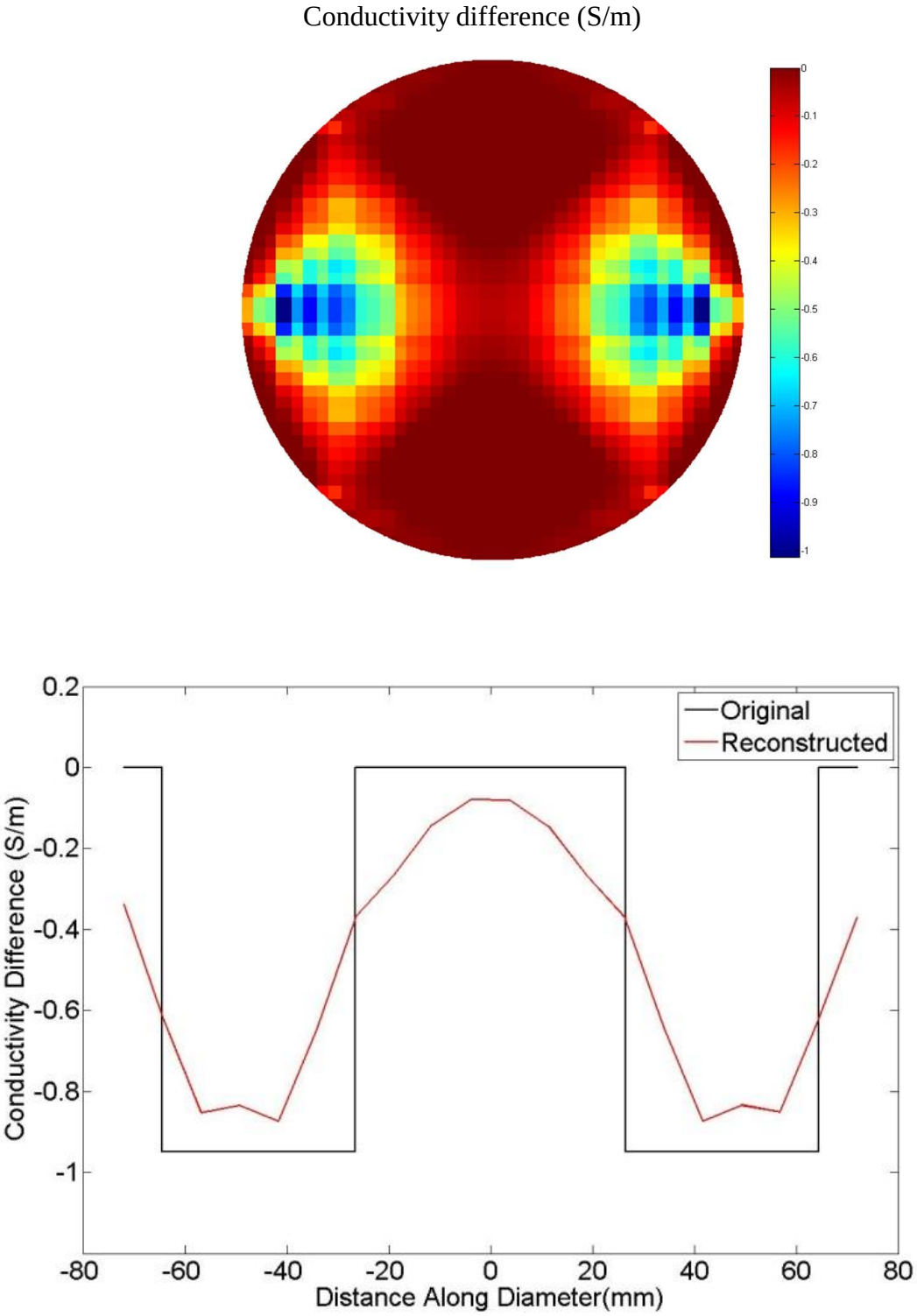


Figure 4-13 CDP and reconstructed image of phantom with two targets close to edge of the tank at electrodes No 1 and 5

## Summary

In order to evaluate the performance of the full array and the hemi-array layouts in realistic conditions, phantom experiments need to be performed. An EIT system was constructed to perform the phantom experiments. In this chapter, the details of the construction and evaluation of the EIT system were presented.

The structure of the hardware and its components were presented. This EIT model has 16 channels and operates in the frequency range of 10 kHz to 100 kHz with a temporal resolution of 100 frames per second. In order to control the data acquisition process, check electrode contact, visualize data and image, the system is connected to a PC.

The EIT system was evaluated to detect anomalies using phantom experiments in the presence of realistic noise. The phantom which was used to evaluate this system consisted of a shallow polymer tank with 8 electrodes in a full array. The phantom experiments were performed with one and two simulated anomalies, close to each other and far from each other to evaluate the accuracy and detectability of the system. The images were reconstructed using the collected data by COMSOL linked with MATLAB.

The results showed that the constructed EIT system was reliable enough to be used for further study. The average SNR value of 43.1 dB and high level of accuracy of 93.5 % for this system were obtained. In the next chapter, this EIT system is used in more phantom experiments with different electrode layouts in order to find an optimised electrode layout for emergency care.

CHAPTER

5

# Electrode Layout Optimization

Different electrode configurations may be more effective for different EIT applications. In this study, phantom experiments were performed, with the aim of finding an optimised electrode configuration to prevent unnecessary moving or lifting of patients who may have spinal injury. This electrode layout may simplify the application of the electrodes in use. In this chapter, three 8 electrode layouts were compared on their ability to detect, localize and size estimation of the anomalies in phantom experiments. The EIT system which constructed and evaluated in chapter 4 was used in the experiments.

## 1. Candidate Electrode Layouts

Three 8-electrode layout strategies and current patterns were investigated. The first one was the Full Array (FA) electrodes layout shown in Figure 5-1(a), where the 8 electrodes were located equally spaced in a single plane around an object. An adjacent current pattern was applied to this layout, that is, current was applied to a pair of adjacent electrodes and resulting voltages across other pairs of adjacent electrodes were measured. The second one was the Hemi-Array (HA) electrode layout shown in Figure 5-1(b), where 8 electrodes were positioned on the anterior of an object in a semi-circular pattern. This layout can be used for a

patient in emergency cases where the head cannot be moved. The electrodes were placed in a single plane with the same angle of 22.5˚ between adjacent electrodes and 225˚ between the bottom pair. An adjacent current pattern was also applied to this layout. In this strategy the first and the last electrodes in the array were opposing, but they were considered adjacent in a circular sense (Cheney et al. 1992). The third investigated electrode configuration was the Semi-Array (SA) layout shown in Figure 5-1(c). The 8 electrodes were placed in a single plane on the anterior of an object in a semi-circular profile with the same angle of 36˚ between adjacent electrodes and 108˚ between the bottom pair. The SA layout was thus a modification of the HA layout. The first and the last electrodes were placed closer to the back of the object and may thus lead to increased sensitivities at the back.

All layouts involved 8 current positions and a total of 40 voltage measurements. In this study, results from experiments performed on a phantom model using all three electrode layouts were compared to determine their ability to detect and localize intracranial haematomas.

To formulate sensitivity matrices, circular head models were constructed with a unit radius and homogeneous conductivity distributions for each 8-electrode layout using finite element modelling (COMSOL, Burlington MA, USA). After creating tetrahedral meshes, the forward models were solved for each current pattern and the sensitivity value corresponding to each mesh element was calculated. Models with 3032 tetrahedral elements for the forward models with FA, HA, and SA electrode configurations were constructed.

## 2. Phantom models

Phantom models were used to allow testing of how each current pattern, electrode layout and reconstruction performed in the presence of realistic noise. The phantoms consisted of a shallow polymer tank, eight electrodes, the background solution, and the blood equivalent anomaly. Each tank had a depth of 110 mm and an inner diameter of 135 mm. The phantoms used FA, SA and HA layouts shown in Figure 5-2 (a), (b) and (c) respectively. Each phantom was equipped with 8 stainless steel electrodes (dia. 10 mm) according to their electrode configuration. 0.6% saline solution with a conductivity of approximately 1.3 S/m, the conductivity of CSF (Oostendorp et al. 2000) was used as the background solution.

Gel anomalies were made using agar powder. A saline solution with the same conductivity as blood (0.67 S/m) was made with a concentration of 0.33% [weight/volume] of sodium chloride in water and transformed to gel by adding agar powder (1.9% by weight). Anomalies

had diameters of 15 mm (a relative radius of about 0.1). A single anomaly was placed in different positions along the α, αβ, β, βγ and γ axes (at θ = 0°, 45°, 90°, 135° and 180°), with the anomaly centre placed successively at relative radial displacement of 0.8 from the tank centre. Five locations in total for each layout as shown in Figure 5-1 and the measurements were performed to study reconstruction, detection and localization characteristics. The aim is to study and compare the ability of the FA, HA and SA layouts to detect and localize these anomalies. Performance of the HA and SA to detect the anomalies where placed far from the electrodes was evaluated to find the dependency of the results to the distance of the anomaly from the electrodes.

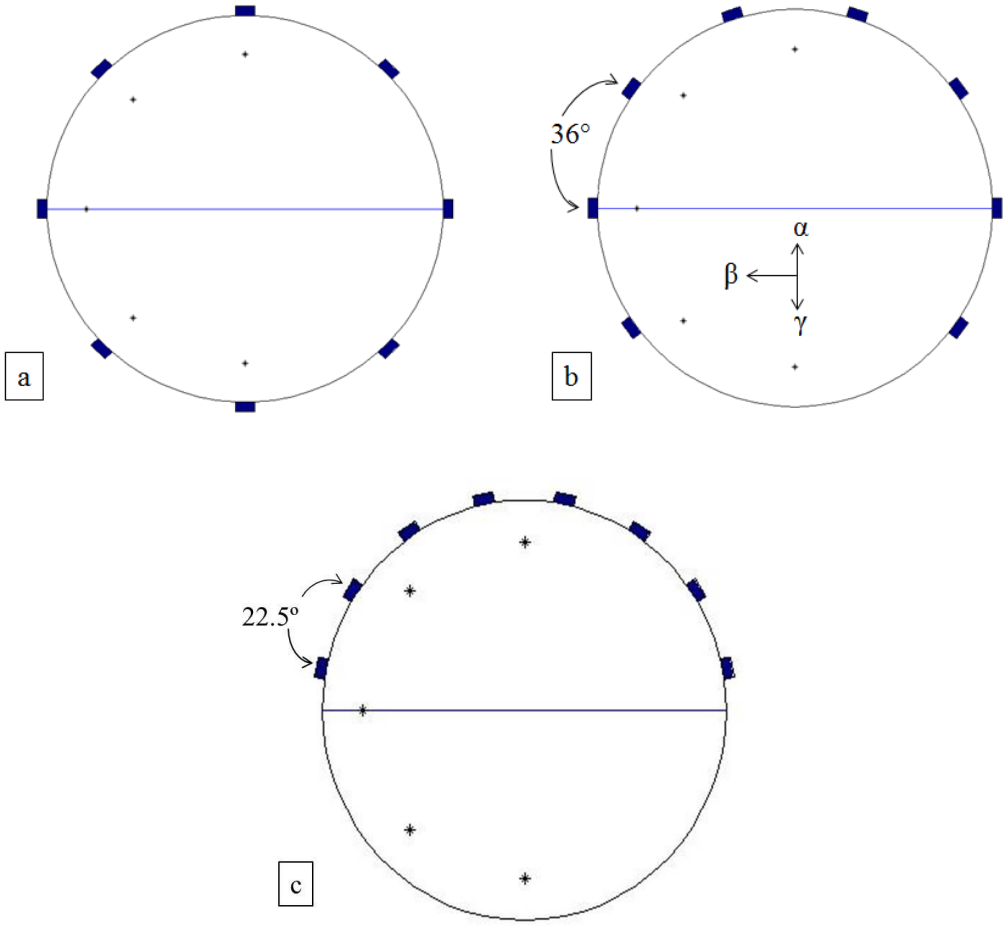


**Figure 5-1:** Electrode positions showing (a) FA, the standard ring layout where the eight electrodes were placed equally spaced around the head. (b) SA, a novel electrode configuration applied to the front of the head separated by angle of 36° in a semi-circular profile. (c) HA, an electrode configuration placed in a semi-circular profile by angle of 22.5°. Stars show the ideal positions of centre of simulated anomalies on sheep's head at relative radius of 0.8 in α, αβ, β, βγ and γ axes directions.

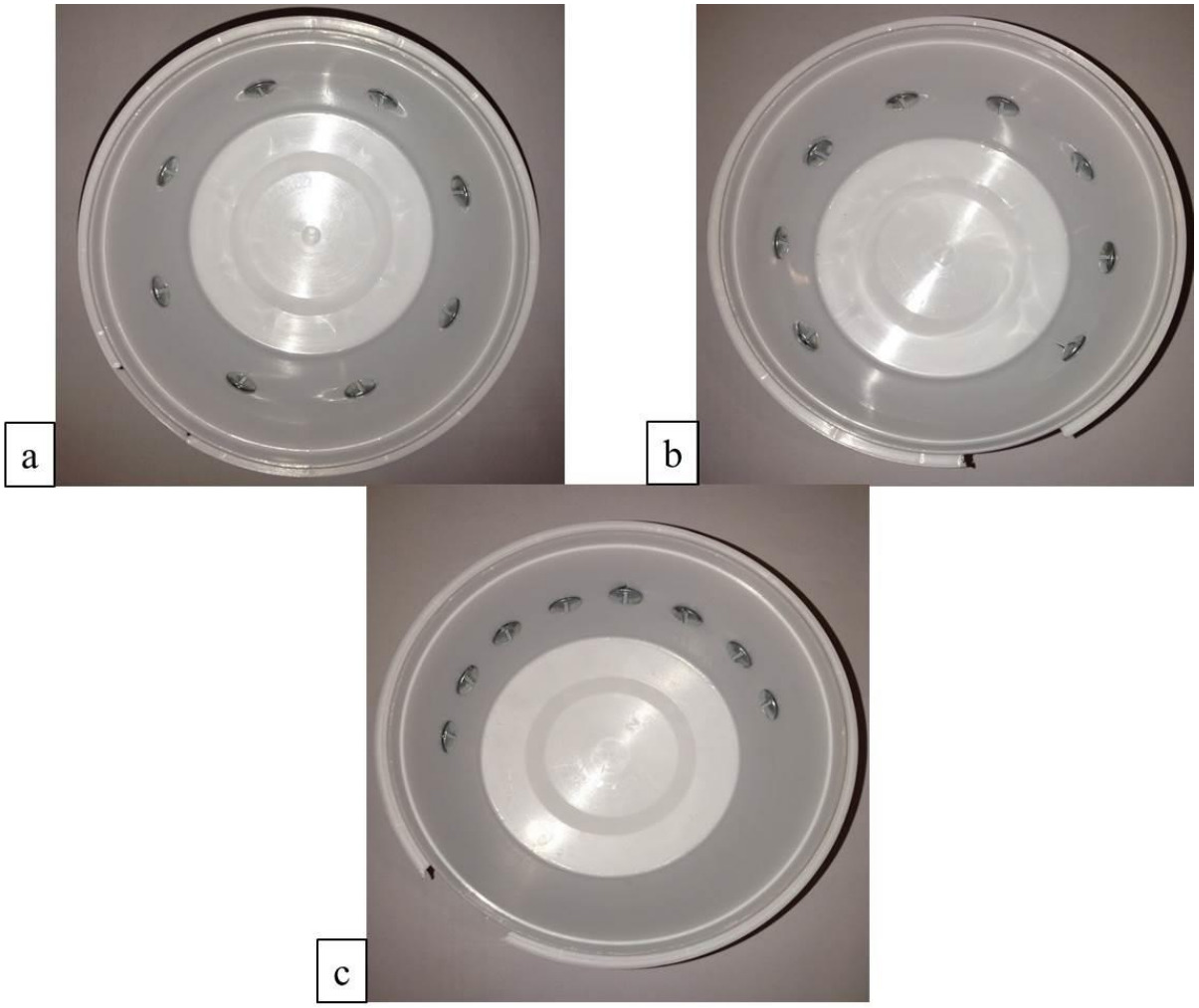


**Figure 5-2:** Phantom models showing (a) FA, the standard ring layout where the eight electrodes were placed equally spaced around the head. (b) SA, a novel electrode configuration applied to the front of the head separated by angle of 36° in a semi-circular profile. (c) HA, an electrode configuration placed in a semi-circular profile by angle of 22.5°. Screws show the electrode positions.

Data was collected with the prototype 16-electrode EIT system described in Chapter 4. This EIT system has 16 channels and operates with a temporal resolution of 100 frames per second. A single frequency of 10 kHz, a constant current of 1mA and 8 channels were used in this experiment. This frequency was chosen because the impedance properties of both anomaly and saline are flat over the interval 10 Hz – 50 kHz (Sadleir et al. 2009, Tang 2010) and 10 kHz was well calibrated in the centre of this range. Ten data sets were collected before anomalies were introduced. These were averaged and used as the reference data set. For each anomaly position, five data sets were collected and averaged as the perturbation data for that anomaly position.

## 3. Reconstruction Method

All the time-difference images in this study were reconstructed from the boundary measurements using a one-step sensitivity based method (equation 31), which has been discussed in detail in Chapter 3.

$$\mathrm{V} = \mathrm{S} \times \Delta\sigma \tag{60}$$

In EIT, the sensitivity matrix is always severely ill-conditioned and data errors will be magnified in the inversion process. Therefore, the inversion of the sensitivity matrix for the FA layout was regularized by employing TSVD. The sensitivity of the HA and SA layouts at the region where the electrode is absent was relatively low. Therefore, improved images may be obtained by weighting reconstruction prior to the inversion. The images from the HA and SA layouts were reconstructed using WMNM and WPI methods. Both methods have been discussed in Chapter 3.

In WMNM method, the sensitivity matrix was made more uniform by weighting with a diagonal matrix of reciprocal norms of sensitivity columns (Clay et al. 2002) via equation (42) and the images were obtained as equation (43).

In the WPI method, the sensitivity matrix was weighted with a diagonal matrix composed of a system blurring property, which was directly calculated from the sensitivity matrix (Sadleir et al., 2008). In the Weighted Pseudo-Inverse (WPI) method, reconstruction was weighted with P prior to pseudo-inversion. The entries of a diagonal weighting matrix (P) were calculated via Eq. (61). The blur matrix (B) is dimensionless and can be pre-calculated from the sensitivity matrix S via Eq. (62). Then the reconstruction was modified to obtain images as Eq. (63).

$$p_j = \left(\sum_{i=1}^{N} B_{ij}^2\right)^{-1}, j = 1,2,\dots,N \tag{61}$$

$$B = \mathrm{S}^{\dagger}\mathrm{S} \tag{62}$$

$$\Delta\sigma = (\mathrm{SP})^{\dagger}\Delta\mathrm{V} \tag{63}$$

The truncation value (*k*) used depended on the data noise level in the voltage measurements (Rust 1998). In phantom experiments, truncation values were chosen after inspecting images reconstructed at the truncation recommended by the *l*-curve procedure. If images with the recommended value were considered reasonable, further reconstructions for the data set were made using this value. If not, another value was chosen with reference to the *l*-curve plot. If this *k* value did not produce reasonable images, the value was decreased until images were considered clear and stable.

## 4. Localisation and Size Estimation

The position of the anomaly (x, y) can be estimated from the reconstructed images by averaging the positions of all elements, weighted by their conductivity changes (Tang *et al.*, 2010) via Eq. (54).

The expression for anomaly location (x, y) is effectively the centre of the reconstructed anomaly. The values $x_i$ and $y_i$ are the coordinates of the centre of each element. The difference between the actual position of the anomaly and its reconstructed location within the xy plane can be calculated as the absolute location errors, $D_{xy}$, quoted as a fraction of the brain radius (Tang *et al.*, 2010) via Eq. (54):

The anomaly volume was assessed with a characteristic parameter called the Quantity Index (QI) defined in Eq. 44 as an EIT image parameter that correlates with the anomaly volume (Sadleir *et al.,* 1998). The QI is the sum of conductivity change multiplied by the area of the element over the image area:

## 5. Phantom Results

The performance of the three electrode layouts, FA, HA and SA on phantom models were compared in terms of localization and size estimation. To improve the images of HA and SA layouts, reconstructions were performed by using weighting methods, WMNM (SW) and WPI (SP) and their performances were compared. The results of the anomaly localization in phantom models are presented in Figure 5-3. The position of the anomalies varied as a function of angle from 0° to 180° with 45° increments at a relative radial displacement of 0.8 from the phantom centre. The discrepancy between the actual and reconstructed locations is

illustrated by arrows. The radial relative localization errors $D_{xy}$ for the layouts are compared in Figure 5-4 and the QI are compared in Figure 5-5.

As expected, the FA electrode layout showed the best performance compared to the HA and SA layouts. FA results were superior to the HA and SA layouts and could localize the anomalies very well. The SA layout using the WPI method also localized the anomalies as well as the FA layout. The worst radial localization error for the FA layout was 0.0500 mm and for the SA(SP) layout this error was 0.1164 mm with the anomaly placed at 135°.

The HA(SW) layout performed very badly with the best radial localization error of 0.0628 with the anomaly placed at 180° and the worst error of 0.8100 mm at 45°. The HA(SP) performed only slightly better than the HA(SW) layout. The HA(SP) performed better than the SA(SW) only for the anomalies at 1°, 45°, 90°. Radial localization errors were larger for reconstruction from the HA with the worst values of 0.8100 mm for the HA(SW) and 0.3123 mm for the HA(SP) compared to the SA with the worst values of 0.2486 for the SA(SW) and 0.1164 mm for the SA(SP). The results showed that the anomaly localization errors were reduced by using WPI method and the reconstruction by SP was more susceptible to the measurement noise.

The FA, HA and SA electrode configurations were compared in terms of the size estimation of the anomalies. The normalized QI values against anomaly position are illustrated in Figure 5-5. The FA layout performed well with the worst QI error of 0.0013 $Sm^2$. The size of the anomalies at 180° was measured to be the worst error value of 0.0277 $Sm^2$ for the HA layout while using the WPI method. The best error value for the HA was also when using WPI method at 0°, 0.0038 $Sm^2$. SA layout performance was acceptable with the worst error value of 0.0262 $Sm^2$ and the best error value of 0.0012 $Sm^2$.

## 6. Discussion

A research group at UCL studied phantom experiments with a hemispherical tank and EEG electrode layout. The results from their experiments showed a localisation error of 3.5% while 31 electrodes were used (Tidswell *et al.*2001). Another study on EEG using 32 electrodes showed a localisation improvement of 2.7 mm on average instead of using 19 electrodes (Yvert *et al.* 1997). Some studies showed that the localization error can be further reduced to 5% of the tank diameter by weighting the sensitivity matrix (Liston *et al.* 2004). Therefore increasing the number of electrodes and weighting methods may possibly improve

localization errors. However, in emergency applications, using an 8 electrodes configuration is preferable to using 32 electrodes due to the faster connection and restriction of the electrode positions.

Reduction in the number of electrodes leads to poorer image properties and an increased uncertainty in size estimations. Restricting electrodes to the posterior of the phantom further reduces overall image quality, increases spatial variance and therefore the variability in size estimation of the anomaly (Sadleir et al. 2008). However, use of an electrode layout that does not require the patient to be moved or lifted would be very convenient for emergency applications. The accuracy of the size estimation of the bleeding in such situations is not extreme while the detection and localization of bleeding are more important. Therefore, simple FA, HA and SA layouts were chosen for this application. Even with this simple approach, the achievement of an 11% relative radial error for SA and 5% for FA in the worst case was deemed to be quite acceptable.

Three electrode configurations were compared on their ability to reconstruct, localize, and size estimation of the anomalies with phantom experiments. The FA layout was found to be more robust than the HA and the SA layouts, having an overall better quality in terms of reconstruction, localization, and size estimation of the anomalies in the regions of interest. Although the SA layout could not perform as well as the FA layout, it may be a more practical layout to use in this application. Studies of the novel SA layout on the phantom model indicated that this electrode layout has a good potential to detect and localize haematomas especially in locations further away from the electrodes compared to the HA layout. The HA layout will not be used in further study because of its poor performance, especially at the regions away from the electrodes. The SA and the FA layouts will be investigated and compared in terms of detection, localization and size estimation of the simulated haematoma on ovine models in the next chapter.

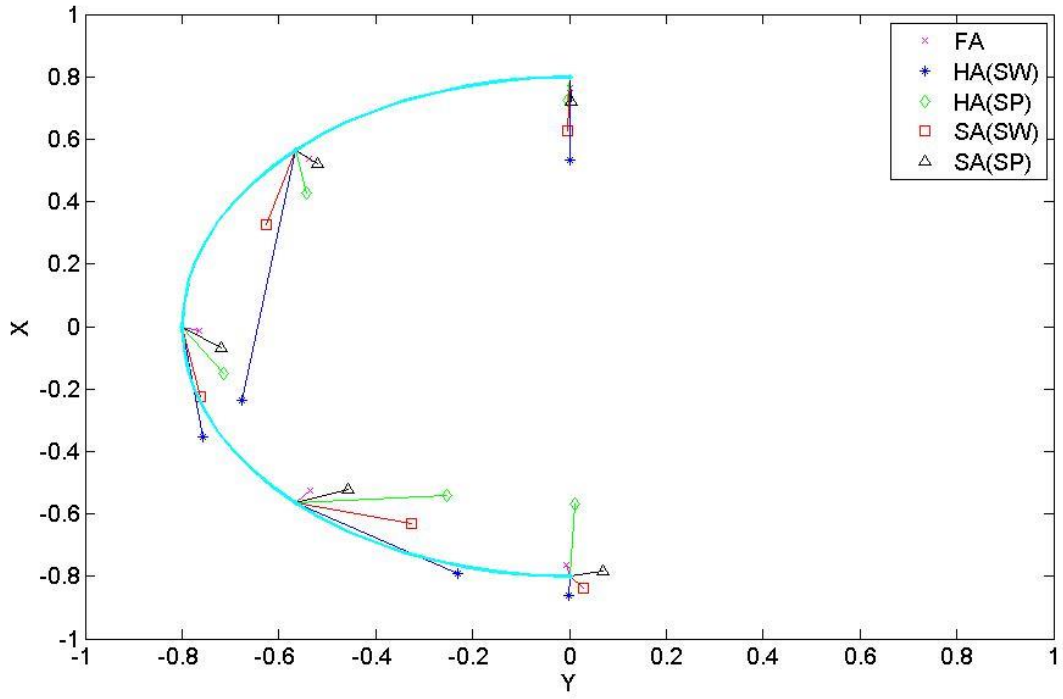


**Figure 5-3:** Localization of the simulated anomalies on phantom models using FA, HA and SA. Results from HA and SA layouts were reconstructed using WMNM (SW) and WPI (SP) methods. Anomaly positions varied as a function of angle (0°, 45°, 90°, 135° and 180°) at relative radial of 0.8.

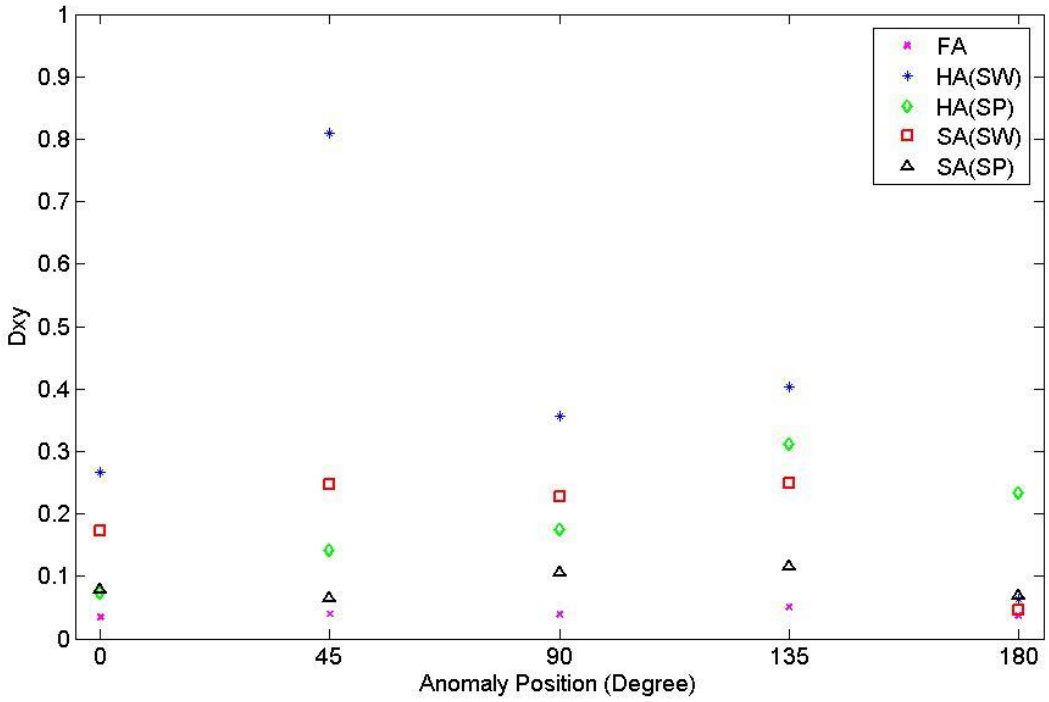


**Figure 5-4:** Radial relative localization errors, Dxy, on phantom models using FA, HA and SA. Results from HA and SA layouts were reconstructed using WMNM (SW) and WPI (SP) methods. Anomaly positions varied as a function of angle (0°, 45°, 90°, 135° and 180°) at relative radial of 0.8.

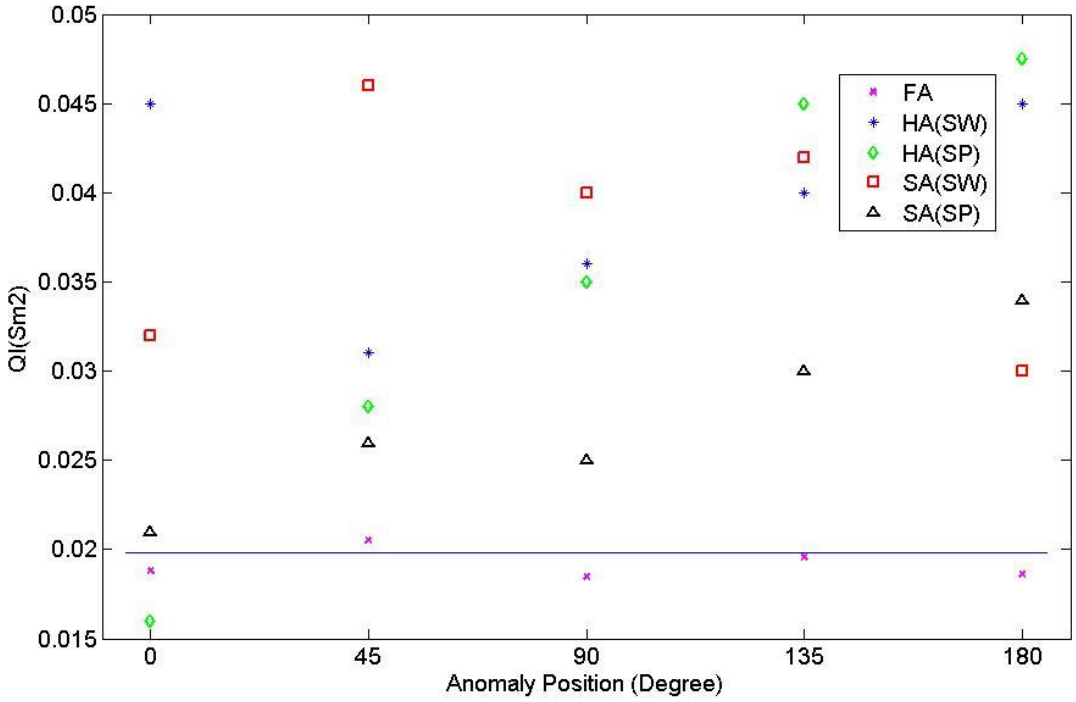


**Figure 5-5:** Quantification Indices, QI, of the simulated anomalies on phantom models using FA, HA and SA. Results from HA and SA layouts were reconstructed using WMNM (SW) and WPI (SP) methods. Anomaly positions varied as a function of angle (0°, 45°, 90°, 135° and 180°) at relative radial of 0.8.

## Summary

In this chapter, three 8-electrode layouts were compared on their ability to detect, localize and estimate the size of the anomalies in phantom experiments. The EIT system which was constructed and evaluated in Chapter 4 was used in the experiments.

The first stage used the full array (FA) electrode layout where the 8 electrodes were located equally spaced in a single plane around an object. The second stage was the hemi-array (HA) electrode layout where 8 electrodes were positioned on the anterior of an object in a semi-circular pattern. The electrodes were placed in a single plane with the same angle of 22.5˚ between adjacent electrodes and 225˚ between the bottom pair. The third electrode configuration investigated was the semi-array (SA) where the 8 electrodes were placed in a single plane on the anterior of an object in a semi-circular profile with the same angle of 36˚ between adjacent electrodes and 108˚ between the bottom pair. The FA and the HA layouts were investigated using the FE models described in Chapter 3. Although the FA had a better performance compared to the HA layout, the HA layout results were acceptable. Therefore the FA and the HA layouts were considered for phantom study in this chapter.

The area of the head which might be on the floor and not accessible is less than the area of the body on the floor thus the electrodes can easily expanded more around the head. Therefore, the SA electrode layout was introduced in this chapter which was more reliable in practice compared to the HA layout. The first and the last electrodes of the SA layout were placed closer to the back of the head and thus lead to increased sensitivities at the back. The HA and SA layouts were considered in this study because of their configurations which can be used for patients in emergency cases where the head cannot be moved. The FA layout was found to be more robust than the HA and the SA layouts, having an overall better quality in terms of detection, localization, and size estimation of the anomalies.

Although the SA layout could not perform as well as the FA layout, it may be a more practical layout to use in emergency care. The results indicated that the SA layout has a good potential to detect and localize anomalies especially in locations further away from the electrodes comparing to the HA layout. The HA layout will not be used in further study because of its poor performance especially at the regions away from the electrodes. Therefore, The SA and the FA layouts are investigated and compared on ovine models in the next chapter.

CHAPTER

# 6

# Studies Using Ovine Model

The performance of EIT was evaluated in this chapter, using the optimised eight-electrode configuration, the SA layout and the standard FA layout. This included an investigation of the SA and the FA configurations to evaluate their ability to detect and localise anomalies similar to haematoma in the human head, for the purpose of early diagnosis. Using the minimum number of electrodes is always desirable in clinical applications since it may also speed up the electrode setup process in emergency cases. The electrode configurations proposed in Chapter 5 were evaluated for the detection and localisation of simulated haematomas *in vitro* using an ovine model. Intracerebral haematoma detection has been considered in previous studies using EIT (Tang *et al* 2010). Epidural and subdural haematomas were considered in this study since their location can represent the worst case with respect to the SA configuration.

## 1. Methods

To reconstruct the conductivity distribution images through the EIT inverse problem the forward problem on a prototype model has to be solved. Initially, a simple forward model based on a circular shape with a homogenous conductivity distribution may be used to

calculate the sensitivity matrices (Bagshaw *et al.* 2003). Better results are obtained if the forward model exactly matches the object in terms of internal conductivity distribution and external geometry. In principle, an incorrect estimate of boundary shape will introduce artefacts and reduce the quality of the reconstructed images. However, more realistic models need to be used carefully since inaccurate prior information may yield images worse than those reconstructed with a simple forward model (Liston *et al*. 2004). In practice, it is difficult to specify an accurate model for an individual head because head geometry varies from patient to patient.

### 1.1.Full and Semi-Array electrode layouts

Two eight-electrode layout strategies were investigated in vitro and compared in terms of their ability to detect and localise intracranial haematomas. The first one was a standard ring layout or Full-Array (Figure 5-1a). The second layout was a novel electrode configuration applied to the front of the head, the Semi-Array (SA) configuration in a semi-circular profile (Figure 5-1b). This layout simplifies the application of the electrodes and avoids the need to move and lift the patient's head. An adjacent current pattern was applied to both layouts, wherein current was applied in turn to pairs of adjacent electrodes, and voltages were measured across other pairs of adjacent electrodes. In the SA, use of this scheme included measurements and current applications between the last-numbered and first electrodes positioned at the end of the array and approximately 108° apart. Both layouts involved 8 current positions and a total of 40 voltage measurements. Experiments were performed on an ovine model using both layouts and the results obtained from the SA layout were compared with data from the standard eight-electrode full-array (FA) layout to determine the ability of the SA to detect and localise intracranial haematomas. Restricting electrodes at the back of the head limits the resolution and thus inferior localisation of the anomaly can be expected, compared to that of the FA layout.

### 1.2.Data generation

In vitro ovine experiments were performed in conjunction with an eight-electrode EIT system to determine the potential of this configuration to provide good results in vivo. To obtain the experimental measurements, a prototype 16-electrode EIT system constructed in the laboratory was used. The structure of this device is presented in Figure 4-1. The system is controlled by a microcontroller connected to a PC through a serial port. A graphical user

interface was developed using Visual Basic (VB). A sinusoidal current generated by a constant current source was injected through one pair of adjacent electrodes and the corresponding boundary potentials were measured over pairs of the remainder of the neighbouring electrodes using a multiplexer. The input pair of electrodes was switched over all adjacent electrodes pairs and the measurement procedure was repeated for all possible adjacent pairs. The performance of this system was previously evaluated using phantom experiments in Chapter 4 (Ayati et al. 2012). For this experiment, a constant current of 1mA at a frequency of 10 kHz and 8 electrodes were chosen.

### 1.3.Experimental setup

Five freshly skinned sheep heads (labelled as A, B, C, D and E) were obtained from a local butcher. The locations of the 8 electrodes for each layout were marked in different colours on the skull. Equal distance between electrodes has been considered around the head for the FA and in the anterior of the head for the SA according to the perimeter measurement of each head. Eight Ag/AgCl disk electrodes (Unimed Electrode Supplies Ltd) were fastened to the skull using conductive paste (Unimed Electrode Supplies Ltd) for the FA layout (Figure 6-1a). These electrodes were also soldered to the wires to connect to the skull on the interior of the head using conductive paste for the SA layout (Figure 6-1b).

A saline solution with the same conductivity as blood (0.67 S/m) was made with a concentration of 0.33% [weight/volume] of sodium chloride in water. In order to localise haematoma *in vitro*, the position of the anomaly has to be known with a good estimation. To simulate a more realistic haematoma in an accurate location, the saline solution was transformed to gel. The saline solution was stirred using a magnetic stir bar at a temperature of 70°C while agar powder was added to achieve the desired gel concentration (1.9% by weight). Then the solution was poured into a 1 cm diameter tube and allowed to cool at room temperature. The gel sample was removed from the tube and cut into one tenth of the diameter of each brain to simulate pockets of blood. The conductivity of the gel sample was measured and found to be the same as the conductivity of the saline solution. A 2-terminal measurement was performed to measure the gel conductivity and the same gel samples were used on each subject. An AC voltage was applied across the gel at a frequency of 10 kHz at room temperature using a waveform function generator connected in series with a digital multimeter to measure the AC current and voltage across the gel. The circuit was calibrated

with multiple known resistances, and the conductivity measurements were compared to published data (Kandadai *et al.* 2012).

All the skulls were cut in approximately half using a bone saw. The top half of the skull was carefully removed and the brain was exposed in order to position the anomalies (Figure 6-2). Gel samples were placed superficially on top of the brain lobe and the top half of the skull was replaced. The anomaly was located in different positions along the α, αβ, β, βγ and γ axes (at θ = 0°, 45°, 90°, 135° and 180°), with the anomaly centre placed successively at a relative radial displacement of 0.8 from the brain centre. Five locations were considered in total as shown in Figure 5-1 and the measurements performed using both layouts for each anomaly to study reconstruction, detection and localisation characteristics. The aim was to study and compare the ability of the SA and FA layouts to detect and localise these anomalies, especially for the SA, and to evaluate the dependency of the results on the distance of the anomaly from the electrodes.

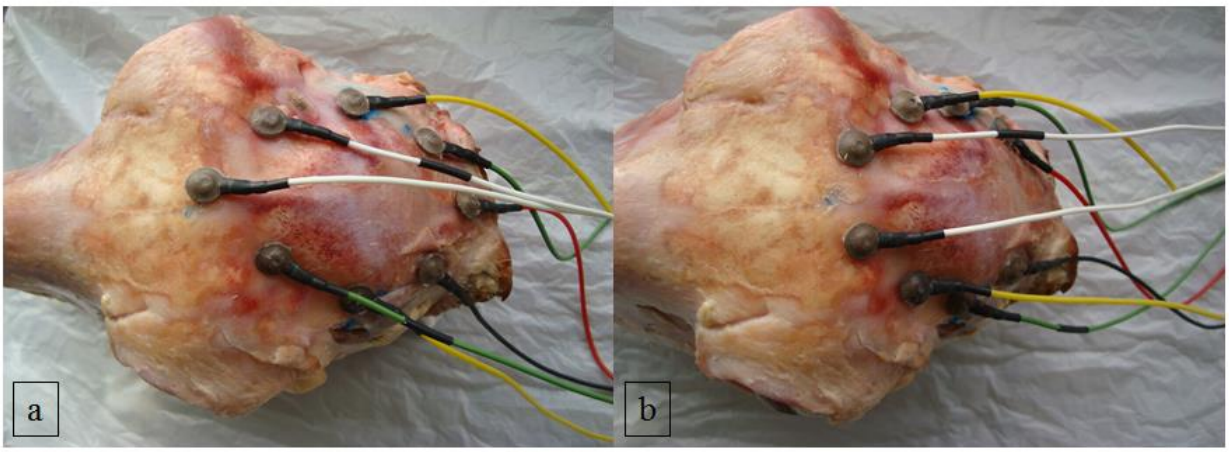


**Figure 6-1:** Electrode positions showing (a) eight Ag/AgCl disk electrodes fastened to the skull using conductive paste for full array layout and (b) electrodes connected to the skull on the interior of the head using conductive paste for semi-array layout.

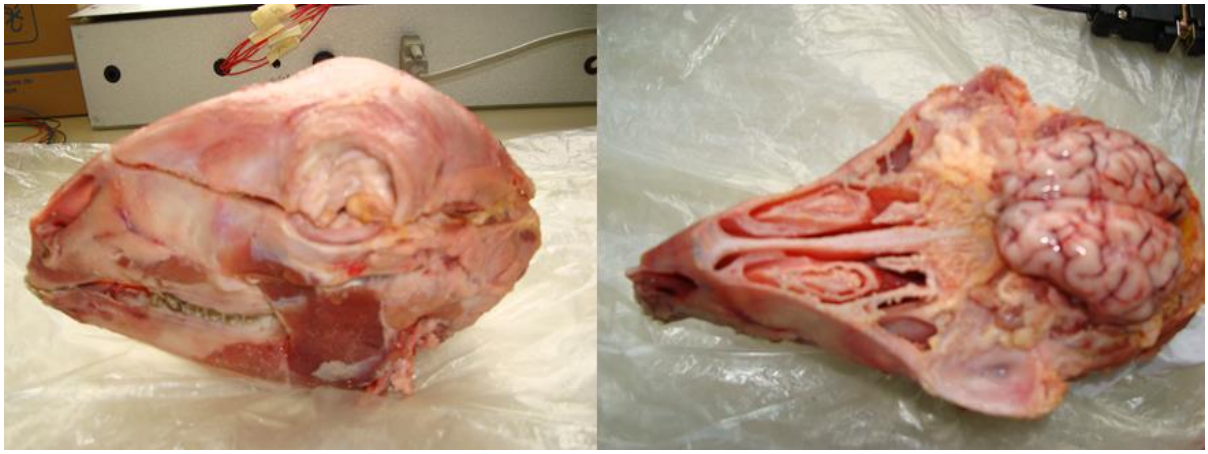

**Figure 6-2:** Skulls were cut in approximately half using a bone saw (left). The top half of the skull was carefully removed and the brain was exposed to place the anomalies (right).

### 1.4.Reconstruction

In this chapter, EIT difference images were reconstructed based on the assumption that the conductivity changes are small enough. The relationship between the boundary voltage measurement changes and internal conductivity changes can be expressed with a sensitivity matrix (S) as in Eq. (60). S was calculated from forward solutions of a two-dimensional disk finite element model with a homogenous conductivity distribution (Bagshaw *et al*. 2003).

Conductivity changes ($\Delta\sigma$) can be determined by inverting the sensitivity matrix; however, S is ill-conditioned and not square. Since the EIT inverse problem is severely ill-posed and a small amount of noise on boundary measurements, $\Delta V$, can cause a large oscillation for the solution, a regularization technique was used to reduce this effect by improving the condition of S (Holder 2005).The Truncated Singular Value Decomposition (TSVD) method which has previously been identified as a suitable regularization method (Oh *et al*. 2009) was used to regularize the inversion of the sensitivity matrix. The truncation point k needs to be chosen carefully, less than or equal to the rank of the matrix, as it would otherwise produce inaccurate images. The truncation point was chosen depending on the noise level in the voltage measurements and the rank of the sensitivity matrix on inspection of the L-curve of experimental data (Hansen *et al.* 1993). The truncation numbers were almost the same for all the datasets. The pseudo-inversion ($S^{\dagger}$) was achieved using TSVD and images were obtained using Eq. (40).

In the SA, measurement sensitivity depends strongly on the anomaly location since the electrodes are not placed all over the head. Some reconstructed anomalies located far from

the electrodes in the posterior region were almost invisible or erroneous when TSVD reconstruction was used. Therefore, in order to enhance image reconstruction quality and improve anomaly localisation, the sensitivity matrix was weighted with a diagonal matrix composed of a system blurring property, which was directly calculated from the sensitivity matrix (Sadleir et al. 2008). In the Weighted Pseudo-Inverse (WPI) method, reconstruction was weighted with P prior to pseudo-inversion. The entries of a diagonal weighting matrix (P) were calculated using Eq. (61) where $ne$ is the total number of elements. The blur matrix (B) is dimensionless and can be pre-calculated from the sensitivity matrix S via Eq. (62). Then the reconstruction was modified to obtain images using Eq. (63).

### 1.5.Localisation

The position of the anomaly (x,y) can be estimated from the reconstructed images by averaging the positions of all elements, weighted by their conductivity changes (Tang *et al.* 2010) via Eq. (54).

The anomaly location (x, y) is effectively the centre of the reconstructed anomaly. The values $x_i$and $y_i$ are the coordinates of the centre and $a_i$ is the area of each element. The difference between the actual position of the anomaly and its reconstructed location within the xy plane can be calculated as the absolute location errors (relative radial error, $D_{xy}$) quoted as a fraction of the brain radius, R, (Tang et al. 2010) via Eq. (56).

### 1.6.Quantification

The anomaly size was assessed with a characteristic parameter, the quantity index (QI), defined in Eq. 44 as an EIT image parameter that correlates with the anomaly size (Sadleir *et al.* 1998). The quantity index is the sum of conductivity change multiplied by the area of the element over the image area. QI values should be constant since the anomaly sizes are the same during the experiment over all the positions.

## 2. Results

The data for intracranial haematomas in five ovine models were successfully collected with the EIT rig and used to reconstruct the images. To improve the SNR of EIT, a sequence of at least 100 frames of data was collected before the anomalies were introduced. These were averaged and used as the reference data set. For each anomaly position, 100 frames of data were collected and averaged as the perturbation data for that anomaly position.

### 2.1.Comparing FA and SA localisation

The simulated haematomas were localised using the reconstructed images. The results of the anomaly localisation in the five ovine models using both FA and SA layouts are presented in Figures 6-3 and 6-4 respectively. The position of the simulated haematomas varied as a function of angle from 0° to 180° with 45° increments at relative radial displacement of 0.8 from the brain centre. Locations were normalized to a circular shape with unit diameter. The discrepancy between the actual and reconstructed locations is illustrated by arrows. For illustration, reconstructed images of the anomalies in subject E using FA configuration are shown in Figure 6-3 and reconstructed images of the anomalies in subject C using SA configuration are shown in Figure 6-4. The simulated anomalies were detected for all the positions using both layouts; however FA results were in general superior to the SA results.
Relative radial localisation errors for five ovine models using FA and SA are shown in Figures 6-5 and 6-6 respectively. As expected, the SA layout localised simulated anomalies as well as the FA layout apart from the anomalies placed far away from the electrodes. Localisation errors were larger for reconstructions of the anomalies at 135° with the worst value of $D_{xy}$ being 0.3265 mm using the SA layout, and 0.0828 mm using the FA layout, both values being with respect to unit radius. The mean and variance of the relative radial errors are presented in Table 6-1. Both the FA and SA electrode layouts could localise simulated haematomas well, producing a maximum mean relative radial error of 0.0714 mm and 0.2364 mm respectively at 135° with respect to the unit radius.

Table 6-1: Comparison of mean and variance of radial relative errors using FA and SA for different anomaly positions

| Anomaly location | FA localization error (mm) | | SA localization error (mm) | |
|---|---|---|---|---|
| | Mean | Variance | Mean | Variance |
| 0° | 0.0564 | $3.2644\times10^{-5}$ | 0.0626 | 0.0024 |
| 45° | 0.0624 | $3.2673\times10^{-5}$ | 0.0733 | $4.3200\times10^{-4}$ |
| 90° | 0.0709 | $1.5502\times10^{-4}$ | 0.1312 | 0.0027 |
| 135° | 0.0714 | $1.1429\times10^{-4}$ | 0.2364 | 0.0081 |
| 180° | 0.0627 | $2.4588\times10^{-4}$ | 0.1118 | 0.0035 |

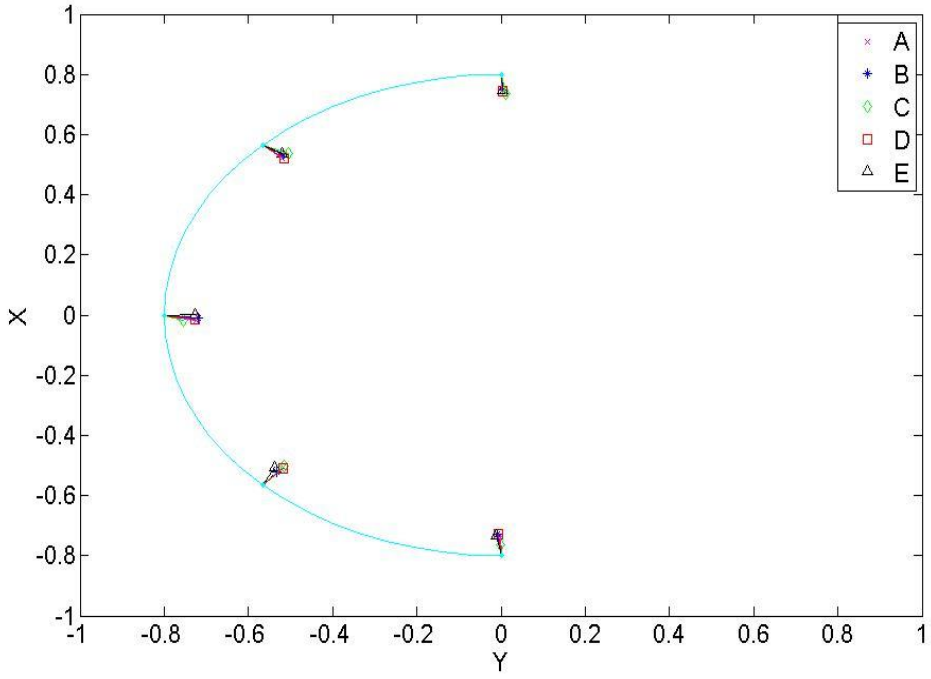


(a)

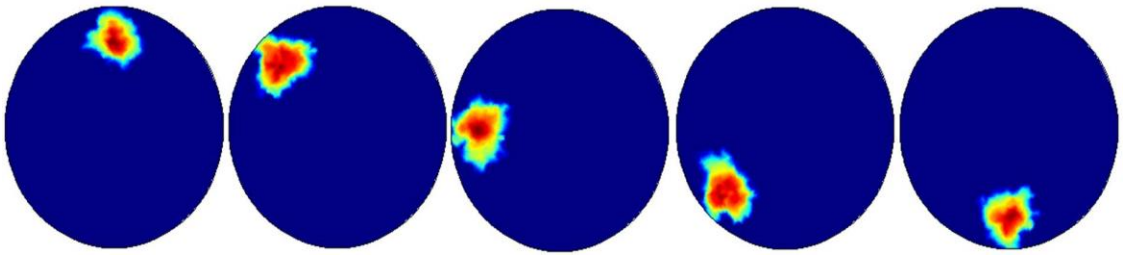

(b)

**Figure 6-3:** (a) Localization of the simulated anomalies on five sheep's head (A, B, C, D and E) at various positions using full array (FA) electrode layout. Anomaly positions varied as a function of angle (0°, 45°, 90°, 135° and 180°) at relative radius of 0.8.

(b) Reconstructed images of the anomalies in subject E.

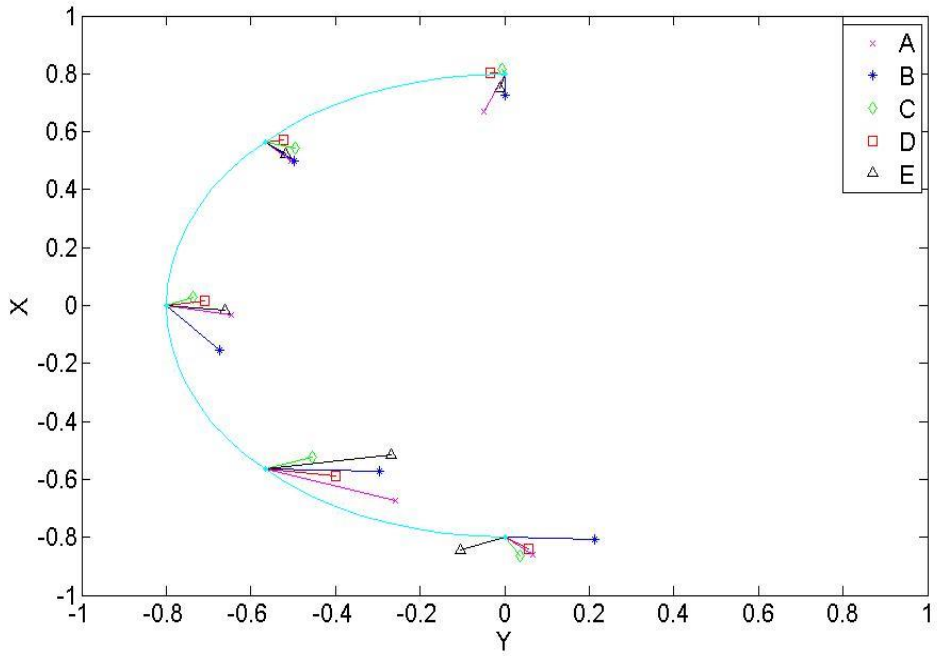


(a)

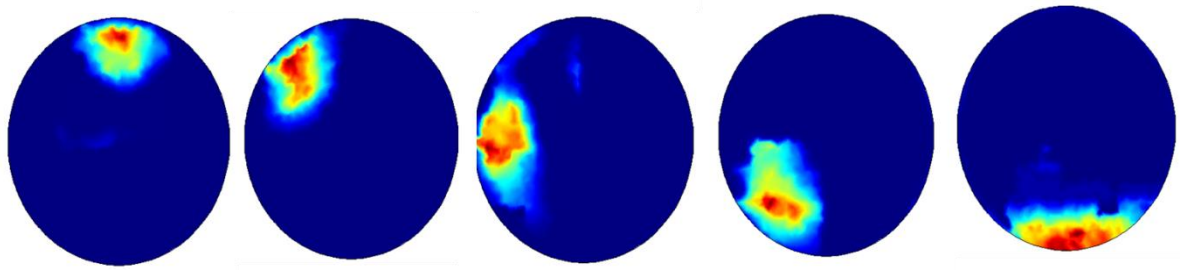

(b)

**Figure 6-4:** (a) Localization of the simulated anomalies on five sheep's head (A, B, C, D and E) at various positions using semi-array (SA) electrode layout. Anomaly positions varied as a function of angle (0°, 45°, 90°, 135° and 180°) at relative radius of 0.8.

(b) Reconstructed images of the anomalies in subject C.

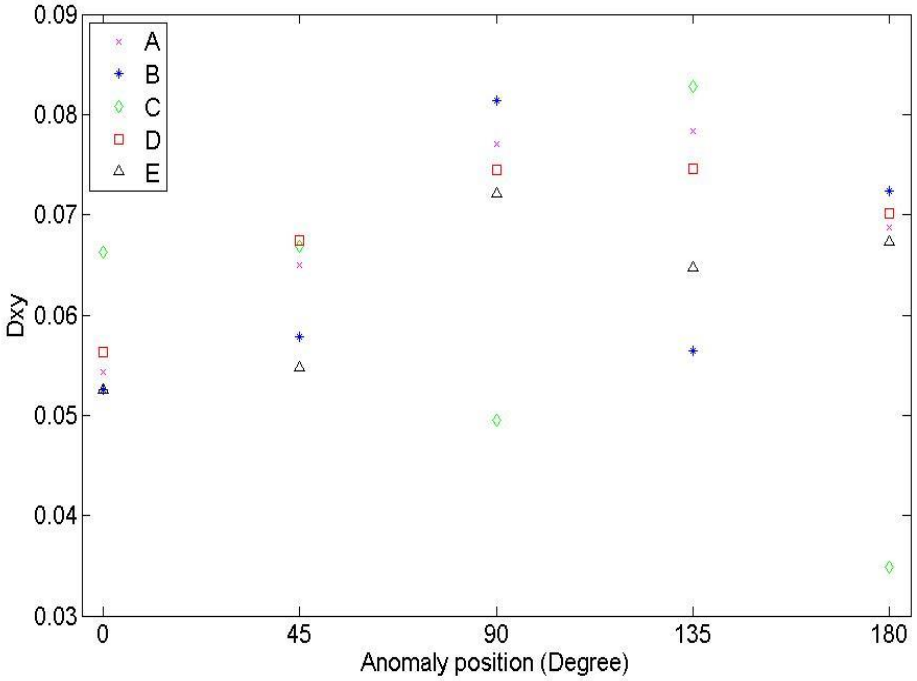


**Figure 6-5:** Relative radius localization errors, Dxy, of the simulated anomalies on five sheep's head (A, B, C, D and E) at various positions using full array (FA) electrode layout. Anomaly positions varied as a function of angle (0°, 45°, 90°, 135° and 180°) at relative radius of 0.8.

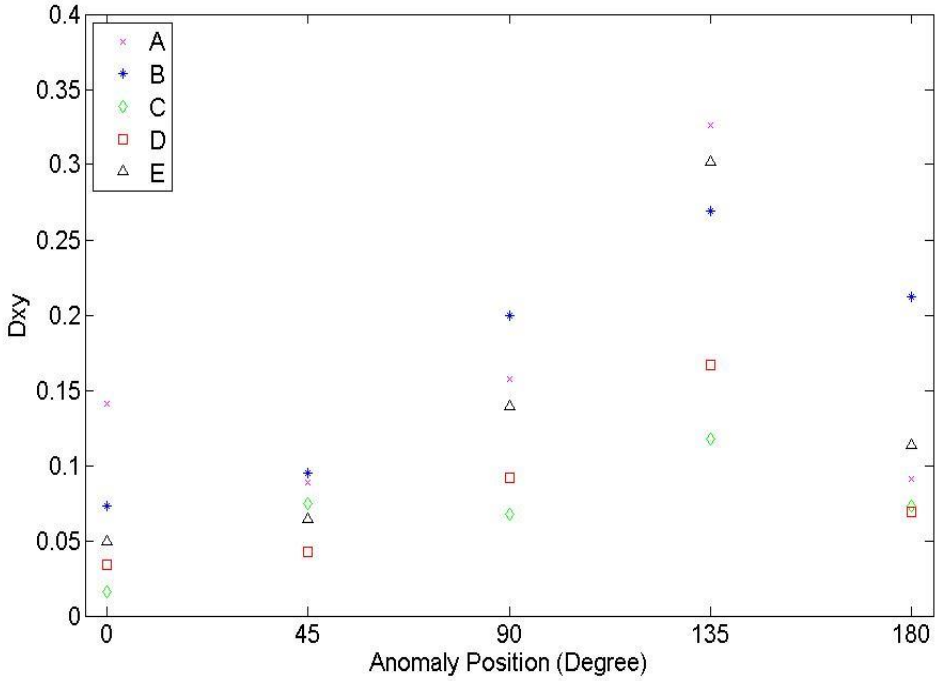


**Figure 6-6:** Radius relative localization errors, Dxy, of the simulated anomalies on five sheep's head (A, B, C, D and E) at various positions using semi-array (SA) electrode layout. Anomaly positions varied as a function of angle (0°, 45°, 90°, 135° and 180°) at relative radius of 0.8.

### 2.2.Comparing FA and SA size estimation

The reconstructed images of the simulated haematomas were gathered and post-processed to determine QI values. The ability of the FA and SA layouts to quantify these anomaly sizes was compared to the actual QI. The normalized QI values for five ovine models using the FA electrode layout over the image plane against anomaly position for five angles are shown in Figure 6-7. For the SA layout, the same positions of anomalies in directions of α, αβ, β, βγ and γ were used. Normalized QI values from the SA reconstructions of simulated anomalies are shown in Figure 6-8. Size estimation results for the FA layout are superior to those for the SA layout. The worst QI error in reconstructions using the FA layout was around 30%. According to the reconstructed images, the size of the simulated anomalies at 0° and 45° (α and αβ) are measured by maximum error of approximately 55% and 50% respectively in the case of the SA electrode layout. For simulated anomalies placed at 90° (β) using the SA layout, although in one case the QI value is large, the worst QI error in the others is about 55%. The SA layout performance to quantify the simulated anomalies at 135° and 180° (βγ and γ) is very poor as in the worst case the anomaly sizes were measured almost three times bigger than their actual size.

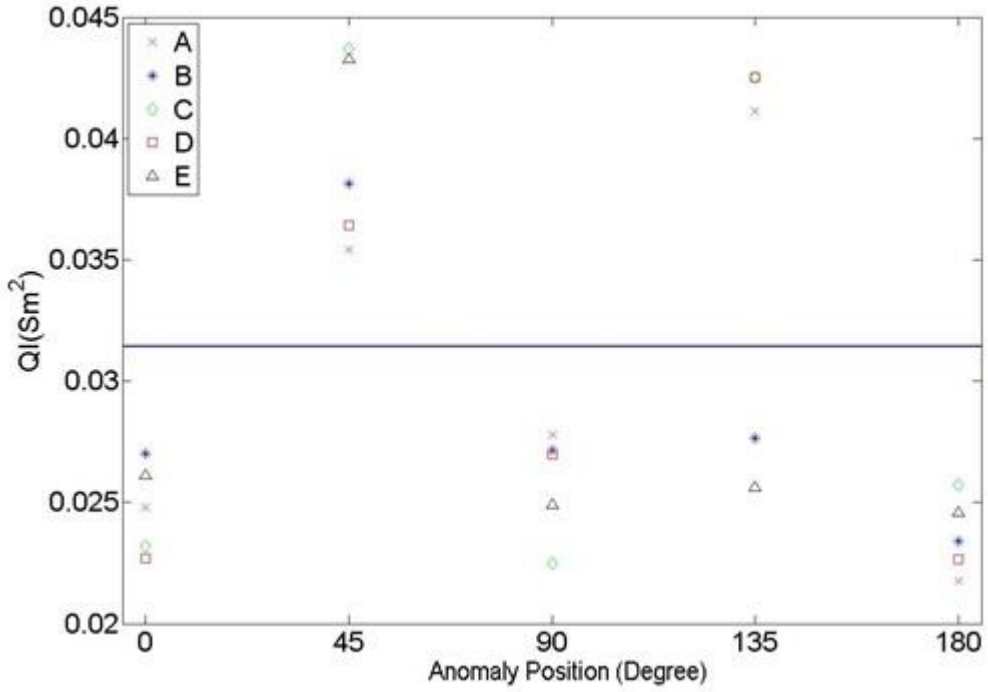


**Figure 6-7:** Quantification Indices, QI, of the simulated anomalies on five sheep's head (A, B, C, D and E) at various positions using full array (FA) electrode layout compared with ideal QI. Anomaly positions varied as a function of angle (0°, 45°, 90°, 135° and 180°) at relative radius of 0.8.

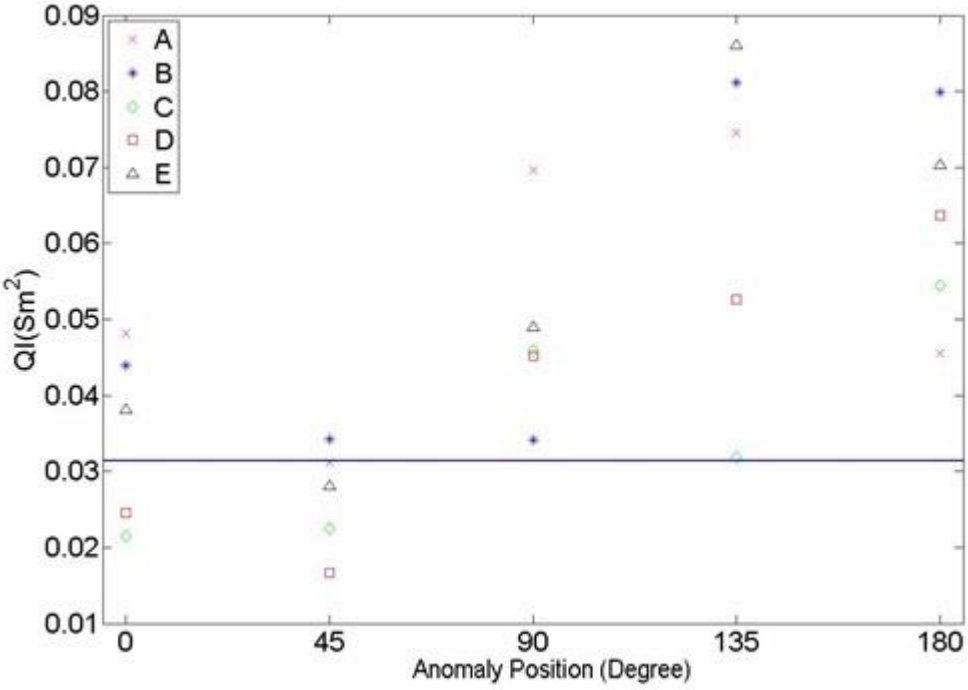


**Figure 6-8:** Quantification Indices, QI, of the simulated anomalies on five sheep's head (A, B, C, D and E) at various positions using semi-array (SA) electrode layout compared with ideal QI. Anomaly positions varied as a function of angle (0°, 45°, 90°, 135° and 180°) at relative radius of 0.8.

## 3. Discussion

### 3.1.Comparison between full array and semi-array layouts

For the first time, animal studies were performed using EIT to detect and localize haematomas within the skull in an ovine model. In five sheep heads, haematomas were simulated by placing gel samples with the same conductivity as blood at different positions. Two eight-electrode layouts were applied to compare their ability to localise and quantify the simulated haematomas. An optimised, novel electrode layout named semi-array (SA) was introduced and its performance was evaluated and compared *in vitro* with a conventional full array electrode layout. The FA layout performed well in both localisation and size estimation of the anomalies. It is believed that the errors in the FA experiments are due to the presence of random and systematic experimental noise. As expected, the SA layout performed well in detecting and localising anomalies close to the electrodes, but slightly worse for anomalies far away from the electrodes. Reduction of the electrodes at the posterior of the head reduced overall image quality and increased uncertainty in estimations of location and size of the anomalies. Large spatial variance and therefore the variability in size estimates of an anomaly because of the restricted number of electrodes at the posterior of the head are inevitable. It is thought that the large size estimation errors may have been caused by the noise-generated artefacts in reconstructions and the electrode positions.

### 3.2.Anomaly size estimation

Although QI values depend on the size of the anomaly, the regularisation method and the sensitivity matrix calculation also affect the size estimation. The FA and SA electrode layouts produce different sensitivities in the region at the back of the head and therefore have different QI accuracy. Large size errors in SA may have been related to the smaller sensitivity at the posterior region of the head, far from the electrodes, combined with measurement noise. However, spatial variation of QI was improved by using blurring properties calculated directly from the sensitivity matrix. The truncation number for each case was chosen based on the noise level in the voltage measurements and the rank of the sensitivity matrix on inspection of the L-curve of experimental data.

### 3.3.Comparing results with earlier studies

Using EIT for clinical applications to detect and image bleeding in an animal model has been proven in previous studies (Xu *et al.* 2011, Xu *et al.* 2010). A group based at the University of Florida has applied EIT to detect intra-ventricular haemorrhage (IVH) for neonate applications (Tang et al. 2010). In their phantom experimental studies, data were collected by a FA layout with 16 electrodes equally spaced around the head, using adjacent current patterns. Their results showed a maximum radial error of 0.1 and QI error of 30% which is better than our size estimation accuracy. (Sadleir et al. 2008) introduced a hemi-array electrode layout for the application of abdominal trauma. QI values of their phantom experimental studies showed a variation of around a factor of 4, the maximum being 220%. Hemi-arrays have been used in vivo to quantify accumulating abdominal fluid (Tucker et al. 2011) and to monitor lung resistivity by Zlochiver *et al* (Zlochiver *et al*. 2007). However, the hemi-array electrode layout failed in this application to detect simulated haematomas using ovine models. It is believed that the presence of the skull and the geometry structure of the head may restrict the use of the hemi-array in this application. However, the optimised SA electrode layout has shown its reliability to detect, localise and quantify the simulated haematomas in this application. According to earlier studies (Yvert *et al.* 1997, Taktak *et al.* 1996), the quality of the images and consequently the localisation and size errors may be improved by increasing the number of electrodes. However, the objective of this concept is to optimize the number and position of the electrodes in order to speed up the electrode setup process and avoid the need to move and lift the patient's head in emergency cases. It is considered that using an eight-electrode configuration is more preferable than using 16 or 32 and that the ensuing results are quite acceptable. Although the use of 2D imaging restricts the z direction localisation, the overall process is faster and the results are reliable enough for a useful application to emergency cases.

## 4. Conclusion

This study indicates the feasibility of detection, localisation and size estimation of haematomas *in vitro* with preliminary EIT imaging on ovine models for the purpose of early diagnosis. Two eight-electrode layouts were compared *in vitro* on their ability to detect, localise and quantify simulated haematomas. As expected, the FA layout was found to be more robust than the SA layout, having an overall better quality on localisation and size estimation of the simulated haematomas. Although using the SA configuration reduces the

sensitivity and accuracy of quantity estimations, an optimized electrode layout that does not require the patient to be lifted for its application would be very convenient for emergency applications where the required accuracy is not critical.

**Summary**

The novel semi-array (SA) layout was introduced in this study. The SA layout was evaluated and compared with the full array (FA) using phantom models in Chapter 5. For the first time, the FA and the SA layouts were investigated to evaluate their ability to detect, localise and estimate the size of the anomalies similar to haematoma in the human head *in vitro* using ovine models, in this chapter. Using the minimum number of electrodes is always desirable in clinical applications since it may also speed up the electrode setup process in emergency cases. The SA layout was considered in this study because of its configuration, which can be used for patients where the head cannot be moved. Epidural and subdural haematomas were considered in this study since their location can represent the worst case with respect to the SA layout. The hemi-array (HA) electrode layout failed in this application to detect simulated haematomas using ovine models. It is believed that the presence of the skull and the geometry structure of the head may restrict the use of the hemi-array in this application.

Five freshly skinned sheep heads were used. All the skulls were cut in approximately half using a bone saw. The top half of the skull was carefully removed and the brain was exposed in order to position the anomalies. The anomalies were placed superficially on top of the brain lobe and the top half of the skull was replaced. The anomaly was located in five locations and the measurements were performed using both layouts.

The FA layout performed well in both localisation and size estimation of the anomalies. As expected, the SA layout performed well in detecting and localising anomalies close to the electrodes, but slightly worse for anomalies far away from the electrodes. Reduction of the electrodes at the posterior of the head reduced overall image quality and increased uncertainty in estimations of location and size of the anomalies. Although using the SA configuration reduces the sensitivity and accuracy of quantity estimations, an optimized electrode layout that does not require the patient to be lifted for its application would be very convenient for emergency applications where the required accuracy is not critical.

CHAPTER

# 7

# Conclusions

Medical imaging has historically played a very significant role in clinical medicine. Amongst other methods, EIT has drawn great attention from a score of researchers in the world. Despite the limitation of EIT in terms of spatial resolution compared to other imaging techniques, it offers a unique combination of advantages. EIT is inexpensive, portable, non-invasive, user-friendly and fast. The purpose of this study was to develop a portable EIT system for emergency medical care.

The conclusions are listed as follows according to the objectives.

1- In order to develop an EIT system for emergency applications, a prototype model of an EIT system was constructed in the laboratory. This system was low-cost and portable. The constructed EIT had 16 channels and operated in the frequency range of 10 kHz to 100 kHz with a temporal resolution of 100 frames per second and a high level of accuracy of 93.5 %. Although most of the currently available EIT systems work with 64 or 32 electrodes, a minimal number of electrodes was chosen in this study for emergency care. Smaller numbers of electrodes speeds up the electrode setup process and avoids the need to move the patient's head in emergency care. The constructed EIT system had the

capability of using 16 electrodes; however, only eight electrodes were used in this study. The system was attached to eight electrodes which could be connected over the phantoms or on the sheep heads. The electrodes were connected to the EIT system using equal length wires to obtain an identical impedance path through all the electrodes in order to reduce the mismatch in electrode impedances.

Connection of the electrodes was an important task during the experiments. The EIT method is very sensitive to the measurements and production of meaningful results was much dependent on the measurements. Therefore, the constructed EIT system had the capability of showing electrode connection failure to the user. Differential imaging was considered in this study, since the difference of two data sets would cancel the errors arising from the uncertain positioning of the electrodes.

The Adjacent method was used in this system due to the simplicity of its algorithm. In this method the sensitivity at the periphery is good but poor at the centre. Using multiple current and extending measurements may improve the performance of the system; however, the hardware complexity will be increased. Compound electrodes should be used in a multiple drive method and may increase the electrode connection time in emergency applications. Epidural and subdural haematomas were considered in this study since their location can represent the worst case with respect to the optimized electrode layout and the Adjacent method was reliable enough to detect this kind of haematoma.

The prototype model was portable; however this system can be easily designed to be smaller in size for its next generation, and thus able to be carried by the patient for continuous monitoring.

2- To investigate an optimized electrode layout to be used in emergency care, the first step was a numerical simulation study on FE models. The full array and hemi-array layouts were simulated using homogenous circular head models. Firstly, the anomalies were introduced to the models with different sizes. Then the anomalies were simulated in different positions with the anomaly centre placed successively at a relative radial displacement of 0, 0.2, 0.4, 0.6 and 0.8 from the centre. Anomaly positions varied as a function of angle from 0° to 180° with 5° increments. The results were obtained using TSVD and WMNM reconstruction methods. The images were reconstructed using the

collected data by COMSOL linked with MATLAB. The simulated anomalies were detected for all the positions using both layouts; however full array results were in general superior to the hemi-array results.

For further investigation of the optimised electrode layout, phantom experiments were conducted. The phantoms with the full array and the hemi-array electrode layouts were prepared. Cylindrical gel samples as simulated anomalies were introduced to the phantoms and the measurements were performed. The electrode layouts were compared in terms of the detection, localization and size estimation of the anomalies. The results were obtained using TSVD and WPI reconstruction methods. As expected, the full array layout had the best performance in general. However the performance of the hemi-array layout was very poor. Thus a novel optimised electrode layout (semi-array) for emergency care was proposed and evaluated in phantom experiments. The performance of the semi-array electrode layout was better in comparison to the hemi-array layout. For the hemi-array and the semi-array layouts, measurement sensitivity depends strongly on the anomaly location since the electrodes are not placed all over the head. Some reconstructed anomalies located far from the electrodes in the posterior region were almost invisible or erroneous for the hemi-array layout; however, they were enhanced by using the semi-array layout.

Using a minimal number of electrodes in an optimised layout is always desirable in clinical applications. The semi-array 8-electrode layout prevents unnecessary movements and the electrode connections to the head would be very quick to configure in emergency care situations. Although the semi-array 8-electrode layout reduced the sensitivity of the measurements, the findings from the phantom experiments indicated its potential to use in emergency applications.

3- The full array and the hemi-array layouts were considered for further study using ovine models. The full array and the hemi-array were compared to detect, localize and quantify intracranial haematomas *in vitro*. This was the first time that an optimized electrode layout had been used for head applications. Sheep's head were used to conduct the experiments. In most of the experiments carried out by other researchers, since the location of the simulated anomalies was not known and the simulated blood was normally injected into the body or the head, localization of the anomalies was not considered and

the quantity of the injected blood was investigated solely. In this new method of experiment, the position of the anomalies was known *a priori* and thus could be compared accurately to the EIT results. To simulate a more realistic haematoma in an accurate location, the saline solution (simulated blood) was transformed to gel. All the skulls were cut and gel samples were placed superficially on top of the brain lobes in different positions. In this method, gel samples could not be injected to the lower layers of the brain. However in order to evaluate the performance of the semi-array layout, simulated haematomas were placed at the posterior region of the head which was the worst position to detect.

This work has achieved some original and unique objectives. This was the first time that ovine model experiments have been used in EIT application. It was also the first time that 8 electrodes in an optimised electrode layout have been used for brain imaging. The investigation into localization of anomalies *in vitro* using ovine models, and the introduction and evaluation of the semi-array layout for brain imaging in an emergency care role, both represent novel work in the field.

The results were obtained using TSVD and WPI reconstruction methods. The full array electrode layout was found to be more robust than the semi-array electrode layout. The maximum mean value of the localization error for the full array layout was 0.0714 mm while for the semi-array layout was 0.2364 mm. The worst QI error in reconstructions was around 30% using the full array layout and about 50% using the semi-array layout. The reconstructed images using the semi-array layout may be further enhanced to reduce large errors by other combinations of the reconstruction methods, or by increasing the number of electrodes. However, the shape of the sheep heads restricted the position and number of electrodes used on the anterior aspect of the head. It should be noted that the semi-array layout was chosen because the focus of this research was to optimize the number and position of the electrodes in order to speed up the electrode setup process, and avoid the need to move and lift the patient's head in emergency cases.

Although the semi-array electrode layout reduces the sensitivity and accuracy of quantity estimations, the promising results indicated that the semi-array layout can be used to detect and monitor haematoma on ovine models and probably extend its application for emergency applications where the required accuracy is not critical. The observations from

these experiments on ovine models were published in two journal papers presented at the end of the thesis.

Thus it is concluded that the EIT has the potential to be used in human applications, specifically for emergency purposes, using the semi-array layout, and in routine monitoring or follow-up using either the full array or semi-array layouts. Hence, further work is warranted to fully investigate the semi-array layout for human applications.

CHAPTER

# 8

# Future Work

The future work is listed as follows.

1- A prototype of an EIT system was constructed and used for phantom and ovine model *in vitro* experiments. One future task would develop this system to be smaller in size to be able to be carried by patients after injury or surgery and warn of the existence of any internal cranial bleeding. The proposed system would also record the patient details, and store these data to present to a surgeon.

2- The Adjacent current pattern method was used in this system. Although it contained all the independent measurements, a number of these measurements were very low in magnitude and were likely to introduce errors when noise was present. The flexibility of selection of current and voltage electrode pairs would improve the current pattern. Using multiple current and extending measurements may improve the performance of the system; however, the hardware complexity will be increased. One future task would include the investigation of a current source for each electrode and a perfect calibration technique. Other future work would be development of the electronic

design to reduce noise, and to introduce flexibility in the selection of current or voltage measurements between electrode pairs.

3- In the electrode connection process, electrode stickers are first put on, then the conducting gel is injected carefully into each electrode, which are then attached to the stickers. The amount of gel injected into each electrode needs to be controlled very carefully. Too much or too little will both cause an electrode contact problem. Having 8 electrodes reduced the time of the electrode connections compared to 16 and 32 electrodes, however the process of individually connecting the electrodes is still time consuming and there are potential failures in positioning and effective connection of the electrodes. One future task which would be very helpful is to have a ready-made electrode head band (belt-like) to place and connect the electrodes properly. Another task would be the development of new types of electrodes which can make the connection process faster.

4- The animal experiments were conducted on sheep heads. The heads did not have skin and the electrodes were connected to the skull. One future task would be to perform more realistic experiments on sheep heads with the skin intact; these were not available in the UK. The heads were cut from the body and therefore the experiments were performed in the absence of CSF and brain pressure. Another future task would be to perform *in vivo* sheep experiments, but these are not possible in the UK. If such experiments were possible, simulated haematomas could also be injected into the head during *in vivo* experiments.

5- As mentioned above, animal tests may not be possible in the UK. One future task would be to develop an alternative EIT system in collaboration with a neurosurgeon, and apply for ethical approval for the collaborating neurosurgeon and other clinicians to collect data whenever a haematoma is suspected or after a haematoma is detected (before surgery), as well collecting data on the same patient after recovery. Obviously, such process would necessitate the system to be efficient, user friendly and very quick to attach to the head.

## Appendix A: MATLAB/COMSOL scripts

### Reconstruct_TSVD.m

```
% %%%%%%%%%%%%%%%%%%%%%%%%%%%%%%%%%%%%%%%%%%%%%%%%%%%%%%%%%%%%%%%%%%%%%%%%%%%%%%%
%
% script is used to obtain SVD image reconstruction.
%
% sensitivity matrix (Sfull)
% & boundary voltage measurements (homo & Dv) are loaded.
%
% homo.mat was measured from the homogenous model
% Dv.mat was measured from the model with anomalies located in angles
% [0, 45, 90, 135, 180]
%
% Sfull is inverted using SVD method.
%
% the conductivity distribution (x) is calculated & saved in a
% Folder named x.
% x is a matrix to show the conductivity of each element over the
% inverse model and will be used to show the images.
%
% Hoda Ayati
%

clear all;
clc

load Sfull.mat;
S = Sfull;
load homo.mat;

[U,s,V] = svd(S);
sinv = zeros(size(s));
Sinv = V*sinv'*U';

for angle = [0:45:180]
    cd Dv
    eval(['load Dv' num2str(angle) '.mat']);
    cd ..
    deltaV = Dv - homo;

    x = Sinv*deltaV;

    cd x
    eval(['save x' num2str(angle) '.mat x']);
    cd ..
end
```

### Reconstruct_WMNM.m

```
% %%%%%%%%%%%%%%%%%%%%%%%%%%%%%%%%%%%%%%%%%%%%%%%%%%%%%%%%%%%%%%%%%%%%%%%%%%%%%%%
%
% script is used to obtain WMNM image reconstruction.
%
% sensitivity matrix (Sfull)
```

```
% & boundary voltage measurements (homo & Dv) are loaded.
%
% homo.mat was measured from the homogenous model
% Dv.mat was measured from the model with anomalies located in angles
% [0, 45, 90, 135, 180]
%
% Sfull is inverted using SVD method.
% W is the weighting matrix calculated from the sensitivity matrix
%
% the conductivity distribution (x) is calculated & saved in a
% Folder named x.
% x is a matrix to show the conductivity of each element over the
% inverse model and will be used to show the images.
%
% Hoda Ayati
%

clear all;
clc

load homo.mat;

load Sfull.mat;
S = Sfull;

k = 16;

% Weighting Matrix
w = zeros(3032,3032);
for ii = 1:3032
  for jj = 1:40
      w(ii,ii) =  w(ii,ii)+(S(jj,ii)^2);
  end
  w(ii,ii) = 1/sqrt(w(ii,ii));
end

SW = S * w;

[U,s,V] = svd(SW);
sinv = zeros(size(s));
ss = svds(SW,k);
for ii = 1:k
  sinv(ii,ii) = 1/ss(ii);
end
SWinv = V*sinv'*U';
W_SWinv = w * SWinv;

for angle = [0:45:180]
    cd Dv
    eval(['load Dv' num2str(angle) '.mat']);
    cd ..
    deltaV = Dv - homo;

    x = W_SWinv *deltaV;

    cd x
    eval(['save x' num2str(angle) '.mat x']);
    cd ..
end
```

**measure_all_8.m**

```
% %%%%%%%%%%%%%%%%%%%%%%%%%%%%%%%%%%%%%%%%%%%%%%%%%%%%%%%%%%%%%%%%%%%%%%%
%
% this function is used to measure boundary voltages from a loaded
% fem structure
%
% solution structure (fem) is an input & boundary voltage measurements (Dv)
% is an output of the function.
%
% The output will be loaded to reconstruct.m to reconstruct images.
%
% location of the electrodes (P) is defined for 8 electrodes in Semi-Array
% layout
%
% Differential voltage measurement is taken from the electrodes according
% to the adjacent method
% inPos and inNeg show the electrode numbers which current injected to and
% voltage is measured from the other pairs of the electrodes
% fem{inPos, inNeg} is a solution from solve.m, while the current injected
% to inPos and inNeg electrodes
%
% to measure voltage values of specified locations (electrode position)
% for a given solution structure, function of measure.m is called.
%          function [v] = measure(fem,P)
%               fem.xmesh = meshextend(fem);
%               v = postinterp(fem, 'V', P);
% P is points of measurements over a given solution (fem)
%
% Hoda Ayati
%

function [Dv] = measure_all_8(fem)

nE = 8; clear i;
Pcomplex_1 =  exp(i*degtorad(-11.5));
Pcomplex_2 =  exp(i*degtorad(17.5));
Pcomplex_3 =  exp(i*degtorad(46.5));
Pcomplex_4 =  exp(i*degtorad(75.5));
Pcomplex_5 =  exp(i*degtorad(104.5));
Pcomplex_6 =  exp(i*degtorad(133.5));
Pcomplex_7 =  exp(i*degtorad(162.5));
Pcomplex_8 =  exp(i*degtorad(191.5));

x_1=real(Pcomplex_1);y_1=imag(Pcomplex_1);
x_2=real(Pcomplex_2);y_2=imag(Pcomplex_2);
x_3=real(Pcomplex_3);y_3=imag(Pcomplex_3);
x_4=real(Pcomplex_4);y_4=imag(Pcomplex_4);
x_5=real(Pcomplex_5);y_5=imag(Pcomplex_5);
x_6=real(Pcomplex_6);y_6=imag(Pcomplex_6);
x_7=real(Pcomplex_7);y_7=imag(Pcomplex_7);
x_8=real(Pcomplex_8);y_8=imag(Pcomplex_8);

P = [x_1, x_2, x_3, x_4, x_5, x_6, x_7, x_8; ...
    y_1, y_2, y_3, y_4, y_5, y_6, y_7, y_8];

clear temp;
index = [];
for ii = 1:nE
    temp = sort(mod([1:nE-3]+ii,nE)+1);
```

```
    index = [index; temp];
end

Dv = zeros(1,nE*(nE-3))';
for k = 1:nE
    inPos = k; inNeg = mod(k,nE)+1;
    femIn = fem{inPos,inNeg};
    [V] = measure(femIn,P);
    V = [V V(1)];
    dVV = diff(V);
    outV = index(k,:);
    dV = dVV(outV);
    Dv([(nE-3)*(k-1)+1:(nE-3)*k]) = dV';
end
```

### SingularImages.m

```
% %%%%%%%%%%%%%%%%%%%%%%%%%%%%%%%%%%%%%%%%%%%%%%%%%%%%%%%%%%%%%%%%%%%%%%%%%%%
%
% this script shows a singular image
%
% all the functions are working only using COMSOL with MATLAB
%
% this script is the geometry of the inverse model which was created in COMSOL
% and transferred to MATALB
% the data of the singular images were loaded to this script and the output is a
% coloured image
%
% Hoda Ayati
%

% COMSOL Multiphysics Model M-file
% Generated by COMSOL 3.4 (COMSOL 3.4.0.248, $Date: 2007/10/10 16:07:51 $)

% Geometry without points

flclear fem

% COMSOL version
clear vrsn
vrsn.name = 'COMSOL 3.4';
vrsn.ext = '';
vrsn.major = 0;
vrsn.build = 248;
vrsn.rcs = '$Name:  $';
vrsn.date = '$Date: 2007/10/10 16:07:51 $';
fem.version = vrsn;

% Geometry
g1=ellip2(1,1,'base','center','pos',[0,0]);

carr={curve2([-1,1],[0,0],[1,1])};
g24=geomcoerce('curve',carr);
carr={curve2([-0.9945218953682733,0.9945218953682733], ...
[-0.10452846326765347,-0.10452846326765347],[1,1])};
g25=geomcoerce('curve',carr);
carr={curve2([-0.9799247046208296,0.9799247046208296], ...
[-0.19936793441719716,-0.19936793441719716],[1,1])};
g26=geomcoerce('curve',carr);
```

```
carr={curve2([-0.9537169507482269,0.9537169507482269], ...
[-0.30070579950427306,-0.30070579950427306],[1,1])};
g27=geomcoerce('curve',carr);
carr={curve2([-0.9205048534524404,0.9205048534524404], ...
[-0.3907311284892737,-0.3907311284892737],[1,1])};
g28=geomcoerce('curve',carr);
carr={curve2([-0.8660254037844387,0.8660254037844387], ...
[-0.4999999999999994,-0.4999999999999994],[1,1])};
g29=geomcoerce('curve',carr);
carr={curve2([-0.7986355100472929,0.7986355100472929], ...
[-0.6018150231520483,-0.6018150231520483],[1,1])};
g30=geomcoerce('curve',carr);
carr={curve2([-0.7132504491541817,0.7132504491541817], ...
[-0.7009092642998509,-0.7009092642998509],[1,1])};
g31=geomcoerce('curve',carr);
carr={curve2([-0.6000000000000001,0.6000000000000001], ...
[-0.8,-0.8],[1,1])};
g32=geomcoerce('curve',carr);
carr={curve2([-0.4226182617406996,0.4226182617406996], ...
[-0.9063077870366498,-0.9063077870366498],[1,1])};
g33=geomcoerce('curve',carr);
g52=mirror(g25,[0,0],[0,1]);
g53=mirror(g26,[0,0],[0,1]);
g54=mirror(g27,[0,0],[0,1]);
g55=mirror(g28,[0,0],[0,1]);
g56=mirror(g29,[0,0],[0,1]);
g57=mirror(g30,[0,0],[0,1]);
g58=mirror(g31,[0,0],[0,1]);
g59=mirror(g32,[0,0],[0,1]);
g60=mirror(g33,[0,0],[0,1]);
g82=mirror(g24,[0,0],[1,0]);
g83=mirror(g25,[0,0],[1,0]);
g84=mirror(g26,[0,0],[1,0]);
g85=mirror(g27,[0,0],[1,0]);
g86=mirror(g28,[0,0],[1,0]);
g87=mirror(g29,[0,0],[1,0]);
g88=mirror(g30,[0,0],[1,0]);
g89=mirror(g31,[0,0],[1,0]);
g90=mirror(g32,[0,0],[1,0]);
g91=mirror(g33,[0,0],[1,0]);
g110=mirror(g52,[0,0],[1,0]);
g111=mirror(g53,[0,0],[1,0]);
g112=mirror(g54,[0,0],[1,0]);
g113=mirror(g55,[0,0],[1,0]);
g114=mirror(g56,[0,0],[1,0]);
g115=mirror(g57,[0,0],[1,0]);
g116=mirror(g58,[0,0],[1,0]);
g117=mirror(g59,[0,0],[1,0]);
g118=mirror(g60,[0,0],[1,0]);
g82=rotate(g82,1.5707963267948966,[0,0]);
g83=rotate(g83,1.5707963267948966,[0,0]);
g84=rotate(g84,1.5707963267948966,[0,0]);
g85=rotate(g85,1.5707963267948966,[0,0]);
g86=rotate(g86,1.5707963267948966,[0,0]);
g87=rotate(g87,1.5707963267948966,[0,0]);
g88=rotate(g88,1.5707963267948966,[0,0]);
g89=rotate(g89,1.5707963267948966,[0,0]);
g90=rotate(g90,1.5707963267948966,[0,0]);
g91=rotate(g91,1.5707963267948966,[0,0]);
g110=rotate(g110,1.5707963267948966,[0,0]);
g111=rotate(g111,1.5707963267948966,[0,0]);
```

```
g112=rotate(g112,1.5707963267948966,[0,0]);
g113=rotate(g113,1.5707963267948966,[0,0]);
g114=rotate(g114,1.5707963267948966,[0,0]);
g115=rotate(g115,1.5707963267948966,[0,0]);
g116=rotate(g116,1.5707963267948966,[0,0]);
g117=rotate(g117,1.5707963267948966,[0,0]);
g118=rotate(g118,1.5707963267948966,[0,0]);

carr={curve2([-0.9986295347545739,0.9986295347545739], ...
[-0.052335956242943835,-0.052335956242943835],[1,1])};
g120=geomcoerce('curve',carr);
carr={curve2([-0.9890158633619168,0.9890158633619168], ...
[-0.14780941112961066,-0.14780941112961066],[1,1])};
g121=geomcoerce('curve',carr);
parr={point2(-1,0)};
carr={curve2([-0.9685831611286312,0.9685831611286312], ...
[-0.2486898871648548,-0.2486898871648548],[1,1])};
g126=geomcoerce('curve',carr);
carr={curve2([-0.938493022759556,0.938493022759556], ...
[-0.34529819899853464,-0.34529819899853464],[1,1])};
g127=geomcoerce('curve',carr);
carr={curve2([-0.8941542368393683,0.8941542368393683], ...
[-0.44775908783876966,-0.44775908783876966],[1,1])};
g132=geomcoerce('curve',carr);
carr={curve2([-0.8367643134589616,0.8367643134589616], ...
[-0.5475632234925503,-0.5475632234925503],[1,1])};
g133=geomcoerce('curve',carr);
carr={curve2([-0.7547095802227721,0.7547095802227721], ...
[-0.6560590289905072,-0.6560590289905072],[1,1])};
g138=geomcoerce('curve',carr);
carr={curve2([-0.6560590289905072,0.6560590289905072], ...
[-0.7547095802227719,-0.7547095802227719],[1,1])};
g139=geomcoerce('curve',carr);
carr={curve2([-0.5,0.5],[-0.8660254037844386,-0.8660254037844386],[1,1])};
g144=geomcoerce('curve',carr);
carr={curve2([-0.300705799504273,0.300705799504273], ...
[-0.9537169507482269,-0.9537169507482269],[1,1])};
g145=geomcoerce('curve',carr);
g146=mirror(g120,[0,0],[1,0]);
g147=mirror(g121,[0,0],[1,0]);
g148=mirror(g126,[0,0],[1,0]);
g149=mirror(g127,[0,0],[1,0]);
g150=mirror(g132,[0,0],[1,0]);
g151=mirror(g133,[0,0],[1,0]);
g152=mirror(g138,[0,0],[1,0]);
g153=mirror(g139,[0,0],[1,0]);
g154=mirror(g144,[0,0],[1,0]);
g155=mirror(g145,[0,0],[1,0]);
g146=rotate(g146,3.141592653589793,[0,0]);
g147=rotate(g147,3.141592653589793,[0,0]);
g148=rotate(g148,3.141592653589793,[0,0]);
g149=rotate(g149,3.141592653589793,[0,0]);
g150=rotate(g150,3.141592653589793,[0,0]);
g151=rotate(g151,3.141592653589793,[0,0]);
g152=rotate(g152,3.141592653589793,[0,0]);
g153=rotate(g153,3.141592653589793,[0,0]);
g154=rotate(g154,3.141592653589793,[0,0]);
g155=rotate(g155,3.141592653589793,[0,0]);
g156=mirror(g120,[0,0],[1,0]);
g157=mirror(g121,[0,0],[1,0]);
g158=mirror(g126,[0,0],[1,0]);
```

```
g159=mirror(g127,[0,0],[1,0]);
g160=mirror(g132,[0,0],[1,0]);
g161=mirror(g133,[0,0],[1,0]);
g162=mirror(g138,[0,0],[1,0]);
g163=mirror(g139,[0,0],[1,0]);
g164=mirror(g144,[0,0],[1,0]);
g165=mirror(g145,[0,0],[1,0]);
g166=mirror(g146,[0,0],[1,0]);
g167=mirror(g147,[0,0],[1,0]);
g168=mirror(g148,[0,0],[1,0]);
g169=mirror(g149,[0,0],[1,0]);
g170=mirror(g150,[0,0],[1,0]);
g171=mirror(g151,[0,0],[1,0]);
g172=mirror(g152,[0,0],[1,0]);
g173=mirror(g153,[0,0],[1,0]);
g174=mirror(g154,[0,0],[1,0]);
g175=mirror(g155,[0,0],[1,0]);
g156=rotate(g156,1.5707963267948966,[0,0]);
g157=rotate(g157,1.5707963267948966,[0,0]);
g158=rotate(g158,1.5707963267948966,[0,0]);
g159=rotate(g159,1.5707963267948966,[0,0]);
g160=rotate(g160,1.5707963267948966,[0,0]);
g161=rotate(g161,1.5707963267948966,[0,0]);
g162=rotate(g162,1.5707963267948966,[0,0]);
g163=rotate(g163,1.5707963267948966,[0,0]);
g164=rotate(g164,1.5707963267948966,[0,0]);
g165=rotate(g165,1.5707963267948966,[0,0]);
g166=rotate(g166,1.5707963267948966,[0,0]);
g167=rotate(g167,1.5707963267948966,[0,0]);
g168=rotate(g168,1.5707963267948966,[0,0]);
g169=rotate(g169,1.5707963267948966,[0,0]);
g170=rotate(g170,1.5707963267948966,[0,0]);
g171=rotate(g171,1.5707963267948966,[0,0]);
g172=rotate(g172,1.5707963267948966,[0,0]);
g173=rotate(g173,1.5707963267948966,[0,0]);
g174=rotate(g174,1.5707963267948966,[0,0]);
g175=rotate(g175,1.5707963267948966,[0,0]);

% Analyzed geometry
clear c s
c.objs={g24,g25,g26,g27,g28,g29,g30,g31,g32,g33,g52,g53,g54,g55,g56, ...
  g57,g58,g59,g60,g82,g83,g84,g85,g86,g87,g88,g89,g90,g91,g110,g111,g112, ...
  g113,g114,g115,g116,g117,g118,g120,g121,g126,g127,g132,g133,g138,g139, ...
  g144,g145,g146,g147,g148,g149,g150,g151,g152,g153,g154,g155,g156,g157, ...
  g158,g159,g160,g161,g162,g163,g164,g165,g166,g167,g168,g169,g170,g171, ...
  g172,g173,g174,g175};
c.name={'B1','B2','B3','B4','B5','B6','B7','B8','B9','B10','B11', ...
  'B12','B13','B14','B15','B16','B17','B18','B19','B20','B21','B22','B23', ...
  'B24','B25','B26','B27','B28','B29','B30','B31','B32','B33','B34','B35', ...
  'B36','B37','B38','B39','B40','B41','B42','B43','B44','B45','B46','B47', ...
  'B48','B49','B50','B51','B52','B53','B54','B55','B56','B57','B58','B59', ...
  'B60','B61','B62','B63','B64','B65','B66','B67','B68','B69','B70','B71', ...
  'B72','B73','B74','B75','B76','B77','B78'};
c.tags={'g24','g25','g26','g27','g28','g29','g30','g31','g32','g33', ...
  'g52','g53','g54','g55','g56','g57','g58','g59','g60','g82','g83','g84', ...
  'g85','g86','g87','g88','g89','g90','g91','g110','g111','g112','g113', ...
  'g114','g115','g116','g117','g118','g120','g121','g126','g127','g132', ...
  'g133','g138','g139','g144','g145','g146','g147','g148','g149','g150', ...
  'g151','g152','g153','g154','g155','g156','g157','g158','g159','g160', ...
  'g161','g162','g163','g164','g165','g166','g167','g168','g169','g170', ...
  'g171','g172','g173','g174','g175'};
```

```
s.objs={g1};
s.name={'E1'};
s.tags={'g1'};

fem.draw=struct('c',c,'s',s);
fem.geom=geomcsg(fem);

% Initialize mesh
fem.mesh=meshinit(fem, ...
                  'hauto',5);

% (Default values are not included)

% Application mode 1
clear appl
appl.mode.class = 'ConductiveMediaDC';
appl.assignsuffix = '_dc';
clear bnd
bnd.type = {'cont','V0'};
appl.bnd = bnd;
clear equ

equ.sigma = V(1:1300,1);
% equ.sigma = V(1:1300,2);
% equ.sigma = V(1:1300,3);
% equ.sigma = V(1:1300,4);
% equ.sigma = V(1:1300,5);
% equ.sigma = V(1:1300,6);
% equ.sigma = V(1:1300,7);
% equ.sigma = V(1:1300,8);
% equ.sigma = V(1:1300,9);
% equ.sigma = V(1:1300,10);
% equ.sigma = V(1:1300,11);
% equ.sigma = V(1:1300,12);
% equ.sigma = V(1:1300,13);
% equ.sigma = V(1:1300,14);
% equ.sigma = V(1:1300,15);
% equ.sigma = V(1:1300,16);
% equ.sigma = V(1:1300,17);
% equ.sigma = V(1:1300,18);
% equ.sigma = V(1:1300,19);
% equ.sigma = V(1:1300,20);

equ.index = 1;
clear i;
for i = 2:1300
    equ.index = [equ.index i];
end

appl.equ = equ;
fem.appl{1} = appl;
fem.frame = {'ref'};
fem.border = 1;
clear units;
units.basesystem = 'SI';
fem.units = units;

% ODE Settings
clear ode
```

```
clear units;
units.basesystem = 'SI';
ode.units = units;
fem.ode=ode;
% Multiphysics
fem=multiphysics(fem);

% Extend mesh
fem.xmesh=meshextend(fem);

% Solve problem
fem.sol=femstatic(fem, ...
                  'solcomp',{'V'}, ...
                  'outcomp',{'V'}, ...
                  'ntol',1e-006);

% Save current fem structure for restart purposes
fem0=fem;

% Plot solution
postplot(fem, ...
         'tridata',{'sigma_dc','cont','internal','unit','S/m'}, ...
         'trimap','jet(1024)', ...
         'title','Surface: Electric conductivity [S/m]', ...
         'geom', 'off',...
         'axis',[-1.6342857142857143,1.6342857142857143,-1.1,1.1]);
```

**Appendix B: PCBs of the EIT system hardware**

*PCB design of MCU*

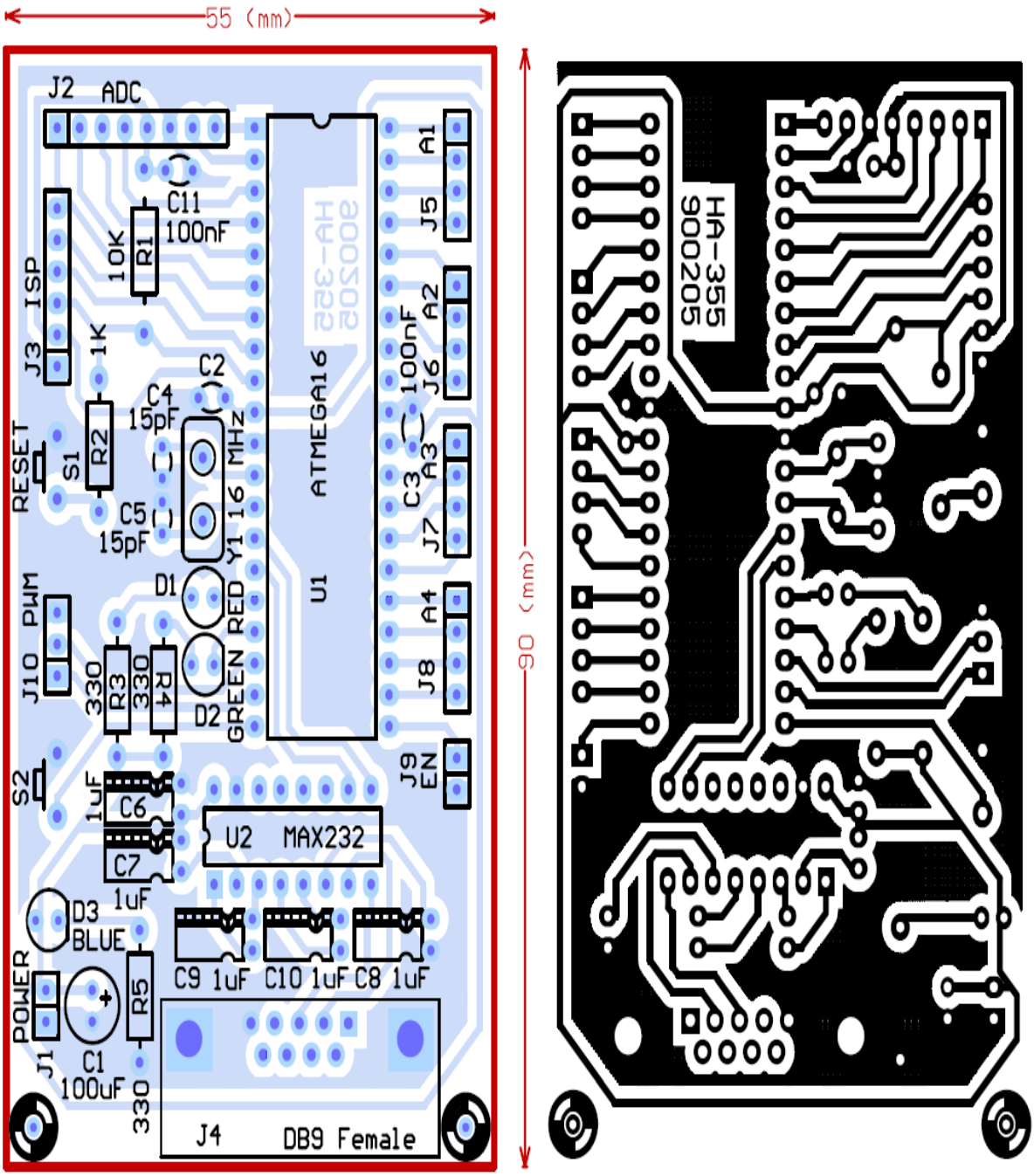

*PCB design of CCS*

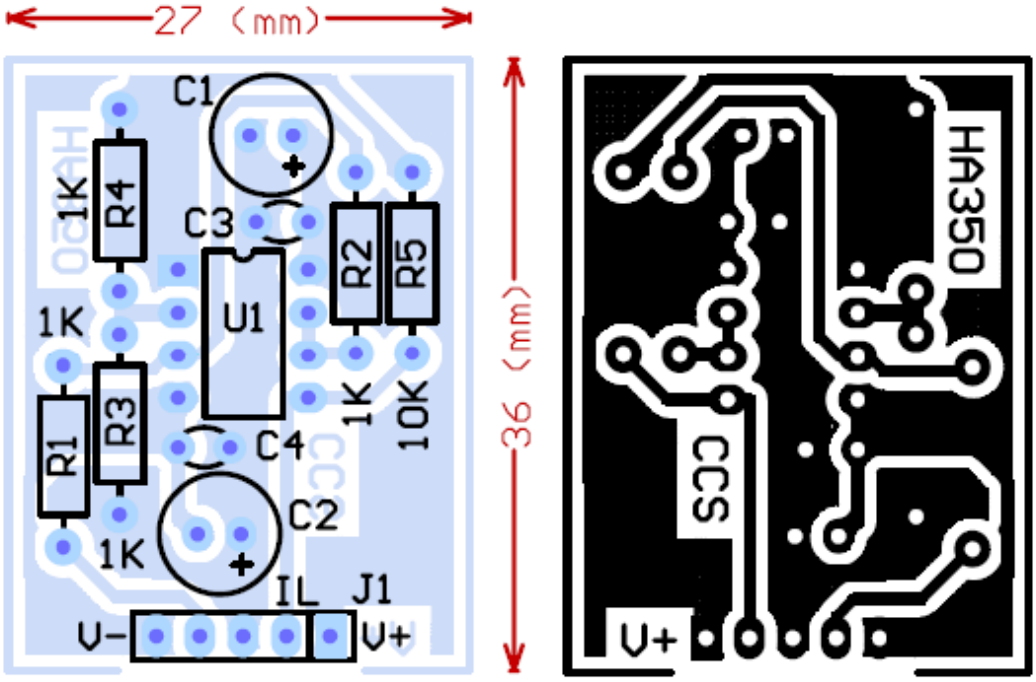

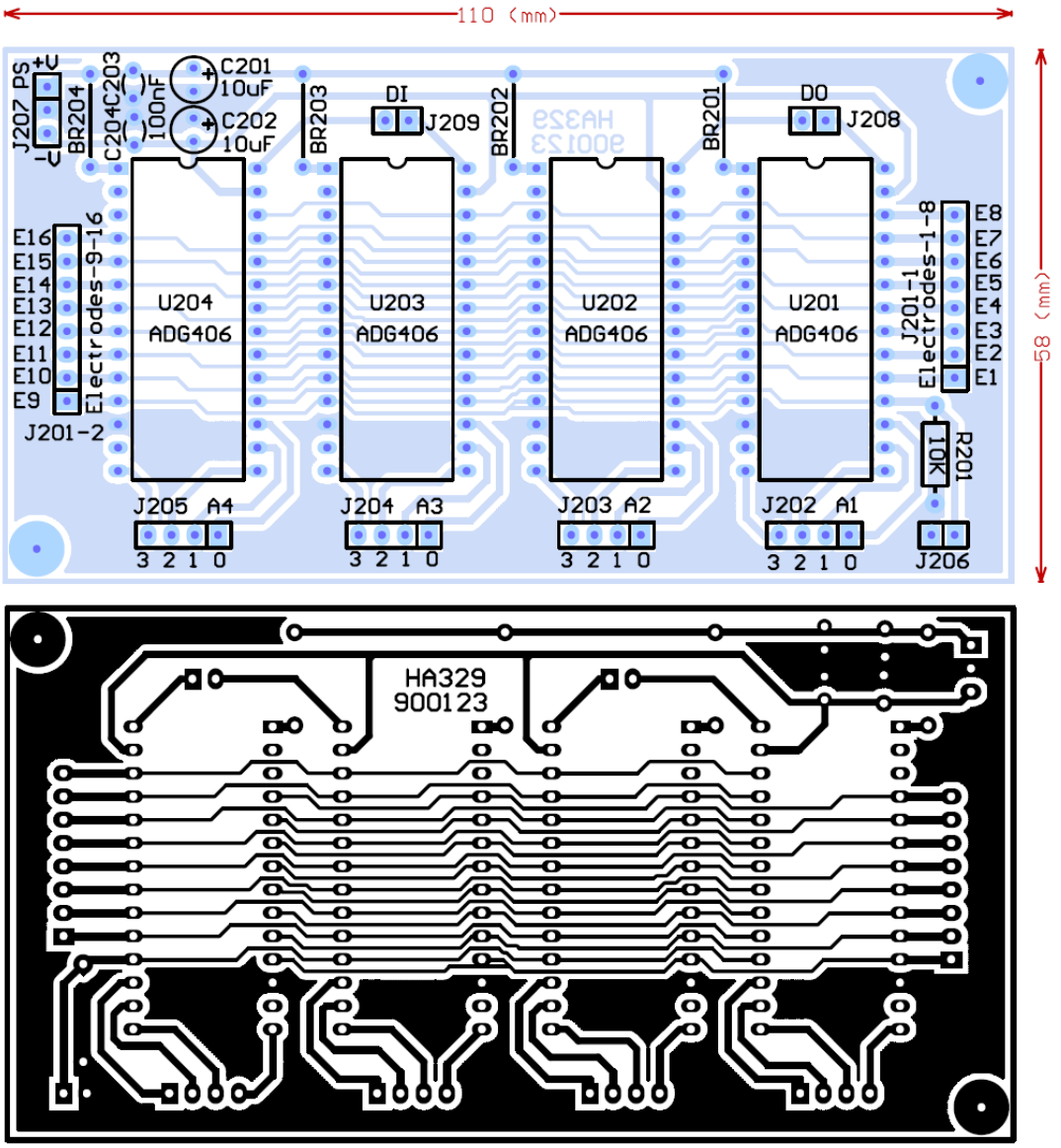
110 (mm)
58 (mm)
J207 PS
BR204
C204
C203
100nF
C201
10uF
C202
10uF
BR203
DI
J209
BR202
BR201
DO
J208
E16
E15
E14
E13
E12
E11
E10
E9
Electrodes-9-16
J201-2
U204
ADG406
U203
ADG406
U202
ADG406
U201
ADG406
J201-1
Electrodes-1-8
E8
E7
E6
E5
E4
E3
E2
E1
10K
R201
J205 A4
3 2 1 0
J204 A3
3 2 1 0
J203 A2
3 2 1 0
J202 A1
3 2 1 0
J206
HA329
900123

**References**


Adler A, Guardo R. Electrical impedance tomography: regularized imaging and contrast detection. Medical Imaging, IEEE Transactions 1996b; 15(2):170-179.

Adler A, Guardo R, Berthiaume Y. Impedance imaging of lung ventilation: do we need to account for chest expansion? Biomedical Engineering, IEEE Transactions 1996a; 43(4):414-420.

Adler A, Amyot R, Guardo R, Bates J, Berthiaume Y. Monitoring changes in lung air and liquid volumes with electrical impedance tomography. Journal of applied physiology 1997; 83(5):1762.

Adler A, Gaggero P, Maimaitijiang Y. Distinguishability in EIT using a hypothesis-testing model. Journal of Physics, Conference Series 2010, 224.

Alessandrini G, Rondi L. Stable determination of a crack in a planar inhomogeneous conductor. SIAM journal on mathematical analysis 1999; 30(2):326-340.

Avis N, Barber D. Image reconstruction using non-adjacent drive configurations (electric impedance tomography). Physiological Measurement 1994; 15:A153.

Ayati S, Bouazza-Marouf K, Kerr D, O'Toole M. Performance evaluation of a digital electrical impedance tomography system. Proceedings of the IASTED international symposia in imaging and signal processing in health care and technology, Baltimore, USA, 2012:101-5.

Bagshaw A, Liston A, Bayford R, Tizzard A, Gibson A, Tidswell A, Sparkes M, Dehghani H, Binnie C, Holder D. Electrical impedance tomography of human brain function using reconstruction algorithms based on the finite element method. Neuroimage 2003; 20(2):752-64.

Barber C, Brown B, Freeston I. Imaging spatial distributions of resistivity using applied potential tomography. Electronics Letters 1983; 19(22):933-935.

Barber D, Brown B. Applied potential tomography. Journal of Physics E: Scientific Instruments 1984; 17:723.

Barber D, Seagar A. Fast reconstruction of resistance images. Clinical Physics and Physiological Measurement 1987; 8:47.

Barber D. A review of image reconstruction techniques for electrical impedance tomography. Medical physics 1989; 16:162.

Barber D. Quantification in impedance imaging. Clinical Physics and Physiological Measurement 1990; 11:45.

Bautz W, Kalender W. Godfrey N. Hounsfield and his influence on radiology. Der Radiologe 2005; 45(4):350-355.

Bayford R, Boone K, Hanquan Y, Holder D. Improvement of the positional accuracy of EIT images of the head using a Lagrange multiplier reconstruction algorithm with diametric excitation. Physiological Measurement 1996; 17:A49.

Bayford R. Bioimpedance tomography (electrical impedance tomography). Annu.Rev.Biomed.Eng 2006; 8:63-91.

Bera TK, Nagaraju J. Studying the resistivity imaging of chicken tissue phantoms with different current patterns in Electrical Impedance Tomography (EIT). Measurement 2012; 45(4):663-682.

Bertero M, Boccacci P. Introduction to inverse problems in imaging. Institute of Physics Publishing. London, 1998.

Blott B, Cox S, Daniell G, Caton M, Nicole D. High fidelity imaging and high performance computing in nonlinear EIT. Physiological Measurement 2000; 21:7.

Blott B, Daniell G, Meeson S. Nonlinear reconstruction constrained by image properties in electrical impedance tomography. Physics in Medicine and Biology 1998; 43:1215.

Boone K, Holder D. Current approaches to analogue instrumentation design in electrical impedance tomography. Physiological Measurement 1996;17:229.

Boone K, Barber D, Brown B. Imaging with electricity: report of the European Concerted Action on Impedance Tomography. Journal of medical engineering & technology Nov-Dec 1997; 21(6):201-32.

Borcea L. A nonlinear multigrid for imaging electrical conductivity and permittivity at low frequency. Inverse problems 2001; 17:329.

Borsic A. Regularisation methods for imaging from electrical measurements, Oxford Brookes University, 2002.

Borsic A, Comina C, Foti S, Lancellotta R, Musso G. Imaging heterogeneities with electrical impedance tomography: laboratory results. Géotechnique 2005; 55(7):539-548.

Brenner S, Scott L. The mathematical theory of finite element methods. Springer-Verlag, New York 1994.

Brown B, Seagar A. The Sheffield data collection system. Clinical Physics and Physiological Measurement 1987; 8:91.

Brown B, Sinton A, Barber D, Leathard A, Mcardle F. Simultaneous display of lung ventilation and perfusion on a real-time EIT system, Engineering in Medicine and Biology Society 1992; 5:1710-1711.

Brown B. Electrical impedance tomography (EIT): a review. Journal of medical engineering & technology 2003; 27(3):97-108.

Campbell J, Harris N, Zhang F, Brown B, Morice A. Clinical applications of electrical impedance tomography in the monitoring of changes in intrathoracic fluid volumes. Physiological Measurement 1994; 15:A217.

Cassen B, Curtis L, Reed C. A sensitive directional gamma ray detector. UCLA, Report 49, University of California, LA, 1949.

Cheney M, Isaacson D, Newell JC, Simske S, Goble J. NOSER: An algorithm for solving the inverse conductivity problem. International Journal of Imaging Systems and Technology 1990; 2(2):66-75.

Cheney M, Isaacson D. Distinguishability in impedance imaging. Biomedical Engineering, IEEE Transactions 1992; 39(8):852-860.

Cheney M, Isaacson D, Newell JC. Electrical impedance tomography. SIAM Review 1999; 41(1):85-101.

Cheng KS, Isaacson D, Newell J, Gisser DG. Electrode models for electric current computed tomography. Biomedical Engineering, IEEE Transactions 1989; 36(9):918-924.

Choi MH, Isaacson D, Saulnier GJ, Newell JC. An iterative approach for applying multiple currents to a body using voltage sources in electrical impedance tomography. Engineering in Medicine and Biology Society Proceedings of the 25th Annual International Conference of the IEEE 2003; 4:3114-3117.

Clay MT, Ferree TC. Weighted regularization in electrical impedance tomography with applications to acute cerebral stroke. IEEE Trans. Med. Imag 2002; 21:629-637.

Cook RD, Saulnier GJ, Gisser DG, Goble JC, Newell J, Isaacson D. ACT3: a high-speed, high-precision electrical impedance tomograph. Biomedical Engineering, IEEE Transactions 1994; 41(8):713-722.

Cornean H, Knudsen K, Siltanen S. Towards a d-bar reconstruction method for three-dimensional EIT. Journal of Inverse and Ill-posed Problems 2006; 14(2):111-134.

Dai M, Wang L, Xu C, Li L, Gao G, Dong X. Real-time imaging of subarachnoid hemorrhage in piglets with electrical impedance tomography. Physiological Measurement 2010; 31:1229.

Dickin F, Wang M. Electrical resistance tomography for process applications. Measurement Science and Technology 1996; 7:247.

Dijkstra A, Brown B, Leathard A, Harris N, Barber D, Edbrooke D. Review clinical applications of electrical impedance tomography. Journal of medical engineering & technology 1993; 17(3):89-98.

Dinsmore J. Traumatic brain injury: an evidence-based review of management. Contin Educ Anaesth Crit Care Pain 2013. Advance Access.

Dong G, Liu H, Bayford RH, Yerworth R, Gao S, Holder D, Yan W. The spatial resolution improvement of EIT images by GVSMP-FOCUSS algorithm. Physiol. Meas. 2004; 25:209-225.

Dong G, Liu H, Bayford RH, Yerworth R, Schimpf PH, Yan W. Spatial resolution improvement of 3D EIT images by the shrinking sLORETA-FOCUSS algorithm. Physiological Measurement 2005; 26:S199.

Elliott A. Nuclear Instruments and Methods in Physics Research Section A: Accelerators, Spectrometers, Detectors and Associated Equipment. Proceedings of the 6th International Workshop on Radiation Imaging Detectors − Radiation Imaging Detectors. 2005; 546(1-2):1-13.

Eyuboglu BM, Brown BH, Barbaer DC. In vivo imaging of cardiac related impedance changes. Engineering in Medicine and Biology Magazine, IEEE 1989; 8(1):39-45.

Faes T, Meij H, Munck J, Heethaar R. The electric resistivity of human tissues (100 Hz-10 MHz): a meta-analysis of review studies. Physiological Measurement 1999; 20:R1.

Frerichs I. Electrical impedance tomography (EIT) in applications related to lung and ventilation: a review of experimental and clinical activities. Physiological Measurement 2000; 21:R1.

Fuks LF, Cheney M, Isaacson D, Gisser DG, Newell J. Detection and imaging of electric conductivity and permittivity at low frequency. Biomedical Engineering, IEEE Transactions 1991; 38(11):1106-1110.

Gagnon H, Cousineau M, Adler A, Hartinger A. A resistive mesh phantom for assessing the performance of EIT systems. Biomedical Engineering 2010; 57(9):2257-2266.

Geddes L, Baker L. The specific resistance of biological material—a compendium of data for the biomedical engineer and physiologist. Medical and Biological Engineering and Computing 1967; 5(3):271-293.

Geselowitz DB. An application of electrocardiographic lead theory to impedance plethysmography. IEEE Trans. Biomed. Eng. 1971; 18:38-41.

Ghahary A, Webster JG. Electrical safety for an electrical impedance tomograph, Engineering in Medicine and Biology Society. Images of the Twenty-First Century., Proceedings of the Annual International Conference of the IEEE Engineering 1990; 2:461-462.

Gisser D, Isaacson D, Newell J. Electric current computed tomography and eigenvalues. SIAM Journal on Applied Mathematics 1990; 50(6):1623-1634.

Goharian M. New hardware and software design for electrical impedance tomography. McMaster University 2007.

Golub GH, Reinsch C. Handbook series linear algebra: singular value decomposition and least squares solutions. Numer. Math. 1970; 14:403-420.

Gorodnitsky IF, Rao BD. Sparse signal reconstruction from limited data using FOCUSS: A re-weighted minimum norm algorithm. IEEE Sig. Proc. 1997; 45(3):600-616.

Graham BM, Adler A. Electrode placement configurations for 3D EIT. Physiol Meas. 2007; 28(7):S29-44.

Hadded W, Chang J. Rosenbury T, Dallum G, Welsch P, Scott D, Duarte D, Acevedo V. Microwave Hematoma Detector for the Rapid Assessment of Head Injuries 2000.

Halter R, Hartov A, Paulsen KD. Design and implementation of a high frequency electrical impedance tomography system. Physiological Measurement 2004; 25:379.

Hansen PC. The truncated SVD as a method for regularization. BIT 1987; 27:543-553.

Hansen P, O'Leary D. The use of the L-curve in the regularization of discrete ill-posed problems. SIAM Journal of Science and Computing 1993;14(6):1487–503.

Hartov A, Mazzarese RA, Reiss FR, Kerner TE, Osterman KS, Williams DB, Paulsen KD. A multichannel continuously selectable multifrequency electrical impedance spectroscopy measurement system. Biomedical Engineering, IEEE Transactions 2000; 47(1):49-58.

Hartov A, Demidenko E, Soni N, Markova M, Paulsen K. Using voltage sources as current drivers for electrical impedance tomography. Measurement Science and Technology 2002; 13:1425.

Heikkinen L, Kourunen J, Savolainen T, Vauhkonen P, Kaipio J, Vauhkonen M. Real time three-dimensional electrical impedance tomography applied in multiphase flow imaging. Measurement Science and Technology 2006; 17:2083.

Henderson RP, Webster JG. An impedance camera for spatially specific measurements of the thorax. Biomedical Engineering, IEEE Transactions 1978; (3):250-254.

Holder D, Temple A. Effectiveness of the Sheffield EIT system in distinguishing patients with pulmonary pathology from a series of normal subjects. Clinical and physiological applications of electrical impedance tomography 1993, pp. 277-298.

Holder D. Electrical impedance tomography methods, history and applications. UK: IOP Publishing 2005.

Hua P, Webster J, Tompkins W. A regularised electrical impedance tomography reconstruction algorithm. Clinical Physics and Physiological Measurement 1988; 9:137.

Hua P, Woo EJ, Webster JG, Tompkins WJ. Iterative reconstruction methods using regularization and optimal current patterns in electrical impedance tomography. Medical Imaging, IEEE Transactions 1991; 10(4), pp. 621-628.

Hua P, Woo EJ, Webster JG, Tompkins WJ. Using compound electrodes in electrical impedance tomography. Biomedical Engineering, IEEE Transactions 1993; 40(1):29-34.

Ijaz UZ, Khambampati AK, Lee JS, Kim S, Kim KY. Nonstationary phase boundary estimation in electrical impedance tomography using unscented Kalman filter. Journal of Computational Physics 2008; 227(15):7089-7112.

Isaacson D. Distinguishability of conductivities by electric current computed tomography. Medical Imaging, IEEE Transactions 1986; 5(2):91-95.

Kaipio JP, Kolehmainen V, Somersalo E, Vauhkonen M. Statistical inversion and Monte Carlo sampling methods in electrical impedance tomography. Inverse problems 2000; 16:1487.

Kallman JS, Berryman JG. Weighted least-squares criteria for electrical impedance tomography. Medical Imaging, IEEE Transactions 1992; 11(2):284-292.

Kandadai M, Raymond J, Shaw G. Comparison of electrical conductivities of various brain phantom gels: Developing a 'brain gel model'. Materials Science and Engineering C 2012; 32:2664-2667.

Kandel ER, Schwartz JH, Jessell TM, Mack S, Dodd J. Principles of neural science. Elsevier New York 1991.

Kao TJ, Isaacson D, Newell JC, Saulnier GJ. A 3D reconstruction algorithm for EIT using a handheld probe for breast cancer detection. Physiol. Meas. 2006; 27:S1-S11.

Kerner TE, Paulsen KD, Hartov A, Soho SK, Poplack SP. Electrical impedance spectroscopy of the breast: clinical imaging results in 26 subjects. Medical Imaging, IEEE Transactions 2002; 21(6):638-645.

Keshtkar A, Keshtkar A. Measured and modelled electrical bio-impedance inside the human normal and malignant bladder epithelium. International Journal of Biomedical Engineering and Technology 2007; 1(2):127-133.

Kohn RV, McKenney A. Numerical implementation of a variational method for electrical impedance tomography. Inverse Problems 1990; 6:389.

Lauterbur PC. Image formation by induced local interactions: examples employing nuclear magnetic resonance. Nature 1973; 242(5394):190-191.

Lee JW, Oh TI, Paek SM, Lee JS, Woo EJ. Precision constant current source for electrical impedance tomography, Engineering in Medicine and Biology Society, 2003. Proceedings of the 25th Annual International Conference of the IEEE 2003; 2:1066-1069.

Lionheart W. EIT reconstruction algorithms: pitfalls, challenges and recent developments. Physiological Measurement 2004; 25:125.

Lionheart W, Polydorides N, Borsic A. The reconstruction problem. Electrical Impedance Tomography: Methods, History and Applications, IOP publishing 2005, pp. 3–63.

Liston A, Bayford R, Holder D. The effect of layers in imaging brain function using electrical impedance tomography. Physiological Measurement, 2004; 25:143-58.

Liu P, Griffiths H. Limitations to the sensitivity of EIT in monitoring tissue temperature in hyperthermia. Clinical and Physiological Applications of Electrical Impedance Tomography 1993, pp. 211-217.

Liu N, Saulnier G, Newell J. A multichannel synthesizer and voltmeter for electrical impedance tomography. Engineering in Medicine and Biology Society Proceedings of the 25th Annual International Conference of the IEEE 2003; 4:3110-3113.

Malmivuo J, Plonsey R. Bioelectromagnetism: principles and applications of bioelectric and biomagnetic fields, Oxford Uni Press 1995.

McArdle FJ, Brown BH, Pearse RG, Barber DC. The effect of the skull of low-birthweight neonates on applied potential tomography imaging of centralised resistivity changes. Clinical Physics and Physiological Measurement, November 1988; 9(4A):55.

McEwan A, Romsauerova A, Yerworth R, Horesh L, Bayford R, Holder D. Design and calibration of a compact multi-frequency EIT system for acute stroke imaging. Physiological Measurement 2006; 27:S199.

Meeson S, Killingback A, Blott B. The dependence of EIT images on the assumed initial conductivity distribution: a study of pelvic imaging. Physics in Medicine and Biology 1995; 40:643.

Metherall P, Barber D, Smallwood R, Brown B. Three dimensional electrical impedance tomography. Nature 1996; 380(6574):509-512.

Miller CE, Henriquez CS. Finite element analysis of bioelectric phenomena. Critical Reviews in Biomedical Engineering 1990; 18(3):207-233.

Molinari M, Cox S, Blott B, Daniell G. Efficient non-linear 3D electrical tomography reconstruction, Proceedings of the 2nd World Congress on Industrial Process Tomography 2001, pp. 424-432.

Moore K, Dalley A, Agur A. Clinically Oriented Anatomy. Wolters Kluwer Health/Lippincott Williams & Wilkins 2010:876-77.

Mueller JL, Isaacson D, Newell JC. A reconstruction algorithm for electrical impedance tomography data collected on rectangular electrode arrays. Biomedical Engineering, IEEE Transactions 1999; 46(11):1379-1386.

Mueller JL, Siltanen S, Isaacson D. A direct reconstruction algorithm for electrical impedance tomography. Medical Imaging, IEEE Transactions 2002; 21(6):555-559.

Murai T, Kagawa Y. Electrical Impedance Computed Tomography Based on a Finite Element Model. IEEE Trans. Biomed. Engr 1985, pp. 177-184.

Murphy D, Burton P, Coombs R, Tarassenko L, Rolfe P. Impedance imaging in the newborn. Clinical Physics and Physiological Measurement 1987; 8:131.

Murphy S, York T. Electrical impedance tomography with non-stationary electrodes. Measurement Science and Technology 2006; 17:3042.

Nachman AI. Global uniqueness for a two-dimensional inverse boundary value problem. The Annals of Mathematics 1996; 143(1):71-96.

Newell J, Isaacson D, Cheney M, Saulnier G, Gisser D, Goble J, Cook R, Edic P. Impedance images of the chest, Engineering in Medicine and Biology Society, 1988. Proceedings of the Annual International Conference of the IEEE 1992, pp. 1752-1753.

Nobes DC. Troubled waters: Environmental applications of electrical and electromagnetic methods. Surveys in Geophysics 1996;17(4):393-454.

Oh S, Tang T, Tucker A, Sadleir R. Normalization of a spatially variant image reconstruction problem in electrical impedance tomography using system blurring properties. Physiological Measurement 2009; 30(3):275–89.

Oh S. Compensation of shape change artifacts and spatially-variant image reconstruction problems in electrical impedance tomography, University of Florida, 2009.

OhioHealth. Types of Brain Injury - Health Information Translations. Developed through a partnership of The Ohio State University Medical Center, Mount Carmel Health and OhioHealth, Columbus, Ohio 2005.

Oostendorp T, Delbeke J, Stegeman D. The conductivity of the human skull: results of in vivo and in vitro measurements. IEEE Trans. Biomed. Engr. 2000; 47:1487-1492.

Patel H, Bouamra O, Woodford M, King A, Yates D, Lecky F, On behalf of theTrauma Audit and Research Network. Trends in head injury outcome from 1989to 2003 and the effect of neurosurgical care: an observational study. Lancet 2005; 366(9496):1538–44.

Paulson K, Breckon W, Pidcock M. Electrode modelling in electrical impedance tomography. SIAM Journal on Applied Mathematics 1992; 52(4), pp. 1012-1022.

Pidcock M, Kuzuoglu M, Leblebicioglu K. Analytic and semi-analytic solutions in electrical impedance tomography. I. Two-dimensional problems. Physiological Measurement 1995a; 16:77.

Pidcock M, Kuzuoglu M, Leblebicioglu K. Analytic and semi-analytic solutions in electrical impedance tomography. II. Three-dimensional problems. Physiological Measurement 1995b; 16:91.

Polydorides N, McCann H. Electrode configurations for improved spatial resolution in electrical impedance tomography. Measurement Science and Technology, 2002; 13:1862.

Rafiei Naeini M. Low-noise measurement techniques for brain function imaging by electrical impedance tomography, University of Manchester, School of Electrical and Electronic Engineering, 2008.

Romsauerova A, McEwan A, Horesh L, Yerworth R, Bayford R, Holder DS. Multi-frequency electrical impedance tomography (EIT) of the adult human head: initial findings in brain tumours, arteriovenous malformations and chronic stroke, development of an analysis method and calibration. Physiological Measurement 2006; 27:S147.

Ross AS. An adaptive current tomograph for breast cancer detection, Rensselaer Polytechnic Institute, Troy, NY, USA, 2003.

Sadleir R, Fox R. Quantification of blood volume by electrical impedance tomography using a tissue equivalent phantom. Physiological Measurement 1998; 19:501–16.

Sadleir R, Fox RA. Detection and quantification of intraperitoneal fluid using electrical impedance tomography. Biomedical Engineering, IEEE Transactions 2001; 48(4):484-491.

Sadleir R, Zhang S, Tucker A, Oh S. Imaging and quantification of anomaly volume using an eight-electrode 'hemiarray' EIT reconstruction method. Physiological Measurement 2008; 29:913-27.

Sadleir R, Tang T. Electrode configurations for detection of intraventricular haemorrhage in the premature neonate. Physiological Measurement 2009; 30:63.

Sansen W, Geeraerts B, Van Petegem W, Dehaene W, Steyaert M. Voltage versus current driven high frequency EIT systems. Biomedical Engineering Days, Proceedings of the International IEEE 1992, pp. 102-106.

Saulnier G, Blue R, Newell J, Isaacson D, Edic P. Electrical impedance tomography. Signal Processing Magazine IEEE 2001; 18(6):31-43.

Saulnier GJ. EIT instrumentation. Electrical Impedance Tomography: Methods, History and Applications, IOP publishing 2005, pp. 65-104.

Seagar AD. Probing with low frequency electric current, University of Canterbury, Christchurch, Newzeland, 1983.

Seppanen A, Vauhkonen M, Somersalo E, Kaipio J. State space models in process tomography—approximation of state noise covariance. Inverse Problems in Science and Engineering 2001a; 9(5):561-585.

Seppanen A, Vauhkonen M, Vauhkonen P, Somersalo E, Kaipio J. State estimation with fluid dynamical evolution models in process tomography-an application to impedance tomography. Inverse Problems 2001b; 17:467.

Sha L, Ward ER, Stroy B. A review of dielectric properties of normal and malignant breast tissue, Proceedings IEEE 2002, pp. 457-462.

Sharifi M, Young B. 3-Dimensional Spatial Monitoring of tanks for the Milk Processing Industry using Electrical Resistance Tomography. Journal of Food Engineering 2011.

Siltanen S, Mueller J, Isaacson D. An implementation of the reconstruction algorithm of A Nachman for the 2D inverse conductivity problem. Inverse Problems 2000; 16:681.

Smallwood R, Nour S, Mangnali Y, Smythe A, Holder D. Impedance imaging and gastric motility. Clinical and Physiological Applications of Electrical Impedance Tomography 1993, pp. 145–153.

Smith R, Freeston I, Brown B, Sinton A. Design of a phase-sensitive detector to maximize signal-to-noise ratio in the presence of Gaussian wideband noise. Measurement Science and Technology 1992; 3:1054.

Smith R, Freeston I, Brown B. A real-time electrical impedance tomography system for clinical use-design and preliminary results. Biomedical Engineering, IEEE Transactions 1995; 42(2):133-140.

Somersalo E, Cheney M, Isaacson D, Isaacson E. Layer stripping: a direct numerical method for impedance imaging. Inverse Problems 1991; 7:899.

Somersalo E, Cheney M, Isaacson D. Existence and uniqueness for electrode models for electric current computed tomography. SIAM Journal on Applied Mathematics 1992; 52(4):1023-1040.

Stefanesco S, Schlumberger C, Schlumberger M. Sur la distribution électrique potentielle autour d'une prise de terre ponctuelle dans un terrain à couches horizontales, homogènes et isotropes 1930.

Stoy RD, Foster KR, Schwan H. Dielectric properties of mammalian tissues from 0.1 to 100 MHz; a summary of recent data. Physics in Medicine and Biology 1982; 27:501.

Rust BW. Truncating the Singular Value Decomposition for Ill-posed Problems. Technical report, National Institute of Standards and Technology, U.S. Dept. of Commerce, 1998. Tech. Report NISTIR 6131.

Taktak A, Record P, Gadd R, Rolfe P. Data recovery from reduced electrode connection in electrical impedance t omography. Med Eng Phys 1996; 18(6):519-522.

Tang M, Wang W, Wheeler J, Mccormick M, Dong X. The number of electrodes and basis functions in EIT image reconstruction. Physiological Measurement 2002; 23:129.

Tang T, Oh S, Sadleir R. A robust current pattern for the detection of intraventricular hemorrhage in neonates using electrical impedance tomography. Ann Biomed Eng 2010; 38(8):2733-47.

Tehrani JN, Anderson C, Jin C, Schaik A, Holder D, McEwan A. Feasibility of electrical impedance tomography in haemorrhagic stroke treatment using adaptive mesh, Journal of Physics: Conference Series 2010, IOP Publishing, pp. 012065.

Thomas D, Siddall-Allum J, Sutherland I, Beard R. Correction of the non-uniform spatial sensitivity of electrical impedance tomography images. Physiological Measurement 1994; 15:A147.

Tidswell T, Gibson A, Bayford RH, HOLDER DS. Three-dimensional electrical impedance tomography of human brain activity. NeuroImage 2001; 13(2): pp. 283-294.

Tossavainen OP, Vauhkonen M, Heikkinen L, Savolainen T. Estimating shapes and free surfaces with electrical impedance tomography. Measurement Science and Technology 2004; 15:1402.

Treasure T. Trauma who cares? A report of the National Confidential Enquiryin to Patient Outcome and Death (NCEPOD); 2007. p. 19.

Tucker AS, Ross E, Paugh-Miller J, Sadleir RJ. In-vivo detection of bleeding simulated in a Peritoneal dialysis model using a hemiarray EIT configuration, Journal of Physics: Conference Series 2010, IOP Publishing 2010, pp. 012063.

Tucker A, Ross E, Paugh-Miller J, Sadleir R. In vivo quantification of accumulating abdominal fluid using an electrical impedance tomography hemiarray. Physiological Measurement 2011; 32(2):151-65.

Vauhkonen M. Electrical Impedance Tomography and Prior Information, Department of Applied Physics. Kuopio University, 1997.

Vauhkonen PJ, Vauhkonen M. Savolainen T, Kaipio JP. Three-dimensional electrical impedance tomography based on the complete electrode model. Biomedical Engineering, IEEE Transactions 1999; 46(9):1150-1160.

Vilhunen T, Heikkinen L, Savolainen T, Vauhkonen P, Lappalainen R, Kaipio J, Vauhkonen M. Detection of faults in resistive coatings with an impedance-tomography-related approach. Measurement Science and Technology 2002; 13:865.

Voss M, Knottenbelt J, Peden M. Patients who reattend after head injury: a high risk group. BMJ 1995; 311(7017):1395-98.

Walker D, Brown B, Hose D, Smallwood R. Modelling the electrical impedivity of normal and premalignant cervical tissue. Electronics Letters 2000; 36(19):1603-1604.

Wardlaw J, Lewis S, Sandercock P, Ricci S, Spizzichino L, the I. Why do Italian stroke patients receive CT scans earlier than UK patients? Postgrad Med J. 1999; 75(879):18–21.

Wexler A, Fry B, Neuman M. Impedance-computed tomography algorithm and system. Applied Optics 1985; 24(23):3985-3992.

Wilson A, Milnes P, Waterworth A, Smallwood R, Brown B. Mk3. 5: a modular, multi-frequency successor to the Mk3a EIS/EIT system. Physiological Measurement 2001; 22:49.

Wi H, Woo EJ. Design of KHU mark2 multi-frequency EIT System. Proc. Int. Conf. on Biomedical Applications of Electrical Impedance Tomography (Manchester) 2009.

Woo EJ, Hua P, Webster JG, Tompkins WJ. A robust image reconstruction algoruthm and its prallel implementation in electrical impedance tomography. Medical Imaging, IEEE Transactions 1993; 12(2):137-146.

Wort PM, Church PM, Gagnon S. Preliminary assessment of electrical impedance tomography technology to detect minelike objects, Proceedings of SPIE 1999:895.

Wysoki M, Nassar C, Koenigsberg R, Novelline R, Faro S, Faerber E. Head trauma: CT scan interpretation by radiology residents versus staff radiologists. Radiology 1998; 208(1):125.

Xu C., Dong X, Fu F, Shuai W, Liu X, Zhang C. A Novel Image Monitoring Software System of Electrical Impedance Tomography for Internal Hemorrhage, World Congress on Medical Physics and Biomedical Engineering Springer 2007, pp. 3882-3885.

Xu C, Wang L, Shi X, You F, Fu F, Liu R, Dai M, Zhao Z, Gao G, Dong X. Real-time Imaging and Detection of Intracranial Haemorrhage by Electrical Impedance Tomography in a Piglet Model. The Journal of international medical research 2010; 38(5):1596-1604.

Xu C, Dai M et al. An optimized strategy for real-time haemorrhage monitoring with electrical impedance tomography. Physiological Measurement 2011; 32(5):585-98.

Yasin M, Böhm S, Gaggero PO, Adler A. Evaluation of EIT system performance. Physiological Measurement 2011; 32(7):851-865.

Yates D. Head Injury: triage, assessment, investigation and early management of head injury in infants, children and adults; Methods, Evidence & Guidance. The Royal College of Surgeons of England, London: National Collaborating Centre for Acute Care 2007.

Yerworth RJ, Bayford R, Cusick G, Conway M, Holder DS. Design and performance of the UCLH Mark 1b 64 channel electrical impedance tomography (EIT) system, optimized for imaging brain function. Physiological Measurement 2002; 23:149.

Yerworth RJ, Bayford R, Brown B, Milnes P, Conway M, Holder DS. Electrical impedance tomography spectroscopy (EITS) for human head imaging. Physiological Measurement 2003; 24:477.

Yvert B, Bertrand O, Thvenet M, Echallier J, Pernier J. A systematic evaluation of the spherical model accuracy in EEG dipole localization. Electroencephalogr Clin Neurophysiol 1997; 102:452–59.

Zadehkoochak M, Blott BH, Hames TK, George RF. Spectral expansion analysis in electrical impedance tomography. J. Phys. D: Appl. Phys. 1991; 24:1911-1916.

Zhang J, Patterson RP. EIT images of ventilation: what contributes to the resistivity changes? Physiol. Meas. 2005; 26:S81–S92.

Zhu Q, Lionheart W, Lidgey F, McLeod C, Paulson K, Pidcock M. An adaptive current tomography using voltage sources. Biomedical Engineering, IEEE Transactions 1993; 40(2):163-168.

Zhu Q, McLeod C, Denyer C, Lidgey F, Lionheart W. Development of a real-time adaptive current tomography. Physiological Measurement 1994; 15:A37.

Zlochiver S, Arad M, Radai M, Barak-Shinar D, Krief H, Engelman T, Ben-Yehuda R, Adunsky A, Abboud S. A portable bio-impedance system for monitoring lung resistivity. Med Eng Phys 2007; 29(1):93-100.

**Publications**

*Medical Engineering & Physics Journal*

G Model
IJBE-2567; No. of Pages 8
ARTICLE IN PRESS

Medical Engineering & Physics xxx (2014) xxx–xxx

Contents lists available at ScienceDirect

Medical Engineering & Physics

journal homepage: www.elsevier.com/locate/medengphy

# *In vitro* localisation of intracranial haematoma using electrical impedance tomography semi-array

S. Bentolhoda Ayati*, Kaddour Bouazza-Marouf, David Kerr

*Wolfson School of Mechanical and Manufacturing Engineering, Loughborough University, Loughborough LE11 3TU, United Kingdom*

ARTICLE INFO

*Article history:*
Received 14 August 2013
Received in revised form 7 September 2014
Accepted 1 October 2014

*Keywords:*
Electrical impedance tomography
Intracranial haematoma
Localisation
Size estimation

ABSTRACT

Electrical Impedance Tomography is a non-invasive and portable method that has good potential as an alternative to the conventional modalities for early detection of intracranial haematomas in high risk patients. Early diagnosis can reduce treatment delays and most significantly can impact patient outcomes. Two eight-electrode layouts, a standard ring full array (FA) and a semi-array (SA), were investigated for their ability to detect, localise and quantify simulated intracranial haematomas *in vitro* on ovine models for the purpose of early diagnosis. SA layout speeds up electrode application and avoids the need to move and lift the patient's head. Haematomas were simulated using gel samples with the same conductivity as blood. Both layouts, FA and SA, could detect the presence of haematomas at any location within the skull. The mean of the relative radial position error with respect to the brain radius was 7% for FA and 6% for SA, for haematomas close to the electrodes, and 11% for SA for haematomas far from the electrodes at the back of the head. Size estimation was not as good; the worst size estimation error for FA being around 30% while the best for SA was 50% for simulated haematomas close to the electrodes.


## 1. Introduction

Head injury is the main cause of death among young adults and children and may become the third greatest global death cause by 2020, due to the substantial number of associated deaths and cases of disability [1]. The UK National Confidential Enquiry into Patient, Outcome and Death (NCEPOD) reported that more than half of the patients that required neurosurgical advice were taken to hospitals with no on-site neurosurgical provision and only 14% of patients requiring secondary transfer to a neurosurgical centre had access to neurosurgical treatment within four hours [2]. Patients treated in a non-neurosurgical centre had a 26% increase in mortality and a 2.15-fold increase in the risk of death compared to patients treated at a neurosurgical centre [3]. First responders need more information on the neurological condition of their patient. In particular, they require information on potentially evolving haematomas which may need prompt and rapid action. This information is vital for proper triage, and to ensure the best possible decisions are made for the patient's welfare.

Haematomas expand and increase the intracranial pressure on the brain. A growing haematoma will cause severe and even permanent damage to the delicate tissue of the brain, morbidity, and eventual death of the patient [4]. Haematomas are classified based on their location. Epidural haematomas form between the skull and the dura-mater. They occur because of trauma and a tear in an artery, often to the temple, where the middle meningeal artery is located. Subdural haematomas occur because of trauma and a tear in veins beneath the dura-mater in the brain. A subdural haematoma is very close to the brain and may cause a serious problem. Intracerebral Haematomas, occur within the brain parenchyma itself due to bleeding from trauma or uncontrolled high blood pressure. The development of the haematoma from benign to symptomatic can be sudden, and a patient can change from lucid to a state of rapid neurological deterioration over a very short-period of time [5]. It is well known that the time from injury-to-diagnosis-to-treatment is a key factor in patient outcome, and must be minimised for a patient to make a full recovery.

Electrical Impedance Tomography (EIT) reconstructs cross-sectional images of the conductivity distribution of the internal components of the brain, based on non-invasive voltage measurements through an array of electrodes on its boundary. Blood has a high electrical conductivity contrast relative to other cranial tissues and thus its appearance can be detected and monitored using EIT [6].

Head injuries and haematoma are often accompanied by other traumatic injuries that can be aggravated by unnecessary movement, including the placing of electrodes around the head. Therefore, it is desirable to develop methods that do not involve

* Corresponding author. Tel.: +44 1509 227566.
*E-mail address:* s.b.ayati@lboro.ac.uk (S.B. Ayati).

http://dx.doi.org/10.1016/j.medengphy.2014.10.001
1350-4533/

Please cite this article in press as: Ayati SB, et al. *In vitro* localisation of intracranial haematoma using electrical impedance tomography semi-array. Med Eng Phys (2014), http://dx.doi.org/10.1016/j.medengphy.2014.10.001

applying electrodes at the back of the head. Placement of the electrodes on the anterior of the head avoids exacerbating existing injuries and removes the need to lift the patient. However, good localisation of a haematoma is hampered by eliminating the electrodes at the back of the head. To conquer the quality reduction of the images and to minimise these errors, several reconstruction strategies have been proposed previously [7]. The purpose of this study is to evaluate the performance of EIT, using optimised eight-electrode configurations. This includes an investigation of the different configurations to evaluate their ability to detect and localise anomalies similar to haematoma in the human head, for the purpose of early diagnosis. Using the minimum number of electrodes is always desirable in clinical applications since it may also speed up the electrode setup process in emergency cases. The proposed electrode configurations are evaluated for the detection and localisation of simulated haematomas *in vitro* using an ovine model. Intracerebral haematoma detection has been considered in previous studies using EIT [8]. Epidural and subdural haematomas are considered in this study since their location can represent the worst case with respect to the SA configuration.

## 2. Methods

In EIT, the process is divided into a forward problem and an inverse problem. To reconstruct the conductivity distribution images through the EIT inverse problem the forward problem on a prototype model has to be solved. For general cases, a numerical method such as finite element analysis is required to implement the model and solve the forward problem. Initially, a simple forward model based on a circular shape with a homogenous conductivity distribution may be used to calculate the sensitivity matrices [9]. Better results are obtained if the forward model exactly matches the object in terms of internal conductivity distribution and external geometry. In principle, an incorrect estimate of boundary shape will introduce artefacts and reduce the quality of the reconstructed images. However, more realistic models need to be used carefully since inaccurate prior information may yield images worse than those reconstructed with a simple forward model [10]. In practice, it is difficult to specify an accurate model for an individual head because head geometry varies from patient to patient.

### 2.1. Full and semi-array electrode layouts

In this study, two eight-electrode layout strategies were investigated *in vitro* and compared in terms of their ability to detect and localise intracranial haematomas. The first one was a standard ring layout or full-array (Fig. 1a), where the eight electrodes were placed equally spaced around the head. The second layout was a novel electrode configuration applied to the front of the head. This so-called semi-array (SA) configuration consisted of a set of eight electrodes separated by angle of 36° in a semi-circular profile (Fig. 1b). This layout simplifies the application of the electrodes and avoids the need to move and lift the patient's head. An adjacent current pattern was applied to both layouts, wherein current was applied in turn to pairs of adjacent electrodes, and voltages were measured across other pairs of adjacent electrodes. In the SA, use of this scheme included measurements and current applications between the last-numbered and first electrodes positioned at the end of the array and approximately 108° apart. Both layouts involved 8 current positions and a total of 40 voltage measurements. Experiments were performed on an ovine model using both layouts and the results obtained from the SA layout were compared with data from the standard eight-electrode full-array (FA) layout to determine the ability of the SA to detect and localise intracranial haematomas. Restricting electrodes at the back of the head limits the resolution and thus inferior localisation of the anomaly can be expected, compared to that of the FA layout.

### 2.2. Data generation

*In vitro* ovine experiments were performed in conjunction with an eight-electrode EIT system to determine the potential of this configuration to provide good results *in vivo*. To obtain the experimental measurements, a prototype 16-electrode EIT system known as the "EITLboro" rig was used. The structure of this device is presented in Fig. 2. The system is controlled by a microcontroller connected to a PC through a serial port. A graphical user interface was developed using Visual Basic (VB). A sinusoidal current generated by a constant current source was injected through one pair of adjacent electrodes and the corresponding boundary potentials were measured over pairs of the remainder of the neighbouring electrodes using a multiplexer. The input pair of electrodes was switched over all adjacent electrodes pairs and the measurement procedure was repeated for all possible adjacent pairs. The performance of this system was previously evaluated using phantom experiments [11]. The results showed a high level of accuracy with an average accuracy of 93.5% for the system. This EIT system has 16 channels and operates with a temporal resolution of 100 frames per second. For this experiment, a constant current of 1 mA at a frequency of 50 kHz and 8 electrodes were chosen.

### 2.3. Experimental setup

Five freshly skinned sheep heads (labelled as A, B, C, D and E) were obtained from a local butcher. The locations of the 8 electrodes for each layout were marked in different colours on the skull. Equal distance between electrodes has been considered around the head for the FA and in the anterior of the head for the SA according to the perimeter measurement of each head. Eight Ag/AgCl disk electrodes (Unimed Electrode Supplies Ltd) were fastened to the skull using conductive paste (Unimed Electrode Supplies Ltd) for the FA layout (Fig. 3a). These electrodes were also soldered to the wires to connect to the skull on the interior of the head using conductive paste for the SA layout (Fig. 3b).

A saline solution with the same conductivity as blood (0.67 S/m) was made with a concentration of 0.33% [weight/volume] of sodium chloride in water. In order to localise haematoma *in vitro*, the position of the anomaly has to be known with a good estimation. To simulate a more realistic haematoma in an accurate location, the saline solution was transformed to gel. The saline solution was stirred using a magnetic stir bar at a temperature of 70 °C while agar powder was added to achieve the desired gel concentration (1.9% by weight). Then the solution was poured into a 1 cm diameter tube and allowed to cool at room temperature. The gel sample was removed from the tube and cut into one tenth of the diameter of each brain to simulate pockets of blood. The conductivity of the gel sample was measured and found to be the same as the conductivity of the saline solution. A 2-terminal measurement was performed to measure the gel conductivity and the same gel samples were used on each subject. An AC voltage was applied across the gel at a frequency of 50 kHz at room temperature using a waveform function generator connected in series with a digital multimeter to measure the AC current and voltage across the gel. The circuit was calibrated with multiple known resistances, and the conductivity measurements were compared to published data [12].

All the skulls were cut in approximately half using a bone saw. The top half of the skull was carefully removed and the brain was exposed in order to position the anomalies (Fig. 4). Gel samples were placed superficially on top of the brain lobe and the top half of the skull was replaced. The anomaly was located in different positions along the $\alpha$, $\alpha\beta$, $\beta$, $\beta\gamma$ and $\gamma$ axes (at $\theta = 0°, 45°, 90°, 135°$

Please cite this article in press as: Ayati SB, et al. *In vitro* localisation of intracranial haematoma using electrical impedance tomography semi-array. Med Eng Phys (2014), http://dx.doi.org/10.1016/j.medengphy.2014.10.001

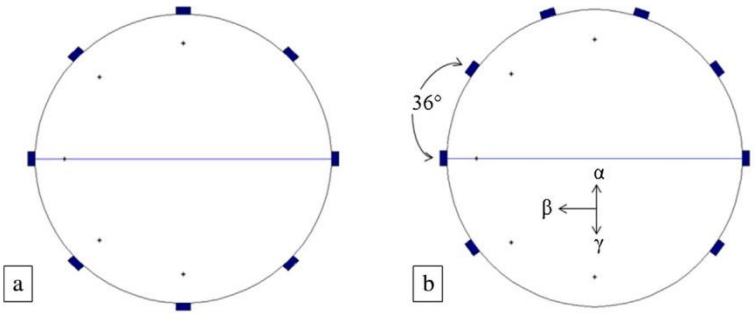


**Fig. 1.** Electrode positions showing (a) the standard ring layout where the eight electrodes were placed equally spaced around the head, and (b) a novel electrode configuration applied to the front of the head separated by angle of 36° in a semi-circular profile. Stars show the ideal positions of centre of simulated anomalies on sheep's head at relative radius of 0.8 in α, αβ, β, βγ and γ axes directions.

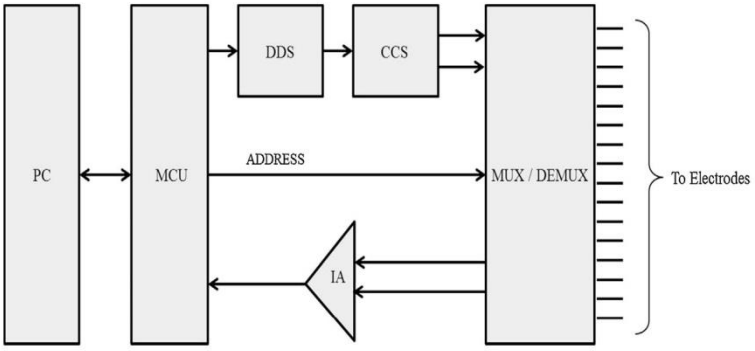


**Fig. 2.** EITLboro architectural overview. This system is based on a microcontroller connected to a PC through a serial port. A graphical user interface was developed using Visual Basic (VB). The Constant Current Source, CCS, generates a constant current fed by a signal generated by the Direct Digital Synthesiser, DDS. The measurements were amplified using an Instrumentation Amplifier (IA) to produce a complete voltage data set.

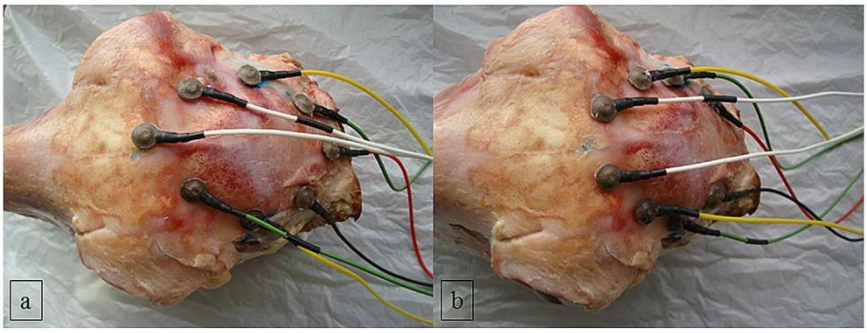


**Fig. 3.** Electrode positions showing (a) eight Ag/AgCl disk electrodes fastened to the skull using conductive paste for full array layout and (b) electrodes connected to the skull on the interior of the head using conductive paste for semi-array layout.

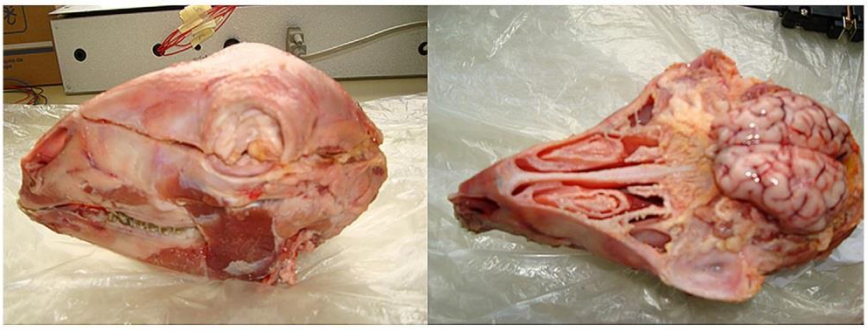

**Fig. 4.** Skulls were cut in approximately half using a bone saw (left). The top half of the skull was carefully removed and the brain was exposed to place the anomalies (right).

Please cite this article in press as: Ayati SB, et al. *In vitro* localisation of intracranial haematoma using electrical impedance tomography semi-array. Med Eng Phys (2014), http://dx.doi.org/10.1016/j.medengphy.2014.10.001

and 180°), with the anomaly centre placed successively at a relative radial displacement of 0.8 from the brain centre. Five locations were considered in total as shown in Fig. 1 and the measurements performed using both layouts for each anomaly to study reconstruction, detection and localisation characteristics. The aim was to study and compare the ability of the SA and FA layouts to detect and localise these anomalies, especially for the SA, and to evaluate the dependency of the results on the distance of the anomaly from the electrodes.

### 2.4. Reconstruction

In this study, EIT difference images were reconstructed based on the assumption that the conductivity changes are small enough. The relationship between the boundary voltage measurement changes and internal conductivity changes can be expressed with a sensitivity matrix ($S$) as in Eq. (1). $S$ was calculated from forward solutions of a two-dimensional disc finite element model with a homogenous conductivity distribution [9].

$$\Delta V = S\Delta\sigma \tag{1}$$

Conductivity changes ($\Delta\sigma$) can be determined by inverting the sensitivity matrix; however, $S$ is ill-conditioned and not square. Since the EIT inverse problem is severely ill-posed and a small amount of noise on boundary measurements, $\Delta V$, can cause a large oscillation for the solution, a regularisation technique was used to reduce this effect by improving the condition of $S$ [6]. The Truncated Singular Value Decomposition (TSVD) method which has previously been identified as a suitable regularisation method [13] was used to regularise the inversion of the sensitivity matrix. The truncation point $k$ needs to be chosen carefully, less than or equal to the rank of the matrix, as it would otherwise produce inaccurate images. The truncation point was chosen depending on the noise level in the voltage measurements and the rank of the sensitivity matrix on inspection of the L-curve of experimental data [14]. The truncation numbers were almost the same for all the datasets. The pseudo-inversion ($S^\dagger$) was achieved using TSVD and images were obtained using Eq. (2).

$$\Delta\sigma = S^\dagger \Delta V \tag{2}$$

In the SA, measurement sensitivity depends strongly on the anomaly location since the electrodes are not placed all over the head. Some reconstructed anomalies located far from the electrodes in the posterior region were almost invisible or erroneous when TSVD reconstruction was used. Therefore, in order to enhance image reconstruction quality and improve anomaly localisation, the sensitivity matrix was weighted with a diagonal matrix composed of a system blurring property, which was directly calculated from the sensitivity matrix [7]. In the Weighted Pseudo-Inverse (WPI) method, reconstruction was weighted with $P$ prior to pseudo-inversion. The entries of a diagonal weighting matrix ($P$) were calculated using Eq. (3) where $ne$ is the total number of elements. The blur matrix ($B$) is dimensionless and can be pre-calculated from the sensitivity matrix $S$ *via* Eq. (4). Then the reconstruction was modified to obtain images using Eq. (5).

$$p_j = \left(\sum_{i=1}^{ne} B_{ij}^2\right)^{-1} \tag{3}$$

$$B = S^\dagger S \tag{4}$$

$$\Delta\sigma = (SP)^\dagger \Delta V \tag{5}$$

### 2.5. Localisation

The position of the anomaly ($x$, $y$) can be estimated from the reconstructed images by averaging the positions of all elements, weighted by their conductivity changes [8] *via* Eqs. (6) and (7):

$$x = \frac{\sum_{ne}^{i=1} \Delta\sigma_i a_i x_i}{\sum_{ne}^{i=1} \Delta\sigma_i a_i} \tag{6}$$

$$y = \frac{\sum_{ne}^{i=1} \Delta\sigma_i a_i y_i}{\sum_{ne}^{i=1} \Delta\sigma_i a_i} \tag{7}$$

The anomaly location ($x$, $y$) is effectively the centre of the reconstructed anomaly. The values $x_i$ and $y_i$ are the coordinates of the centre and $a_i$ is the area of each element. The difference between the actual position of the anomaly and its reconstructed location within the $xy$ plane can be calculated as the absolute location errors (relative radial error, $D_{xy}$) quoted as a fraction of the brain radius, $R$, [8] *via* Eq. (8):

$$D_{xy} = \frac{\sqrt{(\Delta x)^2 + (\Delta y)^2}}{R} \tag{8}$$

### 2.6. Quantification

The anomaly size was assessed with a characteristic parameter, the quantity index (QI), defined in Eq. (9) as an EIT image parameter that correlates with the anomaly size [15]. The quantity index is the sum of conductivity change multiplied by the area of the element over the image area:

$$\mathrm{QI} = \sum_{i=1}^{ne} \Delta\sigma_i a_i \tag{9}$$

where for an element (or pixel) $i$, $\Delta\sigma_i$ is the conductivity change reconstructed in the $i$th element. QI values should be constant since the anomaly sizes are the same during the experiment over all the positions.

## 3. Results

The data for intracranial haematomas in five ovine models were successfully collected with the EITLboro rig and used to reconstruct the images. To improve the SNR of EIT, a sequence of at least 100 frames of data was collected before the anomalies were introduced. These were averaged and used as the reference data set. For each anomaly position, 100 frames of data were collected and averaged as the perturbation data for that anomaly position.

### 3.1. Comparing FA and SA localisation

The simulated haematomas were localised using the reconstructed images. The results of the anomaly localisation in the five ovine models using both FA and SA layouts are presented in Figures 5 and 6 respectively. The position of the simulated haematomas varied as a function of angle from 0° to 180° with 45° increments at relative radial displacement of 0.8 from the brain centre. Locations were normalised to a circular shape with unit diameter. The discrepancy between the actual and reconstructed locations is illustrated by arrows. For illustration, reconstructed images of the anomalies in subject E using FA configuration are shown in Fig. 5 and reconstructed images of the anomalies in subject C using SA configuration are shown in Fig. 6. The simulated anomalies were detected for all the positions using both layouts; however FA results were in general superior to the SA results.

Please cite this article in press as: Ayati SB, et al. *In vitro* localisation of intracranial haematoma using electrical impedance tomography semi-array. Med Eng Phys (2014), http://dx.doi.org/10.1016/j.medengphy.2014.10.001

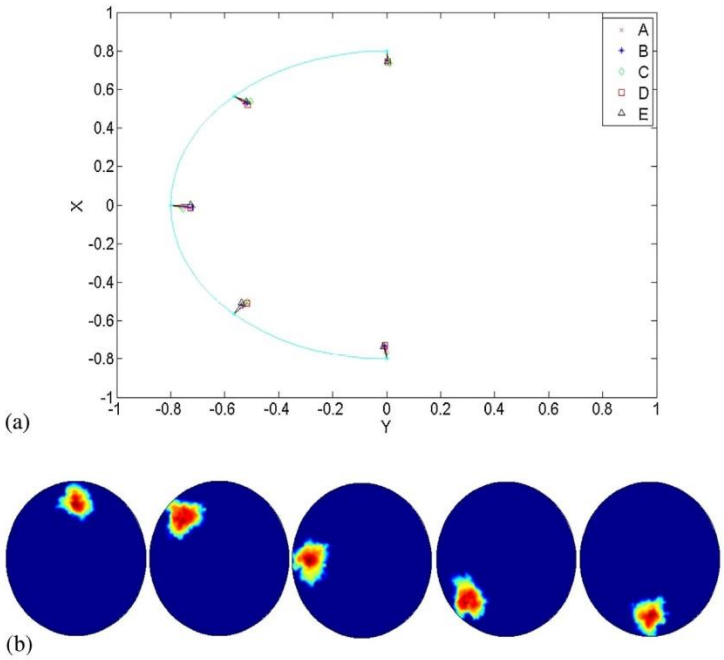


**Fig. 5.** (a) Localisation of the simulated anomalies on five sheep's head (A, B, C, D and E) at various positions using full array (FA) electrode layout. Anomaly positions varied as a function of angle (0°, 45°, 90°, 135° and 180°) at relative radius of 0.8. (b) Reconstructed images of the anomalies in subject E.

Relative radial localisation errors for five ovine models using FA and SA are shown in Figures 7 and 8 respectively. As expected, the SA layout localised simulated anomalies as well as the FA layout apart from the anomalies placed far away from the electrodes. Localisation errors were larger for reconstructions of the anomalies at 135° with the worst value of $D_{xy}$ being 0.3265 using the SA layout, and 0.0828 using the FA layout, both values being with respect to unit radius. The mean and variance of the relative radial errors are presented in Table 1. Both the FA and SA electrode layouts could localise simulated haematomas well, producing a maximum mean

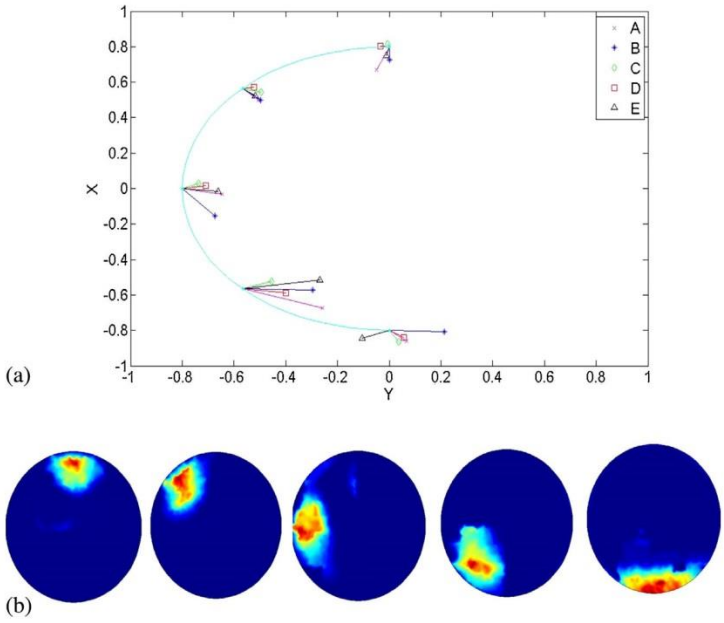


**Fig. 6.** (a) Localisation of the simulated anomalies on five sheep's head (A, B, C, D and E) at various positions using semi-array (SA) electrode layout. Anomaly positions varied as a function of angle (0°, 45°, 90°, 135° and 180°) at relative radius of 0.8. (b) Reconstructed images of the anomalies in subject C.

Please cite this article in press as: Ayati SB, et al. *In vitro* localisation of intracranial haematoma using electrical impedance tomography semi-array. Med Eng Phys (2014), http://dx.doi.org/10.1016/j.medengphy.2014.10.001

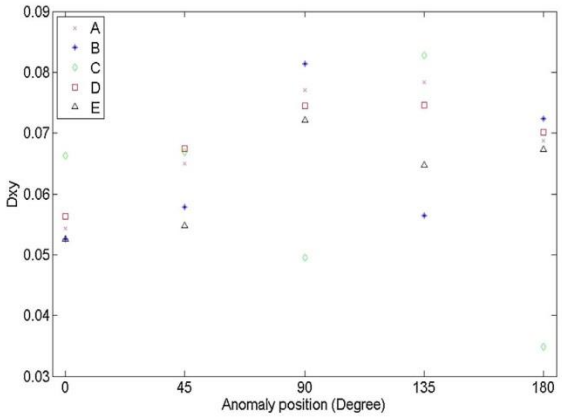


**Fig. 7.** Relative radius localisation errors, $D_{xy}$, of the simulated anomalies on five sheep's head (A, B, C, D and E) at various positions using full array (FA) electrode layout. Anomaly positions varied as a function of angle (0°, 45°, 90°, 135° and 180°) at relative radius of 0.8.

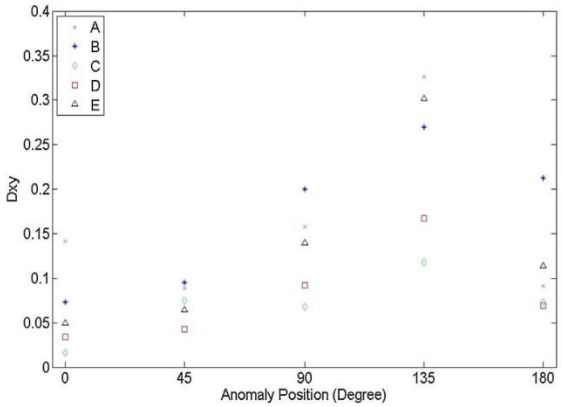


**Fig. 8.** Radius relative localisation errors, $D_{xy}$, of the simulated anomalies on five sheep's head (A, B, C, D and E) at various positions using semi-array (SA) electrode layout. Anomaly positions varied as a function of angle (0°, 45°, 90°, 135° and 180°) at relative radius of 0.8.

relative radial error of 0.0714 and 0.2364 respectively at 135° with respect to the unit radius.

### 3.2. Comparing FA and SA size estimation

The reconstructed images of the simulated haematomas were gathered and post-processed to determine QI values. The ability of the FA and SA layouts to quantify these anomaly sizes was compared to the actual QI. The normalised QI values for five ovine models using the FA electrode layout over the image plane against

**Table 1**
Comparison of mean and variance of radial relative errors using FA and SA for different 1 anomaly positions.

| Anomaly location | FA localisation error | | SA localisation error | |
|---|---|---|---|---|
| | Mean | Variance | Mean | Variance |
| 0° | 0.0564 | $3.2644 \times 10^{-5}$ | 0.0626 | 0.0024 |
| 45° | 0.0624 | $3.2673 \times 10^{-5}$ | 0.0733 | $4.3200 \times 10^{-4}$ |
| 90° | 0.0709 | $1.5502 \times 10^{-4}$ | 0.1312 | 0.0027 |
| 135° | 0.0714 | $1.1429 \times 10^{-4}$ | 0.2364 | 0.0081 |
| 180° | 0.0627 | $2.4588 \times 10^{-4}$ | 0.1118 | 0.0035 |

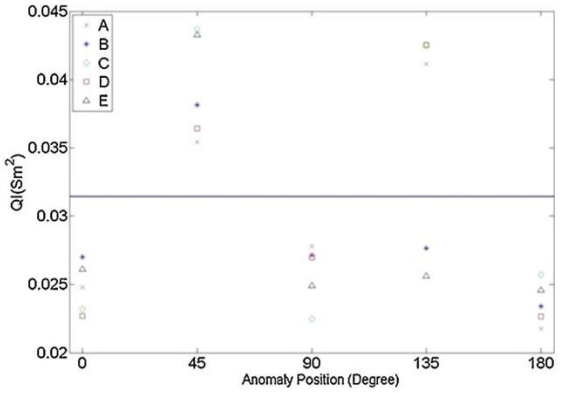


**Fig. 9.** Quantification Indices, QI, of the simulated anomalies on five sheep's head (A, B, C, D and E) at various positions using full array (FA) electrode layout compared with ideal QI. Anomaly positions varied as a function of angle (0°, 45°, 90°, 135° and 180°) at relative radius of 0.8.

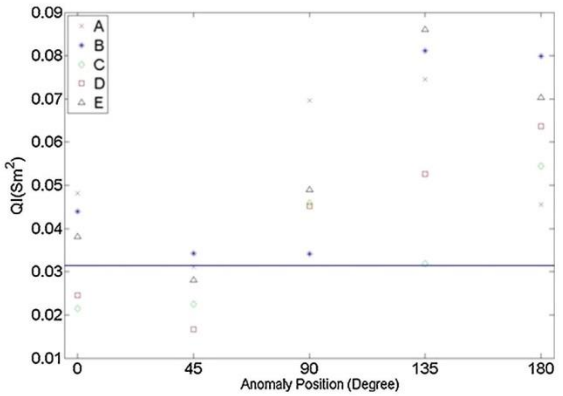


**Fig. 10.** Quantification Indices, QI, of the simulated anomalies on five sheep's head (A, B, C, D and E) at various positions using semi-array (SA) electrode layout compared with ideal QI. Anomaly positions varied as a function of angle (0°, 45°, 90°, 135° and 180°) at relative radius of 0.8.

anomaly position for five angles are shown in Fig. 9. For the SA layout, the same positions of anomalies in directions of α, αβ, β, βγ and γ were used. Normalised QI values from the SA reconstructions of simulated anomalies are shown in Fig. 10. Size estimation results for the FA layout are superior to those for the SA layout. The worst QI error in reconstructions using the FA layout was around 30%. According to the reconstructed images, the size of the simulated anomalies at 0° and 45° (α and αβ) are measured by maximum error of approximately 55% and 50% respectively in the case of the SA electrode layout. For simulated anomalies placed at 90° (β) using the SA layout, although in one case the QI value is large, the worst QI error in the others is about 55%. The SA layout performance to quantify the simulated anomalies at 135° and 180° (βγ and γ) is very poor as in the worst case the anomaly sizes were measured almost three times bigger than their actual size.

## 4. Discussion

### 4.1. Comparison between full array and semi-array layouts

For the first time, animal studies were performed using EIT to detect and localise haematomas within the skull in an ovine model.

Please cite this article in press as: Ayati SB, et al. *In vitro* localisation of intracranial haematoma using electrical impedance tomography semi-array. Med Eng Phys (2014), http://dx.doi.org/10.1016/j.medengphy.2014.10.001

In five sheep heads, haematomas were simulated by placing gel samples with the same conductivity as blood at different positions. Two eight-electrode layouts were applied to compare their ability to localise and quantify the simulated haematomas. An optimised, novel electrode layout named semi-array (SA) was introduced and its performance was evaluated and compared *in vitro* with a conventional full array electrode layout. The FA layout performed well in both localisation and size estimation of the anomalies. We believe that the errors in the FA experiments are due to the presence of random and systematic experimental noise. As expected, the SA layout performed well in detecting and localising anomalies close to the electrodes, but slightly worse for anomalies far away from the electrodes. Reduction of the electrodes at the posterior of the head reduced overall image quality and increased uncertainty in estimations of location and size of the anomalies. Large spatial variance and therefore the variability in size estimates of an anomaly because of the restricted number of electrodes at the posterior of the head are inevitable. We believe that the large size estimation errors may have been caused by the noise-generated artefacts in reconstructions and the electrode positions.

### 4.2. Anomaly size estimation

Although QI values depend on the size of the anomaly, the regularisation method and the sensitivity matrix calculation also affect the size estimation. The FA and SA electrode layouts produce different sensitivities in the region at the back of the head and therefore have different QI accuracy. Large size errors in SA may have been related to the smaller sensitivity at the posterior region of the head, far from the electrodes, combined with measurement noise. However, spatial variation of QI was improved by using blurring properties calculated directly from the sensitivity matrix. The truncation number for each case was chosen based on the noise level in the voltage measurements and the rank of the sensitivity matrix on inspection of the L-curve of experimental data.

### 4.3. Comparing results with earlier studies

Using EIT for clinical applications to detect and image bleeding in an animal model has been proven in previous studies [16,17]. A group based at the University of Florida has applied EIT to detect intra-ventricular haemorrhage (IVH) for neonate applications [8]. In their phantom experimental studies, data were collected by a FA layout with 16 electrodes equally spaced around the head, using adjacent current patterns. Their results showed a maximum radial error of 0.1 and QI error of 30% which is better than our size estimation accuracy. Sadleir et al. [6] introduced a hemi-array electrode layout for the application of abdominal trauma. QI values of their phantom experimental studies showed a variation of around a factor of 4, the maximum being 220%. Hemi-arrays have been used *in vivo* to quantify accumulating abdominal fluid [18] and to monitor lung resistivity by Zlochiver et al. [19]. However, the hemi-array electrode layout failed in our application to detect simulated haematomas using ovine models. We believe that the presence of the skull and the geometry structure of the head may restrict the use of the hemi-array in this application. However, our optimised SA electrode layout has shown its reliability to detect, localise and quantify the simulated haematomas in this application. According to earlier studies [20,21], the quality of the images and consequently the localisation and size errors may be improved by increasing the number of electrodes. However, the objective of this concept is to optimise the number and position of the electrodes in order to speed up the electrode setup process and avoid the need to move and lift the patient's head in emergency cases. We believe that using an eight-electrode configuration is more preferable than using 16 or 32 and that the ensuing results are quite acceptable. Although the use of 2D imaging restricts the $z$ direction localisation, the overall process is faster and the results are reliable enough for a useful application to emergency cases.

### 4.4. Comparing EIT with current modalities

Haematomas are typically diagnosed by neurological assessment in the emergency room followed by a Computed Tomography (CT) scan. CT scanners are not portable and thus diagnosis cannot be made until the patient is delivered to the hospital. Moreover, CT scanning is not always available for 24 hours a day, and in cases of multiple traumas, it may not be possible to scan the patient until they have been adequately stabilised [22]. Although the sensitivity and resolution of Magnetic Resonance Imaging (MRI) is higher than CT, the transporting requirement of ill patients and equipment compatibility restrict use of this method. EIT is a non-invasive, portable, low-cost, operator independent method that has the potential to monitor and measure the progress of internal bleeding. EIT offers a good alternative to the conventional modalities for early detection, localisation and size estimation of haematomas in high risk patients. Early diagnosis can reduce treatment delays, save on costs and waste, and most significantly, positively impact patient outcomes. Treatment delays can thus be mitigated by giving better and earlier information on haematomas at the triage stage.

## 5. Conclusion

This study indicates the feasibility of detection, localisation and size estimation of haematomas *in vitro* with preliminary EIT imaging on ovine models for the purpose of early diagnosis. Two eight-electrode layouts were compared *in vitro* on their ability to detect, localise and quantify simulated haematomas. As expected, the FA layout was found to be more robust than the SA layout, having an overall better quality on localisation and size estimation of the simulated haematomas. Although using the SA configuration reduces the sensitivity and accuracy of quantity estimations, an optimised electrode layout that does not require the patient to be lifted for its application would be very convenient for emergency applications where the required accuracy is not critical.

## Funding

None.

## Ethical approval

Not required.

## Conflict of interest

None declared.

## References

[1] Dinsmore J. Traumatic brain injury: an evidence-based review of management. Contin Educ Anaesth Crit Care Pain 2013. Advance Access.
[2] Treasure T. Trauma who cares? A report of the National Confidential Enquiry into Patient Outcome and Death (NCEPOD); 2007. p. 19.
[3] Patel H, Bouamra O, Woodford M, King A, Yates D, Lecky F, On behalf of the Trauma Audit and Research Network. Trends in head injury outcome from 1989 to 2003 and the effect of neurosurgical care: an observational study. Lancet 2005;366(9496):1538–44.
[4] Voss M, Knottenbelt J, Peden M. Patients who reattend after head injury: a high risk group. BMJ 1995;311(7017):1395–8.
[5] D'Antoni AV. In: Moore KL, Dalley AF II, Agur AMR, editors. Clinically Oriented Anatomy. 7th ed. Baltimore, MD: Lippincott Williams & Wilkins; 2014. p. 1134.
[6] Holder D. Electrical impedance tomography methods, history and applications. UK: IOP Publishing; 2005.

Please cite this article in press as: Ayati SB, et al. *In vitro* localisation of intracranial haematoma using electrical impedance tomography semi-array. Med Eng Phys (2014), http://dx.doi.org/10.1016/j.medengphy.2014.10.001

[7] Sadleir R, Zhang S, Tucker A, Oh S. Imaging and quantification of anomaly volume using an eight-electrode 'hemiarray' EIT reconstruction method. Physiol Meas 2008;29:913–27.
[8] Tang T, Oh S, Sadlier R. A robust current pattern for the detection of intraventricular hemorrhage in neonates using electrical impedance tomography. Ann Biomed Eng 2010;38(8):2733–47.
[9] Bagshaw A, Liston A, Bayford R, Tizzard A, Gibson A, Tidswell A, et al. Electrical impedance tomography of human brain function using reconstruction algorithms based on the finite element method. Neuroimage 2003;20(2):752–64.
[10] Liston A, Bayford R, Holder D. The effect of layers in imaging brain function using electrical impedance tomography. Physiol Meas 2004;25:143–58.
[11] Ayati S, Bouazza-Marouf K, Kerr D, O'Toole M. Performance evaluation of a digital electrical impedance tomography system. In: Proceedings of the IASTED international symposia in imaging and signal processing in health care and technology. 2012. p. 101–5.
[12] Kandadai M, Raymond J, Shaw G. Comparison of electrical conductivities of various brain phantom gels: developing a 'brain gel model'. Mater Sci Eng C 2012;32:2664–7.
[13] Oh S, Tang T, Tucker A, Sadleir R. Normalization of a spatially variant image reconstruction problem in electrical impedance tomography using system blurring properties. Physiol Meas 2009;30(3):275–89.
[14] Hansen P, O'Leary D. The use of the L-curve in the regularization of discrete ill-posed problems. SIAM J Sci Comput 1993;14(6):1487–503.
[15] Sadleir R, Fox R. Quantification of blood volume by electrical impedance tomography using a tissue equivalent phantom. Physiol Meas 1998;19:501–16.
[16] Xu C, Dai M, You F, Shi X, Fu F, Liu R, et al. An optimized strategy for real-time haemorrhage monitoring with electrical impedance tomography. Physiol Meas 2011;32(5):585–98.
[17] Xu CH, Wang L, Shi XT, You FS, Fu F, Liu RG, et al. Real-time imaging and detection of intracranial haemorrhage by electrical impedance tomography in a piglet model. J Int Med Res 2010;38(5):1596–604.
[18] Tucker A, Ross E, Paugh-Miller J, Sadlier R. In vivo quantification of accumulating abdominal fluid using an electrical impedance tomography hemiarray. Physiol Meas 2011;32(2):151–65.
[19] Zlochiver S, Arad M, Radai M, Barak-Shinar D, Krief H, Engelman T, et al. A portable bio-impedance system for monitoring lung resistivity. Med Eng Phys 2007;29(1):93–100.
[20] Yvert B, Bertrand O, Thvenet M, Echallier J, Pernier J. A systematic evaluation of the spherical model accuracy in EEG dipole localization. Electroencephalogr Clin Neurophysiol 1997;102:452–9.
[21] Taktak A, Record P, Gadd R, Rolfe P. Data recovery from reduced electrode connection in electrical impedance tomography. Med Eng Phys 1996;18(6):519–22.
[22] Wardlaw J, Lewis S, Sandercock P, Ricci S, Spizzichino L. Why do Italian stroke patients receive CT scans earlier than UK patients? Postgrad Med J 1999;75(879):18–21.

Please cite this article in press as: Ayati SB, et al. *In vitro* localisation of intracranial haematoma using electrical impedance tomography semi-array. Med Eng Phys (2014), http://dx.doi.org/10.1016/j.medengphy.2014.10.001

International Journal of Computers and Applications, Vol. 36, No. 2, 2014

# HAEMATOMA DETECTION USING EIT IN A SHEEP MODEL

S. B. Ayati,* Kaddour Bouazza-Marouf,* David Kerr,* and Michael O'Toole**


## Abstract

Performance evaluation of a portable digital electrical impedance tomography system to detect haematomas using phantom and sheep models is presented. Experiments have been performed using 8-electrode full array configuration. Conductivity changes were detected in phantom model while anomalies were placed at centre and close to the edge of the tank. Bleeding rate was successfully monitored in sheep model while blood-like conductivity solution was injecting via the brainstem. EIT images were reconstructed sequentially for different injection volumes and the quantity index (QI) was calculated as a function of the injected solution volume. The results show a linear relationship of QI to the injected volume. Images of the sheep experiment with the simulated haematomas, blood-like conductivity gel, placed on top of the parietal lobes of the brain on the left and right sides were reconstructed and haematomas are clearly detected and localized. These experiments prove that the detection and quantification of haematomas in the brain is possible and encourage further investigation for medical applications.



## Key Words

Electrical impedance tomography, haematoma, sheep model, assistive medical technology, medical image processing


## 1. Introduction

Intracranial haematomas are pockets of blood that build-up within the cranial vault as a result of haemorrhage from a head injury. The haemorrhage is an active bleeding and the haematoma's excess blood is not reabsorbed into the body system and may also increase in size and become a serious condition. These pockets expand and increase the intracranial pressure on the brain, causing impairment of the ability of the brain to function and worsening the neurological condition of the patient. If left unchecked, the growing haematoma will cause severe and even permanent damage to the delicate tissue of the brain, the morbidity and eventually death of the patient. The development of the haematoma from benign to symptomatic can be sudden, and a patient can change from lucid to a state of rapid neurological deterioration over a very short period of time [1].

Acute imaging of the head is the first action when a patient arrives in the emergency department on suspicion of head injury to identify the necessity of urgent (treatments) surgical intervention or stabilization to prevent further injury. The current appropriate imaging technique used in the acute phase is CT scanning. However CT scanning or MRI in the UK are not always available for 24 h a day, and in cases of multiple traumas, it may not be possible to scan the patient until they have been adequately stabilized. The transporting requirement of ill patients and equipment compatibility restrict using this method for the acute care. These imaging techniques are not portable and suitable for continuous monitoring and involve large personnel or equipment cost [2].

There is a direct and urgent clinical need for a robust, easy to use and low-cost system which can accurately detect the presence of a haematoma in high risk patients. A device of this nature can reduce treatment delays, save on costs and waste, and most significantly, positively impact patient outcomes. It also provides a primary and possibly sole method of haematoma detection when CT scanning or MRI is unavailable or impossible. Treatment delays are mitigated by giving better and earlier information on haematomas at the triage stage. The time from injury to treatment is a key factor in patient recovery, and earlier diagnosis leads to earlier treatment.

Electrical impedance tomography (EIT) is a non-invasive, non-radiating, non-ionizing and inexpensive technique. EIT has the capability of long-term monitoring and can be used to approximately localize the bleeding site. EIT is a medical imaging technique which reconstructs cross-sectional images of the electrical property distribution of an object within a body based on voltage measurements on its boundary. Data acquisition is performed through an array of electrodes which are attached to the surface of the body. EIT has been extensively researched in various clinical applications due to its potential to distinguish between healthy and abnormal components of an organ [3].

EIT is a relatively new medical imaging modality and present significant possibilities for medical application, including head and abdominal imaging. The aim of this

* Wolfson School of Mechanical and Manufacturing Engineering, Loughborough University, UK; e-mail: {Bent, s.b.ayati}@lboro.ac.uk
** School of Computer Science, University of Manchester, UK; e-mail: Michael.OToole@cs.man.ac.uk
*Recommended by Dr. M. Hamza*
*(DOI: 10.2316/Journal.202.2014.2.202-3834)*

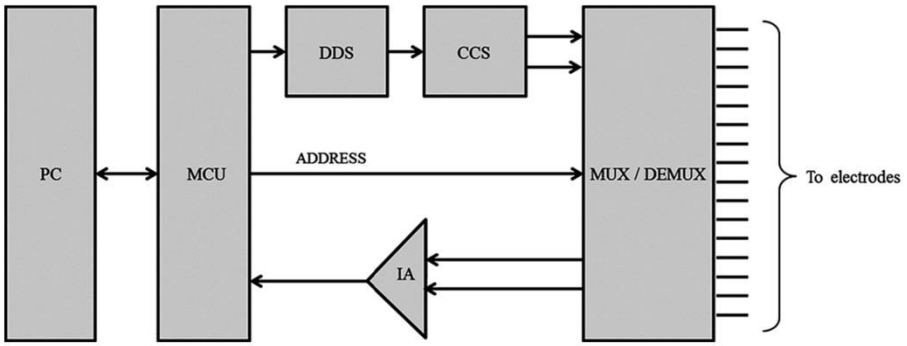


Figure 1. EIT system architecture.

paper is to evaluate the sensitivity of a digital EIT system constructed in our laboratory to detect and localize simulated haematomas in phantom and sheep models. The relationship between the injected simulated blood and the conductivity distribution in EIT images was investigated in a sheep's head.

## 2. Materials and Methods

### 2.1 System Specification and Methods

The structure of the designed EIT system based on a microcontroller is presented in Fig. 1. The system is controlled by a microcontroller connected to a PC through a serial port (RS232). A graphical user interface was developed using Visual Basic (VB). The Constant Current Source (CCS) generates a constant sinusoidal current fed by a sinusoidal signal of the same frequency generated by the Direct Digital Synthesizer (DDS).

The current was injected through one pair of adjacent electrodes and the corresponding boundary potentials were measured over pairs of the remainder of the neighbouring electrodes using a multiplexer. The input pair of electrodes was switched over all adjacent pair electrodes and the measurement procedure was repeated for all possible adjacent pairs. The measurements were amplified using an Instrumentation Amplifier (IA) to produce a complete voltage data set. The performance of this system was previously evaluated using phantom experiments [4].

This multi-frequency EIT system has 16 channels and operates in the frequency range of 25–100 kHz with the temporal resolution of 100 frames per second. For this experiment, a constant current of 1 mA at a single frequency of 50 kHz and 8 electrodes were chosen.

### 2.2 Phantom Configuration

The EIT system is evaluated using phantom experiments in the presence of realistic noise. The phantom system consists of a shallow nylon tank, 8 electrodes, the background solution and the simulated anomalies (cucumber segments). The tank has a depth of 80 mm and an inner diameter of 144 mm. The phantom is equipped with 8 stainless steel screws as point electrodes (diameter 10 mm) equally spaced in a ring around the tank wall. All the lead wires are of equal lengths to obtain an identical impedance path through all the electrodes in order to reduce the mismatch in electrode impedances. 0.38% saline solution with the conductivity of approximately 1 S/m is used for the background solution. Cylindrical pieces of cucumber with the conductivity of 0.05 S/m are used as anomalies. The anomalies have a diameter of approximately 40 mm and the same height as the tank.

### 2.3 Sheep Preparation

Two fresh sheep heads were obtained from a local butcher and skinned. The locations of the 8 electrodes of the full array configuration were marked on the skull with the equal distance between electrodes. Eight 10 mm Ag/AgCl disk electrodes (Unimed Electrode Supplies Ltd) were fastened to the skull using conductive paste (Unimed Electrode Supplies Ltd).

A saline solution with the same conductivity as blood (0.67 S/m) was made with the concentration of 0.33% [weight/volume] of sodium chloride in water. In the first sheep's head the blood-equivalent saline was injected near the ventricles via the brainstem. The injections were made in increments of 0.5–9 ml using a long syringe. Blood has higher conductivity than brain tissue (0.17 S/m) thus increases in blood volume should result in increase of conductivity increment in the reconstructed images [5].

In the above experiment, blood was spread out inside the skull without any limitation because of the absence of CSF and brain pressure. In order to simulate a more realistic haematoma in an accurate location, the saline solution was transformed to gel. The saline solution was stirred using a magnetic stir bar at a temperature of 70°C while agar powder (Fisher Scientific) was added to achieve the desired gel concentration (1.7% by weight). Then the solution was poured into a tube with the diameter of 1 cm and allowed to cool at room temperature. The gel sample was removed from the tube and cut to lengths of 3 mm to use as pockets of blood. The conductivity of the gel sample was measured and found to be the same as the conductivity of the saline solution. An AC voltage was applied across the gel at a frequency of 50 kHz at room temperature using

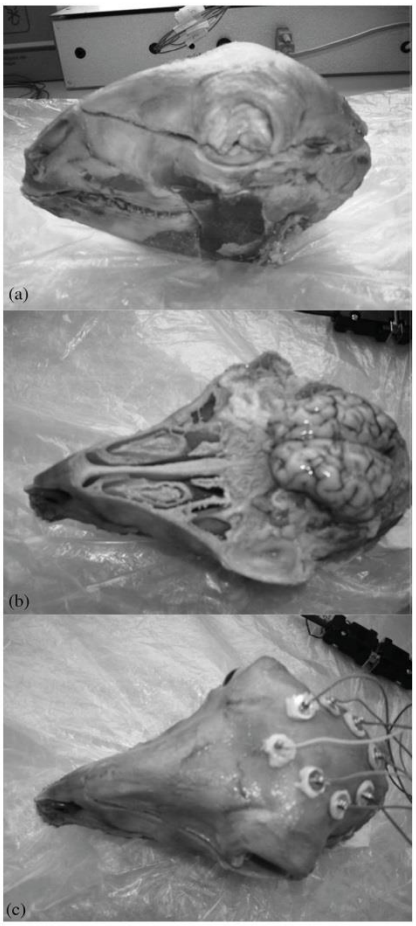


Figure 2. (a) Side view of sheep with cut skull; (b) top view with complete brain out; and (c) top view with full array electrodes attached.

a waveform function generator connected in series with a digital multimeter to measure the AC current and AC voltage across the gel.

For the second sheep's head, the skull was cut approximately in half as shown in Fig. 2 using a bone saw. The top half of the skull was carefully removed and the brain was exposed. A gel sample was placed on top of the parietal lobes at approximately the middle of the posterior quarter of the brain on the left and right sides. The top half of the skull was replaced and the measurement was performed.

### 2.4 Reconstruction and Processing

EIT is composed of forward problem and inverse problem. The forward problem is to predict the measured boundary electric potentials from the known applied current density and conductivity distribution. The aim of the inverse problem which is also known as image reconstruction is to estimate the conductivity distribution from a known set of boundary voltage measurements.

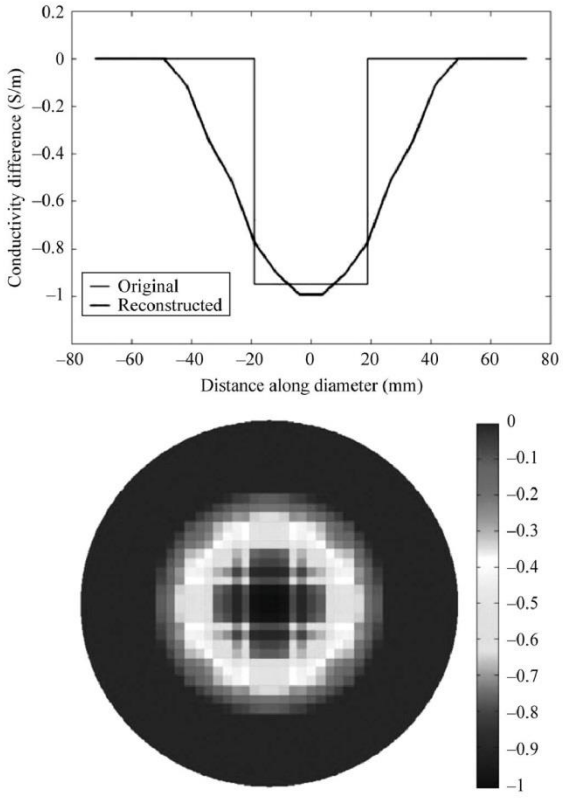


Figure 3. DRP and reconstructed image of phantom with one target at centre.

For the forward problem the complete electrode model was used and defined by the following equations (1–4):

$$\nabla \cdot (\sigma \nabla u) = 0 \quad \text{on } \Omega \tag{1}$$

$$u + z_l \sigma \frac{\partial u}{\partial n} = V_l \quad \text{on } \varepsilon_l, l = 1, 2, \ldots, L \tag{2}$$

$$\int_{\varepsilon_l} \sigma \frac{\partial u}{\partial n} ds = I_l \quad \text{on } \varepsilon_l, l = 1, 2, \ldots, L \tag{3}$$

$$\sigma \frac{\partial u}{\partial n} = 0 \quad \text{on } \partial\Omega \backslash \{\varepsilon_1 \cup \varepsilon_2 \cup \ldots, \varepsilon_L\} \tag{4}$$

To provide the forward solution, the finite element method (FEM) was used in Comsol (Comsol Multiphysics).

The images were reconstructed using the sensitivity method. The sensitivity matrix was calculated from forward solutions of a two-dimensional disk model. The model was discretized to 3032 second-order triangular finite elements. The conductivity distribution of the brain tissue is generally not known *a priori* and therefore $S$ was calculated assuming a homogenous conductivity distribution. To determine the conductivity changes, the sensitivity matrix was inverted as (5):

$$\triangle\sigma \cong S^{\dagger} \triangle V \tag{5}$$

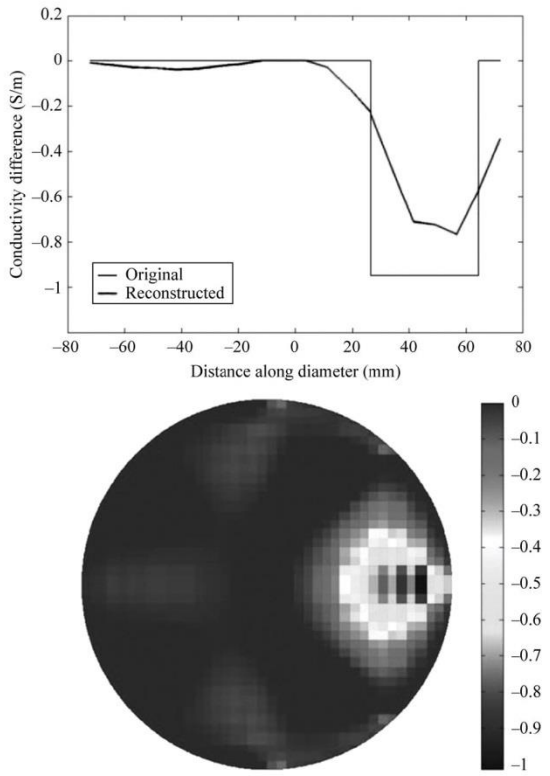


Figure 4. DRP and reconstructed image of phantom with one target close to edge of the tank.

where $S^{\dagger}$ is the Moore-Penrose pseudo inverse of $S$. Since the EIT inverse problem is severely ill-posed and a small amount of noise on boundary measurements, $\triangle V$, can cause a large oscillation for the solution, $\triangle\sigma$, a regularization technique was used to reduce this effect by improving the conditioning of $S$. The truncated singular value decomposition (TSVD) method which has previously been identified as a suitable regularization method [6] was used to regularize the inversion of the sensitivity matrix. The truncation point $k$, needs to be chosen carefully, less than or equal to the rank of the matrix, as it would otherwise produce inaccurate images. The truncation point was chosen on inspection of the L-curve of experimental data [7].

The quantity index (QI) is defined as an EIT image parameter that correlates with the anomaly volume. The QI is the integral of conductivity change multiplied by the area of the element over the image area as (6):

$$QI = \sum_{i=1}^{ne} \triangle\sigma_i a_i \tag{6}$$

where, for an element (or pixel) $i$, $\triangle\sigma_i$ is the conductivity change reconstructed in the $i$th element, $a_i$ is the area of each element and $ne$ is the total number of elements.

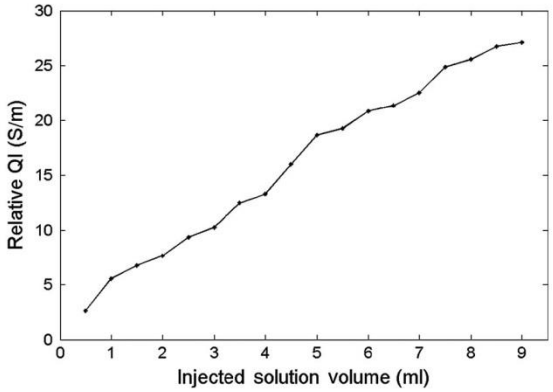


Figure 5. QI as a function of injected saline solution volume.

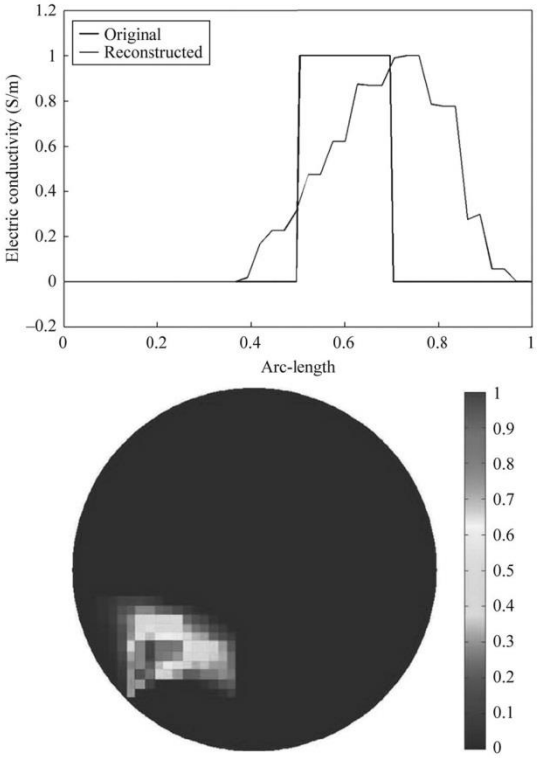


Figure 6. DCP and reconstructed image of the haematoma on top of the left parietal lobe.

The position of the anomaly $(x, y)$ can be estimated from reconstructed images using by (7, 8):

$$x = \frac{\sum_{i=1}^{ne} \triangle\sigma_i a_i x_i}{\sum_{i=1}^{ne} \triangle\sigma_i a_i} \tag{7}$$

$$y = \frac{\sum_{i=1}^{ne} \triangle\sigma_i a_i y_i}{\sum_{i=1}^{ne} \triangle\sigma_i a_i} \tag{8}$$

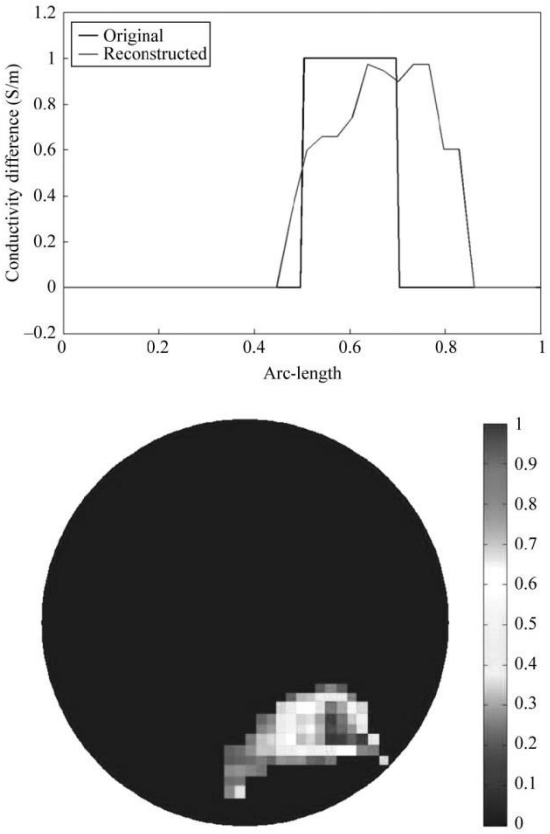


Figure 7. DCP and reconstructed image of the haematoma on top of the right parietal lobe.

The expression for anomaly location $(x, y)$ is effectively the centre of the reconstructed anomaly. The values $x_i$ and $y_i$ are the coordinates of the centre of each element. Diametric conductivity plot (DCP) is the conductivity difference profile of the model based on the diameter passing through the reconstructed object centre. It is plotted in terms of the arc-length of the diameter.

## 3. Results

Figures 3 and 4 show DRP and the reconstructed images of the phantom with single target from the potential data. The images are successfully reconstructed and the targets at different positions are clearly detected. In the images the blue region which represents conductivity decreasing of 0.95 S/m appeared in the image in accordance with the position of the target. The single target placed at the centre is illustrated in Fig. 3, and close to the edge of the tank at electrode No. 1 is shown in Fig. 4. It is observed that the reconstructed DRPs almost follow the DRP of the original object.

In the first sheep's head, where the blood-like solution was injected into the ventricles, the location of the solution was not accurately known. Therefore, the EIT images were reconstructed sequentially and the QI was calculated as a function of the injected solution volume as shown in Fig. 5. The plot shows the linear relationship between QI and injected volume. The calculated QI increased as more solution is injected.

In the second sheep's head, a simulated haematoma was placed at a certain position. DCP and the reconstructed image of the brain with such a haematoma placed on top of the left parietal lobe are shown in Fig. 6. It can be seen that the image is successfully reconstructed and the haematoma is clearly detected. In the image, the red region (which represents a conductivity increase of approximately 1 S/m) appeared in the image in accordance with the position of the haematoma. It is observed that the reconstructed DCP almost follows the DCP of the original object. The centre of the reconstructed anomaly on the left side was calculated as $(-0.5240R, -0.4584R)$ where $R$ is the radius of the imaged brain.

DCP and the reconstructed image of the brain with a haematoma placed on top of the right parietal lobe are also shown in Fig. 7. In the reconstructed image the main perturbation is produced close to the correct location with localized changes corresponding to the haematoma. The reconstruction shows the haematoma on the right side and the reconstructed DCP almost follows the DCP of the original object. The centre of the reconstructed anomaly on the right side was calculated as $(0.4043R, -0.5282R)$.

## 4. Conclusion

Images of conductivity changes are successfully reconstructed with single anomalies in phantom model while the anomaly placed at the centre and close to the edge of the tank. Simulated haematoma are also detected and localized in sheep's head. The experiment, in which simulated bleeding rate was monitored continuously, does establish that haematoma with a volume of less than 2 ml can be quantified and detected. The exact position of the simulated haematoma could not be detected since the simulated blood was spread out inside the skull in the absence of CSF and brain pressure, and its position was unknown. Therefore the simulated blood solution was transformed to gel with the same conductivity as blood and placed in a certain position. Simulated haematomas in sheep model were clearly detected and localized using our developed system. The presented results demonstrate that our EIT system is sensitive to the conductivity variation and has the potential to produce reliable and localized images from the boundary potential measurements. These phantom and sheep experiments prove that the detection and quantification of haematomas in the brain is possible and encourage further investigation for medical applications.

## References

[1] T. Mertol, M. Guner, U. Acar, H. Atabay, and U. Kirisoglu, Delayed traumatic intracerebral hematoma, *British Journal of Neurosurgery*, *5*(5), 1991, 491–498.

[2] D. Yates, *Head injury: triage, assessment, investigation and early management of head injury in infants, children and adults; methods, evidence and guidance* (The Royal College of Surgeons of England, London: National Collaborating Centre for Acute Care, 2007).

[3] D.S. Holder, *Electrical impedance tomography: methods, history and applications* (GB: Institute of Physics, 2005).
[4] S. Bentolhoda Ayati, K. Bouazza-Marouf, D. Kerr, and M. O'Toole, Performance evaluation of a digital electrical impedance tomography system, *Imaging and Signal Processing in Health Care and Technology* (ISPHT 2012), Baltimore, MD, 2012, 101–105.
[5] L.A. Geddes and L.E. Baker, The specific resistance of biological material – a compendium of data for the biomedical engineer and physiologist, *Medical & Biological Engineering*, *5*(3), 1967, 271–293.
[6] S. Oh, T. Tang, A. Tucker, and R. Sadleir, Normalization of a spatially variant image reconstruction problem in electrical impedance tomography using system blurring properties, *Physiological Measurement*, *30*(3), 2009, 275–289.
[7] P.C. Hansen and D.P. O'Leary, The use of the L-curve in the regularization of discrete ill-posed problems, *SIAM Journal of Science and Computing*, *14*(6), 1993, 1487–1503.

## Biographies

*S. B. Ayati* obtained her B.Sc. in Electrical Engineering from Azad University, Iran. After completing her M.Sc. at Kingston University in London, she briefly worked at Azad University in Iran as a part-time lecturer before moving to Loughborough University to commence her Ph.D. studies. She is currently a Ph.D. student at Loughborough University in the United Kingdom. Her research interest is medical imaging and electrical impedance tomography.

*Kaddour Bouazza-Marouf* is reader in Mechatronics in Medicine at Loughborough University and fellow of the Institution of Mechanical Engineers. He teaches Control Engineering and Robotics. His main research area is Mechatronics in Medicine/Surgery, in particular invasive and non-invasive robotic/computer assistance in orthopaedic surgery, mechatronic assistance in neurosurgery and medical devices.

*David Kerr* is a senior lecturer in Optical Engineering and Computer vision. He obtained his Ph.D. in 1992 for work on "The Extraction of Displacement Data from Electronic Speckle Pattern Interferometric Fringe Patterns using Digital Image Processing Techniques." His research interests include automatic visual inspection, digital image processing, interferogram analysis and laser applications. He is the author of over 40 papers in the fields of image processing, fringe analysis and optical engineering.